NUREG/CR-6507
PSU/ME-97-7321

Critical Heat Flux (CHF) Phenomenon on a Downward Facing Curved Surface

Prepared by
F. B. Cheung, K. H. Haddad, Y. C. Liu

Department of Mechanical Engineering
The Pennsylvania State University

Prepared for
U.S. Nuclear Regulatory Commission

AVAILABILITY NOTICE

Availability of Reference Materials Cited in NRC Publications

Most documents cited in NRC publications will be available from one of the following sources:

1. The NRC Public Document Room, 2120 L Street, NW., Lower Level, Washington, DC 20555-0001
2. The Superintendent of Documents, U.S. Government Printing Office, P. O. Box 37082, Washington, DC 20402-9328
3. The National Technical Information Service, Springfield, VA 22161-0002

Although the listing that follows represents the majority of documents cited in NRC publications, it is not intended to be exhaustive.

Referenced documents available for inspection and copying for a fee from the NRC Public Document Room include NRC correspondence and internal NRC memoranda; NRC bulletins, circulars, information notices, inspection and investigation notices; licensee event reports; vendor reports and correspondence; Commission papers; and applicant and licensee documents and correspondence.

The following documents in the NUREG series are available for purchase from the Government Printing Office: formal NRC staff and contractor reports, NRC-sponsored conference proceedings, international agreement reports, grantee reports, and NRC booklets and brochures. Also available are regulatory guides, NRC regulations in the *Code of Federal Regulations,* and *Nuclear Regulatory Commission Issuances.*

Documents available from the National Technical Information Service include NUREG-series reports and technical reports prepared by other Federal agencies and reports prepared by the Atomic Energy Commission, forerunner agency to the Nuclear Regulatory Commission.

Documents available from public and special technical libraries include all open literature items, such as books, journal articles, and transactions. *Federal Register* notices, Federal and State legislation, and congressional reports can usually be obtained from these libraries.

Documents such as theses, dissertations, foreign reports and translations, and non-NRC conference proceedings are available for purchase from the organization sponsoring the publication cited.

Single copies of NRC draft reports are available free, to the extent of supply, upon written request to the Office of Administration, Distribution and Mail Services Section, U.S. Nuclear Regulatory Commission, Washington, DC 20555-0001.

Copies of industry codes and standards used in a substantive manner in the NRC regulatory process are maintained at the NRC Library, Two White Flint North, 11545 Rockville Pike, Rockville, MD 20852-2738, for use by the public. Codes and standards are usually copyrighted and may be purchased from the originating organization or, if they are American National Standards, from the American National Standards Institute, 1430 Broadway, New York, NY 10018-3308.

DISCLAIMER NOTICE

This report was prepared as an account of work sponsored by an agency of the United States Government. Neither the United States Government nor any agency thereof, nor any of their employees, makes any warranty, expressed or implied, or assumes any legal liability or responsibility for any third party's use, or the results of such use, of any information, apparatus, product, or process disclosed in this report, or represents that its use by such third party would not infringe privately owned rights.

NUREG/CR-6507
PSU/ME-97-7321

Critical Heat Flux (CHF) Phenomenon on a Downward Facing Curved Surface

Manuscript Completed: March 1997
Date Published: June 1997

Prepared by
F. B. Cheung, K. H. Haddad, Y. C. Liu

Department of Mechanical Engineering
The Pennsylvania State University
137 Reber Building
University Park, PA 16802-1412

Prepared for
Division of Systems Technology
Office of Nuclear Regulatory Research
U.S. Nuclear Regulatory Commission
Washington, DC 20555-0001
NRC Job Code J6030

HH

ABSTRACT

This report describes a theoretical and experimental study of the boundary layer boiling and critical heat flux phenomena on a downward facing curved heating surface, including both hemispherical and toroidal surfaces. A subscale boundary layer boiling (SBLB) test facility was developed to measure the spatial variation of the critical heat flux and observe the underlying mechanisms. Transient quenching and steady-state boiling experiments were performed in the SBLB facility under both saturated and subcooled conditions to obtain a complete database on the critical heat flux. To complement the experimental effort, an advanced hydrodynamic CHF model was developed from the conservation laws along with sound physical arguments. The model provides a clear physical explanation for the spatial variation of the CHF observed in the SBLB experiments and for the weak dependence of the CHF data on the physical size of the vessel. Based upon the CHF model, a scaling law was established for estimating the local critical heat flux on the outer surface of a heated hemispherical vessel that is fully submerged in water. The scaling law, which compares favorably with all the available local CHF data obtained for various vessel sizes, can be used to predict the local CHF limits on large commercial-size vessels.

CONTENTS

Page

Abstract iii

Executive Summary xv

Abbreviations xvii

1. Introduction 1
    - 1.1 Background 1
    - 1.2 Major Objectives 1
    - 1.3 Physical Significance of the Project 2

2. Literature Survey 5
    - 2.1 Quenching Experiments 5
        - 2.1.1 Inclined, Downward Facing, Flat Heating Surfaces 5
        - 2.1.2 Cylindrical Heating Surfaces 6
        - 2.1.3 Spherical Heating Surfaces 6
            - 2.1.3.1 Local Variation of the Boiling Curve 6
            - 2.1.3.2 Effect of the Sphere Diameter 8
    - 2.2 Steady-State Heating Experiments 8
        - 2.2.1 Inclined, Downward Facing, Flat Heating Surfaces 8
            - 2.2.1.1 Effect of the Angle of Inclination on the Boiling Curve 8
            - 2.2.1.2 Bubble Dynamics on Inclined Flat Surfaces 10
        - 2.2.2 Cylindrical Heating Surfaces 11
            - 2.2.2.1 Local Variation of the Boiling Curve 11
            - 2.2.2.2 Bubble Dynamics on a Cylindrical Heating Surface 14
            - 2.2.2.3 Effect of the Cylinder Diameter 14

2.2.3 Toroidal and Spherical Heating Surfaces 14

2.2.3.1 Local Variation of the Boiling Curve 14

2.2.3.2 Bubble Dynamics on a Torispherical Surface 15

2.3 Effect of Subcooling 18

2.4 Relationship Between Quenching Data and Steady-State Data 19

2.5 Critical Heat Flux Models 19

2.5.1 CHF Models for Upward Facing Flat Plates 19

2.5.2 CHF Models for Spherical Heating Surfaces 22

2.6 References 24

3. Experimental Method 29

3.1 Experimental Apparatus 29

3.1.1 Water Tank and Condenser Assembly 29

3.1.1.1 Water Tank 29

3.1.1.2 Condenser 34

3.1.2 Segmented Hemisphere 34

3.1.3 Continuous Vessels for Steady-State Experiments 37

3.1.4 Test Vessel Using Cartridge Heaters 37

3.1.5 Continuous Vessels for Quenching Experiments 40

3.1.6 Data Acquisition System 42

3.1.7 Power Control System for CHF Measurement 43

3.2 Experiment Procedure 43

3.2.1 Water Preparation 45

3.2.2 Quenching Experiments 45

3.2.3 Steady State Experiments 45

3.3 Data Reduction 45

3.3.1 Inverse Heat Conduction Programs for Quenching Experiments 45

3.3.2 Inverse Heat Conduction Programs for Steady State Experiments 46

3.3.3 Error Estimates 47

3.4 References 48

4. Experimental Results 49

4.1 Quenching Experiments 49

4.1.1 Dynamic Behavior of the Two-Phase Boundary Layer During Transient Quenching 49

4.1.2 Local Variation of the Boiling Curve on the Outer Surface of a Heated Hemispherical Vessel 54

4.1.2.1 Saturated Boiling 54

4.1.2.2 Subcooled Boiling 56

4.1.3 Variations of the Local Critical Heat Flux 59

4.2 Steady State Experiments 59

4.2.1 Observation of the Steady-State Two-Phase Boundary Layer 59

4.2.2 Effect of Subcooling on the Behavior of the Two Phase Boundary Layer 62

4.2.3 Variation of the Vapor Size Along the Vessel Outer Surface 66

4.2.4 High-Heat-Flux Nucleate Boiling Regime 66

4.2.5 Steady-State Heat Transfer Measurements 67

4.2.6 Comparison of the Steady State and Transient Quenching Results 72

4.3 Summary of the CHF Data Obtained in the SBLB Facility 72

4.3.1 Comparison with the Full-Scale Data 72

4.3.2 Correlation of the SBLB Critical Heat Flux Data 72

4.4 References 76

5. Theoretical Modeling 77

5.1 Introduction 77

5.2 Upward Facing Surfaces 77

5.3 Downward Facing Hemispherical Surfaces 78

5.3.1 Behavior of the Micro-Layer 79

5.3.2 Occurrence of the Local CHF 80

5.4 Two-Phase Boundary Layer Analysis 82

5.5 Initial Conditions and the Universal Constant 84

5.6 Spatial Variation of the Critical Heat Flux 86

5.7 Liquid Entrainment and the Constant-Void-Fraction Postulation 89

5.8 Comparison with the SBLB Data 90

5.9 References 92

6. Development of the Scaling Law 95

6.1 Saturated Boiling Conditions 95

6.2 Subcooled Boiling Conditions 97

6.3 Application to Commercial-Size Vessels 97

6.4 References 103

7. Conclusions 105

7.1 Major Conclusions 105

7.2 References 106

Appendices

Appendix A Development of an Inverse Heat Conduction Code for the Segmented Hemispherical Test Vessel. A-1

Appendix B. Measurement Errors B-1

Appendix C. Steady-State Nucleate Boiling Data for a Downward Facing Hemispherical Surface C-1

Appendix D. Preliminary Scaling Analysis of the Effects of Thermal Insulation on the Cooling of the Lower Head in a Flooded Cavity D-1

Appendix E. Hydrodynamic CHF Model for Downward Facing Torispherical Surfaces E-1

Figures

Figure 1 Boundary Layer Boiling on the Exterior Surface of a Reactor Lower Head

Figure 2 Schematic of Configuration I Employed in the ULPU Experiments

Figure 3 Reference Reactor Power Shape Employed in the ULPU Experiments

Figure 4 Schematic of Configuration II Employed in the ULPU Experiments

Figure 5 Schematic of the CYBL Facility at Sandia National Laboratory

Figure 6 Various Regimes of Downward Facing Boiling Proposed by Chu et al. (1993) in the CYBL Experiments

Figure 7 The Proposed CHF Mechanisms Based on Helmholtz Instability (Carey 1992)

Figure 8 The Vapor Column Spacing in the Critical Heat Flux Model by Zuber (1959)

Figure 9 The Model of Haramura and Katto (1983) for Forced Convection Boiling

Figure 10 The Vapor Removal Mechanism Proposed by Den and Leinhard (1972)

Figure 11 The Model of Haramura and Katto (1983) for Forced Convection Boiling on a Horizontal Cylinder

Figure 12 Pictorial View of the Water Tank and the Condenser Assembly

Figure 13 Front View of the SBLB Water Tank Without the Condenser

Figure 14 Side View of the SBLB Water Tank with the Condenser

Figure 15 Connection Between the Tank Wall and the Tank Cover

Figure 16 Connection Between the Windows and the Tank

Figure 17 Schematic of the Vertical Sliding Mechanism in the Middle of the Tank

Figure 18 Top View of the Water Tank Showing the Locations of the Immersion Heaters

Figure 19 Schematic of the Condenser Housing

Figure 20 Side View of the Segmented Hemispherical Test Vessel

Figure 21 Schematic of the Supporting Mechanism Used to Pull the Segments Together

Figure 22 Locations of the Thermocouples in the First Segment

Figure 23 Top and Side Views of the Thermocouple Locations in the Second Segment

Figure 24 Top and Side Views of the Thermocouple Locations in the Third Segment

Figure 25 Top and Side Views of the Thermocouple Locations in the Fourth Segment

Figure 26 Top and Side Views of the Thermocouple Locations in the Fifth Segment

Figure 27 Top and Side Views of the Mold Used to Shape the Nichrome Coils

Figure 28 Side View of the Thick Aluminum Test Section in the Bottom Center Region of the Vessel

Figure 29 Top View of the Thick Aluminum Test Section

Figure 30 Thermocouple Locations on the Test Vessels for the Quenching Experiments

Figure 31 Schematic of the Power Control System

Figure 32 Configuration of the Control Volume and the Node Distribution in the Data Reduction Analysis

Figure 33 Schematic of the Two-Phase Boundary Layer Configuration in the Three Sequential Stages of Quenching

Figure 34 Sequence of Events Observed in the Initial and Intermediate Stages of Quenching

Figure 35 Sequence of Events Observed in the Intermediate and Final Stages of Quenching

Figure 36 Typical Temperature-Time Histories at Various Wall Locations During Quenching

Figure 37 Boiling Curves at Different Locations Along the Heating Surface (Saturated Boiling: Water at 100°C)

Figure 38 Boiling Curves at Different Locations Along the Heating Surface (Subcooled Boiling: Water at 97°C)

Figure 39 Boiling Curves at Different Locations Along the Heating Surface (Subcooled Boiling: Water at 93°C)

Figure 40 Boiling Curves at Different Locations Along the Heating Surface (Subcooled Boiling: Water at 90°C)

Figure 41 Boiling Curves at Different Subcooling Levels ($\ell/L = 0$)

Figure 42 Boiling Curves at Different Subcooling Levels ($\ell/L = 0.2$)

Figure 43 Boiling Curves at Different Subcooling Levels ($\ell/L = 0.35$)

Figure 44 Boiling Curves at Different Subcooling Levels ($\ell/L = 0.5$).

Figure 45 Boiling Curves at Different Subcooling Levels ($\ell/L = 0.75$).

Figure 46 Variation of the Critical Heat Flux with Subcooling at Different Locations on the Vessel Outer Surface

Figure 47 Spatial Variation of the Critical Heat Flux for Saturated and Subcooled Boiling

Figure 48 Configuration of the Two-Phase Boundary Layer in Steady-State Boiling

Figure 49 Nucleate Boiling in the Bottom Center Region of the Vessel at a Low Heat Flux Level

Figure 50 Nucleate Boiling in the Bottom Center Region of the Vessel at an Intermediate Heat Flux Level

Figure 51 Nucleate Boiling in the Bottom Center Region of the Vessel at a High Heat Flux Level

Figure 52 Nucleate Boiling in the Bottom Center Region of the Vessel With Heating of the Outer Segment Only

Figure 53 Variation of the Cyclic Ejection Frequency with the Heat Flux Level

Figure 54 Typical Time Responses of the Local Wall Temperature Following a Step Increase in the Wall Heat Flux

Figure 55 Steady-State Nucleate Boiling Measured at the Bottom Center of the Vessel ($\theta = 0°$)

Figure 56 Steady-State Nucleate Boiling Data Measured at an Off-Center Location ($\theta = 18°$)

Figure 57 Steady-State Nucleate Boiling Data Measured at an Off-Center Location ($\theta = 36°$)

Figure 58 Steady-State Nucleate Boiling Data Measured at an Off-Center Location ($\theta = 60°$)

Figure 59 Steady-State Nucleate Boiling Data Measured at an Off-Center Location ($\theta = 75°$)

Figure 60 Comparison of the Steady-State and Transient Quenching Data ($T_{water} = 100°$)

Figure 61 Comparison of the Steady-State and Transient Quenching Data ($T_{water} = 97°$)

Figure 62 Comparison of the Steady-State and Transient Quenching Data ($T_{water} = 93°$)

Figure 63 Comparison of the Steady-State and Transient Quenching Data ($T_{water} = 90°$)

Figure 64 Comparison of the Small-Scale and the Full-Scale CHF Data

Figure 65 Empirical Correlation of the SBLB Critical Heat Flux Data

Figure 66 Schematic of the Micro-Layer Underneath an Elongated Vapor Slug

Figure 67 Configuration of the Two-Phase Boundary Layer on the Outer Surface of a Heated Hemispherical Vessel

Figure 68 Spatial Variation of the Local Thickness of the Two-Phase Boundary Layer

Figure 69 Spatial Variation of the Local Vapor Velocity in the Two-Phase Boundary Layer

Figure 70 Spatial Variation of the Local Liquid Velocity in the Two-Phase Boundary Layer

Figure 71 Spatial Variation of the Local Critical Heat Flux on the Heating Surface

Figure 72 The Predicted Local Void Fraction Profiles in the Two-Phase Boundary Layer

Figure 73 Comparison of the Predicted Critical Heat Fluxes with Experimental Data

Figure 74 Spatial Variation of the Critical Heat Flux on the Outer Surface of a Hemispherical Vessel

Figure 75 Scaling of the Vessel Size Effect on the CHF Limit

Figure 76 Comparison of the Scaling Law for Saturated Boiling with CHF Data

Figure 77 Experimental Data Showing the Effect of Subcooling on the Local Critical Heat Flux

Figure 78 Comparison of the Scaling Law for Subcooled Boiling with CHF Data

Figure 79 Schematic of a Hemispherical Reactor Vessel in a Flooded Cavity

Figure 80 Application of the CHF Scaling Law: Baseline Case ($R = 2$m, $P \sim 1$atm)

Figure 81 Application of the CHF Scaling Law: Smaller vessel ($R = 1.5$m, $P \sim 1$atm)

Figure 82 Application of the CHF Scaling Law: Larger Vessel ($R = 3$m, $P \sim 1$ atm)

Figure 83 Application of the CHF Scaling Law: Higher Pressure ($R = 2$m, $P \sim 2$atm)

Figure A.1 Grid Structure for the First and Second Segments

Figure A.2 Grid Structure for the Third Segment

Figure A.3 Grid Structure for the Fourth Segment

Figure C.1 Nucleate Boiling Heat Transfer Coefficients at the Bottom Center of the Heated Vessel ($\theta = 0°$)

Figure C.2 Nucleate Boiling Heat Transfer Coefficients at an Off-Center Location ($\theta = 18°$)

Figure C.3 Nucleate Boiling Heat Transfer Coefficients at an Off-Center Location ($\theta = 36°$)

Figure C.4 Nucleate Boiling Heat Transfer Coefficients at an Off-Center Location ($\theta = 60°$)

Figure C.5 Nucleate Boiling Heat Transfer Coefficients at an Off-Center Location ($\theta = 75°$)

Figure D.1 Schematic of the AP600 Reactor Vessel Thermal Insulation System

Figure D.2 Schematic of the Control Volume (C.V.) Selected for the Insulation System

Figure E.1 Schematic of the Two-Phase Boundary Layer on the Outside of a Torispherical Heating Surface

Figure E.2 The Micro-Layer and the Vapor Slug at the Bottom Center of the Vessel

Tables

Table 1 Relevant CHF Data Obtained Through Steady-State and Transient Quenching Experiments Using Water

Table 2 Scan Rates of the Data Acquisition System at Different Resolution Settings

Table 3 Comparison of the Local Critical Heat Fluxes Measured at Various Test Facilities Under Saturated and Subcooled Boiling Conditions

Table C-1 Steady State Nucleate Boiling Data at the Bottom Center of the Hemispherical Test Vessel ($\theta = 0°$)

Table C-2 Steady State Nucleate Boiling Data at an Off-Center Location ($\theta = 18°$)

Table C-3 Steady State Nucleate Boiling Data at an Off-Center Location ($\theta = 36°$)

Table C-4 Steady State Nucleate Boiling Data at an Off-Center Location ($\theta = 60°$)

Table C-5 Steady State Nucleate Boiling Data at an Off-Center Location ($\theta = 75°$)

EXECUTIVE SUMMARY

The pool boiling and critical heat flux phenomena on a downward facing curved surface and the resulting two-phase boundary layer flow behavior are investigated experimentally and theoretically in this project. The primary objectives are to seek a fundamental understanding of the boundary layer boiling process and to determine the spatial variation of the critical heat flux (CHF) along the heating surface. This technical information represents one of the essential elements that are needed in assessing the efficacy of external cooling of core melt by cavity flooding as a severe accident management strategy. A subscale boundary layer boiling (SBLB) test facility, consisting of a pressurized water tank with a condenser unit, a heated hemispherical/toroidal vessel, and a data acquisition/photographic system, has been developed to simulate the boiling process on the external bottom surface of a reactor vessel. The facility, which can be operated at a pressure up to 20 psig, is used to perform photographic studies and heat transfer measurements on continuous and segmented vessels of varying sizes. Transient quenching and steady-state boiling experiments have been conducted in the facility under well controlled saturated and subcooled conditions. Based upon the experimental observations, key parameters and flow quantities that contribute to the occurrence of the CHF state have been identified and an advanced hydrodynamic CHF model has been developed.

Results obtained in this project indicate that for both saturated and subcooled boiling, the two-phase boundary layer flow is three-dimensional although it is axisymmetrical. Large elongated vapor slugs tend to form in the bottom region whereas those in the upper positions of the vessel are considerably smaller. Because of the activities of the large elongated vapor slugs, there are strong upstream influences throughout the two-phase boundary layer. These 3-D flow configurations as well as the divergence effect of the flow cannot be simulated by two-dimensional experiments or by downward facing inclined flat plates. Consistent with the observed flow behavior, the local boiling curve and the critical heat flux are found to vary significantly along the vessel outer surface. In particular, the local critical heat flux increases by more than 100% from the bottom center to the upper edge of the vessel. Subcooling tends to decrease the bubble size and increase the local CHF values. The nucleate boiling heat fluxes measured under steady-state conditions are consistently higher than those determined from transient quenching experiments. However, the two sets of data tend to merge together as the CHF limit is approached. In particular, the local CHF values deduced from the transient quenching data appear to be very close to those obtained in the steady-state boiling experiments. The present results have been compared with available 2-D full-scale CHF data. It is found that the differences between the subscale and full-scale CHF data are relatively small except in a region very close to the bottom center. The relatively large difference in the CHF value at the bottom center between the subscale and full-scale results is not due to the difference in the physical size of the test vessel. Rather, it is caused by the divergence effect which was not simulated in the 2-D full-scale tests. The angular position of the curved heating surface and the degree of subcooling of water have dominant effects on the local critical heat flux. They totally dwarf the effect of the physical dimensions of the test vessel.

To supplement the experimental work, a comprehensive theoretical model has been successfully developed to predict the critical heat flux (CHF) limit for pool boiling on the outer surface of a heated hemispherical vessel. The model considers the existence of a micro-layer underneath an elongated vapor slug on the downward facing curved heating surface. The micro-layer is treated as a thin liquid film with numerous micro-vapor jets penetrating through it. The micro-jets have the characteristic size dictated by Helmholtz instability. Local dryout is considered to occur when the supply of fresh

liquid from the two-phase boundary layer to the micro-layer is not sufficient to prevent depletion of the liquid film by boiling. A boundary layer analysis, treating the two-phase motion as an external buoyancy-driven flow, is performed to determine the liquid supply rate and thus the local critical heat flux. The model provides a clear physical explanation for the spatial variation of the CHF observed in experiments and for the weak dependence of the CHF data on the physical size of the vessel.

Based upon the hydrodynamic CHF model developed in this project, a scaling law has been successfully developed for estimating the local critical heat flux on the outer surface of a heated hemispherical vessel that is fully submerged in water. The scaling law accounts for the effects of the size of the vessel, the level of liquid subcooling, the intrinsic properties of the fluid, and the spatial variation of the local critical heat flux along the heating surface. It is found that for vessels with diameters considerably larger than the characteristic size of the vapor masses, the size effect on the local critical heat flux is limited almost entirely to the effect of subcooling associated with the local liquid head. When the subcooling effect is accounted for separately, the local CHF limit is nearly independent of the vessel size. Based upon the scaling law developed in this work, it is possible to merge, within the experimental uncertainties, all the available local CHF data obtained for various vessel sizes under both saturated and subcooled boiling conditions into a single curve. Applications of the scaling law to commercial-size vessels have been made for various system pressures and water levels above the heated vessel. Over the range of conditions explored in this study, the local CHF limit is found to increase by a factor of two or more from the bottom center to the upper edge of the vessel. Meanwhile, the critical heat flux at a given angular position of the heated vessel is also found to increase appreciably with the system pressure and the water level. The present scaling law, which represents the first attempt to predict the effects of vessel size and the angular position of the vessel outer surface on the local CHF limit, can be used to predict the critical heat flux on large commercial-size vessels.

ABBREVIATIONS

ALWR	Advanced Light Water Reactor
CHF	Critical Heat Flux
CYBL	Cylindrical Boiling Facility
DCH	Direct Containment Heating
LOX	Liquid Oxygen
MCCI	Molten Core-Concrete Interaction
NRC	Nuclear Regulatory Commission
RPV	Reactor Pressure Vessel
SBLB	Subscale Boundary Layer Boiling Facility
THL	Thermal Hydraulic Laboratory
TMI	Three Mile Island

1 INTRODUCTION

1.1 Background

In-vessel coolability of core melt is an important issue in addressing a postulated inadequate core cooling event in nuclear reactors. In such an event, a significant amount of core material can become molten and relocate downward into the lower head of the reactor vessel, as happened in the TMI accident. To assure long-term retention and cooling of the core melt within the reactor vessel, it is essential to demonstrate that the lower vessel head remains intact and mechanically strong enough to accommodate the core melt. If this can be done, then concerns about ex-vessel cooling and containment failure and risk can be minimized.

In recent years, the concept of external passive cooling of the reactor vessel has been considered to be the most reliable means of decay heat removal during a severe accident. In this concept, water is made available on the bottom side of the reactor lower head by flooding the reactor cavity as illustrated in Figure 1. As the lower head is heated by the pool of core melt resulting from the accident, the decay heat generated in the melt is removed from the bottom surface of the reactor vessel by downward facing boiling of the water in the flooded cavity. If this mode of external cooling is effective throughout the post-accident stage, then thermal failure of the reactor vessel can be prevented and the core melt will remain in-vessel.

One major uncertainty involved in the external cooling of core melt by cavity flooding is the critical heat flux on the bottom surface of the reactor vessel. For the case in which the critical heat flux for downward facing boiling is higher than the local heat flux from the core melt to the vessel wall, nucleate boiling will be the prevailing mode of heat transfer on the bottom surface. Thus the temperatures of the vessel wall can be maintained well below the failure temperature of the steel structure. However, if the downward facing boiling situation and the thermal loading conditions are such that the local heat flux from the core melt to the vessel wall exceeds the critical heat flux, then transition to film boiling will occur on the bottom surface. Under such circumstances, the temperatures of the vessel wall would rise very rapidly toward the failure temperature of the carbon steel structure, and the integrity of the reactor lower head could be severely jeopardized. In spite of its importance, very little is known about the critical heat flux on a downward facing curved surface. Thus far, there is no scaling laws that can be confidently used to estimate the critical heat flux on the bottom surface of a reactor vessel.

1.2 Major Objectives

In this project, the critical heat flux on downward facing hemispherical and toroidal surfaces are studied experimentally and theoretically. The goal is to establish a proper scaling law and develop a design correlation for prediction of the critical heat flux on the exterior surface of a commercial-size reactor vessel. In addition to the critical heat flux, the regime of nucleate boiling in the high-heat-flux region and the resulting liquid/vapor motions are observed in detail to seek a better understanding of the underlying mechanisms. Note that as vapor bubbles grow and depart from the heating surface, they tend to flow upward along the curved bottom surface of the vessel. This results in a two-phase liquid/vapor bubble boundary layer, driven by buoyancy under the influence of gravity, along the heating surface. The formation of the two-phase boundary layer, which is a direct consequence of vapor generation on the heating surface, may in turn affect the process of nucleate boiling and thus the value of CHF. In the present study, special attention is given to the behavior of the two-phase boundary layer as the condition of CHF is approached. The major objectives are:

- To observe the characteristic features of the two-phase liquid/vapor bubble boundary layer on a downward facing curved heating surface, including the behavior of the vapor

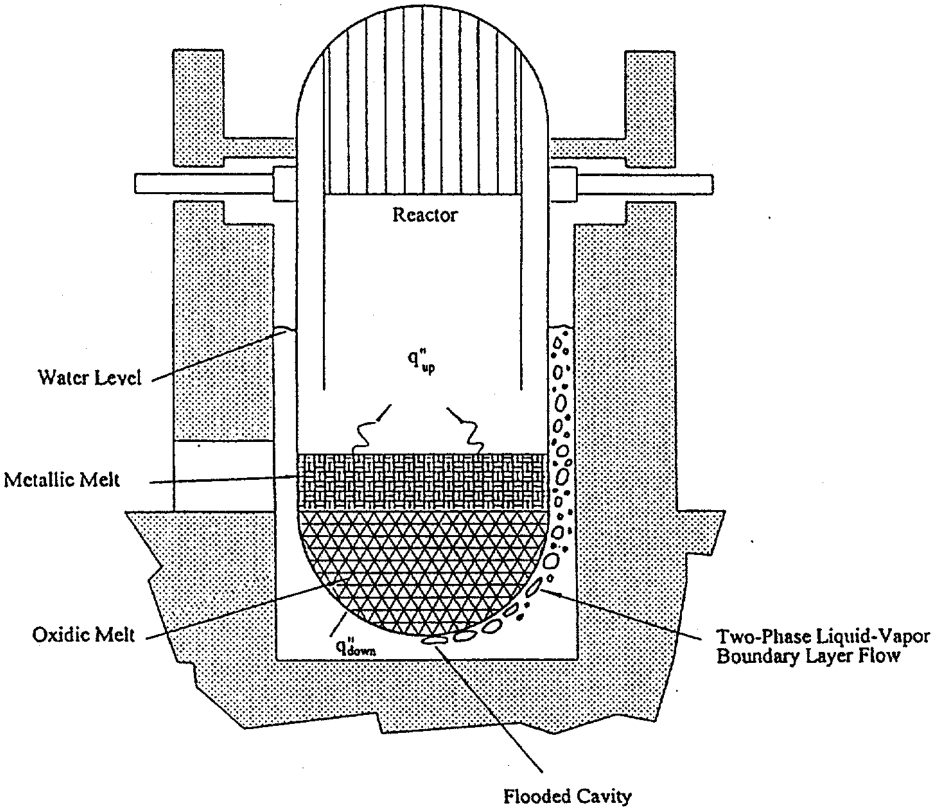

Figure 1. Boundary Layer Boiling on the Exterior Surface of a Reactor Lower Head

phase (*i.e.*, bubble generation, growth, departure, flow and agglomeration), liquid motion, and void distribution along the heating surface.

- To perform heat transfer measurements of downward facing boiling at different locations on the heating surface (varying from the bottom center to the top of the heated segment) and to determine the critical heat flux of the system as limited by the maximum rate of nucleate boiling.

- To obtain a complete database for CHF on a downward facing curved surface by studying the effects of subcooling and the height of the heated segment on downward facing boiling using heated hemispherical and toroidal vessels of various sizes.

- To develop a comprehensive model for downward facing boiling on a curved surface taking full account of the formation of an external free-convection two-phase boundary layer along the heating surface, and to validate the model using the experimental data to be obtained in the project.

- To establish a proper scaling law and develop a design correlation that can be used to predict the rate of downward facing boiling and the value of CHF on the external bottom surfaces of commercial-size vessels such as the lower head of an ALWR.

The design correlation developed in the project is further tested against additional downward facing boiling data that become available elsewhere during the time frame that the project is being performed.

1.3 Physical Significance of the Project

The present project provides the much needed CHF data and the basic information for designers of advanced reactors to realistically evaluate the concept of external cooling of core melt by cavity flooding. A useful guidance can be established for the selection of a suitable configuration for the reactor lower head. On the other hand, for a given reactor configuration, it is possible to predict whether or not the local heat flux from the core melt would exceed the critical heat flux for downward facing boiling on the bottom surface of the lower head over an anticipated range of accident conditions. In view of this, the research project could provide immediate benefit to researchers and engineers who are currently engaged in the design and safety studies of advanced reactors.

It should be noted that the reactor cavity for most ALWRs could readily be flooded with water under severe accident conditions. Design features of most ALWRs have the provision for substantial water accumulation within the containment during numerous postulated accident sequences. Based on most ALWR containment configurations and the operation of several passively actuated safety injection systems, the water level developed inside containment during accident conditions would be sufficient to submerge both the reactor pressure vessel (RPV) lower head and a substantial fraction of the vessel cylinder.

With water covering the lower external surfaces of the RPV, should the accident progress to the slumping of core debris into the lower vessel plenum, significant energy (i.e., decay heat) could be removed through the vessel wall by nucleate boiling on the vessel outer surface. Assessments of internal circulation within the debris and the energy transferred to the wall show that the heat flux from the molten corium to the vessel wall may be of the order of 10^5 W/m^2. If this heat load could be removed by nucleate boiling on the vessel outer surface, the reactor vessel may be sufficiently cooled so as to prevent downward failure of the reactor vessel and release of the core debris into containment. Thus, the occurrence of nucleate boiling at lower surface of the RPV submersed in a pool of water under severe accident conditions could eliminate considerations of ex-vessel events such as:

- direct containment heating (DCH),
- molten core-concrete interactions (MCCI),
- ex-vessel debris coolability, and,
- ex-vessel fission product release,

each of which may challenge the reactor containment design pressure. The present project aims at developing a useful scaling law for the CHF limit that can be used to evaluate the downward facing boiling process that can occur at the RPV lower surfaces of an ALWR under severe accident conditions.

In addition to benefiting the design of ALWRs, the research project could also benefit the utility section in conjunction with accident management of existing light water reactors that are currently in operation. If an unlikely event of core meltdown does occur in one of these reactors, then the accident might be mitigated simply by flooding the reactor cavity with water. The success of this strategy depends largely on the rate of downward facing boiling on the external bottom side of the reactor vessel in question. If the configuration of the reactor lower head and the depth of the melt pool resulting from the accident are such that the heat flux from the core melt can be removed by nucleate boiling of water in the cavity without exceeding the CHF limit, then the vessel wall can be maintained at relatively low temperatures to prevent thermal failure of the lower head.

Finally it should be noted that the fundamental knowledge obtained in the research project could benefit the heat transfer community in general as well as researchers in other technological areas. A better understanding of the effects of surface configuration on nucleate boiling and the value of CHF could prove to be valuable in promoting the method of cooling of high-power-density electronic devices and in the management of cryogenic fluids. The latter is related to the phenomena of boiling of liquid fuel such as LOX from downward facing curved surfaces commonly encountered in rocket and spacecraft applications.

2 LITERATURE SURVEY

Experimental studies of pool boiling using the method of steady state heating or transient quenching are critically reviewed in this section. The heating surfaces that have been explored experimentally include flat, cylindrical, spherical, and toroidal surfaces. The issues that are covered here and which are thought to be relevant to the present work include the effects of the surface geometry and the local angle of inclination on the boiling phenomenon. Also covered is the effect of the heater size and the dynamics of the bubbles during nucleate boiling, which is especially important for formulating a sound physical model for the two phase boundary layer boiling process. Other topics that are included in this review include the effect of subcooling on pool boiling, and the relationship between the results obtained through steady state experiments and those obtained through the quenching method. Besides the experimental work, a comprehensive review is also included of the various models for the critical heat flux phenomenon.

2.1 Quenching Experiments

This part is divided into three major sections, with each section dealing with the literature concerning pool boiling on a heating surface that is either flat, cylindrical, or spherical. Within each of these sections, results of previous experimental investigations on the effect of the surface inclination and the bubble dynamics are reviewed.

2.1.1 Inclined, Downward Facing, Flat Heating Surfaces

Test samples with flat surfaces do not seem to be a popular choice for quenching experiments. This is reflected in the relatively small number of sources that were found to employ such a heating surface in this type of experiments.

Reference 1 investigated the effect of the angle of inclination on downward facing boiling by carrying out quenching experiments in saturated water. The test section was a small copper disk with a thickness of 1.28×10^{-2} m and a diameter of 5.08×10^{-2} m. They found that the angle of inclination had an important effect on heat transfer in all boiling regimes. Their results indicated that the minimum film boiling and the transition boiling heat fluxes decreased as the inclination changed from vertical ($\theta = 90^\circ$) to horizontally facing downward ($\theta = 0^\circ$). The reduction in the heat flux was much bigger for $\theta = 0^\circ$ than for the other angles of inclination. The critical heat flux also decreased, from 8.5×10^5 to 2×10^5 W/m^2, when the surface inclination changed from vertical to downward facing. On the other hand, the rate of nucleate boiling was enhanced as the inclination changed in the same direction except when $\theta = 0^\circ$. The effect of the orientation on the nucleate boiling heat flux was much stronger at lower wall superheats than at higher wall superheats.

Reference 2 quenched two 0.1 m thick aluminum cylindrical disks with a diameter of 0.61 m in saturated water. One of the disks had a flat downward facing surface and the other had a radius of curvature of 3.35 m. The three different boiling regimes, i.e., film, transition, and nucleate, were observed. Initially, the liquid-vapor interface appeared to be stable. As time proceeded, groups of bulges started moving around the edges of the test surface. The number and locations of the bulges increased in time while traveling inward to extend across the whole surface. Transition boiling then took place which was characterized by intermittent direct liquid-solid contacts and a liquid-vapor interface with growing and receding bulges which had a dimension of the order of 0.01 m. The CHF condition was reached as characterized by a cyclic explosive vaporization. The cycle started with the surface covered with a vapor layer. A small indentation appeared in the film leading to direct liquid-solid contact. This resulted in an expanding circular region of intense vaporization. During the expansion process, the vapor film outside the circle traveled toward the edge and it eventually released into the liquid bath. This cyclic motion had a period of 0.29 and 0.27 seconds for the flat surface and the curved surface, respectively.

As time passed, the explosions became less far reaching and less violent. Eventually, the process entered the nucleate boiling regime. The observations confirmed that nucleate boiling was also a cyclic phenomenon. Bubbles nucleated at different locations and then coalesced with neighboring bubbles to form larger bubbles. At high heat fluxes, a single large bubble covered almost the entire surface at the end of the coalescence process. This large bubble then broke into several smaller bubbles before escaping from underneath the surface. At intermediate heat fluxes the large bubble did not grow to cover the entire surface. When the heat flux was low, the nucleation sites became far apart and bubble coalescence became increasingly local in scale. As the heat flux became even lower, the surface became covered with few growing bubbles and most of the surface was in direct contact with liquid.

Heat transfer measurements were also made by Ref. 2. Their results indicated that the critical heat flux was between 0.4-0.6 MW/m^2 and the corresponding wall superheat was 30°C. The experimental uncertainty was approximately ± 20%. The CHF for the curved surface was reported to be essentially the same as that for the flat surface.

2.1.2 Cylindrical Heating Surfaces

Similar to the case with flat surfaces, test samples with cylindrical surfaces do not seem to be a popular choice for quenching experiments. The only relevant study was the work reported in Ref. 3. They used a horizontal copper tube with a diameter of 0.127 m and a water pool to investigate the variation of the boiling curve along the outside surface of the tube. Their results showed a considerable variation in the heat flux around the cylinder. They found that the maximum CHF having a value above 10^6 W/m^2, occurred at the top of the tube and the minimum took place 30° down from the top.

2.1.3. Spherical Heating Surfaces

2.1.3.1. Local Variation of the Boiling Curve

Most quenching experiments were performed using test samples with spherical surfaces. Reference 4 studied the quenching of silver spheres with a diameter of 5.08×10^{-2} m in oil. They observed that the oil film collapsed first at the top of the vessel and then propagated downward toward the bottom center. In the lower half of the sphere, the local maximum boiling heat transfer coefficient occurred near the bottom center and decreased toward the equator. Away from the maximum heat flux region, the boiling curves at various locations, in the lower half of the vessel, were very similar.

Reference 5 performed quenching experiments in nitrogen using a shrouded aluminum hollow sphere with a 6.35×10^{-3} m wall thickness and a 0.1016 m diameter. The shroud diameter was varied to assess its effect. The shroud-sphere spacing did not have any noticeable effect on the boiling phenomenon. They observed that the vapor layer usually collapsed first at the top of the sphere and last at the bottom of the vessel. In the lower half of the sphere, the maximum heat flux took place at the bottom center of the vessel. The data did not show a clear trend in the variation of the CHF from the bottom center to the side of the vessel.

Reference 6 conducted quenching experiments in nitrogen, Freon-12, and Freon-22 using spheres made of various metals and with diameters ranging from 0.635 to 10.16×10^{-2} m. Using a 5.08×10^{-2} m vessel, he found that only the region near the critical heat flux was dependent on the location along the heating surface. The CHF increased from the bottom of the sphere toward the top until it reached a maximum 45° from the top center, which was then followed by a decrease in the critical heat flux all the way to the top.

Reference 7 studied the quenching of copper spheres, with a diameter of 2.54×10^{-2} m, in saturated methanol. Their results showed a definite variation in the boiling curve with the location on the outside surface. The temperature at the bottom center was always lower than that at the equator, which in turn was lower than the temperature at the top center. They observed that the CHF occurred first at the bottom, where it was highest, and then propagated toward the top of the sphere where it was the lowest.

Reference 8 quenched copper spheres in nitrogen. He found that only the nucleate boiling region was dependent on the location on the vessel surface. Thermocouples were monitored at the top, the equator, and the bottom center of the vessel. The results depicted a heat transfer coefficient that was highest at the bottom and smallest at the top. It was observed that the CHF always occurred first at the top and then propagated toward the bottom.

Reference 9 used spheres to conduct quenching experiments in liquid Nitrogen. The sphere diameters they used ranged from 0.635 to 10.16 x 10^{-2} m. The critical heat flux was found to be dependent on the angular position and the metal of the vessel, but the location where the CHF was maximum and minimum were not consistent from metal to metal. In the lower half of the spheres, the critical heat flux was generally lower at the bottom center and higher at the equator.

Reference 10 quenched a 2.54 x 10^{-2} m outside diameter hollow hemisphere in water and methanol. They found that generally the peak heat flux occurred first at the bottom of the vessel and then propagated toward the top. The region that experienced the CHF first had also the higher peak heat flux. They were able to derive boiling curves for two locations on the outside of the vessel. One location was 45° away from the bottom center, and the second was 45° from the top center of the vessel. The results for methanol indicated a higher peak heat flux in the upper half of the vessel for the saturated boiling case. This trend was reversed as the subcooling increased. They also reported that the liquid-vapor interface was very wavy at the beginning of the film boiling process due to the intense vapor generation. This interface became smooth at the end of the film boiling process.

Reference 11 carried out quenching experiments in subcooled Freon-113 using a hollow copper sphere with a diameter of 3.84 x 10^{-2} m and a wall thickness of 2.8 x 10^{-3} m. They observed that the collapse of the vapor layer in the film boiling region took place first on the support stem that was attached to the sphere. Then the breakup of the layer started propagating toward the bottom center of the vessel. When the stem was wrapped with an insulation, the vapor layer collapsed at almost the same time over the whole sphere. In the lower half of the vessel, they found that the nucleate boiling was independent of the angular position along the outside surface of the vessel. In this part of the sphere, variation between locations was observed only around the critical heat flux point with the minimum occurring at the bottom center and the maximum at the equator. The nucleate boiling region was found to be dependent on the angular position in the upper half of the vessel all the way to the CHF. The differences between the critical heat fluxes at various angular positions were more pronounced in this part of the vessel than in the lower half of the sphere.

Reference 12 performed quenching experiments in saturated water using two copper test sections of the same diameter (50.8 mm) and radius of curvature (148 mm), but with different thicknesses (12.8 mm and 20 mm). They were capable of deriving boiling curves at six locations along the outside surface, which covered the region from the bottom center ($\theta = 0^\circ$) to the point where the local angle of inclination θ was equal to 8.26°. In the nucleate boiling region, it was found that the heat flux increased, for the same wall superheat, with increasing values of θ in the low heat flux region. At heat fluxes close to and including the maximum heat flux point, the heat flux started to go down with increasing values of the local angle of inclinations. The CHF at the bottom center was estimated to be 0.53 MW/m^2 for the thin test section and 0.6 MW/m^2 for the thick one.

Reference 12 also reported a lower maximum heat flux for the thinner test section they used. Their results also showed that the thickness of the test section did not affect the order of occurrence of the CHF point. For both test sections used, CHF occurred first at the lower most position then at the higher locations in an orderly sequence. The difference in time between subsequent CHF occurrences increased as the thickness of the test section increased.

It is clear that the literature does not agree on the variation of the boiling curve along the outer surface of spherical vessels. Earlier studies reported here (Refs. 4, 5, and 7) suggest that the maximum heat flux would occur at the bottom center of the vessel, which is in contradiction with recent studies (Refs. 6 and 11) that suggest the occurrence of the maximum CHF at the equator. Other authors (Refs. 9 and 10) obtained inconclusive results regarding the location where the maximum critical heat flux would occur. In the nucleate boiling region, Ref. 8 reported that in this region the boiling curve would depend on the location on the heating surface, whereas Ref. 11 reported that such a dependency did not exist.

2.1.3.2. Effect of the Sphere Diameter

Reference 13 quenched a 12.7 mm and a 25.4 mm copper spheres in liquid nitrogen. They were able to derive boiling curves that were based on an average boiling heat flux. Their results showed that there was no effect of size in all boiling regimes.

2.2. Steady State Heating Experiments

This part is divided into three major sections where each section focuses on the literature concerning pool boiling on a heating surface that is either flat, cylindrical, or toroidal. Each one of these sections contains experimental findings pertaining to the effect of inclination on nucleate pool boiling and to the characteristics of the bubble behavior.

2.2.1. Inclined, Downward Facing, Flat Heating Surfaces

Contrary to the case of transient quenching, steady state experiments using flat surfaces are very common. This is probably due to the fact that it is much easier to place heating elements on a flat surface than on any of the other two types of surfaces.

2.2.1.1. Effect of the Angle of Inclination on the Boiling Curve

Reference 14 studied the boiling of water off the flat end surface of downward facing cylindrical copper rods with a diameter equal to 25 or 50 mm under normal pressure. These rods were surrounded by a refractory insulating material with a larger outside diameter equal to 50, 100 or 200 mm. Steady state experiments were then carried out with different combinations of the diameters of the copper rod and the insulating material. The heat flux was found to be lower for the same surface temperature when the diameter of the copper rod and that of the insulating material were increased. It was also found that the critical heat flux level varied, when the diameters of the two elements changed, from a minimum of 2.32×10^5 W/m^2 to a maximum of 9.87×10^5 W/m^2. The excess surface temperature at which the burnout limit occurred also varied between 16 and 28 °C.

Reference 15 carried out steady state heating experiments in subcooled isopropyl alcohol at atmospheric pressure using a 3.175 x 101.6 x 0.0254 mm chromax strip. Three surface orientations were tested: horizontally upward facing, vertical and horizontally downward facing. Their results indicated that the nucleate boiling heat flux was higher for the vertical surface than for the upward facing surface. The downward facing surface had a lower nucleate heat flux level than the other two orientations. The authors reported a higher critical heat flux level for the vertical surface than for the upward facing heating surface. The downward facing surface had a lower critical heat flux than the other two orientations.

Reference 16 set out to prove the link between the surface orientation and the nucleate boiling level. The general belief before they carried out their work was that orientation had an effect on boiling only in the critical heat flux region, because the latter was a hydrodynamically controlled phenomena. On the other hand, the nucleate boiling phenomenon was considered to be localized and therefore independent of the surface orientation. One of the large faces of a 50.8 x 50.8 x 34.9 cm copper block was used as the heating surface to conduct steady state boiling experiments under normal pressure using distilled water. The heat flux was varied between 0.016 and 0.112 MW/m^2, and the orientation was varied between upward facing ($\theta = 0^\circ$) to vertical ($\theta = 90^\circ$). The heat transfer coefficient *h* was found to change by as much as 25%, for the same heat flux, when the surface configuration changed between the two extreme positions. Also, it was found that *h* increased and the number of nucleation sites decreased as θ increased. The latter was explained by the fact that the path length of the departing bubbles increased with increasing θ leading to more agitation. As a result, the contribution of one bubble toward the heat transfer coefficient increased and less nucleation sites were needed to remove the same heat flux.

Reference 17 studied the effect of orientation on the boiling of liquid helium by performing steady state heating experiments using a stainless steel plate. The angle of inclination θ was varied from 0° (horizontally upward facing) to 180° (horizontally downward facing). His results showed that the nucleate boiling was enhanced when the orientation angle increased up to 150°. The latter enhancement was more evident at lower heat flux levels. When θ was 180°, a sudden drop in the nucleate boiling curve was observed. He also found that the critical heat flux decreased as the angle of inclination increased.

Reference 18 carried out steady state boiling experiments using Freon over a wide range of orientation angles with heat flux levels varying from 0.014 to 0.180 MW/m^2. The heating surface was one of the large faces of a 37 x 25 x 1.2 mm copper block. The surface orientation was varied from upward facing ($\theta = 0^\circ$) to downward facing ($\theta = 180^\circ$). The heat flux and the heat transfer coefficient were found to increase for the same wall superheat as the inclination angle θ increased up to a value of 150°. At higher orientation angles, both the heat flux and the heat transfer coefficient started decreasing rapidly.

Reference 19 also investigated experimentally the effect of surface orientation on the nucleate boiling heat transfer. Water at atmospheric pressure was used as the boiling medium. The heat flux level was varied from 5×10^3 to 7×10^5 W/m^2. The heating surface was a 42 x 175 mm copper piece. The inclination angle was varied from upward facing ($\theta = 0^\circ$) to the point where $\theta = 175^\circ$. When the heat flux was low, the boiling curve shifted upward as the orientation angle θ increased. At high heat flux levels, the various boiling curves for different values of θ merged together into a common boiling curve with a slight deviation in the direction opposite to that at low heat fluxes. Three nucleate boiling regions were identified with respect to the effect of the orientation. The low heat flux region was characterized by a significant orientation effect. The high heat flux region was marked by the disappearance of the effect of the orientation angle, and an intermediate heat flux region where the orientation effect was neither negligible nor significant. The heat transfer coefficient *h* was found to be dependent on the surface inclination and the heat flux level. At low heat flux levels, *h* increased with increasing θ. For high heat flux levels, *h* was almost constant for θ values up to 175°. When the inclination angle was further increased, the heat transfer coefficient dropped rapidly to a minimum.

Reference 20 carried out steady state heating experiments in R-11 at pressures of 1 and 2 atm using a copper heating surface of diameter 7.8×10^{-2} m. Data points in the nucleate and the film boiling regions were obtained. Their results showed that the superheat, in the nucleate boiling region, decreased as the inclination angle θ increased from 0°, i.e., horizontally facing upward, to 165° at low heat flux levels. Beyond a certain heat flux, the superheat remained approximately constant for all inclinations except for the case when the surface was horizontally facing downward where there was a sudden increase in the wall superheat. Reference 20 deduced that there were at least two types of heat transfer mechanisms associated with nucleate boiling from inclined surfaces. First, there was the evaporative mechanism, which was present for any surface orientation and was dependent on the heat flux level. Second, there was the bubble agitation mechanism which was a strong function of the surface orientation. At low heat flux levels, the evaporation mechanism was weak and the effect of the orientation became apparent. When the heat flux was high, the effect of the inclination was minimal, because the evaporative mechanism was dominant.

Reference 21 also investigated the dependence of the boiling heat transfer on the orientation. They performed steady state heating experiments in liquid nitrogen using samples made of copper and aluminum that were 50 x 50 x 6 mm in size. Their results confirmed the findings of previous investigators. They found that nucleate boiling was enhanced at low heat fluxes when the orientation angle θ, where θ was zero when the surface was upward facing, was increased. The boiling curves for various angles of orientation merged together at higher heat fluxes. The critical heat flux was found to decrease with increasing θ values. At $\theta = 176^\circ$ the CHF value was only 30-40% of the value at $\theta = 0^\circ$ where the critical heat flux was equal to 19.1×10^4 W/m^2.

Reference 22 performed their steady state heating experiments at atmospheric pressure using saturated liquid helium and the flat end surface of a copper cylinder that was 20 mm in diameter and 30 mm in length. Both the nucleate and the film boiling regimes were investigated. Their experimental results showed a clear dependence of the nucleate boiling heat flux on the surface orientation. In agreement with most of the previous studies, the heat flux increased when the inclination angle θ varied from 0° (upward facing) to 175°. On the other hand, the critical heat flux decreased when θ changed between the same two limiting values.

All of the previous studies confirm the fact that orientation has a significant effect on the nucleate boiling heat transfer all the way up to the critical heat flux limit. There is a general agreement in the literature that the horizontal downward facing position results in the lowest nucleate boiling heat transfer. The reported results also agree that the nucleate boiling heat transfer is enhanced as the surface orientation is tilted further away from the horizontal upward facing position.

Among all the investigations reported previously, only the earliest one (Ref. 15) reported that the CHF increases when the surface orientation changes from horizontally upward facing to vertical. All the latest studies (Refs. 17, 19, 21 and 22) showed that the critical heat flux is highest when the surface is horizontally upward facing, and it starts going down as the inclination is increased toward the downward facing position.

2.2.1.2 Bubble Dynamics on Inclined Flat Surfaces

Steady state experiments offer a unique opportunity to study closely the characteristics of nucleate boiling, because the same cyclic process of bubble growth and departure is repeated indefinitely at a given heat flux level. Under such an experimental condition, Ref. 14 reported the bubble behavior for boiling of water from the flat face of a cylindrical downward facing copper rod. They observed that small bubbles started to form when the heat flux level was increased beyond the free convection level. These bubbles gathered together to form a single steam blanket with a nearly perfect circular shape. The blanket kept growing as more and more liquid evaporated and started loosing its circular shape when it occupied about 80% of the surface. When the edge of the blanket reached the periphery of the surface of the cylinder, the blanket quickly slid along the surface and escaped allowing the process to be repeated again. When the heat flux was increased further, the motion of the vapor blanket became faster and the frequency of escape increased. When the steam blanket escaped the surface, a new blanket was formed rapidly while a liquid film of water was still in contact with the surface of the copper rod. As the heating level was increased further, the life of the liquid film on the surface became shorter and shorter.

Reference 19 observed the dynamics of the bubbles growing on the surface of a rectangular copper block submerged in water. They found that in the low heat flux region, the bubble frequency decreased and the bubble diameter increased for larger values of θ, which represented a departure from the horizontal upward facing position. When the surface was facing upward, bubbles detached the surface as isolated bubbles. This trend held true for θ values up to 120°. For inclination angles beyond 150°, bubbles grew rapidly as soon as they detached from the surface. Then, the enlarged bubbles rose up in an elongated form along the surface. As a result, the isolated bubbles disappeared as the inclination angle increased. In the medium heat flux region, coalesced bubbles existed with isolated bubbles, which covered most of the surface for θ values less than 120°. When θ was greater than 150°, clusters of small bubbles existed between the enlarged bubbles. In the high heat flux region, bubble generation was very vigorous that coalesced bubbles prevailed all over the surface for all the inclination angles.

Reference 19 explained that in the low heat flux region the heat transfer was mainly controlled by the stirring action of isolated bubbles for θ less than 120°. Therefore, the heat transfer coefficient would be larger for a higher bubble frequency when isolated bubbles prevailed over the surface. For θ larger than 150°, the heat transfer became controlled by two mechanisms. One was the sensible heat removal by the movement of the elongated bubbles rising along the surface, and the second was the latent heat removal by the evaporation of the liquid film underneath the elongated bubbles. When these two mechanism were present, the heat transfer coefficient would be independent of the number of nucleation sites and the nucleation characteristics of the surface. In the high heat flux region, the flow conditions next to the heating surface became important and the movement of the large bubbles did not play a major role anymore. In this case, the flow conditions next to the surface were controlled by the nucleation underneath the elongated bubbles.

Reference 20 used a flat copper disk and liquid nitrogen for their steady state experiments. For the case when θ was 0°, corresponding to the horizontal upward facing position, the authors explained that buoyancy acted to break the vapor layer and keep it unstable. When the surface was upward facing and inclined, the vapor flowed along the surface and broke at the trailing edge. As a result, the average film thickness would be larger than in the case when θ was 0°. For the inclined surface facing downward, buoyancy would act to stabilize the vapor layer along the surface making liquid access more difficult. The horizontal surface facing downward (i.e., θ = 180°) would have the lowest heat transfer, for in this case the buoyancy force had no component along the heating surface.

Reference 21 used aluminum and copper rectangular blocks submerged in liquid nitrogen in their steady state experiments. At low heat flux levels, they observed that for θ values between 0°, corresponding to the horizontal upward facing position, and 90° the heat transfer was governed by the motion of individual bubble columns. For θ greater than 90°, the bubbles originating at an active nucleation site remained in contact with the surface for longer periods of time and grew to larger dimensions. The residence time of the bubbles and the percentage of the surface they cover decreased for smaller values of the orientation angle. At high heat flux levels and θ greater than 90°, a vapor cloud was observed over the entire surface while patches of boiling liquid were in direct contact with the surface. The vapor blanket grew bigger with time until it was removed by buoyancy forces. This allowed new liquid to wet the surface and boiling was initiated again.

2.2.2. Cylindrical Heating Surfaces

2.2.2.1. Local Variation of the Boiling Curve

Reference 23 used a 6.35 mm tube to conduct steady state experiments in liquid nitrogen. They observed that the top of the tube was always hotter than the bottom. The temperature variation around the tube was more pronounced in the lower heating range tested. When the temperature difference between the top of the tube and the liquid was 9.18 K, it was 8.28 K at the side and 7.38 K at the bottom. In another case when the temperature at the top of the tube was 20.52 K, it was 20.34 K at the side and bottom.

Reference 24 boiled methanol and n-hexane on the outside of copper tubes. Their results showed that there was considerable variation in the nucleate boiling heat transfer coefficient around the tube circumference especially at low heat flux levels. The location with the maximum *h* value was the bottom of the tube for methanol and the sides for n-hexane. The minimum heat transfer coefficient always occurred at the top.

Reference 25 used a 16 mm copper tube for their steady state experiments in liquid nitrogen. They were able to measure a temperature variation along the circumference of the tube, where the top of the tube was always found to be hotter than the bottom. This was true in all boiling regimes except in the film boiling region, where no temperature variation was reported.

Reference 26 conducted a full scale reactor vessel simulation of downward facing boiling around the stagnation point ($-30^\circ<\theta<30^\circ$). The hemispherical shape was simulated by a cylindrical copper slice with a uniform thickness, height, and radius of curvature that were chosen equal to 0.15 m, 0.076 m, and 1.76 m respectively. Figure 2 depicts the heater block, which is represented by the hatched surface area. The block was divided into several heating zones that could be heated independently. One set of experiments, which aimed at estimating the CHF around $\theta=0^\circ$ (i.e., the bottom center), consisted of supplying a constant heat flux symmetrically to a certain number of heating zones adjacent to and including the bottom center. A certain fraction of this heat flux was supplied to the rest of the heating zones.

The second set of experiments was designed to estimate the critical heat flux at any specific location θ_m along the surface. The method required that the superficial vapor velocities, expressed as volumetric flow rate per unit width, in the experiment matched up with those of the prototype for all the downstream locations $\theta > \theta_m$. When $\theta < \theta_m$, the vapor flow rate built up gradually and smoothly approached the value required at $\theta = \theta_m$. Figure 3 shows the reference reactor power shape and the shape used in the simulations. The heat load of Figure 3 was corrected for the effect of conduction inside the wall.

During the experiments, it was observed that a small reduction in the heat flux below some level resulted in increasingly delayed boiling crisis at a certain location on the surface. As a result, the authors reported two estimates of the variation of the CHF with location. One was based on a 50 minute wait for the boiling crisis to occur, which was referred to as a conservative bound, given by

$$\begin{aligned} q_{\max}''(\theta) &= 300\text{kW}/\text{m}^2 \quad \theta < 5^\circ \\ &= 300 + 12.6\theta^\circ\text{kW}/\text{m}^2 \quad 5^\circ < \theta < 30^\circ \end{aligned} \tag{2.1}$$

A deterministic bound, which was based on 120 minute wait, was also reported where,

$$\begin{aligned} q_{\max}''(\theta) &= 276\ \text{kW}/\text{m}^2\ \theta < 5^\circ \\ &= 276 + 12.6\theta^\circ\ \text{kW}/\text{m}^2\ 5^\circ < \theta < 30^\circ \end{aligned} \tag{2.2}$$

In a second set of experiments, Reference 27 simulated a full side of a reactor lower head from the bottom center all the way up to the equator ($0^\circ < \theta < 90^\circ$). Figure 4 shows a schematic of their experimental arrangement. The dashed lines in the figure represent the capability of the experimental apparatus to simulate an insulation placed next to the outside surface of the reactor lower head. The copper block used to simulate the reactor lower head had the same height, thickness, and radius of curvature as the geometry described previously that targeted the region around the bottom center. Due to the large gravity head present in this case, there was a 14 K subcooling at the base of the copper block.

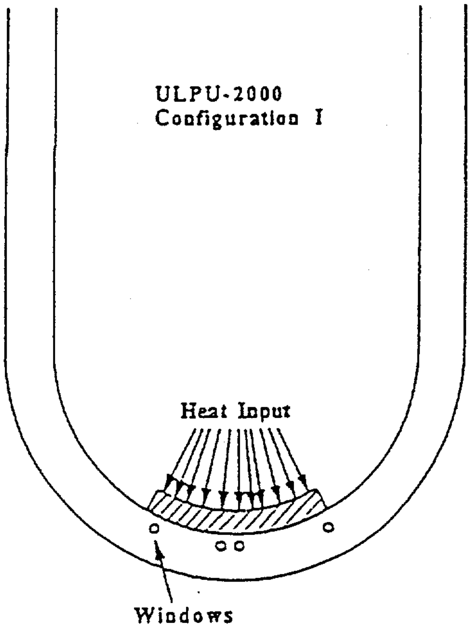

Figure 2 Schematic of Configuration I Employed in the ULPU Experiments.

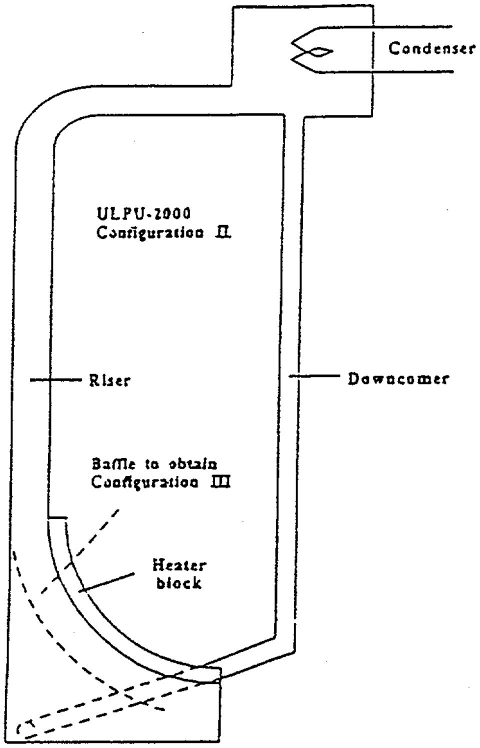

Figure 4. Schematic of Configuration II Employed in the ULPU Experiments

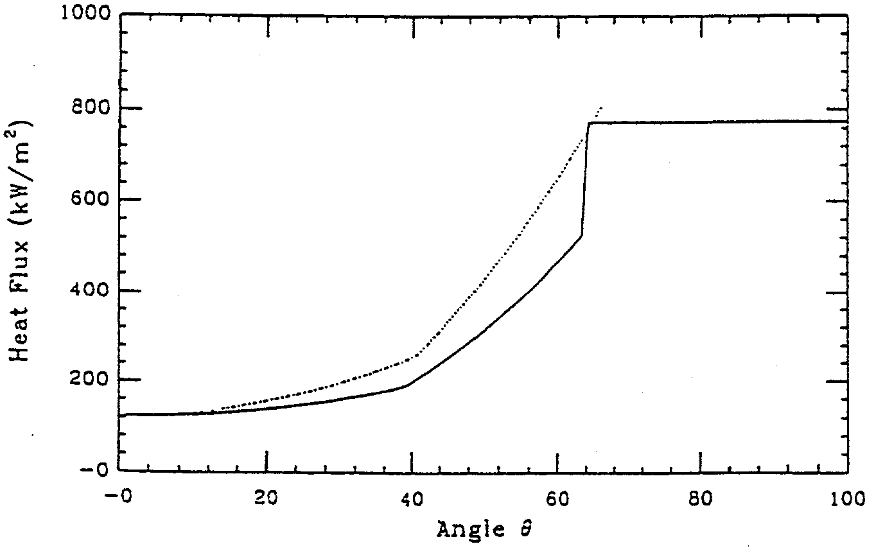

Figure 3. Reference Reactor Power Shape Employed in the ULPU Experiments

Among the two types of experiments performed, one targeted the region next to the bottom center where $\theta = 0^\circ$. It consisted of supplying a uniform heat flux to heating zones adjacent to and including the bottom center. The rest of the downstream locations were heated according to the reference reactor power shape shown in Figure 3.

It was found to be necessary to decrease the maximum heat flux near $\theta = 90^\circ$, otherwise the CHF would always occur in the latter region instead of around the bottom center. The second set of experiments simulated the CHF at different θ_m locations using the same requirements employed by Ref. 27. For $0^\circ < \theta_m < 30^\circ$, it was necessary to decrease the heat flux around $\theta = 90^\circ$ to force the CHF to occur at the desired location close to the bottom center of the block. Their results indicated that the configuration of Figure 4 had a much higher tolerance to boiling crisis than the earlier configuration of Figure 2. Also, it was found that the variation of CHF with angular position was composed of two linear regions. It was stated that this reflected the significantly different flow regimes observed in the vicinity of the bottom center and in the downstream region away from the base. The CHF variation was estimated by,

$$\begin{aligned} q_{\max}''(\theta) &= 500 \\ &\quad + 13.3\theta^\circ \ \mathrm{kW/m^2} \ \ \theta < 15^\circ \\ &= 540 \\ &\quad + 10.7\theta^\circ \mathrm{kW/m^2} \ \ 15^\circ < \theta < 90^\circ \end{aligned} \tag{2.3}$$

2.2.2.2. Bubble Dynamics on a Cylindrical Heating Surface

Reference 24 performed steady state heating experiments to study pool boiling in methanol and n-hexane on the outside of copper tubes with diameters of 50.8 and 31.75 mm. They observed that the bubbles formed at the bottom of the tubes were larger than those formed on the sides.

2.2.2.3. Effect of the Cylinder Diameter

Reference 28 reported on the effect of heater size based on boiling experiments using organic liquids and liquid mixtures. He used wires with diameters that ranged from 0.8 to 6.4 mm. The critical heat fluxes for the pure organic liquids were found to be independent of size for heater diameter greater than 2.4 mm. When the diameter was less than 1.6 mm, the CHF was 15 to 40% higher than in the larger diameter case. Ref. 28 noted that the latter behavior of the small diameter elements was contradictory to the data reported by Ref. 29.

Reference 29 investigated the boiling of R-113 on the outside of tubes with diameters ranging from 6 to 50.8 mm. They found that the heat transfer coefficient for tubes was higher than that for flat plates at the same conditions. Reference 29 attributed this increase to the two-phase convection effects of the bubble stream. The heat transfer coefficient was found to decrease when the tube diameter increased in the range between 6 and 30 mm. When the tube size was further increased beyond 30 mm, h varied only slightly.

2.2.3. Toroidal and Spherical Heating Surfaces

The study of Ref. 30 was the only investigation that employed a completely spherical shape in performing steady state experiments. They used a 63.5 mm aluminum hollow sphere and liquid nitrogen as the boiling medium. The surface was heated by radiation from a heating wire that was mounted on the outside of a smaller sphere placed at the center of the larger outer vessel. Temperatures readings from five thermocouples were used to get an average temperature for the whole surface of the vessel. The work did not lead to any information concerning the local variation of the boiling curve.

2.2.3.1. Local Variation of the Boiling Curve

Reference 31 used the CYBL (Cylindrical Boiling) facility at Sandia National Laboratories for a full scale simulation of downward facing boiling on the exterior surface of a reactor lower head. A schematic of the facility is shown in

Figure 5. The simulated reactor vessel was a torispherical vessel made of 0.016 m thick stainless steel with a crown radius of curvature of 3.35 m and a knuckle radius of curvature of 0.66 m. This setup was used to carry out steady state heating experiments by heating the vessel using an array of radiant lamp panels, which were capable of delivering a heat flux level of up to 4 x 10^5 W/m^2. Two types of steady heating experiments were performed. The first applied a uniform heat flux to the vessel, and the second delivered a higher heat flux near the edge. The observed subcooling near the bottom ranged from 9 to 10 K. For all the experiments performed, the bottom center was found to have the highest temperature even when the edge heat flux was higher than that at the center.

2.2.3.2. Bubble Dynamics on a Torispherical Heating Surface

In their CYBL experiments that used a toroidal downward facing surface, Ref. 31 were able to follow the bubble behavior very closely. Visual observations revealed that the subcooled nucleate boiling was cyclic and had four distinct phases: direct liquid-solid contact, bubble nucleation and growth, coalescence, and vapor mass dispersion (ejection). It appeared that the waves of vapor originated from the bottom center of the vessel, even though vapor was produced over the entire surface. It was observed that the frequency of the cyclic/pulsating pattern in the bottom center increased with heat flux while the rate of increase decreased with heat flux. This frequency was about 2 Hz for heat fluxes above 10^5 W/m^2.

The bubbles were found to originate first near the bottom center and subsequently progressed toward the outside. Then, these bubbles coalesced forming a large bubble that covered an area with a diameter as large as 1 m. It was also observed that the size of the vapor mass increased rapidly with heat flux at low heat flux levels, while increasing only slightly with heat flux at high heat flux levels. The maximum thickness of the large vapor mass ranged from one to three centimeters for the range of heat flux considered. After growing, the vapor mass dispersed in the form of an expanding flat ring. Eventually, the ring became unstable and broke into smaller arc segments. Then, the broken vapor segments condensed in the subcooled water. Figure 6 shows the various important mechanisms of the ex-vessel boiling process proposed by Ref. 31.

Close observations of the large vapor mass, that was forming around the bottom center of the vessel, also revealed that it was in fact a collection of smaller coalescing vapor bubbles. At the surface, individual nucleating sites were feeding the envelope of the vapor mass. This picture was similar to that observed by Ref. 32 for nucleate boiling on an upward facing surface and adopted by Ref. 33 to model critical heat flux. Ref. 31 also reported that the nucleation site density was a factor of 2 or 3 lower than that reported for an upward facing surface.

The CHF data obtained through steady state experiments that used water is summarized in Table 1 along with the data derived from transient quenching experiments.

2.3. Effect of Subcooling

The water that floods the reactor lower head in the case of a severe accident is usually not saturated. Also, the height of the column of water above the reactor lower head is several meters tall, which would result in a subcooling of about 10 to 14 K at the bottom of the lower head when the water is saturated at the top of the column. As a result, understanding the effect of subcooling on pool boiling from downward facing curved surfaces is important in assessing the concept of cavity flooding to prevent vessel failure.

Reference 33 investigated the effect of subcooling on the boiling of water on the outside of a horizontal copper tube with a diameter of 0.127 m. Their results showed a linear relationship between the average critical heat flux and the subcooling level. Also, it was found that the locations of the maximum and the minimum critical heat flux changed as the level of subcooling increased. This clearly demonstrated

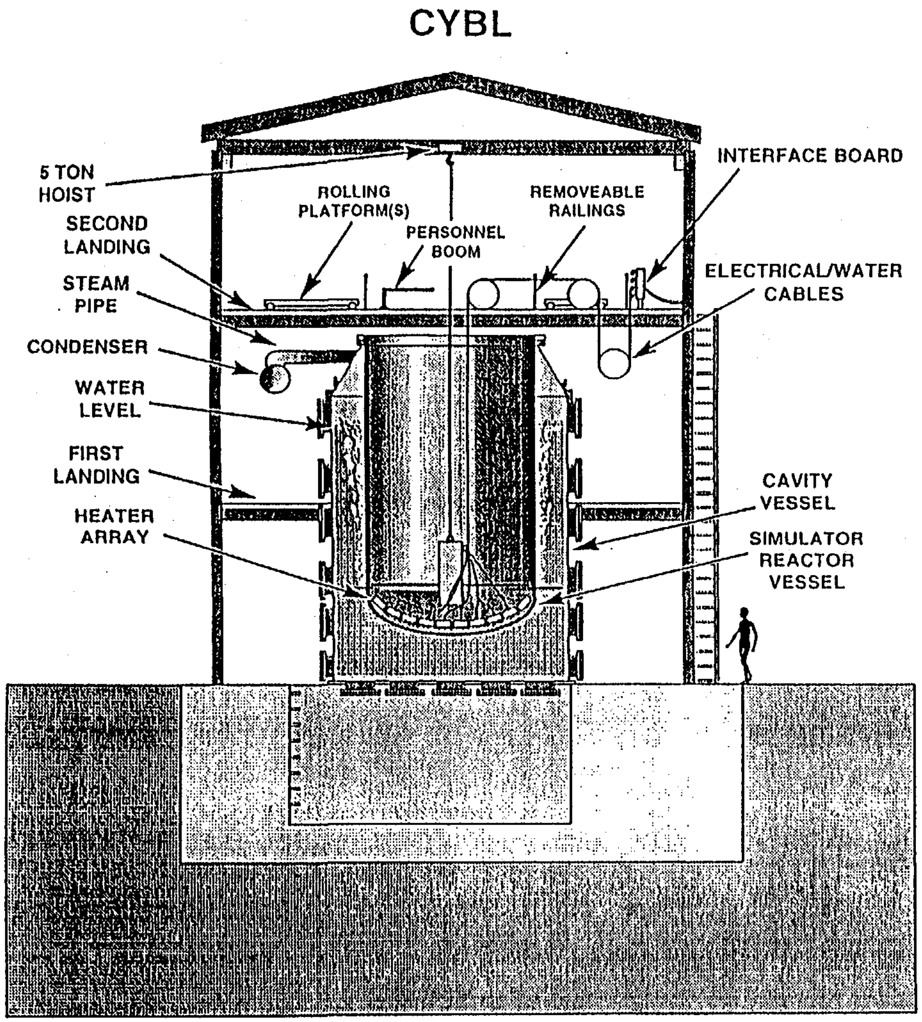

Figure 5. Schematic of the CYBL Facility at Sandia National Laboratory.

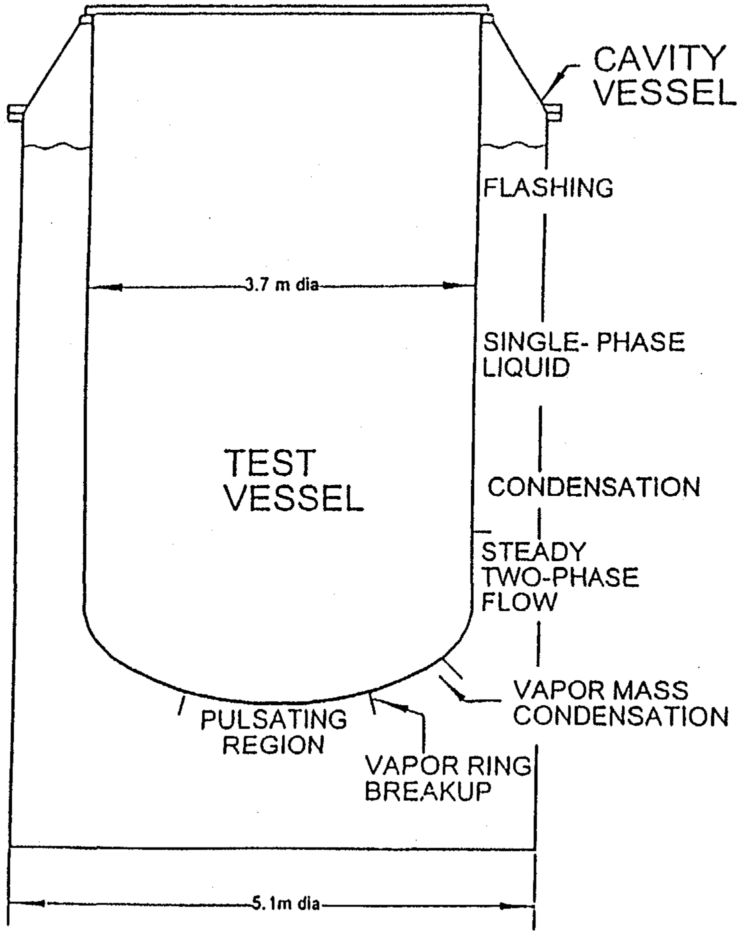

Figure 6. Various Regimes of Downward Facing Boiling Proposed by Chu et al. (1993) in the CYBL Experiments.

Table 1. Relevant CHF Data Obtained Through Steady-State and Transient Quenching Experiments Using Water

Source	Heating Method	Heating Surface	Angle of Inclination (θ)*	Subcooling Level (K)	Critical Heat Flux (KW/m^2)
Ishigai et al. 1961	Steady-state heating	Downward facing flat surface	0°	0	232-987
Theofaneous et al. 1994	Steady-state heating	2-D simulation	$-30^\circ<\theta<30^\circ$	0	50 minute wait: 300 if $\theta<5^\circ$ $300+12.6\theta^\circ$ if $5^\circ<\theta<30^\circ$ 120 minute wait: 276 if $\theta<5^\circ$ $276+12.6\theta^\circ$ if $5^\circ<\theta<30^\circ$
Theofaneous and Syril 1994	Steady-state heating	2-D-full-side simulation	$0^\circ<\theta<15^\circ$	14	$500+13.3\theta^\circ$
			$15^\circ<\theta<90^\circ$	14	$540+10.7\theta^\circ$
Thibault and Hoffman 1978	Quenching	Outside of a 12.7 cm cylinder	0°	0	1045
				10	1395
			90°	0	1100
				10	1550
Guo and El-Genk 1991	Quenching	Cylindrical flat disk	0°	0	200
			90°	0	850
Guo and El-Genk 1994	Quenching	Spherical surface	0°	0	570
Chu et al. 1994	Quenching	Downward facing flat and toroidal surfaces	0°	0	400-600

* The angle of inclination θ is zero at the bottom center for cylindrical and spherical surfaces. For flat surfaces, θ is zero when the surface is horizontal downward facing

the important effect subcooling had on the flow characteristics around the cylinder. Another result confirmed by their experiments was that the nucleate boiling region extended to higher wall superheats as subcooling increased.

Reference 34 used a 19 mm copper sphere to study the effect of subcooling on pool boiling in distilled water. He found that the critical average peak heat flux around the sphere increased non-linearly with increasing subcooling levels. The non-linearity increased at lower water temperatures. Reference 34 noted that at high subcooling levels, the quenching process could not be assumed quasi-static due to the very high cooling rates. The CHF varied from 7 x 10^5 W/m^2 at zero subcooling to 5 x 10^6 W/m^2 at 60 K subcooling. Also, the wall superheat corresponding to the CHF and the minimum heat flux increased as the subcooling level increased. It was observed that the ratio of the critical heat flux to the minimum heat flux was found to decrease as the subcooling became higher.

Reference 10 investigated the effect of subcooling by quenching a hollow hemisphere in methanol and water. They observed that the collapse of the vapor film was much faster as the subcooling level increased. The relationship between the CHF and the subcooling level was almost linear.

Reference 11 reported a stronger dependence on the angular position at larger subcooling levels when they quenched a hollow copper sphere in Freon-113.

2.4. Relationship Between Quenching Data and Steady-State Data

An important part of the present project is to determine the local boiling curves on the external surfaces of hemispherical and toroidal vessels using the transient quenching method, and to confirm the nucleate boiling portion of the curves by the steady state heating method. The questions that arise are how do these two sets of data compare in the nucleate boiling region, and what kind of precautions need to be taken to maximize the agreement between them.

Reference 35 compared steady state and transient quenching pool boiling data using water, Freon-113, and nitrogen. In general, the film boiling portion of the boiling curve, except near the Leidenfrost point, did not vary that much when obtained through steady state heating or transient quenching. In the nucleate boiling region, significant differences were reported between the two sets of data in the case of water and Freon-113. Reference 35 attributed this to the fact that they used different surfaces for transient quenching and steady state heating. Also, they noticed the formation of various deposits on the boiling surface which could have altered the boiling curve.

Reference 36 carried out steady state and transient quenching experiments in Freon-113 using a small copper sphere and compared the boiling curves obtained by the two methods. They obtained very good agreement in the film boiling region. In the nucleate boiling domain, the steady state heat flux values were somewhat higher than those obtained through the quenching method. The authors suspected that this could have been due to the interference from the magnetic field produced by the induction heating method that they used.

Reference 37 carried out another set of steady state and quenching experiments to check if the difficulties encountered by Ref. 36 could be overcome. They employed electric resistance heating instead of induction heating. The heating surface was a horizontal cylindrical copper block. A very good agreement was obtained in the nucleate boiling region between the data from steady state heating and that from transient quenching.

References 38 and 39 evaluated the conditions for transient quenching and the effect of metal properties on the resulting boiling curves. Their results showed that a complete boiling curve giving the correct relationship between the boiling heat flux and the wall superheat for nucleate, transition and film boiling can be deduced by a slow quenching technique.

These studies stress that the two types of experiments be conducted in very comparable conditions, which include using the same type of heating surface and the same conditions for the liquid bath. Also, it is important that the system being quenched has a sufficient thermal capacity so that the process can be considered quasi-steady.

2.5. Critical Heat Flux Models

Reference 40 provided a good summary of the four different mechanisms that have been postulated to cause the boiling crisis in the conventional pool boiling:

(i) When the heat flux increases, the bubbles that are generated at the horizontal upward facing surface coalesce to form vapor columns as shown in Figure 7a. These columns contain liquid droplets that tend to fall back to the surface. It is postulated that vapor blanketing of the surface occurs when the vapor velocity in the column becomes high enough to carry the liquid droplets away from the surface.

(ii) An increase in the surface heat flux leads to an increase in the nucleation site density. Eventually, a critical bubble packing is reached that prevents the liquid from traveling toward the upward facing surface, which leads to the formation of a vapor blanket over portions of the surface.

(iii) Due to an increase in the heat flux, the bubbles that form at the surface coalesce to form vapor jets or columns as shown in Figure 7a. Burnout occurs when the Helmholtz instability of the large vapor jets leaving the surface deforms the jets which prevents the liquid from reaching portions of the surface. As the liquid evaporates at the locations that are prevented from receiving new liquid due to the distortion of the vapor jets, a vapor blanket is formed over part or all of the surface.

(iv) Large vapor bubbles are formed at high heat fluxes and they are supplied with vapor through several small jets at their base, as shown in Figure 7b. The liquid film underneath the large bubble is assumed to be of very small thickness so that the jets within it are not Helmholtz unstable. It is also postulated that the liquid layer thickness is proportional to the Helmholtz unstable wavelength of the small jets. Before the occurrence of the CHF, the large vapor bubbles hover over the small jets until they get big enough to detach from the heating surface. Burnout is assumed to take place when the thin liquid film underneath the large bubble evaporates completely during the hovering time needed for the large bubble to escape.

2.5.1 CHF Models for Upward Facing Flat Plates

Reference 41 was the first to propose the analogy between flooding and the CHF condition which falls under mechanism (i) described above. This similarity was first mentioned by Bonilla and Perry in 1941 as reported by in Ref. 42, but it seems that Ref. 41 was the first to pursue the idea. The latter used dimensional analysis and arrived at the following relation for the maximum heat flux:

$$\bar{q}''_{\mathrm{CHF}} = C_k \rho_v{}^{1/2} h_{fg} \left[g(\rho_f - \rho_g)\sigma \right]^{1/4} \qquad (2.4)$$

In the above expression, C_k is a constant that Reference 41 assigned the value 0.131 to it based on maximum heat flux data. However, the data were for horizontal cylinders and other configurations different from the infinite flat plate geometry for which the model was supposed to apply.

Under mechanism (iii), Ref. 43 was the first who proposed a similarity between the Taylor wave motion and the boiling crisis. This coupled with arguments that were published in the soviet literature influenced Ref. 42 to include Taylor wave motion and Helmholtz instability as very important elements in his hydrodynamic CHF

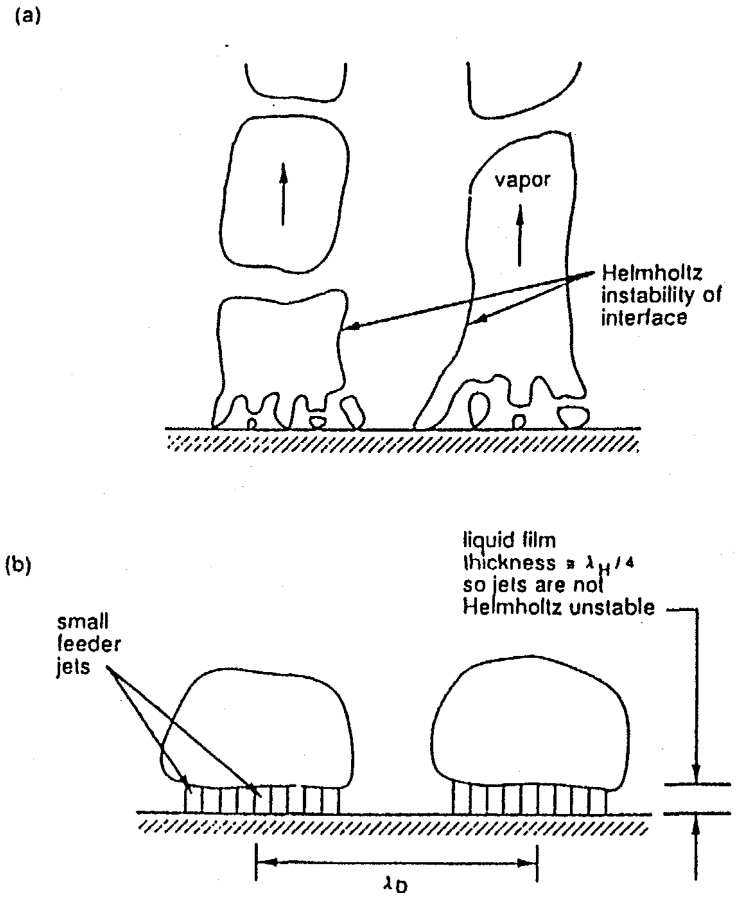

Figure 7 . The Proposed CHF Mechanisms Based on Helmholtz Instability (Carey 1992).

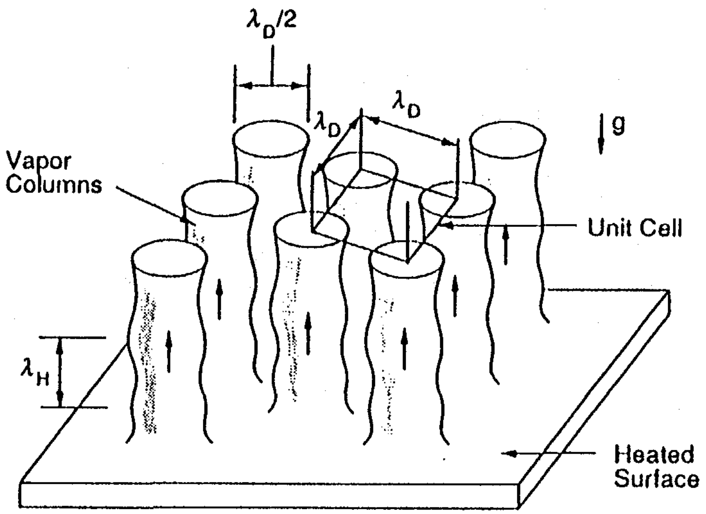

Figure 8. The Vapor Column Spacing in the Critical Heat Flux Model by Zuber (1959).

model. His model, with the suggested refinements of Refs. 44 and 45, is based on the following assumptions:

- Burnout is attained when the interface of the large vapor columns leaving the surface becomes Helmholtz unstable.
- The vapor columns leave the surface in a rectangular array, as shown in Figure 8. The centerline distance between columns is the most dangerous wavelength associated with the two-dimentional wave pattern for Taylor instability of the horizontal interface between a simi-infinite liquid region above a layer of vapor.
- The radius of the vapor column is assumed to be $\lambda_D/4$, where λ_D is the critical Taylor wavelength.
- The Helmholtz-unstable wavelength of the columns is taken equal to the Taylor wave node spacing λ_D.

Based on these assumptions, the following expression was derived for the critical heat flux:

$$\bar{q}_{\max}'' = 0.149 \rho_g h_{fg} \left[\frac{\sigma(\rho_f - \rho_g) g}{\rho_g^2} \right]^{1/4} \qquad (2.5)$$

The model of Ref. 42 was criticized for the fact that it did not account for the effects of geometry, surface condition, and the wetting characteristics of the heater surface on the CHF condition. Reference 46 used the mechanical energy stability criterion to predict the CHF in pool boiling. However, they retained the vapor column instability mechanism of Ref. 42. Their model was based on the fact that a system is in stable equilibrium if

$$(\Delta E)_{SV} \leq 0 \qquad (2.6)$$

where E is the system energy. For nucleate boiling, this relation means that the mechanism of vapor removal remains stable as long as the net mechanical energy transfer to the system is negative. Violation of this inequality marks the occurrence of CHF. Using this principle, Ref. 46 were able to show that the results of their analysis are consistent with the Zuber-Helmholtz instability model. At the same time, they showed that their method eliminates the need for information regarding the Helmholtz-unstable wavelength. This is replaced by the need for information or assumptions regarding the bubble departure diameter when the vapor column breaks up.

The model that falls under mechanism (iv) was proposed by Ref. 47. They postulated that a large bubble hovers over a number of small jets that supply the large bubble with vapor. This bubble grows in size until its buoyancy is large enough to pull it upward away from the surface. One very important assumption of their model is the fact that the thickness of the liquid film is smaller than the Helmholtz-unstable wavelength for the vapor jets so that they are not Helmholtz unstable. They further assumed that the liquid layer thickness is $\lambda_H/4$, where λ_H is the Helmholtz wavelength, and that the bubbles are arranged in a rectangular array with a centerline spacing equal to λ_D, where λ_D is the Taylor wavelength. Burnout is assumed to occur when the liquid underneath the large bubbles evaporates completely before the bubble is released. Based on these assumptions, the following expression was derived for the critical heat flux:

$$\frac{\bar{q}_{\max}''}{\rho_g^{1/2} h_{fg} [\sigma(\rho_f - \rho_g) g]^{1/4}} = \left(\frac{\pi^4}{2^{11} 3^2} \right)^{1/16} \left(\frac{A_v}{A_w} \right)^{5/8} \left(1 - \frac{A_v}{A_w} \right) \left[\frac{(\rho_f / \rho_g - 1)}{[(11/16)(\rho_f / \rho_g) + 1]^{3/5}} \right]^{5/16} \qquad (2.7)$$

where A_v/A_w is the ratio of the cross-sectional area of the vapor stems to the heater surface area. A good agreement with the Zuber CHF relation can be obtained if the latter area ratio is taken equal to

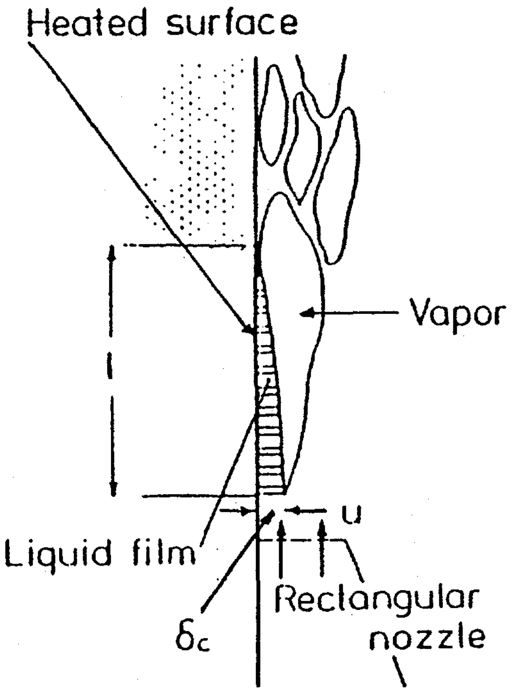

Figure 9. The Model of Haramura and Katto (1983) for Forced Convection Boiling.

$$\frac{A_v}{A_w} = 0.584\left(\frac{\rho_g}{\rho_f}\right)^{0.2} \qquad (2.8)$$

In a series of experiments, the large bubbles have been observed to be separated from the liquid sublayer by large vapor jets, which suggests that the liquid layer underneath the large bubbles could be fed with new liquid on a continuous basis. This is contradictory to the assumption of the model in Ref. 47, which postulates that the liquid is not replenished until the large bubble departs.

Reference 47 also applied their new model to forced convection boiling over a vertical flat plate. The situation is illustrated in Figure 9 where vapor stems maintain a continuous vapor flow blanketing. The liquid film is also moving under the vapor blanket with a thickness that is decreasing in the direction of the flow due to evaporation. Their model ignores the phenomena of deposition and entrainment of the droplets. They further assumed that fresh liquid enters the liquid sublayer at a constant velocity u. CHF was presumed to occur when the heat transferred from the heated surface of length l is equal to the latent heat of vaporization of all the liquid flowing into the liquid film. This resulted in the following expression for the CHF:

$$\frac{\bar{q}_{CHF}''}{\rho_f \; u h_{fg}} = 0.175\left(\frac{\rho_g}{\rho_f}\right)^{0.467}\left(\frac{\sigma}{\rho_f \; u^2 l}\right)^{1/3} \qquad (2.9)$$

It should be noted that all the existing hydrodynamic CHF models were developed for the horizontally upward facing direction. The effect of the orientation of the heating surface on the critical heat flux has not been modeled heretofore.

2.5.2. CHF Models for Spherical Heating Surfaces

Reference 48 developed a model, which was based on the hydrodynamic theory of Zuber, to predict the average critical heat flux from spheres. The vapor removal configuration from the sphere was dependent on the size of the sphere relative to the most susceptible Taylor-unstable wavelength λ_D. They assumed that when the diameter of the vessel was lower than the critical wavelength, $2R \leq \lambda_D / 3$, the vapor from the lower hemisphere slid up and eventually formed a single jet above the sphere, as shown in Figure 10a. They also assumed that the wavelength of the Helmholtz unstable disturbance was equal to the Rayleigh-unstable wave in the jet. As a result, the ratio of the average heat flux of the sphere to that for an upward facing flat plate, as predicted by Zuber, was given by,

$$\left|\frac{\bar{q}_{\max}''}{\bar{q}_{maxF}}\right|_{small\ R'} = \frac{12\sqrt{2}}{\pi}\ \frac{[(R' + 0.5\Delta)\Delta]^{3/4}}{R'^{2}} \tag{2.10}$$

where Δ was related to R' through an experimental correlation and R' was given by,

$$R' = R\sqrt{g(\rho_f - \rho_g)/\sigma} \tag{2.11}$$

When $2R > \lambda_D$, it was assumed that four jets instead of one rose from the back of the vessel, as shown in Figure 10b. The wavelength of the Helmholtz unstable disturbance was taken equal to the most rapidly collapsing Taylor-unstable wavelength. This led to the following expression for the ratio of the heat fluxes for the case of large diameter spheres:

$$\left|\frac{\bar{q}_{\max}''}{\bar{q}_{maxF}}\right|_{Large\ R'} = \frac{8(3)^{3/4}}{\pi}\ \frac{(R' + 0.5\Delta)\Delta}{R'^{2}} \tag{2.12}$$

In both the case with small diameter spheres and that with large diameter spheres, the critical heat flux was attained when the escaping jets reached the velocity at which they were Helmholtz unstable. Also, it was assumed that the velocity in the vapor blanket at the equator was equal to the velocity in the jet.

After consulting available experimental data, Ref. 48 was able to derive a relationships between R' and Δ, which lead to the following expressions for the heat flux ratios:

$$\left|\frac{\bar{q}_{\max}''}{\bar{q}_{maxF}}\right|_{Large\ R'} = 0.84;\ R' > 5.44 \tag{2.13}$$

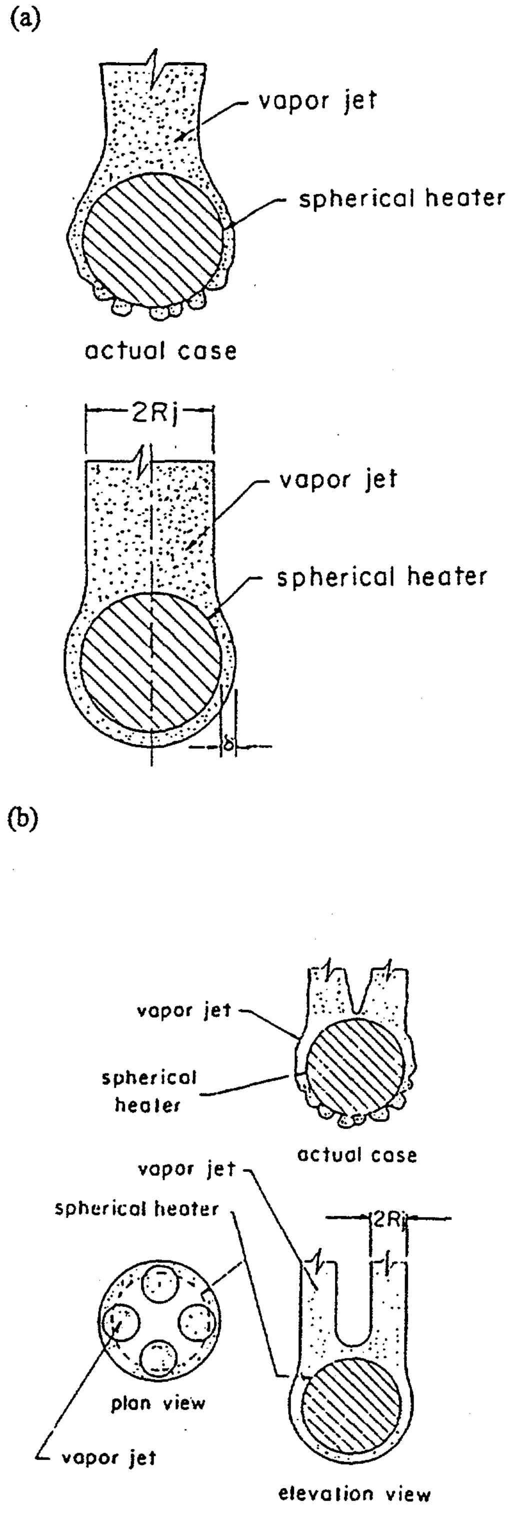

Figure 10. The Vapor Removal Mechanism Proposed by Den and Leinhard (1972).

$$\left|\frac{\bar{q}_{\max}''}{\bar{q}_{maxF}}\right|_{Small\ R'} = \frac{1.734}{\sqrt{R'}};\quad R' < \pi \qquad (2.14)$$

Reference 47 used the same rationale they used to develop a model for forced convection boiling over a vertical flat plate to generate a model for forced convection boiling over a cylinder as shown in Figure 11. The liquid film covers the whole surface of the cylinder while getting thinner toward the back due to evaporation. If *l* is replaced by $\pi d/2$ in equation (2.9), the CHF expression for a cylinder derived by Ref. 47 can be obtained,

$$\frac{\bar{q}_{\max}''}{\rho_f\ u h_{fg}} = 0.151\left(\frac{\rho_g}{\rho_f}\right)^{0.467}\left(\frac{\sigma}{\rho_f\ u^2 d}\right)^{1/3} \qquad (2.15)$$

It should be noted that all the existing hydrodynamic CHF models for curved heating surfaces (i.e., 2-D horizontal cylinders or 3-D spherical surfaces) were based on the assumption of a uniform CHF value over the entire heating surface. Thus far, no theoretical study has been attempted to discern the spatial variation of the critical heat flux along the outer surfaces of heated spheres and horizontal cylinders.

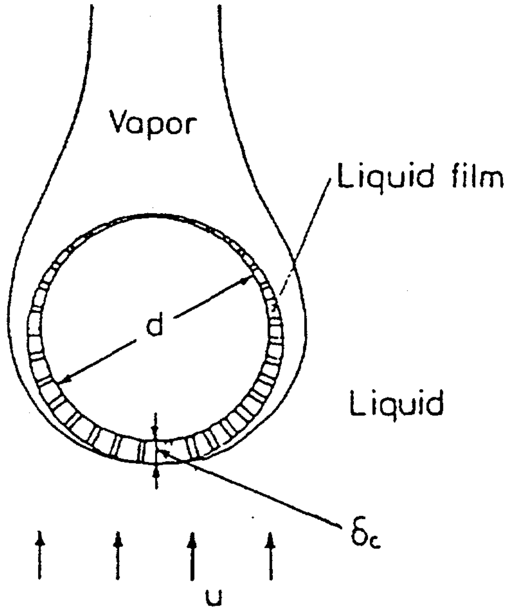

Figure 11. The Model of Haramura and Katto (1983) for Forced Convection Boiling on a Horizontal Cylinder.

2.6 References

1. Guo, Z. and El-Genk, M. S., "An experimental study of the effect of surface orientation on boiling heat transfer during quenching", ASME Winter Annual Meeting, Paper No. 91-WA-HT-1, Atlanta, GA, 1991.

2. Chu, T. Y., Brainbridge, B. L., Bentz, J. H. and Simpson, R. B., "Observations of quenching downward facing surfaces", Sandia Report, SAND93-0688, 1994.

3. Thibault, J. and Hoffman, T. W., "Local boiling heat flux density around a horizontal cylinder under saturated and subcooled conditions", Proc. Sixth Int. Heat Transfer Conf., Toronto, Vol. 1, pp. 199-204, 1978.

4. Stolz, G., Paschkis, V., Bonilla, C. F. and Acevedo, G., "Thermal considerations in oil quenching", J. of the Iron and Steel Institute, Vol. 193, No. 2, pp. 116-123, 1959.

5. Manson, L., "Cooldown of shrouded spherical vessels in liquid Nitrogen", Adv. Cryogenic Eng., Vol. 12, pp. 373-380, 1966.

6. Hwalek, J. J., The Quenching Method of Determining Boiling Curves on Spheres, Ph.D Thesis, Department of Chemical Engineering, University of Illinois, Urbana, 1982.

7. Ungar, E. K. and Einchhorn, R., "Local surface boiling heat transfer from a quenched sphere", ASME technical 82-HT-27, 1982.

8. Irwing, M. E., The Angular Variation of Temperatures Within Copper Spheres Quenched in Liquid Nitrogen, M.S. Thesis, Department of Chemical Engineering, University of Illinois, Urbana, 1984.

9. Irwing, M. E. and Westwater, J. W., "Limitations for obtaining boiling curves by the quenching method with spheres", Proc. of the Eighth Int. Heat Transfer Conference, Vol. 4, pp. 2061-2065, 1986.

10. Subramanian, S. and Witte, L. C., "Quenching of a hollow sphere", ASME J. Heat Transfer, Vol. 109, pp. 262-264, 1987.

11. Dix, D. and Orozco, J., "An experimental study in nucleate boiling heat transfer from a sphere", ASME J. Heat Transfer, Vol. 112, pp. 258-263, 1990.

12. El-Genk, M.S. and Glebov, A.G., "Transient Pool Boiling from Downward Facing Curved Surfaces," Int. J. Heat and Mass Transfer, Vol. 38, 2209-2224, 1995.

13. Merte, H. and Clark, J. A., "Boiling heat transfer with cryogenic fluids at standard, fractional, and near-zero gravity", ASME J. Heat Transfer, Vol. 86, No. 3, 1964.

14. Ishigal, S., Inoue, K., Kiwaki, Z. and Inai, T., "Boiling heat transfer from a flat surface facing downward", Int. Heat Transfer Conf., Aug. 29-Sep. 1, Paper No. 26, 1961.

15. Githingi, P. M. and Sabersky, R. H., "Some effects of the orientation of the heating surface in nucleate boiling", J. Heat Transfer, Vol. 85, pp.379, 1963.

16. Marcus, B. D. and Dropkin, D., "The effect of surface configurations on nucleate boiling heat transfer", Int. J. Heat Mass Transfer, Vol. 6, pp. 863-867, 1963.

17. Vishnev, I. P., "Effect of orienting the hot surface with respect to the gravitational field on the critical nucleate boiling of a liquid", Inzhenerno-Fizicheskii Zhurnal, Vol. 24, No. 1, pp. 59-66, 1973.

18. Chen, Li-Ting, "Heat transfer to pool boiling freon from inclined heating plate", Lett Heat Mass Transfer, Vol. 5, pp. 111-120, 1978.

19. Nishikawa, K., Fujita, Y., Uchida, S. and Ohta, H., "Effect of surface configuration on nucleate boiling heat transfer", Int. J. Heat Mass Transfer, Vol. 27, No. 9, 1559-1571, 1984.

20. Jung, D. S., Venart, J. E. S. and Soussa, A. C. M., "Effects of enhanced surfaces and surface orientation on nucleate and film boiling heat transfer in R-11", Int. J. Heat Mass Transfer, Vol. 30, No. 2, pp. 2627-2639, 1987.

21. Beduz, C., Scurlock, R. G. and Sousa, A. J., "Angular dependence of boiling heat transfer", Advances in Cryogenic Eng., R. W. Fast, ed., Plenum Press, New York, Vol. 33, pp. 363-370, 1988.

22. Nishio, S. and Chandratilleke G. R., "Steady-state pool boiling heat transfer to saturated liquid helium at atmospheric pressure", JSME Int. J., Series I, Vol. 32, No. 4, pp. 639-645, 1989.

23. Haselden, G. G. and Peters, J. I., "Heat transfer to boiling liquid oxygen and liquid nitrogen", Trans. of the Institutions of Chemical Engineers, Vol. 27, pp. 201-208, 1949.

24. Lance, R. P. and Myers, J. E., "Local boiling coefficient on a horizontal tube", A.I.Ch.E J., Vol. 4, No. 1, pp. 75-80, 1958.

25. Flynn, T. M., Draper, J. W. and Roos, J. J., "The nucleate and film boiling curve of liquid nitrogen at one atmosphere", Adv. Cryogenic Eng., Vol. 7, pp. 537-545, 1961.

26. Theofaneous, T. G., Syri, S, Salmassi, T., Kymäläinen, O. and Tuomisto,H., "Critical heat flux through curved, downward facing,

thick walls", Nuclear Engineering and Design, Vol. 151, pp.247-258, 1994.

27. Theofaneous, T. G. and Syri, S., "The coolability limit of a lower reactor pressure vessel head", Proc. NURETH-7, 1995.
28. Carne, M., "Some effects of test section geometry, in saturated pool boiling, on the critical heat flux for some organic liquids and liquid mixtures", Chemical Engineering Progress Symposium Series, Vol. 61, No. 59, pp. 281-289, 1964.
29. Cornwall, K., Schuller, R.B. and Einarsson, J.G., "The influence of diameter on nucleate boiling outside tubes," Proc. Of the seventh Int. Heat Transfer Conf., Vol. 4, pp. 47-53, 1982.
30. Rhea, L.G. and Nevins, R. G.., "Nucleate boiling heat transfer from an oscillating sphere in liquid nitrogen," Adv. Cryogenic Eng., Vol. 14, pp. 178-184, 1968.
31. Chu, T.Y., Bentz, J.H. and Simpson, R.B., "Observation of the Boiling Process from a Large Downward-Facing Torispherical Surface", 30th National Heat Transfer Conference, 1995.
32. Gaertner, R.F., "Photographic study of nucleate pool boiling on a horizontal surface", Trans. Am. Soc. Mech. Engrs., Series C, J. Heat Transfer, Vol. 87, pp. 17-29, 1965.
33. Katto, Y., "Critical Heat Flux," Advances in Heat Transfer, Vol. 17, pp. 1-65, 1985.
34. Dhir, V.K., "Study of transient transition boiling heat fluxes from spheres subjected to forced vertical flow", Proc. Of the sixth Int. Heat Transfer Conf., Vol. 1, pp. 451-456, 1978.
35. Bergles, A.E. and Thompson, W.G., "The relationship of quench data to steady state pool boiling data", Int. J. Heat Mass Transfer, Vol. 13, pp. 58-68, 1970.
36. Veres, D. R. and Florschuetz, L. W., "A comparison of transient and steady-state pool-boiling data obtained using the same heating surface", ASME J. Heat Transfer, Vol. 93, pp. 229-232, 1971.
37. Owens, F. L. and Florschuetz, L. W., "Transient vs steady-state nucleate boiling", ASME J. of Heat Transfer, Vol. 94, pp. 331-333, 1972.
38. Peyayopanakul, W. and Westmaster, J. W., "Evaluation of the unsteady-state boiling quenching method for determining boiling curves", Int. J. Heat Mass Transfer, Vol. 21, pp. 1437-1445, 1978.
39. Lin, D. and Westwater, J. W., "Effect of metal thermal properties on boiling curves obtained by the quenching method", Proc. Seventh Int. Heat Transfer Conf., Vol. 4, pp. 155-160, 1982.
40. Carey, V. P., Liquid-Vapor Phase-Change Phenomenon, Hemisphere Publishing Corporation, 1992.
41. Kutateladze, S. S., "On the transition to film boiling under natural convection", Kotloturbostroenie, No. 3, pp. 10, 1948.
42. Zuber, N., "Hydrodynamics aspects of boiling heat transfer", AEC Rep., AECU-4439, June, 1959.
43. Chang, Y.P., "A theoretical analysis of heat transfer in natural convection and in boiling", Trans. ASME, Vol. 79, pp. 1501, 1957.
44. Lienhard, J. H., Dhir, V. K. and Riherd, D. M., "Peak pool boiling heat-flux measurements on finite horizontal flat plates", Trans. Am. Soc. Mech. Engrs., Series C, J. Heat Transfer, Vol. 95, pp. 477-482, 1973.
45. Lienhard, J. H. and Dhir, V. K., "Hydrodynamic predictions of peak pool-boiling heat fluxes from finite bodies", Trans.

Am. Soc. Mech Engrs., Series C, J. Heat Transfer, Vol. 95, pp. 152-158, 1973.

46. Lienhard, J. H. and Hassan, Mojibul, "On predicting boiling burnout with the mechanical energy stability criterion", Trans. Am. Soc. Mech. Engrs., Series C., J. Heat Transfer, Vol. 101, pp.276-279, 1979.

47. Haramura, Y. and Katto, Y., "A new hydrodynamic model of critical heat flux, applicable widely to both pool and forced convection boiling on submerged bodies in saturated liquids", Int. J. Heat Mass Transfer, Vol. 26, No. 3, pp. 389-399, 1983.

48. Lienhard, J. H. and Dhir, V. K., "Extended hydrodynamic theory of the peak and minimum pool boiling heat fluxes", NASA CR-2270, July, 1973.

3 EXPERIMENTAL METHOD

3.1. Experimental Apparatus

The experimental apparatus employed in this study consisted of a water tank and condenser assembly, segmented and continuous vessels for steady state and quenching experiments, a data acquisition system, and a photographic system.

3.1.1 Water Tank and Condenser Assembly

In this project, a series of steady state and quenching experiments had to be performed in a water bath maintained at prescribed temperature and pressure conditions. The medium in which these experiments were to be performed had to sustain a gage pressure of up to 138 KPa. Therefore, it was decided to manufacture a cylindrical tank equipped with a reflux condenser. Figure 12 shows a picture of the tank and condenser assembly that was taken in the Thermal Hydraulics Laboratory (THL) on the second floor of the Mechanical Engineering Building where the experiments were performed. The THL has a convertible ceiling that can be opened and extended to the floor above. It is equipped with high power supply and advanced instrumentations suitable for flow visualization, flow measurement, pressure drop measurement, temperature measurement, power control, and heat flux measurement.

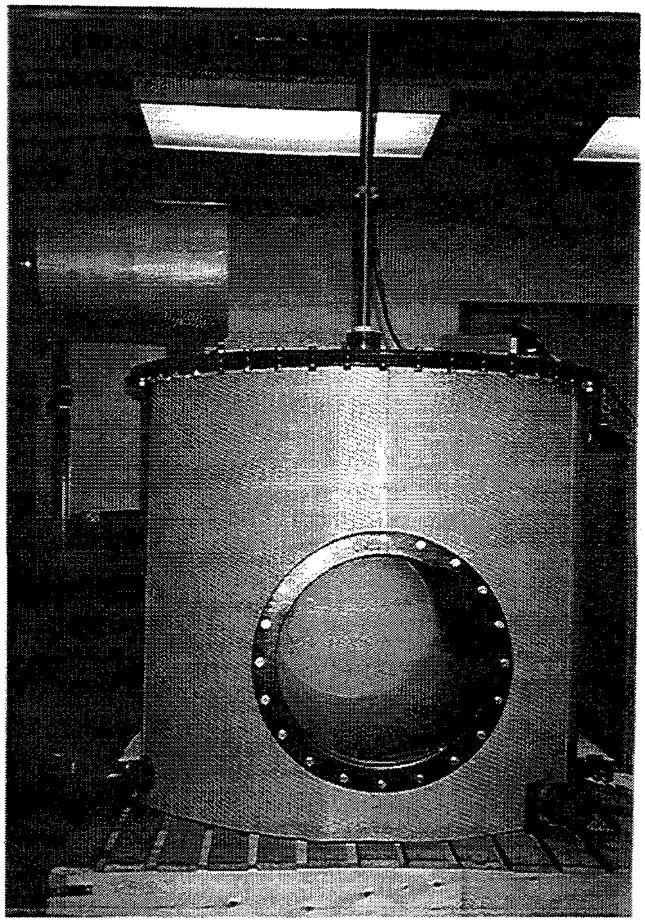

Figure 12. Pictorial View of the Water Tank and the Condenser Assembly.

3.1.1.1. Water Tank

The size of the tank was designed to be large enough to accommodate hemispherical and toroidal vessels of diameters up to 0.5 m and to minimize the effect of recirculation motions created by the boiling process. At the same time, it was very important not to make the tank too large that it would not be possible to transport it to the desired location inside the building where the experiments were to be performed. The major constraint was the size of the doors that the tank had to be carried through inside the building where the THL was located. Taking these factors into consideration, it was decided to build a tank with a diameter of 1.22 m and a height of 1.14 m.

It was necessary to choose the material the tank was going to be made of. This material had to be strong to sustain the highest pressure that would be attained, and not too expensive due to the limited fund that was available to spend on this item. These criteria eliminated copper and aluminum as possible candidates for the former was too expensive and the latter lacked the desired strength. Stainless steel was also abandoned because it was expensive and it was going to increase the manufacturing cost substantially because it was hard to machine and roll. Finally, it was decided to use carbon steel for it was strong to sustain the high pressure and within the available budget. It should also be noted that carbon steel is the actual wall material used in commercial-sized reactor vessels.

One major shortcoming of carbon steel was that it was susceptible to corrosion. Therefore, special precautions had to be taken to protect the tank wall from the intense corrosive effect of steam and hot water. To do this, the interior surface of the tank was thoroughly polished and then coated with high-temperature corrosion- and moisture-resistant durable paints. This was very important for the success of the visualization studies that were carried out during this project.

After performing an analysis of the stresses imposed on the tank wall at the highest pressure, it was decided to use a wall thickness of 6.35 mm. For the tank bottom and the tank top cover, a thickness of 12.7 mm was used. Figures 13 and 14 show the tank with all its dimensions. Figure 14 also shows the condenser which was not included in Figure 13 to be able to show the features of the mechanism used to slide the vessels vertically inside the tank. The cover was fastened to the tank using bolts and a large gasket was used to prevent any leaks as shown in Figure 15.

One major task of the project was to perform a visualization study of the phenomenon of downward facing boiling taking place on the outer surface of the vessels. Therefore, it was important to install large viewing windows to observe, video-tape, and take pictures of the two phase boundary layer developing along the downward facing curved heating surfaces. The size of the large windows was chosen so it could allow observing the whole surface of the largest vessels that were used. Two large windows were placed on two opposite sides of the tank. One was used for the recording system along with light sources and the other was used for additional lighting as deemed necessary. The small window was used to observe the water level while the tank was being filled with water and to know the exact location of the vessel inside the space above the water level. The large windows were made with 25.4 mm thick acrylic plexiglass. The small window was made of the same material with a thickness of 12.7 mm. The glass was fastened to the tank by placing a ring on the outside of the window that was bolted to a flange as shown in Figure 16. An o-ring seal was used to prevent any leaks around the windows.

A very important component of the tank that needed to be properly designed was the guidance mechanism as shown in Figure 17. This component allowed the tube connected to the test vessel to slide vertically. The guidance mechanism had also to be leak tight which was especially important at higher pressures. After the tube was slid to the desired position, the o-rings around the tube were tightened by turning the outer nut, which pushed down against the upper brass cylinder placed on top of the upper o-ring. As a result, the two o-rings were squeezed against the tube and the connection was sealed. When it was time to move the tube again, the outside nut was loosened to allow the tube to move freely in the vertical direction.

The guidance mechanism was part of the access hole of the top cover, which was needed to mount the vessels to the tube so they could be tested. This was done when the water inside the tank was relatively cold, otherwise the hot steam that would escape from the access hole would make it very hard to mount the vessel.

To heat the water to a desired temperature, the tank was equipped with three immersion heaters with a total power of 36 KW. Three identical power supplies were installed in the lab where each line had a voltage of 240 V and a maximum current capacity of 50 A. Using all these heaters, it would take about 4 hours to boil the water inside the tank. Due to the height of the water level, there would be a small temperature gradient within the water with the hot liquid accumulating at the top. Three thermocouples were installed along the inside of the tank wall to access the temperature variation within the water. All of these thermocouples were inserted inside the tank at the same location shown under item "m" in Figure 14. One sensed the temperature at the same level as location "m", another was bent upward to measure the temperature at the water surface, and the third was bent downward to keep track of the temperature very close to the bottom of the tank.

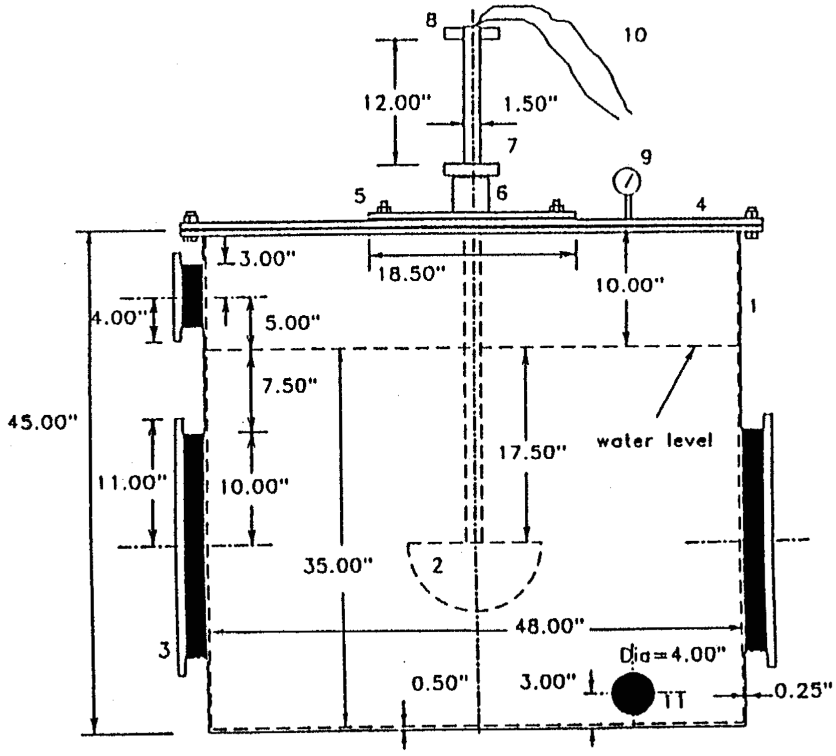

1	Cylindrical Tank
2	Hemispherical Vessel
3	Viewing Window
4	Tank Cover
5	Tank Acess Hole Cover
6	Vertical Guidance Mechanism
7	Stopping Mechanism
8	Handle
9	Pressure Gage
10	Thermocouples and Power Supply Lines
11	Immersion Heater

Figure 13. Front View of the SBLB Water Tank Without the Condenser.

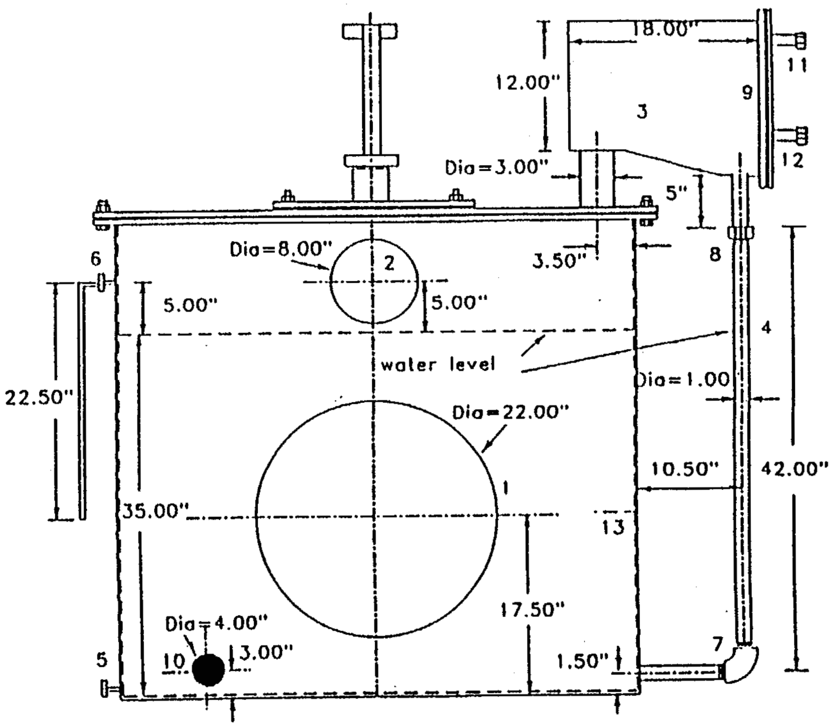

1	Large Viewing Window
2	Small Viewing Window
3	Condenser
4	Condensate Return
5	Drain
6	Water Inlet and Pressure Relief Valve
7	Elbow
8	Pipe Connection
9	Condenser Access Door
10	Immersion Heater
11	Cold Water Inlet
12	Hot Water Outlet
13	Thermocouple Access Hole

Figure 14. Side View of the SBLB Water Tank with the Condenser.

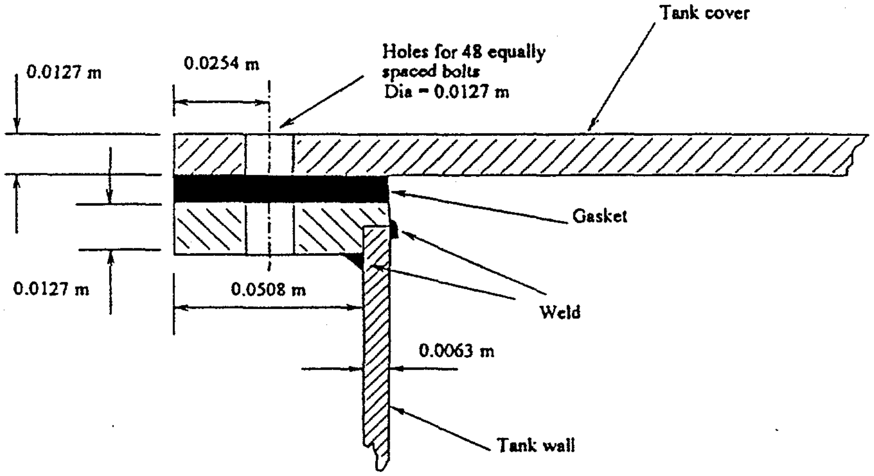

Figure 15. Connection Between the Tank Wall and the Tank Cover.

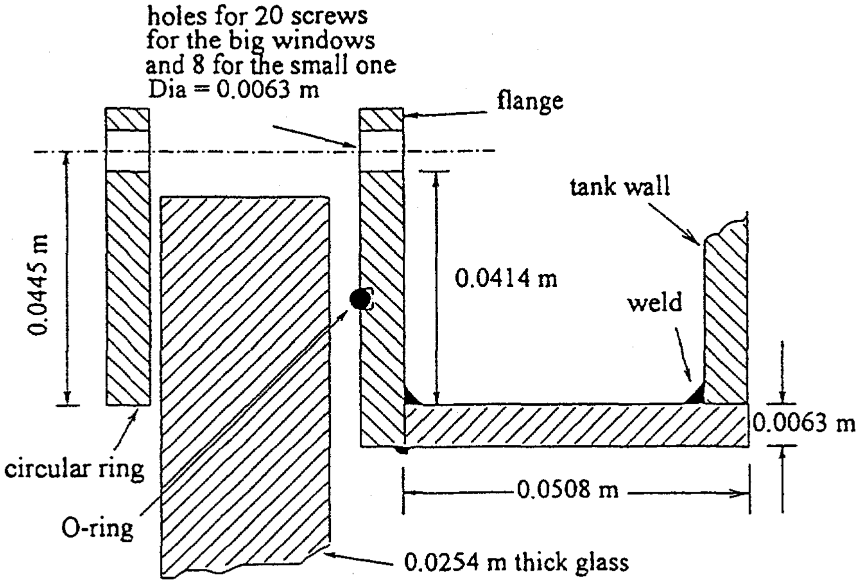

Figure 16. Connection Between the Windows and the Tank.

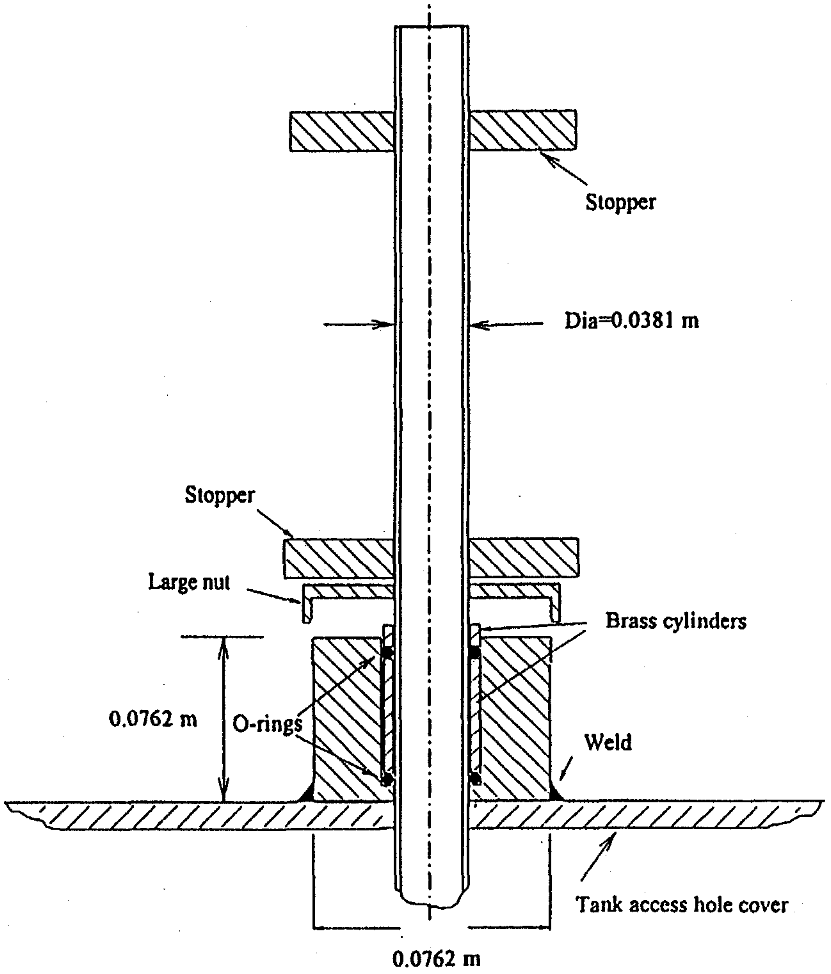

Figure 17. Schematic of the Vertical Sliding Mechanism in the Middle of the Tank.

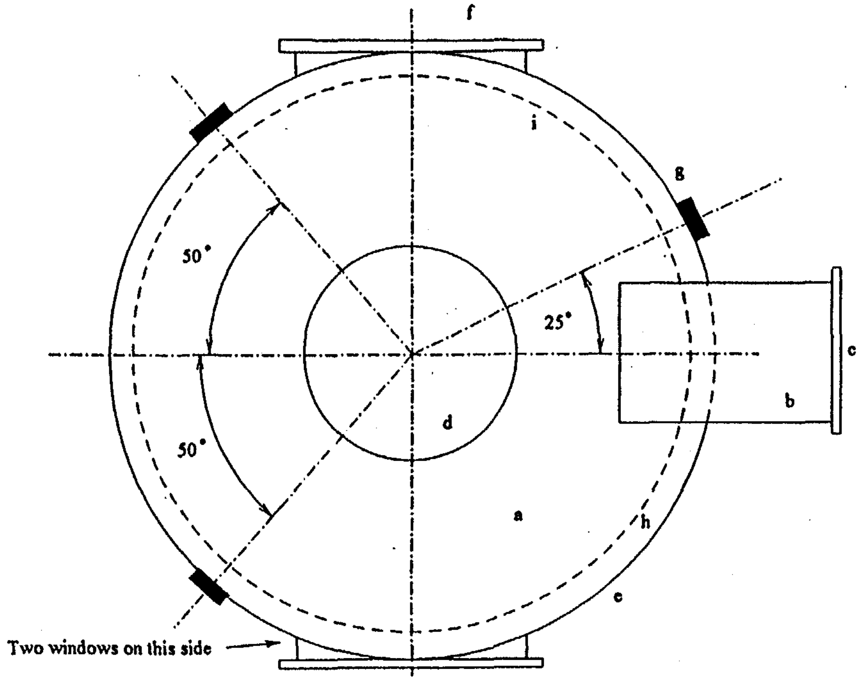

a	Tank cover
b	Condenser
c	Condenser access door
d	Tank access hole
e	Viewing window
f	Viewing window
g	Immersion heater
h	Flange
i	Inside of the tank wall

Figure 18. Top View of the Water Tank Showing the Locations of the Immersion Heaters.

The three heaters were spread along the circumference of the tank wall, as shown in Figure 18, so that the heating could be as uniform as possible. They were placed at location that were relatively away from places where potential leaks could develop. It was thought that below the windows, the condenser and the valve used to fill the tank with water were all locations that should be avoided. As a result, it was not possible to keep the same angle between two adjacent heaters.

3.1.1.2. Condenser

When the pressure inside the tank was above atmospheric, the reflux condenser was employed. The housing of the condenser was made out of a cylindrical pipe with a diameter of 0.355 m. Water vapor entered the condenser through an opening with a diameter of 76 mm. The housing of the condenser was tilted slightly (see Figure 19) downward in the direction of steam flow so that the condensate flowed toward the 25 mm pipe and could not return directly toward the water surface inside the tank. This made it possible to avoid the extra disturbance to the water bath that would occur if the condensate had dropped directly on the water surface.

A 12.7 mm O.D soft copper tubing with a 1.588 mm wall thickness was used to form a helical coil that would fit inside the condenser housing. One end of the coil was connected to a tap water supply line and the other end discharged into a drain. The length of the tubing used was estimated based on a total heat load that corresponded to a heat flux of 1 x 10^6 W/m^2 from a 0.3048 m hemispherical vessel. The maximum water flow rate from the line was estimated to be 0.18 x 10^{-3} kg/s. Using appropriate correlations for the inside and the outside heat transfer coefficients, it was decided to use a tube length of 10 m.

3.1.2. Segmented Hemisphere

The segmented hemisphere had a wall thickness of 12.7 mm as shown in Figure 20. Each segment of the hemisphere was machined separately and at the end the five segments were assembled together. The hemisphere, its cover, and the pipe that connected it to the tank cover were all made of stainless steel to avoid corrosion. The flange that was connected to the cover of the vessel was welded to the top segment, and it was used to support four screws that were used to tighten all the segments together as shown in Figures 20 and 21.

The segments were separated by an insulating layer made of high temperature silicon rubber material to minimize the heat transfer between the segments and to prevent any leaks from taking place. When it was not compressed, the insulating layer ring had a thickness of 5.08 mm. After it was compressed, the thickness reduced to 2.58 mm. There was a perfect seal between the insulating layer and the two segments which helped prevent any leaks from occurring. If this layer had been used by itself, however, there would have been no guarantee that the spacing between two adjacent segments would be 2.58 mm with the four long screws being tightened. To overcome this problem, it was decided to use four small solid stainless steel spheres, with a diameter of 5.08 mm, between every two adjacent segments. The spheres were equally distributed along the circumference at every interface. At each location where these balls were placed, a dip with a depth of 1.27 mm was machined inside each of the two segments. As a result, when the four long screws were tightened, the insulating layer was compressed uniformly to 2.58 mm at all the interfaces.

The cover of the hemisphere was fastened to the flange through a series of screws. An o-ring seal was used between the cover and the flange. The o-ring was placed on the inside of the screws, further away from the outside surface of the vessel, so that there was no direct path for the water to leak to the inside of the vessel. It was very important to make the vessel leak tight so that the heating elements and the thermocouples would function properly. The cover was connected to the stainless steel pipe through a pipe connection.

The segmented hemisphere had a total of 25 thermocouples having the same diameter of 1.016 mm but with different depths. The steady-state temperatures recorded by the thermocouples were

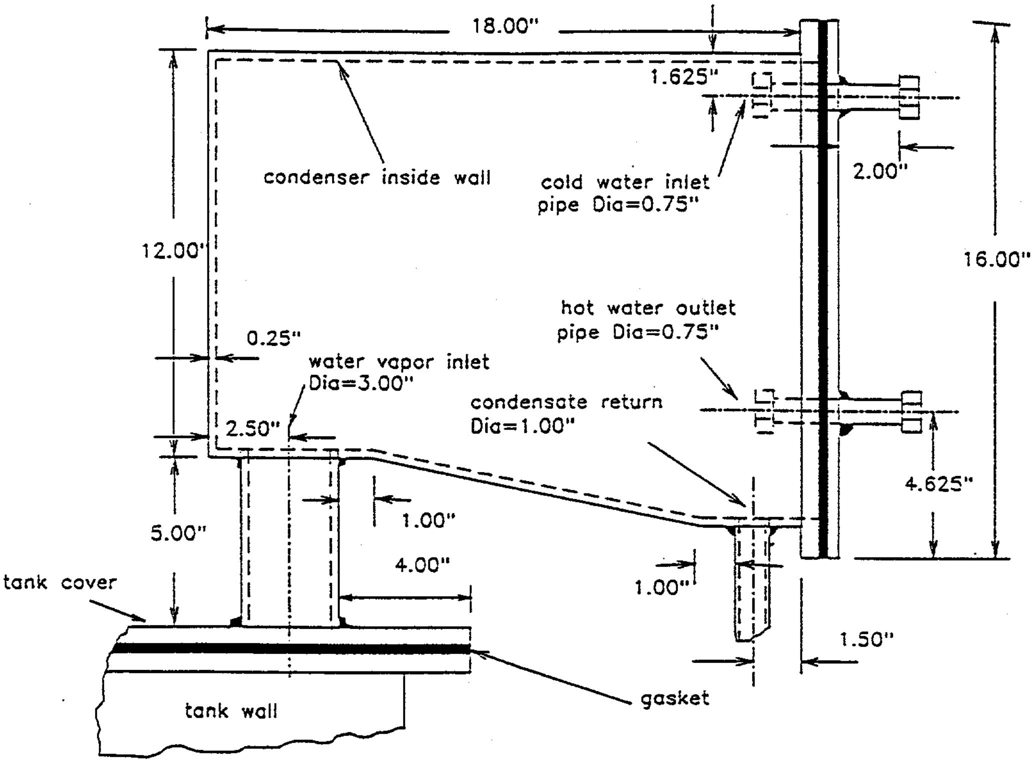

Figure 19. Schematic of the Condenser Housing.

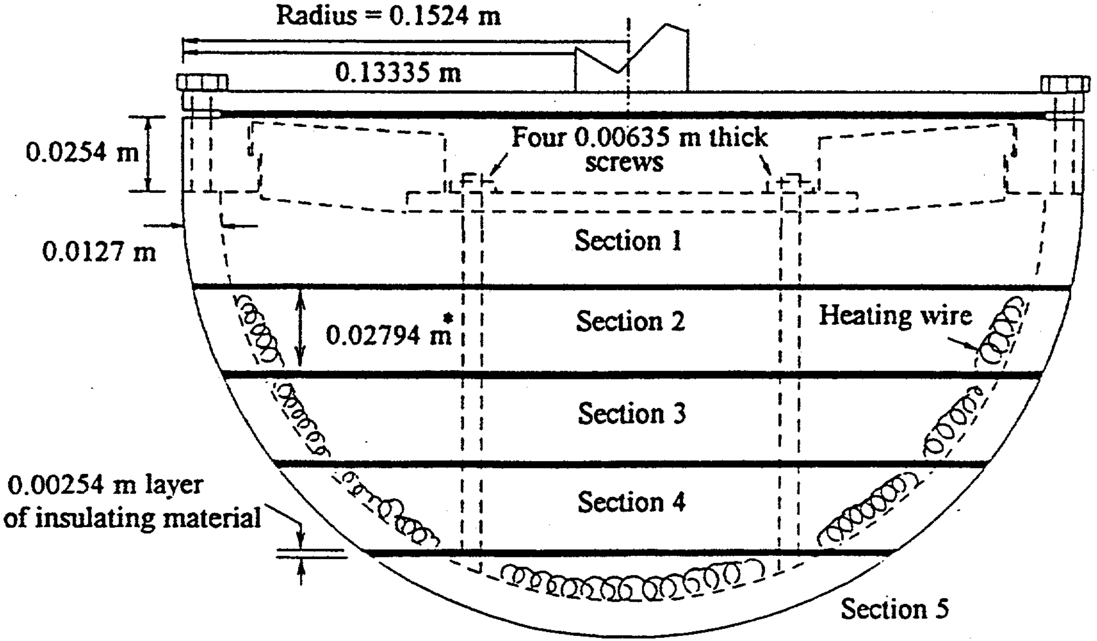

Figure 20. Side View of the Segmented Hemispherical Test Vessel.

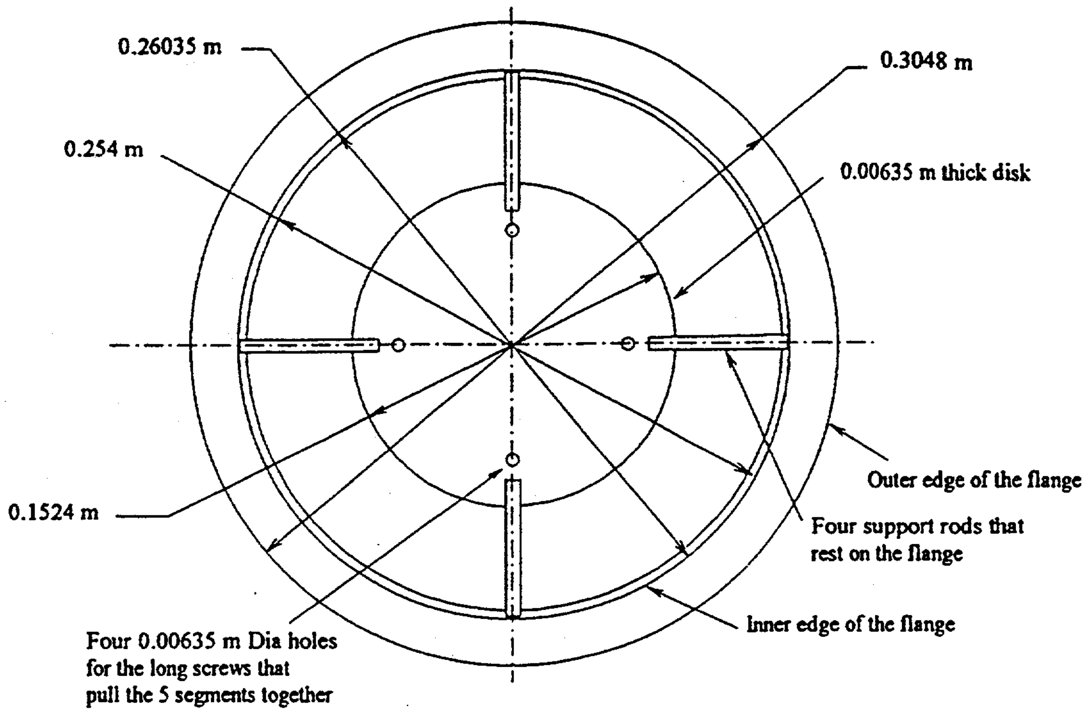

Figure 21. Schematic of the Supporting Mechanism Used to Pull the Segments Together.

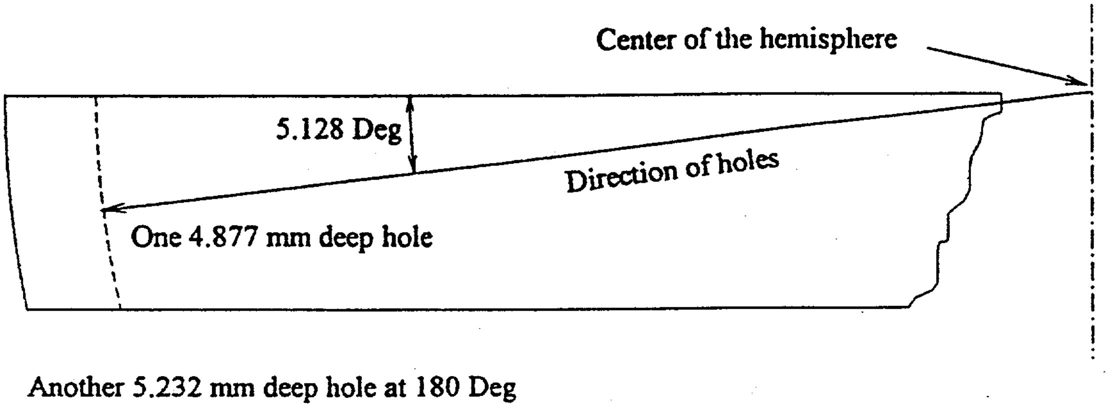

Figure 22. Locations of the Thermocouples in the First Segment.

going to be used in an inverse heat conduction analysis to determine the local boiling heat transfer coefficient along the outside surface of the vessel. The first top segment, which was not heated directly, had two thermocouple holes at 180° from each other, as shown in Figure 22. Segments 2, 3, and 4 had the same total number of thermocouple holes shown in Figures 23, 24, and 25. Four of the five holes of each of these segments were placed next to each other. The fifth was placed on the opposite side of the circumference to check the symmetry of the heated segment. For the bottom segment, eight thermocouple holes were used as shown in Figure 26. The various figures show the slopes of the lines along which the thermocouple holes were drilled. These lines are defined by the center of the vessel and the location of the thermocouple hole, which was drilled along the local radial direction.

3.1.3. Continuous Vessels for Steady-State Experiments

Before installing the nichrome coil on the segmented vessel, several other hemispherical and toroidal vessels with various sizes were used to gain experience with mounting nichrome coil on curved surfaces. These vessels were purchased from a supplier with a relatively low price, which was a much more attractive option than using the expensive segmented vessels to find out the best way to mount nichrome coil on curved surfaces. When forming the nichrome wire into a shape that would fit nicely to the inner surface of the vessel, it was important that the spacing between adjacent wire loops remained the same throughout the surface so that the same heat flux would be supplied everywhere on the back surface of the vessel. In order to have full control over the wire spacing, a mold of the inside of the hollow vessel was formed using Plaster Pairs. When the mold cured, the desired layout of the wire was marked on the back of the mold. The coil density depended on the desired maximum heat flux and the size of the nichrome wire used. Then nails were placed at selected locations on the back of the mold to help support the wire while it was being formed according to the layout highlighted on the back surface of the mold.

The resistance of the wire per foot, the maximum voltage of the variac, and the maximum current the wire could carry dictated the length of nichrome wire per circuit. Starting at the bottom center location on the mold, the wire was wrapped around the nails to form the first loop of heating wire. Then the process was repeated until the whole wire length for the first circuit was used up. Other circuits were then installed until the whole surface was covered with nichrome coil as shown in Figure 27. During this process, it was very important to make sure that adjacent wire loops were not touching each other. Current would always follow the path of least resistance, which meant that it would bypass a whole loop of wire if it was in contact with an adjacent loop.

It was then necessary to move the wire from the mold and place it on the back of the vessel while making sure the nichrome coil retained its shape. Therefore, a high-temperature cement called OB600 from Omega Engineering Inc. was applied at selected locations on the nichrome wire while it was still mounted to the mold. This was the same cement used to attach the formed wire to the back surface of the vessel. OB600 had a high dielectric strength, which was necessary to prevent any short circuiting.

Before attaching the formed wire to the interior side of the vessel,, a thin layer of OB600 was applied to the inner surface of the vessel to prevent any direct contact between the wire and the metallic vessel. This was important for the proper operation of the nichrome coil and the thermocouples attached to the surface. After the shaped wire was placed on the surface, the cement was applied to attach the coil to the vessel to allow for good thermal contact.

3.1.4 Test Vessel Using Cartridge Heaters

To perform a special study of the high-heat-flux boiling regime around the bottom center, an aluminum test vessel was prepared to accommodate the use of cartridge heaters instead of nichrome coil. The main problem with

(a) Top View

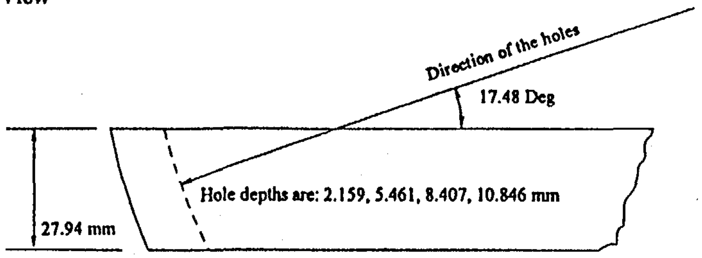

Adjacent holes form an angle of 3 Deg with the center of the vessel
Another 7.417 mm deep hole at 180 Deg from the deepest hole

(b) Side View

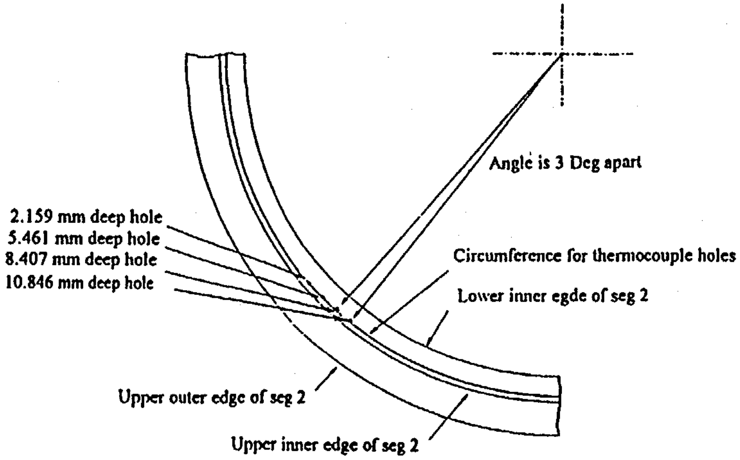

Figure 23. Top and Side Views of the Thermocouple Locations in the Second Segment.

(a) Top View

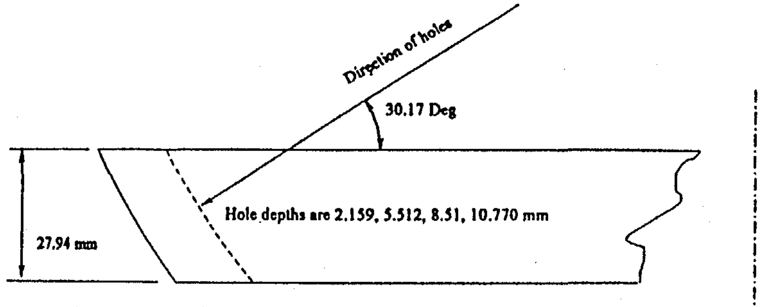

Adjacent holes form an angle of 3 Deg with the center of the hemisphere
Another 7.163 mm deep hole at 180 Deg from the deepest hole

(b) Side View

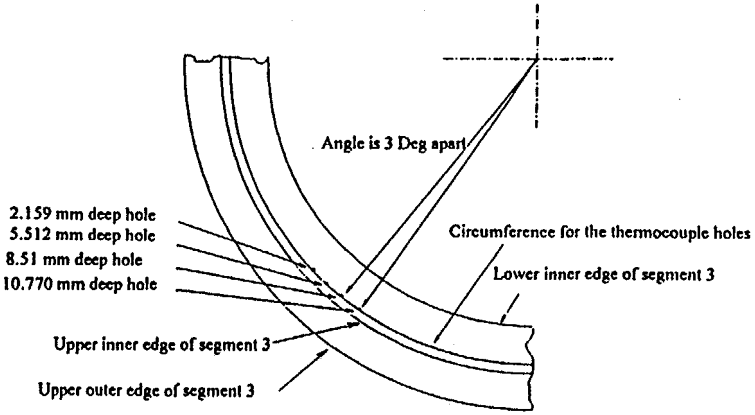

Figure 24. Top and Side Views of the Thermocouple Locations in the Third Segment.

(a) Top View

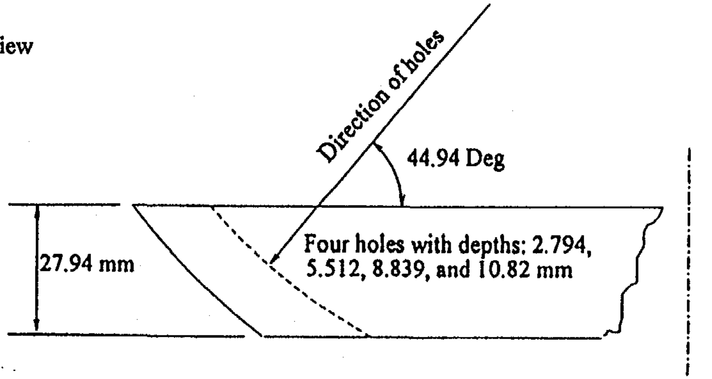

Adjacent holes form an angle of 3 Deg with the centre of the hemisphere
Another 8.077 mm deep hole at 180 Deg from the deepest hole

(b) Side View

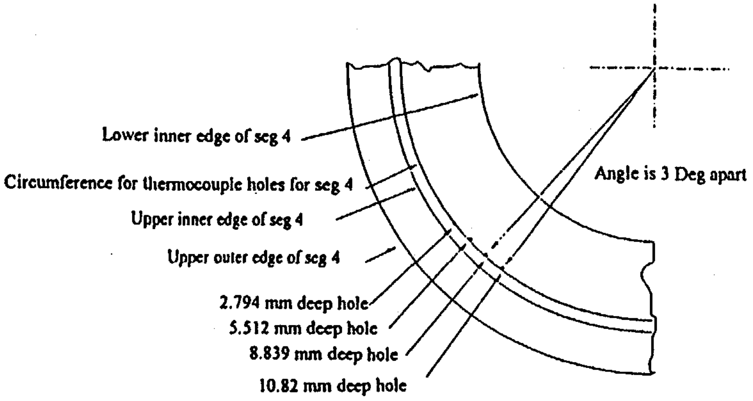

Figure 25. Top and Side Views of the Thermocouple Locations in the Fourth Segment.

(a) Top View

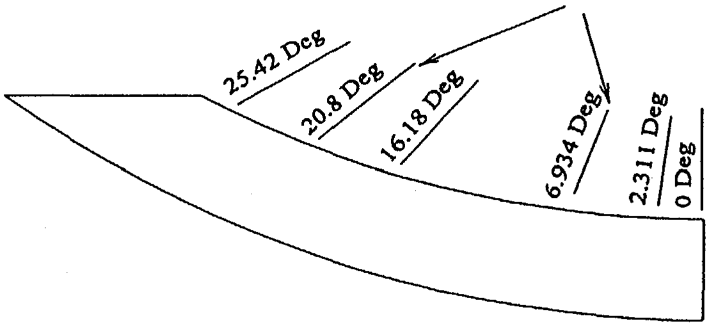

(b) Side View

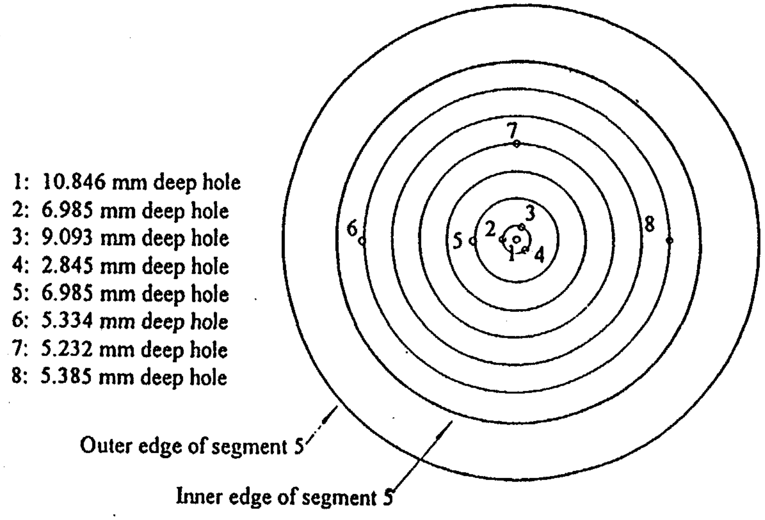

Figure 26. Top and Side Views of the Thermocouple Locations in the Fifth Segment.

commercially available hemispheres was the fact that they could only be obtained with a wall thickness of 6.35 mm. This thickness was much smaller than the length of any commercially available cartridge heater. Therefore, it was decided to weld a thick aluminum test section to a hemispherical vessel such that the use of cartridge heaters could be accommodated.

The wall around the bottom center region of the test vessel was removed and it was replaced by a thick aluminum test section, which had been previously machined on the outside to match the spherical surface of the vessel, as shown in Figure 28. The thickness of the test section was chosen so it could accommodate 31.75 mm long cartridge heaters from Watlow corporation. The test section consisted of an inner part and an outer part that were welded together. The weld that kept the two parts together was placed on the outside at the interface between the two segments and it was the main region of contact between the two sections. Everywhere else along the circumference that separated the inner part and the outer part, there was a 3.18 mm air gap to minimize conduction heat transfer between the adjacent pieces. A 3.18 mm groove was also placed along the outer circumference of the outer part to minimize the conduction to the wall of the hollow hemisphere. Detailed dimensions of the test section are shown in Figure 29.

The cartridge heaters chosen were 31.75 mm long and 9.52 mm thick. For the proper operations of these heaters, it was very important to minimize the air gap between the heaters and the test section. Therefore, the holes for the heaters were drilled and then reamed to provide a 0.0254 mm fit. Before inserting them in the holes, the heaters were treated with a special coating called Watlube from Watlow. This product protects against high temperature oxidation and more importantly it enhances the heat transfer between the heaters and the test section. Each heater had a power rating of 400 W when subjected to a voltage of 120 V. It was decided to use five heaters for the inner segment and fifteen heaters for the outer segment, as shown in Figure 29. This would allow heat flux levels of up 1.2 MW/m^2 to be achieved.

In order to measure the temperatures of the outside surfaces of the inner and the outer segments, four K-type thermocouples with stainless steel sheathing were inserted from the interior of the test section. Four thermocouple holes were drilled inside the inner and the outer segments, as shown in Figure 29. The depths of the two inner holes were chosen so that the sensing tips of the thermocouples would be about 1.588 mm away from the outside surface of the test section, whereas the two other holes were placed very close to the interior surface of the test section to monitor the temperatures in the hottest regions of the segments.

3.1.5. Continuous Vessels for Quenching Experiments

Continuous hemispherical vessels made of aluminum and toroidal vessels made of carbon steel were used to conduct quenching experiments to investigate the spatial variation of the boiling curve along the outer surface of the heating surface. The vessels had an outside diameter ranging from 0.152 to 0.305 m and a wall thickness of 6.35 mm. Aluminum was chosen for the hemispherical vessels because of its low price, high specific heat, and high thermal conductivity. A flange was welded to the vessel to allow for the mounting of a cover and an o-ring seal for leak tightness. For the purpose of comparison, continuous hemispherical vessels made of stainless steel were also used.

In order to derive the local boiling curve at different locations along the surface, a total of sixteen 30 gauge K-type thermocouples were placed along an arc that started at the bottom center and ended close to the upper edge of the vessel as shown in Figure 30. Three other thermocouples were equally spaced on the circumference half way between the bottom center and the equator to check the uniformity of the heating of the hemisphere. In order to mount the thermocouples to the vessel, 1.59 mm holes with a depth of 1.59 mm were drilled along the radius at the various locations. An aluminum-zinc based solder with a melting point of about 350 °C was used to attach the thermocouple bead to the vessel wall.

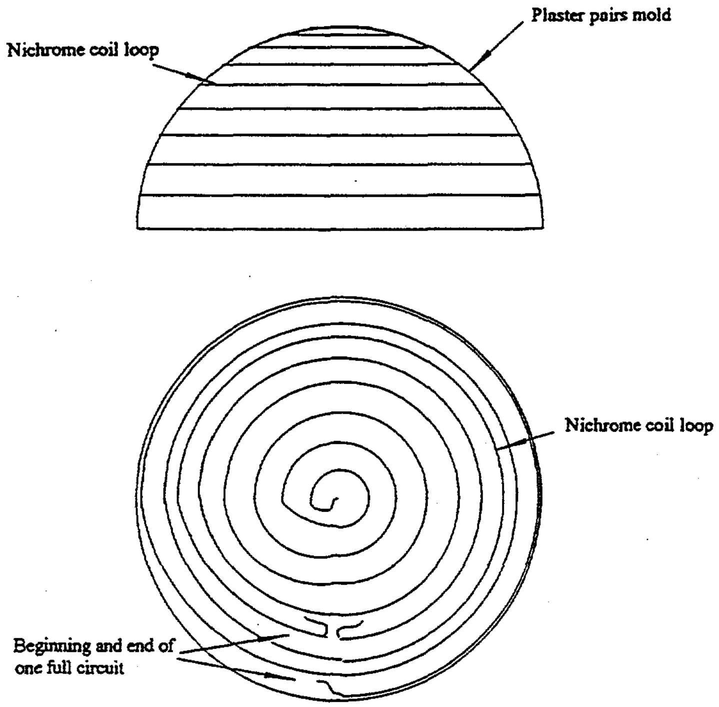

Figure 27. Top and Side Views of the Mold Used to Shape the Nichrome Coils.

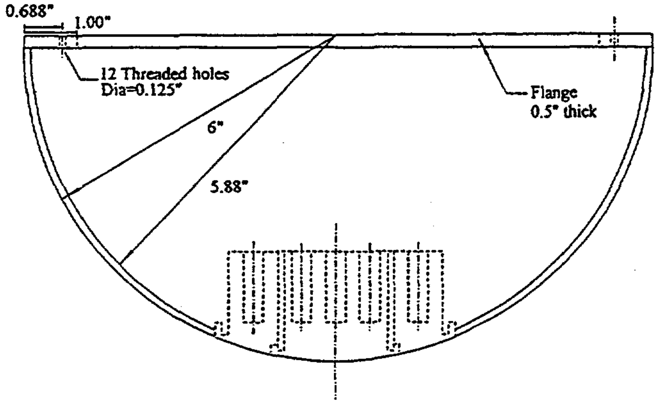

Figure 28. Side View of the Thick Aluminum Test Section in the Bottom Center Region of the Vessel.

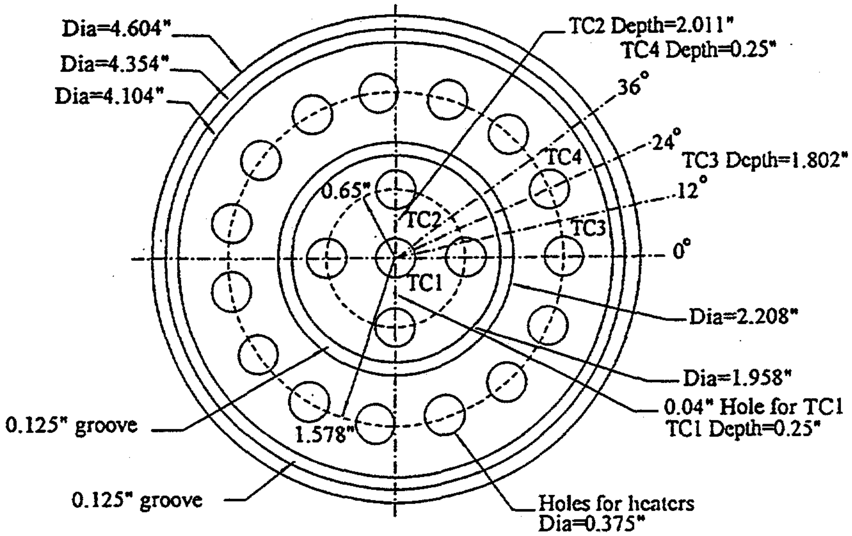

Figure 29. Top View of the Thick Aluminum Test Section.

3.1.6. Data Acquisition System

In the transient quenching and the steady state experiments, the temperatures at various locations in the vessels had to be monitored. This was accomplished by using a 25 MHz 386 IBM compatible personal computer along with a data acquisition system. Two Strawberry Tree ACPC-16 boards were installed inside the PC. Each of these boards had 16 analog inputs and 16 digital input/output channels. Therefore, the system was capable of monitoring up to 32 thermocouple signals.

The ACPC-16 board was capable of resolutions in the range between 12 and 16 bits, which was equivalent to 0.024% and 0.0015% of full scale, respectively. Each of the boards had six voltage ranges that could be set according to the sensor used. The boards also had a high noise rejection integrating converter, which helped reject 50/60 Hz AC power line interference when used in the "low noise mode". The ACPC-16 units were also capable of accurate cold junction compensation and linearization for thermocouple devices. The two ACPC-16 boards were connected to a total of four Strawberry Tree T12 boards, which in turn were connected to the thermocouples. Each of the T12 boards had 8 analog inputs and 8 digital input/output channels. An IBM 386 personal computer was employed to connect to four T12 terminal panels, which in turn were connected to thermocouples that sensed the temperatures of the vessel mounted to the tank.

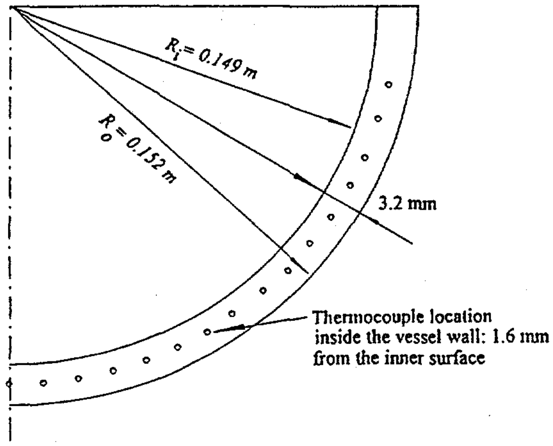

Figure 30. Thermocouple Locations on the Test Vessels for the Quenching Experiments.

The highest sampling rate possible was dependent on the resolution chosen. There was a trade off between higher resolution and higher sampling rates. In the steady state experiments, having high sampling rates was not important. Therefore, the highest "low noise resolution" was used to help minimize the effect of the interference from the AC power line and the nichrome coil used to heat the vessels. In the quenching experiments, using a high sampling rate was important especially when the time constant of the vessel was low. Table 2 lists the variation of the scan rate as a function of the resolution employed as supplied by the manufacturer of the boards. These rates are based on an IBM PC running at 4.77 MHz. Since the computer used during this project was faster, these rates would be somewhat higher in our case.

These scan rates are the time it would take the board to read a single channel mounted by itself and with a series of other sensors. The total sampling rate is the value listed in the table multiplied by the total number of thermocouples to be monitored. The sampling rate needed for the board to read one channel accounts for the time necessary for the analog to digital converter to perform its task and the settling period required when moving from one channel to the next. When reading multiple channels, a small initial pulse of potential develops when the multiplexer moves on to the next channel. Therefore, it is necessary to allow for a settling period before taking the reading on the next channel.

In order to take full advantage of the speed offered by the ACPC boards, a program DATACOL for quenching and steady state experiments was written in compiled BASIC to monitor the thermocouple signals. . At the beginning of the program, the resolution, the number of thermocouples to be traced, and the type of sensors used were declared. Then the program performed a calibration of all the analog input channels. The driver of the board offered two ways that could be used to collect the data. One consisted of scanning every thermocouple signal once before dumping all the values into a file. This method slowed down the process because of the time needed to log the data into the file. The second method read all the thermocouple signals multiple times while storing the readings in memory. It was only at the end that all the data collected was dumped into a file. The latter method was the one used in the BASIC program. The number of times the sensors were scanned and the scanning rate depended on the duration of the boiling process.

During the quenching experiments, it was necessary to heat the vessel to a desired temperature before quenching it into the water bath. Therefore, a second program TEMPDIS was written to allow for the monitoring of the vessel temperature while it was being heated by displaying the temperatures at various locations on the screen. This program scanned all the thermocouples once during a specified time period. Then the temperatures collected were displayed on the screen before the thermocouples were scanned again.

3.1.7 Power Control System for CHF Measurement

When the critical heat flux was reached during steady state heating experiments, any further increase in the power input would result in the onset of film boiling. This was characterized by a sudden large increase in the temperature of the heating surface. In order to protect the vessel against any possible meltdown, a control mechanism was installed to discontinue the power supply to the heaters when a significant jump in the vessel temperature was detected in the high heat flux regime.

The control system consisted of a data acquisition system, a constant DC power source, a solid state relay, and thermocouples to measure the vessel wall temperature, as shown in Figure 31. The solid state relay had a low voltage side connected to the constant DC power source, and a high voltage side connected to the variac supplying the heaters. The solid state relay was necessary because the high voltage of the variac could not be connected directly to the digital I/O channel of the data acquisition board.

To carry out the control strategy, a control routine was created using the computer program Quicklog from Strawberry Tree Inc. This routine started by collecting the temperatures of the vessel wall at several desired locations. These temperatures were then compared to a set point value of 200 °C, which was much higher than the expected wall temperature that was characteristic of nucleate boiling in water. Wall temperatures higher than 200 °C could have only been due to the occurrence of the critical heat flux. Under normal operating conditions, the vessel wall temperature would be less than 200 °C and the digital I/O channel connected to the solid state relay would be closed. This allowed the high voltage side of the solid state relay to stay closed and for the desired power to be delivered to the vessel. When a wall temperature greater than 200 °C was detected, the digital I/O channel became open. As a result, the low voltage side of the solid state relay was not powered anymore and the power supply to the heaters was discontinued, which prevented any further substantial increase in the vessel wall temperature.

3.2. Experimental Procedure

The vessel was first mounted to the vertical sliding mechanism in preparation for quenching or steady state experiments. To achieve this, the tank access hole cover and the sliding mechanism attached to it were removed from the tank assembly. Then the power supply and the thermocouple wires, that were attached to the interior side of the vessel, were inserted inside the stainless steel pipe used to position the vessel at the desired vertical location. The pipe coupling welded to the vessel cover and the male connection attached to the stainless steel pipe were subsequently screwed together to seal the connection.

Before mounting the vessel, the tank access hole cover, and the sliding mechanism to the tank assembly, the heating surface was cleaned. First the surface was polished with #220 emery paper, and then it was cleaned thoroughly with acetone. In the meantime, a special procedure was followed to prepare the water in the tank prior to a run.

Table 2 Scan Rates of the Data Acquisition System at Different Resolution Settings

Resolution	Scan Rate (Single Channel)	Scan Rate (Multiple Channels)
low noise mode: (0.0015 %)	60 Hz	60 Hz
16 bits: 0.0015 %	225 Hz	200 Hz
15 bits: 0.003 %	440 Hz	360 Hz
14 bits: 0.006 %	830 Hz	640 Hz
13 bits: 0.012 %	1500 Hz	960 Hz
12 bits: 0.024 %	2500 Hz	1300 Hz

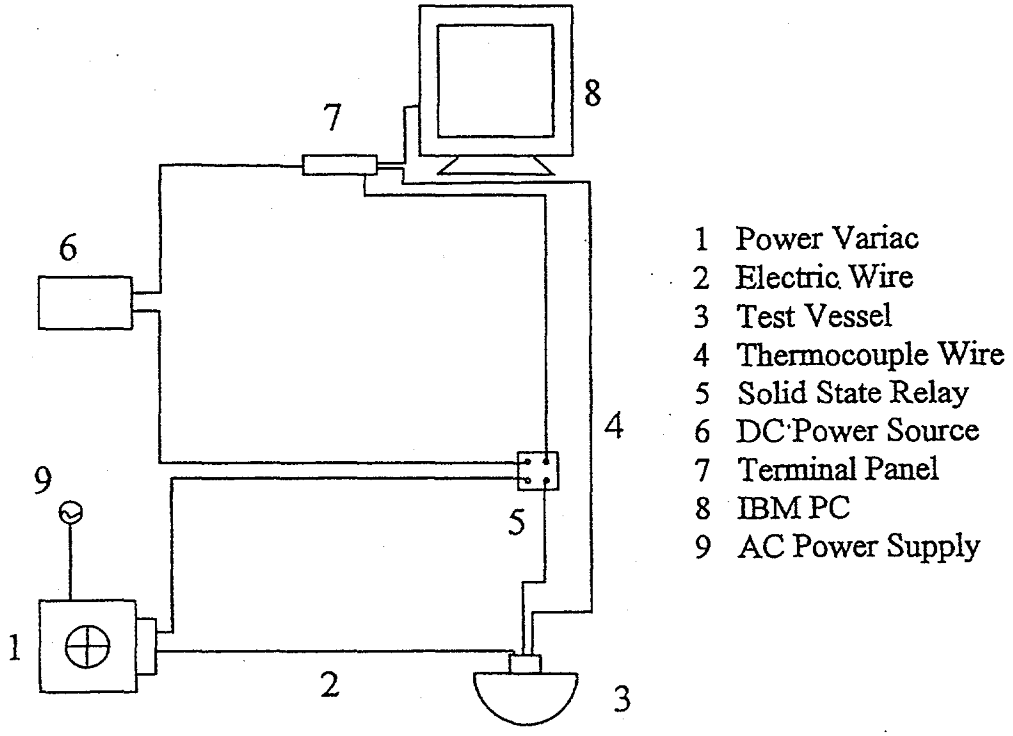

Figure 31. Schematic of the Power Control System.

3.2. 1 Water Preparation

After the vessel was put in place, a hose was connected to a tap water supply line in order to bring the water level inside the tank to about 0.838 m. The hose was equipped with a filter to get rid of any unwanted particles. When the desired water level was attained, the faucet was turned off and the three immersion heaters were turned on. It took about four hours to heat the water to the saturation temperature. At this point, the heaters were kept on for another 15 minutes to degas the water. Then the heaters were turned off to let the water cool back down to room temperature. A pump was then used to circulate the water through the filter again. This helped remove the particles that precipitated during the heating process. The heaters were turned on again to heat the water to the desired temperature. If the temperature fell below the desired value during the experiment, one of the heaters was turned on for a short while (usually one or two minutes) to bring it back up. Before each experiment, the water was given time to become completely quiescent.

3.2.2. Quenching Experiments

The various thermocouples attached to the interior side of the test vessel were connected to the terminal panels of the data acquisition system. Then the program TEMPDIS was run to monitor the heating of the vessel by displaying the temperatures at all the thermocouple locations on a computer screen. The heating continued until the vessel temperature reached 350 °C. Higher temperatures would have lead to the melting of the solder that was holding the thermocouples in place.

When the heating was over, the cover underneath the vessel was removed and the computer was set to start the collection of the quenching data. The vessel was then submerged in the water bath, and the computer was activated to start the data collection program DATACOL. The stopper on the stainless steel pipe were preset in advance to allow the vessel to be submerged about 0.304 m below the water level inside the tank.

When it was decided to video tape the event, a high resolution CCD video camera by Sony as well as a high-speed camera by Kodak were set up to record the quenching process through one of the large viewing windows. The lighting level and position were adjusted before hand for the fast quenching process. The cameras and the lights were turned on at the same time the vessel started to be lowered toward the water bath.

3.2.3 Steady State Experiments

After the vessel was mounted to the sliding mechanism and left suspended above the water level inside the tank, the power supply cables and the thermocouple wires were connected to the variacs and the data acquisition system, respectively. Each variac circuit was equipped with an ammeter that allowed the power supplied to that specific circuit to be determined. Next, the vessel was submerged about 0.304 m below the water level. Then the power to the variacs was turned on to give the desired heat flux at the vessel surface. At the same time the program TEMPDIS was running to keep track of the temperature variations at various locations inside the vessel. The thermocouple readings were used to determine whether the system reached steady state or not. Once it was decided that steady state was achieved, the program TEMPDIS was terminated, and the program DATACOL was executed to scan the thermocouple readings for a specific period of time and save them into a file.

Whenever it was decided to video tape the event, the high resolution CCD video camera by Sony was turned on after the desired steady state had been reached. Then, the lighting was adjusted until a satisfactory image of the vessel was obtained.

3.3. Data Reduction

3.3.1. Inverse Heat Conduction Program for Quenching Experiments

An inverse heat conduction code was developed for reducing the local boiling curves from the transient temperature data recorded in the quenching experiments. The code was based on the finite difference method using the control volume approach. Figure 32 shows the configuration of the control volume and the node distribution. The wall thickness was not drawn to scale in the figure. If the heat transfer coefficient is estimated to be 15 KW/(m^2-K), which is expected to be a high estimate for downward facing boiling, then using a wall thickness of 6.35 mm, the Biot number can be shown to be about 0.25. Therefore, it is reasonable to assume that the local temperature of the vessel does not vary significantly along the radial location.

The volume of node *1* that represents the bottom center is given by

$$V_1 = \frac{\pi}{3}(R_o^3 - R_i^3)[1 - \cos(\frac{\Delta\theta}{2})] \quad (3.1)$$

and the volume of any of the other nodes *n* is

$$V_n = \frac{\pi}{3}(R_o^3 - R_i^3) \\ [\cos\theta - \cos(\theta + \Delta\theta)] \quad (3.2)$$

where R_o and R_i are the outside and the inside vessel diameters respectively, θ is the local angle of inclination, and $\Delta\theta$ is the node size in the θ-direction. An energy balance on the node represented by node *n* gives

$$\rho C_p V_n (T_n^k - T_n^{k+1}) \\ = [(Q_c)_{n-1} - (Q_c)_n - (Q_b)_n - (Q_i)_n]\Delta t \quad (3.3)$$

where T_n^k and T_n^{k-1} represent the local temperatures at the time steps *k* and *k-1*, respectively, Δt the time step, $(Q_c)_{n-1}$ the heat conducted into the control volume, $(Q_c)_n$ the heat conducted out of the control volume, $(Q_b)_n$ the local heat removal from the outer surface by boiling, and $(Q_i)_n$ the heat loss to the interior of the vessel. The conduction heat transfer area between nodes *n-1* and *n* is Ac_{n-1} and it is given by

$$Ac_{n-1} = \frac{\pi}{2}\sin\theta(R_o^2 - R_i^2) \quad (3.4)$$

The boiling heat transfer area for node *n*, other than the bottom center node, is A_{bn} which is expressed by

$$Ab_n = \pi R_o^2[\cos\theta - \cos(\theta + \Delta\theta)] \quad (3.5)$$

and for the bottom center node it is

$$Ab_1 = \pi R_o^2[1 - \cos(\frac{\Delta\theta}{2})] \quad (3.6)$$

Since all the test vessels were tightly sealed, the quantity $(Q_i)_n$ was found to be about two orders of magnitude smaller than the other heat rates in equation (3.3). The other three quantities in equation (3.3) are given by

$$(Q_c)_{n-1} = \frac{1}{\Delta s}\lambda Ac_{n-1}(T_{n-1}^k - T_n^k) \quad (3.7)$$

$$(Q_c)_n = \frac{1}{\Delta s}\lambda Ac_n(T_n^k - T_{n+1}^k) \quad (3.8)$$

$$(Q_b)_n = Ab_n(q_b'')_n \quad (3.9)$$

where $(q_b'')_n$ is the local boiling heat flux and Δs is the distance between two adjacent nodes. These expressions for the various heat rates can be replaced in equation (3.3) which can then be solved for the local boiling heat flux (see Ref. 1).

3.3.2. Inverse Heat Conduction Programs for Steady State Experiments

Inverse heat conduction programs were developed to deduce the steady state variation of the heat transfer coefficient along the outer surface of the segmented hemisphere. A separate program is needed for each of the four heated segments of the stainless steel hemisphere. Each of these programs employs a constant heat flux boundary condition on the interior side of the vessel wall. This heat flux is equal to the resistance heating delivered by the nichrome coil mounted on the interior of the wall of each segment. An adiabatic boundary condition is assured by the use of an insulating layer between adjacent segments. The temperatures recorded by the various thermocouples, embedded at different locations inside the vessel wall, are used to close the system of equations so that local heat transfer

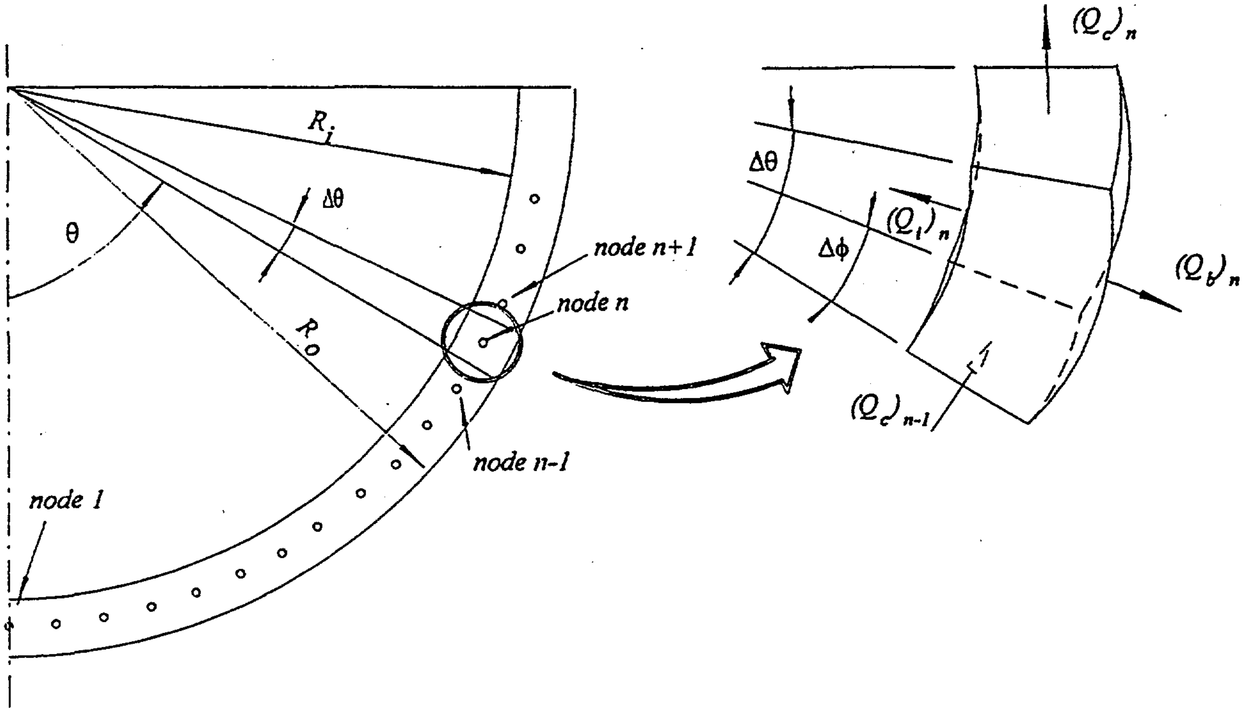

Figure 32 Configuration of the Control Volume and the Node Distribution in the Data Reduction Analysis

coefficients on the outer surface of the vessel can be estimated.

Based on the five temperature readings from the thermocouples, it is be possible to estimate the heat transfer coefficient, *h*, at five locations along the outer surface of each of segments 2, 3, and 4. The eight thermocouples installed inside the wall of segment 5 are be used to generate eight estimates of *h* along the outside surface of bottom center portion of the hemisphere.

The conduction inside the wall of each segment is described by the conduction equation written in spherical coordinates. It is assumed that the temperature is symmetric with respect to the axis of the sphere that passes through the bottom center of the vessel. Therefore, the temperature is only a function of the radial location inside the vessel wall and the azimuthal angle θ. Based on these assumptions, the conduction equation was discretized using the finite difference method. An inverse heat conduction code was developed accordingly as reported in the thesis work of Ref. 2. A detailed description of the code is given in Appendix A.

3.3.3 Error Estimates

For both the transient quenching and steady-state boiling experiments, a selected number of runs were repeated under the same experimental conditions to check the reproducibility of the data. In all cases, the results obtained in two separate runs under identical conditions were found to be highly comparable, with the CHF values well within ±15%, which is quite good for boiling data. The uncertainty in the embedded thermocouple locations was about ±0.001m, the maximum error in the temperature readings was ±0.1°C, and the error in the calculated local CHF values was about $\pm 0.050\ \text{MW/m}^2$ for saturated boiling and ±0.075 MW/m^2 for subcooled boiling. A detailed discussion of the measurement errors is given in Appendix B.

3.4 References

1. Cheung, F.B. and Haddad, K.H., "Observation of the Dynamic Behavior of the Two-Phase Boundary Layers in the SBLB Experiments," Proceedings of the 23rd Water Reactor Safety Meeting, Washington, D.C., Vol. 2, 87-112, 1994.
2. Liu, Y.C., "Inverse Heat Conduction in a Segmented Hemispherical Vessel with Downward Facing Boiling Boundary Conditions," M.S. Thesis, Department of Mechanical Engineering, The Pennsylvania State University, 1995.

4 EXPERIMENTAL RESULTS

4.1. Quenching Experiments

Using the continuous hemispherical test vessels, quenching experiments were performed to observe the dynamic behavior of the two-phase boundary layer and to assess the variation of the boiling curve along the outer surface of the vessel.

4.1.1. Dynamic Behavior of the Two-Phase Boundary Layer During Transient Quenching

A Kodak Ektapro high speed video system and a Minolta X-370 high speed camera were used to video tape and photograph, respectively, the quenching events. After video taping the events, the characteristics of the transient two-phase boundary layer were examined by playing the video tape in slow motion. Quenching of the hemispherical test vessels was performed with water temperatures ranging from 90 °C to 100 °C. For all the experiments performed, it was found that the rate of quenching increased by almost an order of magnitude when the subcooling level changed from 0 °C to 10 °C. However, the evolution of the boiling process with time remained essentially the same for both saturated and subcooled boiling.

Before discussing the observed events, it is useful to briefly review the events in a conventional quenching process. When a superheated solid object is suddenly quenched into a saturated liquid, film boiling of the liquid first takes place around the hot object. As the solid temperature drops below the minimum film boiling temperature, transition boiling occurs. On the surface of the object, the activities of vapor film breakdown and release increase progressively in time, and at the peak of these activities, the critical heat flux is reached. Beyond this point, the solid object cools off quickly and approaches the liquid temperature, marking the end of the quenching process. The above scenario holds for flat plates and disks facing horizontally upward and for objects with relatively small physical dimensions and/or curvatures, where changes in the boiling regime from film to transition and then to nucleate take place almost uniformly over the entire surface. For these objects, the critical heat flux does not change spatially from point to point along the surface. Thus the value of CHF can be uniquely determined for given shape and orientation of the object, as summarized in Ref. 1.

The sequence of events observed in this study was quite different from the conventional one described above, mainly because of the size and the downward facing orientation of the heating surface. Changes in the boiling regime from film to transition and then to nucleate did not take place uniformly over the external bottom surface of the hemispherical vessel during the quenching process. Rather, transition from film to nucleate boiling first occurred at the upper edge of the vessel. It then propagated downward along the curved heating surface, and eventually reached the bottom center of the vessel (see Figure 33). Evidently, the dynamic behavior of the two-phase boundary layer changed not only with time but also with the spatial location along the vessel surface. Thus the rate of quenching was highly non-uniform over the external surface of the vessel. Physically, this implies that the boiling characteristics could vary significantly along the vessel wall.

By studying the recorded events on the video tape, the transient quenching process was found to consist of three sequential stages. These are: (i) the initial stage of quenching during which the entire external bottom surface of the vessel was in film boiling, (ii) the intermediate stage of quenching during which film, transition, and nucleate boiling occurred simultaneously in various parts of the external surface, and (iii) the final stage of quenching during which nucleate boiling was the only mechanism for vapor generation on the external surface.

At the beginning of the quenching process, the entire surface of the vessel was covered by a vapor layer indicating the existence of film

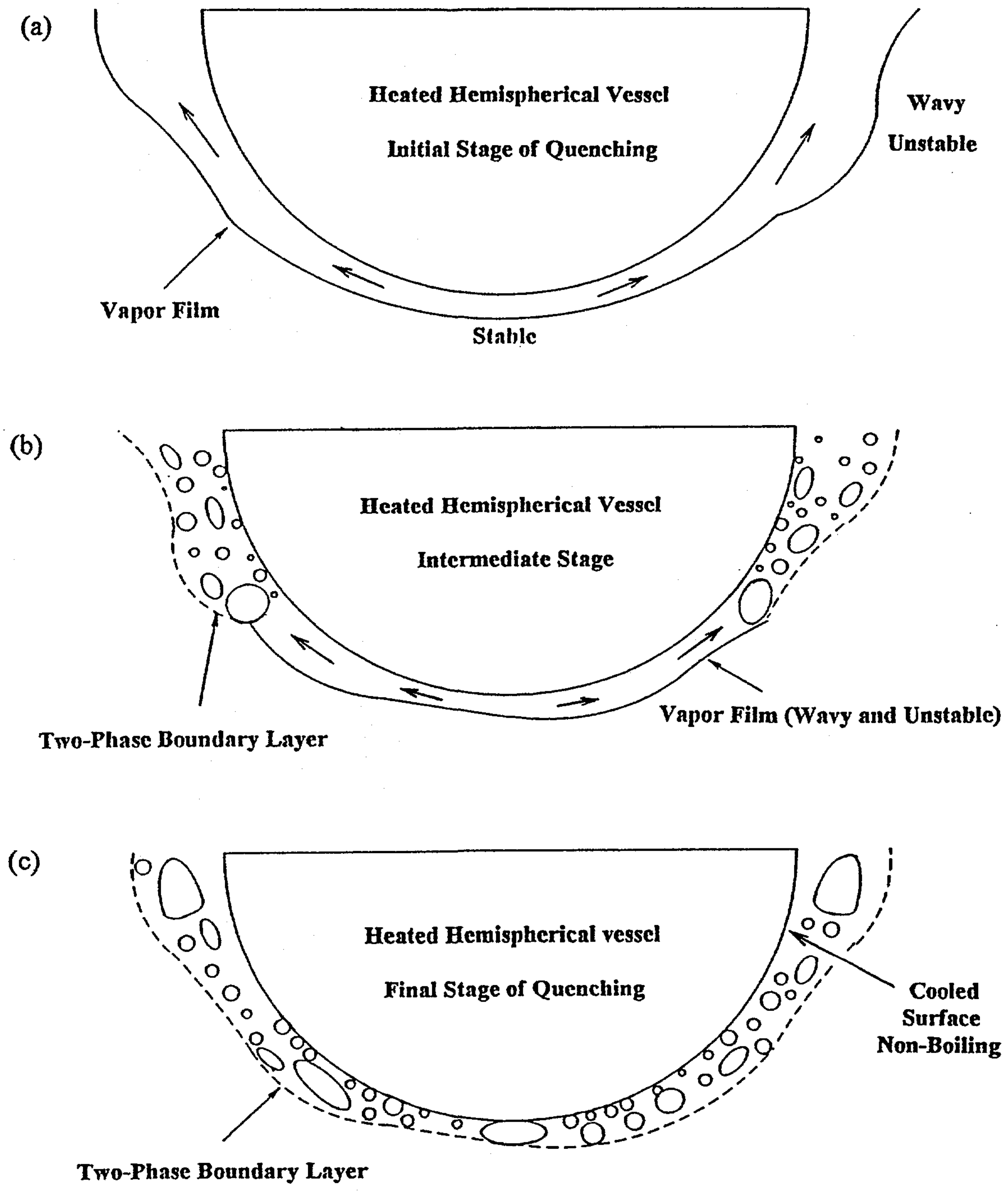

Figure 33. Schematic of the Two-Phase Boundary Layer Configuration in the Three Sequential Stages of Quenching.

boiling everywhere on the surface of the hemisphere, as shown in Figures 34(a) and 34(b). The picture shown in Figure 34(a) was taken at the very early stages of the quenching process. At this time, the wall temperature was still well above the minimum film boiling temperature and the vapor generation was intense, which caused the vapor film to be wavy especially in the upper portion of the vessel. Evidently, the two-phase boundary layer was in the turbulent film boiling flow regime. As the wall temperature approached the minimum film boiling temperature, the vapor generation decreased and the film became smooth. At this time, the two-phase boundary layer was in the laminar film boiling flow regime, as shown in Figure 34(b).

Note that the configuration of the vapor film was not uniform but varied considerably along the surface. Near the bottom center of the vessel, the film appeared to be very smooth and stable. On the contrary, it appeared to be highly wavy and unstable in the upper portion of the vessel. A physical explanation for this is that the bottom center of the vessel was facing horizontally downward. The local vapor film was very stable under the influence of buoyancy. This is not true for the upper portion of the vessel which had relatively large angles of inclination with respect to the horizontal direction. Another explanation for the spatial variation of the vapor film configuration is that all the vapor generated in the lower portion of the vessel flowed upward along the curved surface. This resulted in significant increases in the vapor velocity and film thickness in the upper portion of the vessel. The local film Reynolds number based upon the local vapor velocity and film thickness became large enough to render the local vapor film wavy and unstable.

When the local vessel temperature dropped below the minimum film boiling temperature, transition boiling and then CHF occurred first at the top of the hemisphere, with the rest of the vessel still in film boiling covered with a vapor layer, as shown in Figure 34(c). The point of transition then propagated downward until it reached the bottom center of the vessel. At this time, the upper portion of the hemisphere was already in the CHF state, as shown in Figure 34(d). Figure 35(a) corresponded to the time immediately after the CHF state when the local wall temperature, near the top of the vessel, dropped quickly toward the saturation temperature. No vapor bubbles were being generated in the upper region of the vessel. The CHF state then propagated toward the bottom center of the vessel, as shown in Figure 35(b).

After the CHF took place throughout the whole surface, nucleate boiling became the only means of vapor production on the vessel outer surface. At this stage, most of the bubbles were generated in the region around the bottom center while the rest of the surface was non-boiling, as shown in Figure 35(c). The presence of vapor bubbles in the upper region of the vessel was mainly due to the upstream effect of the two-phase boundary layer flow along the curved heating surface. Eventually, the bubble generation around the bottom center stopped when the local wall temperature cooled down toward the saturation temperature (see Figure 35(d)).

When the water was subcooled, the time duration occupied by each of the above three stages of quenching was found to decrease substantially. In general, the larger the subcooling, the shorter was the time duration. For the cases with water temperatures at 90°C and 93°C, the intermediate stage was so short that the state of CHF was attained almost immediately after the onset of transition boiling. Also, the turbulent film boiling flow regime was not observed in the initial stage of quenching. This was probably due to the fact that the minimum film boiling temperature might have increased with subcooling. It should be noted that with subcooling, there was natural convection cooling of the vessel at the end of the quenching process. Although the entire vessel outer surface was non-boiling, the wall temperature continued to drop until it reached the subcooled water temperature.

The previous observations indicated that the dynamic behavior of the two-phase boundary layer depended strongly upon the water subcooling and the local position along the

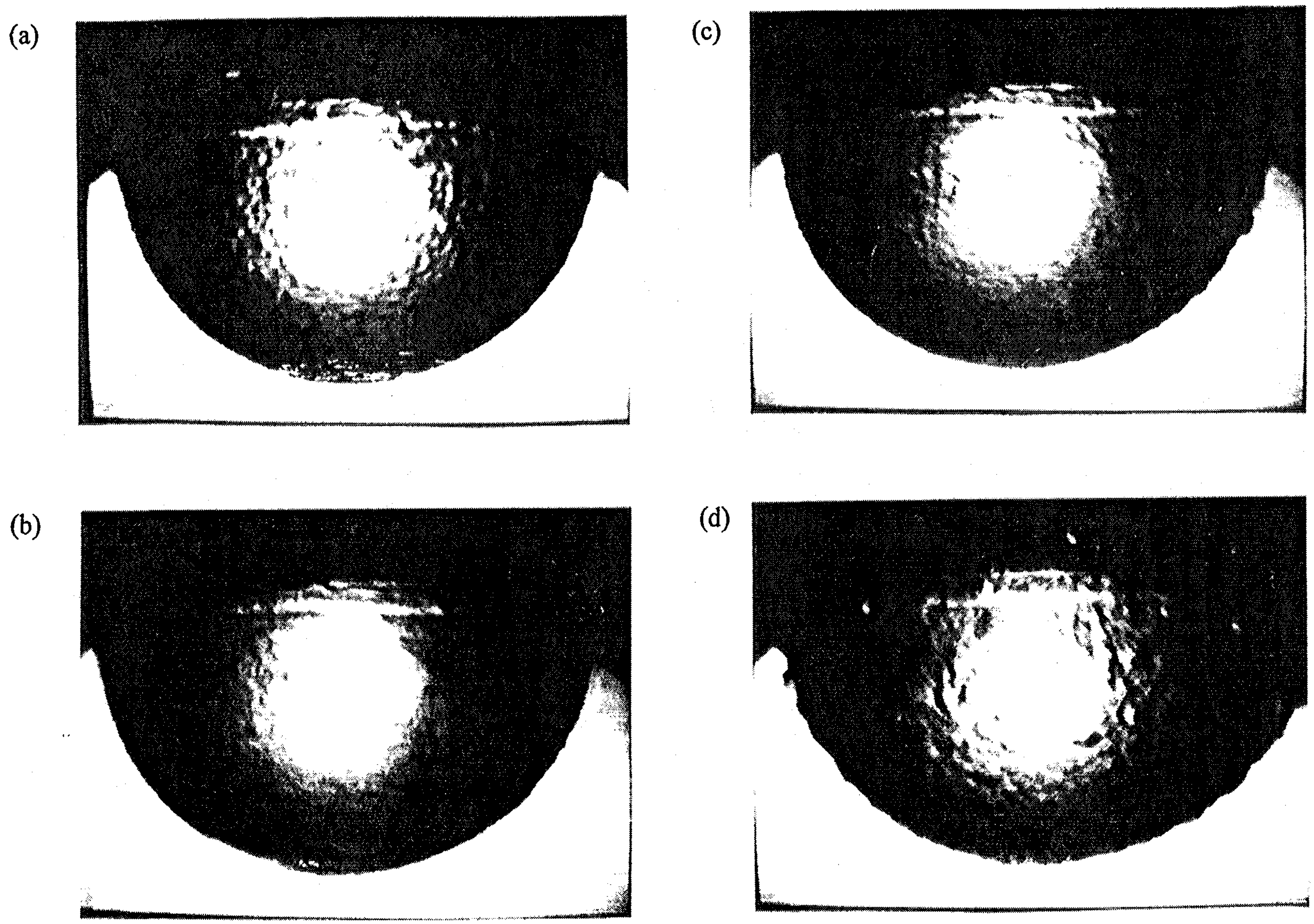

Figure 34. Sequence of Events Observed in the Initial and Intermediate Stages of Quenching.

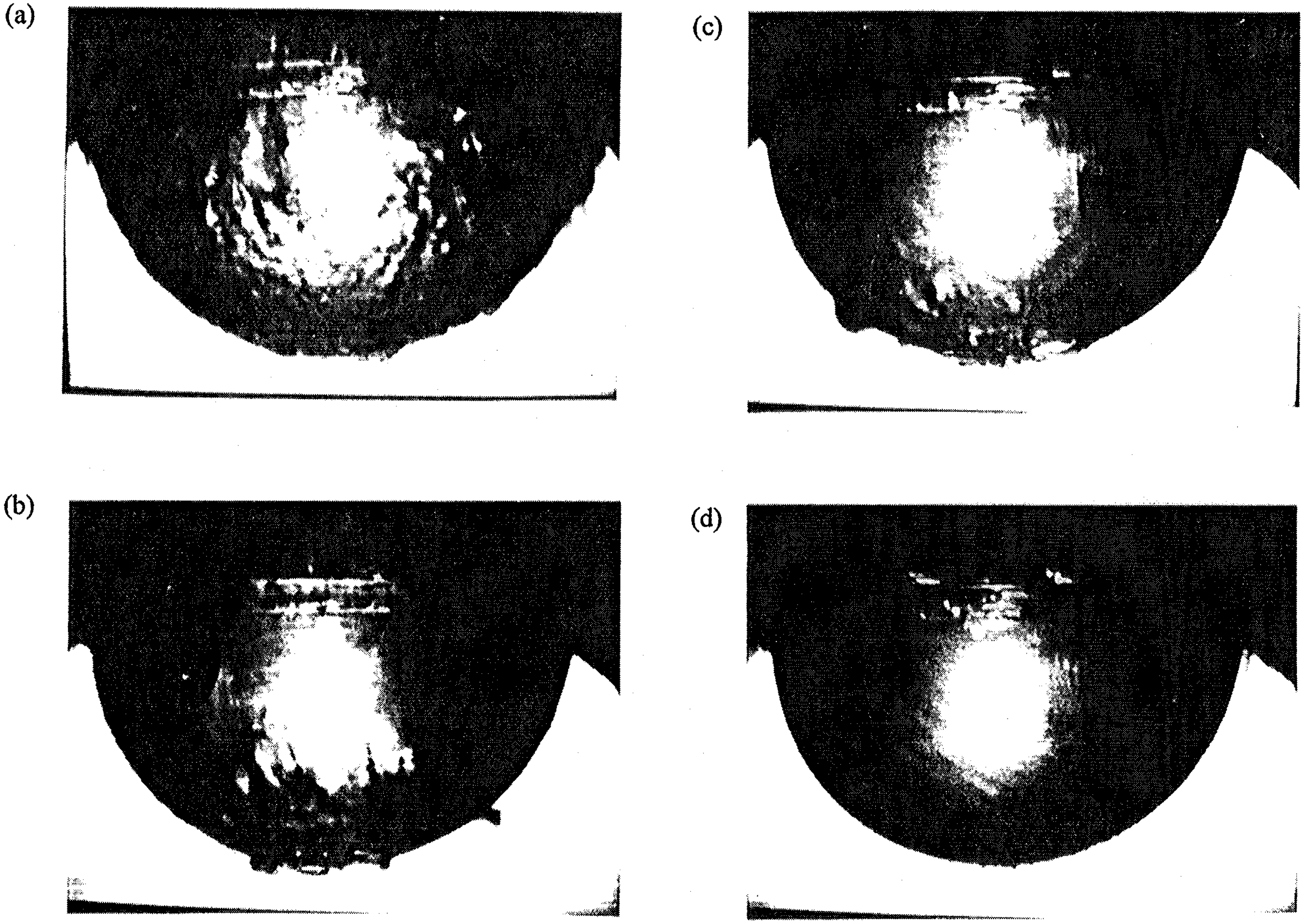

Figure 35. Sequence of Events Observed in the Intermediate and Final Stages of Quenching.

curved heating surface. Although the bottom center of the vessel was submerged first in the water bath, it took longer to quench than the rest of the heating surface. These results clearly indicated that there were significant variations of the local boiling curve and the local critical heat flux from the bottom center to the upper edge of the vessel. The experiments also revealed that the cooling rate of the vessel increased by almost an order of magnitude when the water temperature changed from 100 °C to 90 °C. Evidently, subcooling had a significant effect on the boiling curve.

4.1.2. Local Variation of the Boiling Curves on the Outer Surface of a Heated Hemispherical Vessel

The transient quenching data obtained in this study included results from quenching 8" (~0.2 m) and 12" (~0.3 m) stainless steel and aluminum hemispherical vessels in water. Local boiling curves were deduced using the data reduction method described in the previous section. When compared at the same dimensionless wall location, ℓ/L, having a value of zero at the bottom center and unity at the upper edge of the vessel, the local boiling curves for the two vessel sizes and two wall materials were found to be essentially the same. The differences were well within the uncertainties of the experiments. In particular, the error associated with the temperature measurements was estimated to be ±0.1°C whereas the error associated with the boiling heat flux was $\pm$ 0.05 MW/m^2 (see Appendix B). Since the boiling data for the 12" (~0.3 m) aluminum vessel were most complete, they were chosen to be presented in this section.

4.1.2.1 Saturated Boiling

Typical temperature-time histories at several locations along the vessel outer surface during a transient quenching experiment are shown in Figure 36. The figure shows the temperature history at three different ℓ/L values, where L is the total arc length (i.e., total heating length) from the bottom center to the upper edge of the vessel and l is the arc length (i.e., local heating length) corresponding to the location in question. Initially, the vessel was cooling down very slowly because it was still suspended in air. As soon as the vessel was submerged in water on the outside, the cooling rate at all the locations in the figure increased marking the beginning of the film boiling regime. Then the temperature of the vessel kept going down until the CHF point that was marked by a very rapid drop in the wall temperature. The location closest to the upper edge of the vessel reached the CHF first, and the one closest to the bottom center reached it last, which was in agreement with the observed dynamics of the two-phase boundary layer.

Figure 37 shows the local boiling curves for the saturated boiling case. There was a significant variation of the boiling curves along the vessel wall, which was consistent with the observed behavior of the two-phase boundary layer. In general, the boiling curve shifted upward as ℓ/L was increased. The CHF value increased from a minimum of about 0.4 MW/m^2 at the bottom center to around 0.9 MW/m^2 at $\ell/L = 0.75$. On the other hand, the local wall superheat corresponding to the CHF changed very little along the vessel outer surface.

The value of 0.4 MW/m^2 at the bottom center is higher than the value suggested by Theofaneous et al. (1994a) of 0.28 MW/m^2, which was obtained using a 2-D cylindrical representation of the region around and including the bottom center. It was expected that the 2-D cylindrical simulation would lead to a lower CHF value at the bottom center than the actual 3-D boiling phenomenon on the outside of the hemispherical vessel. This was due to the fact that bubbles in the 2-D case could escape from around the bottom center only in a single azimuthal angle direction, whereas in the 3-D situation, they could travel along the surface in all directions once they formed at the bottom center. The divergence effect that was present near the bottom center of the hemispherical center was absent in the 2-D case.

Guo and El-Genk (1991) predicted a value of 0.2 MW/m^2 for a downward facing flat surface. This

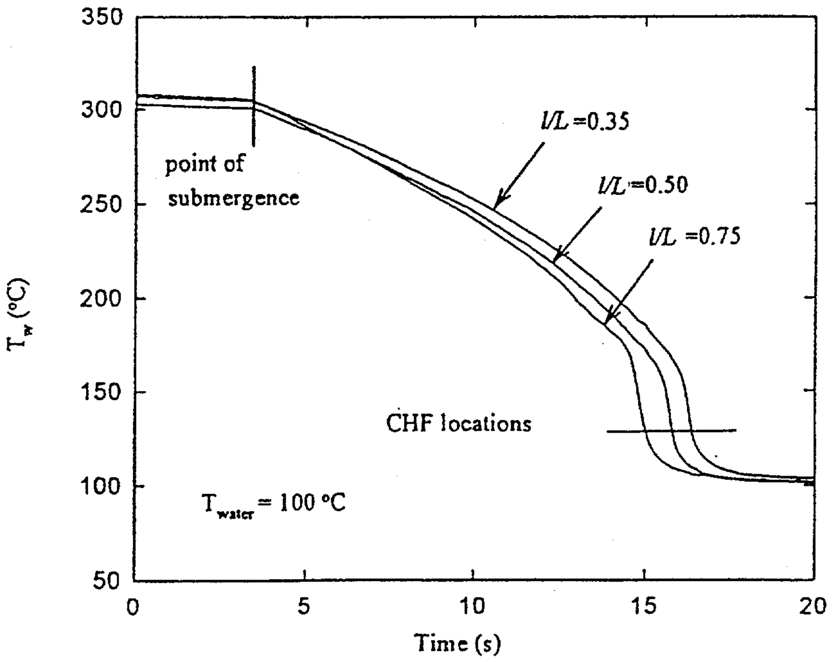

Figure 36. Typical Temperature-Time Histories at Various Wall Locations During Quenching.

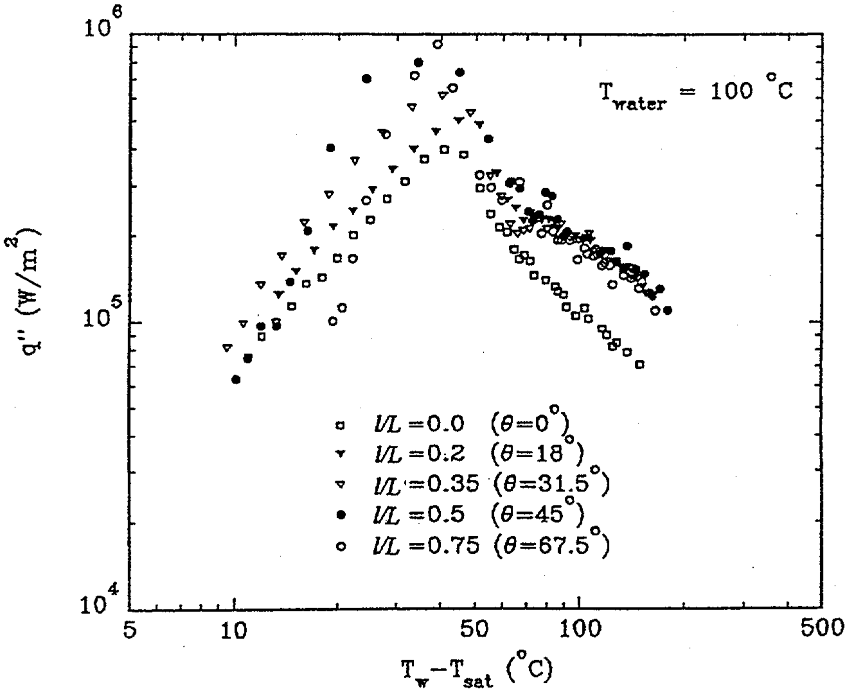

Figure 37. Boiling Curves at Different Locations Along the Heating Surface (Saturated Boiling: Water at 100°C).

value was smaller than 0.4 MW/m^2, obtained from the experiments carried out during this project, and smaller than 0.28 MW/m^2 reported by Theofaneous et al. (1994a). These differences were also expected since it was much harder for the vapor bubbles to escape from underneath a flat heating surface than any of the other two geometries. Guo and El-Genk also reported a large variation in the wall superheat (from 12 °C to 35 °C) when the heating surface changed its orientation from horizontally downward facing to vertical. This was different from the modest wall superheat variation at the CHF point depicted in Figure 37 when θ changed from 0° (i.e., $\ell/L = 0$) to 67.5° (i.e., $\ell/L = 0.75$). The data of Guo and El-Genk also predicted a large increase in the CHF (from 0.2 MW/m^2 to 0.31 MW/m^2) and the wall superheat (from 12 °C to 23 °C) when the angle of inclination changed from 0° to 5°. Such a sharp increase was not obtained in the case of the hemispherical vessel used in this study, as shown in Figure 36.

4.1.2.2. Subcooled Boiling

Each one of Figures 38, 39 and 40 shows five boiling curves at the same subcooling level for five different locations on the vessel surface. Experiments were conducted for water temperatures of 97 °C, 93 °C, and 90 °C. For all three subcooling cases, the CHF varied significantly with location on the outer surface of the vessel. When the water was subcooled, the wall superheat at the bottom center was much higher than that at the other four locations. This finding was different from the saturated boiling case in which all the wall superheats, at different locations on the outside of the hemisphere, were approximately the same. This was in agreement with observations of the two-phase boundary layer under steady state conditions, which revealed that subcooling altered the bubble size and dynamics especially at the bottom center.

To help illustrate the effect of subcooling further, Figures 41 to 45 were constructed to show on the same graph the boiling curves at a given location for different subcooling levels. From these figures, it can be seen that subcooling had important effects on the boiling curves at all wall locations considered. This effect was especially important at the bottom center, where higher subcooling levels resulted in significantly higher CHF values and wall superheats. The nucleate boiling regime was also affected by the degree of subcooling, and this was especially pronounced at the bottom center. This strong dependence on the level of subcooling in the nucleate boiling region was not observed in the conventional pool boiling case, as reported in Ref. 1. For the conventional case of pool boiling from an upward facing surface, it is widely recognized that subcooling has very little, if any, effect on nucleate boiling heat transfer. As the subcooling level is increased, the wall-to-liquid temperature difference obviously increases which tends to give rise to a higher nucleate boiling heat flux. However, increasing the subcooling level generally leads to a decrease in the size of the vapor bubbles which in turn would reduce the level of heat transfer enhancement associated with local bubble agitation. The net result is that these two opposing effects approximately compensate for each other, resulting in very little change in the nucleate boiling heat flux with subcooling.

For nucleate boiling on a downward facing hemispherical surface, the resulting vapor bubble motions are characterized by the flow of a two-phase liquid/vapor boundary layer along the curved heating surface. The local boiling heat flux depends not only on the local events (i.e., local bubble-induced agitation and phase change process) at a given angular position, but also on the upstream conditions of the two-phase boundary layer flow. As the degree of subcooling is increased, the bubble size decreases. This would reduce not only the local bubble agitation on the heating surface but also the resulting superficial velocity of the two-phase boundary layer. As a result, both the level of heat transfer enhancement associated with local bubble agitation and the convective heat transfer associated with the two-phase boundary layer flow would be reduced. This reduction in the local heat transfer cannot be compensated by the increase in the wall-to-liquid temperature

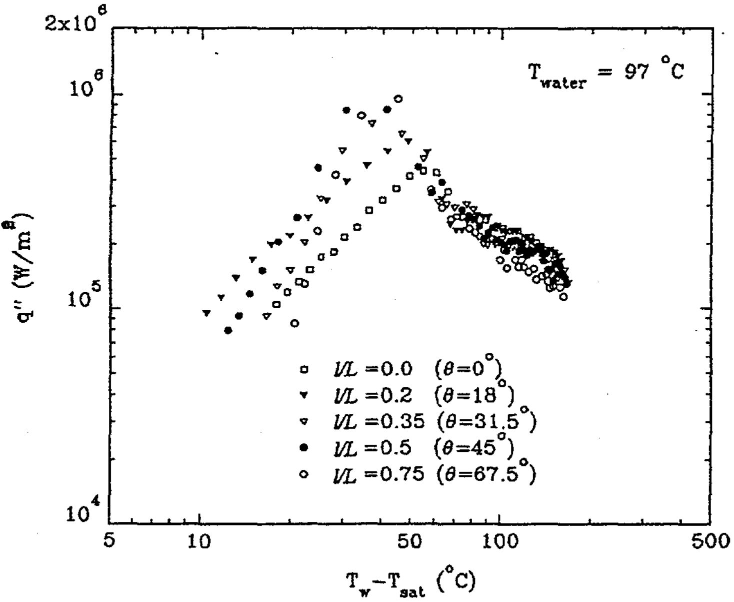

Figure 38. Boiling Curves at Different Locations Along the Heating Surface (Subcooled Boiling: Water at 97°C).

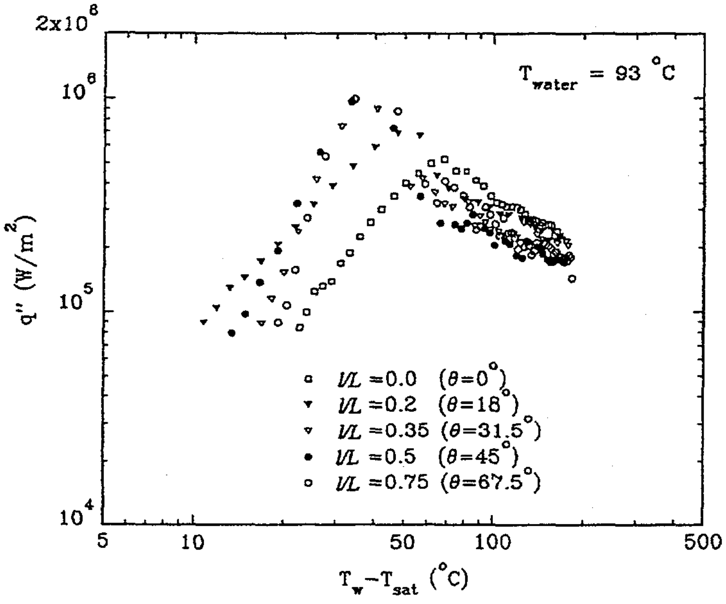

Figure 39. Boiling Curves at Different Locations Along the Heating Surface (Subcooled Boiling: Water at 93°C).

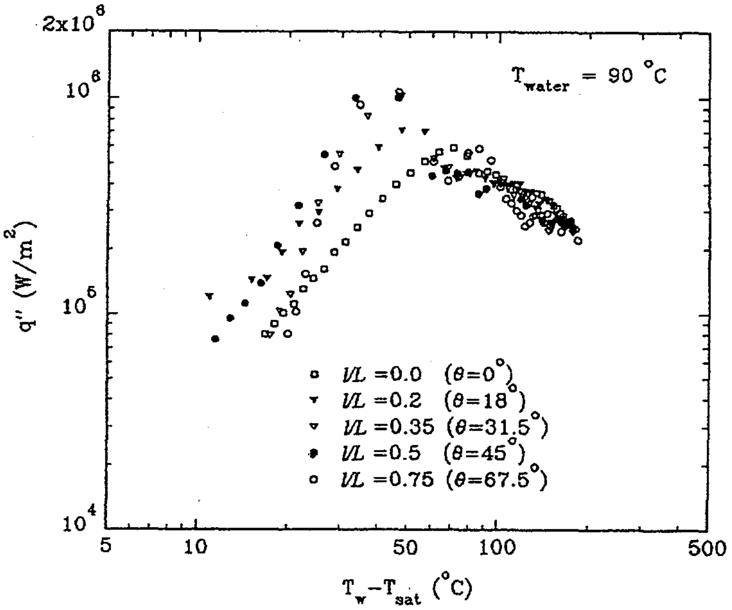

Figure 40. Boiling Curves at Different Locations Along the Heating Surface (Subcooled Boiling: Water at 90°C).

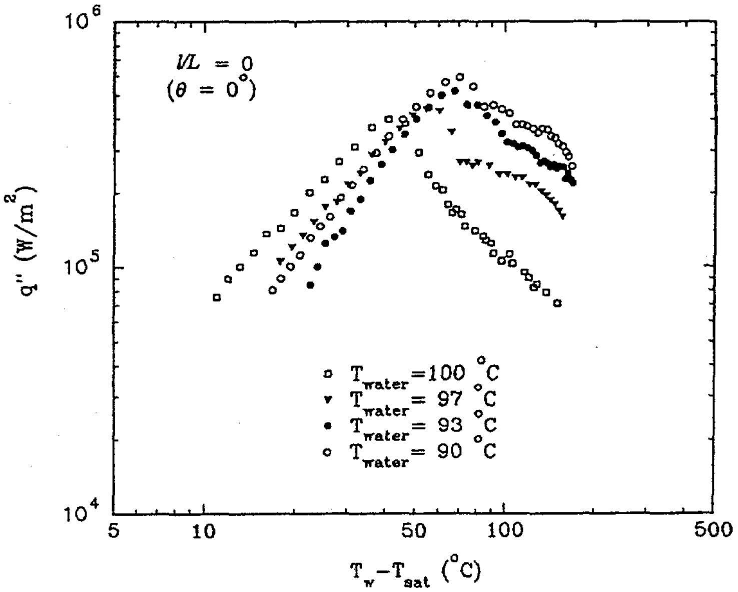

Figure 41. Boiling Curves at Different Subcooling Levels (*l/L* = 0).

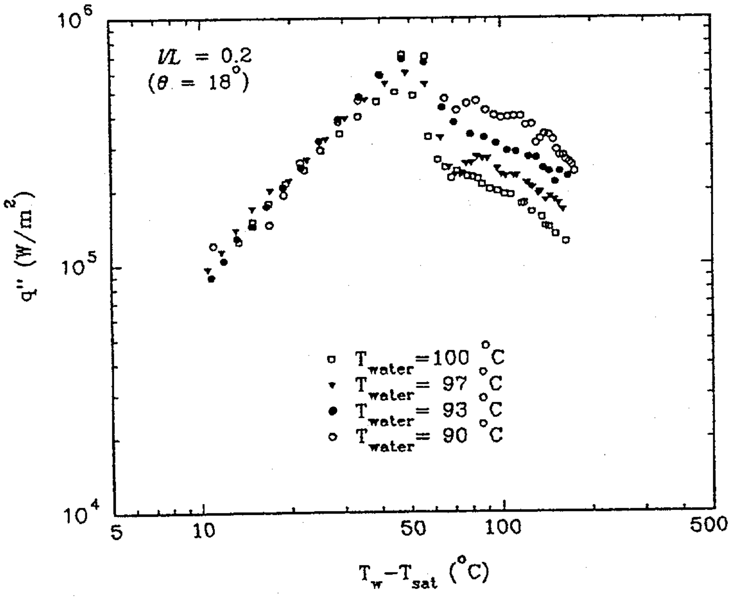

Figure 42. Boiling Curves at Different Subcooling Levels (*l/L* = 0.2).

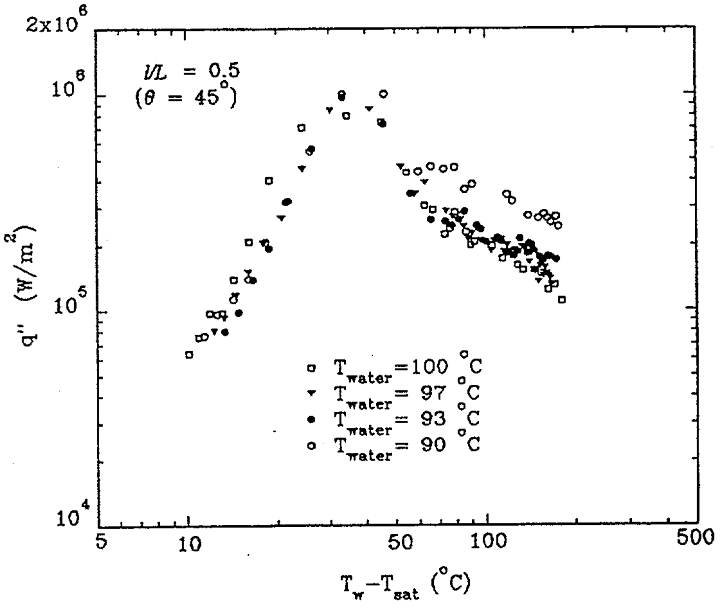

Figure 44. Boiling Curves at Different Subcooling Levels (*l/L* = 0.5).

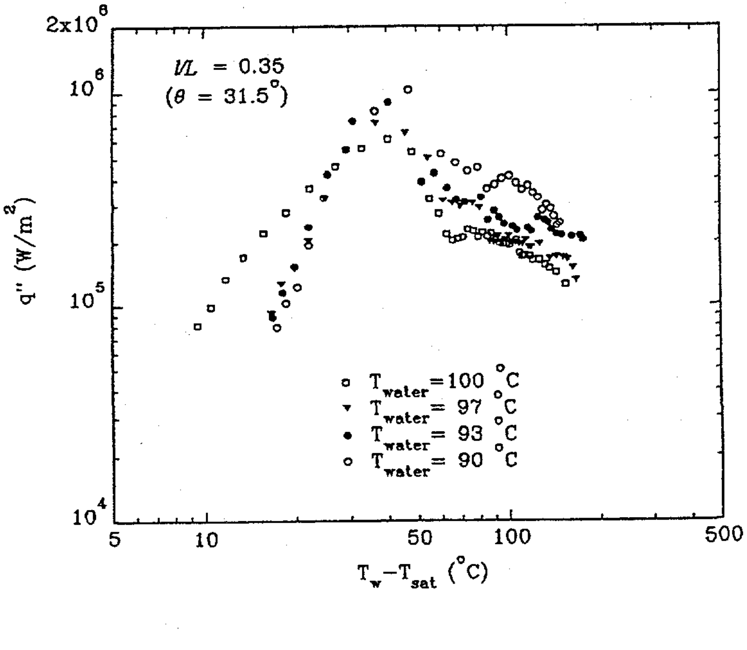

Figure 43. Boiling Curves at Different Subcooling Levels (*l/L* = 0.35).

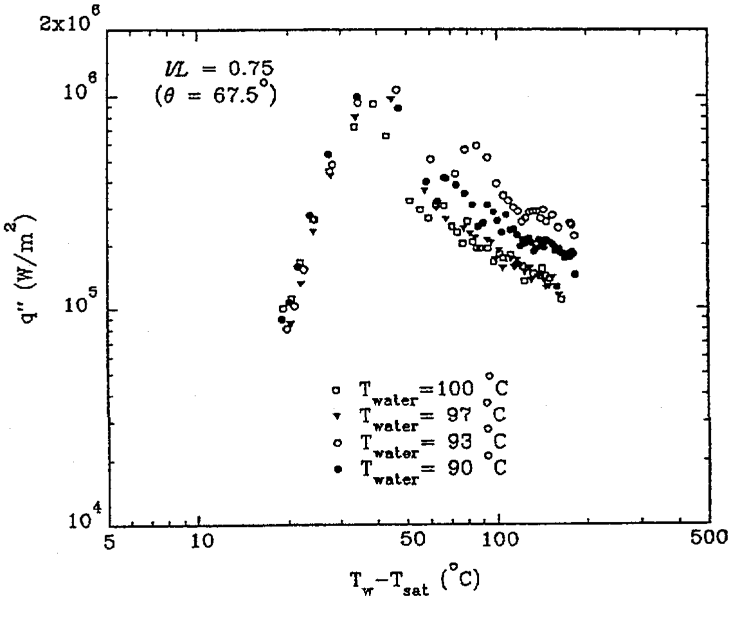

Figure 45. Boiling Curves at Different Subcooling Levels (*l/L* = 0.75).

difference. The net result is that the local boiling heat flux decreases as the degree of subcooling is increased.

It should be noted that a similar trend was observed by Ref. 2. They measured the local boiling heat flux around a horizontal cylinder under saturated and subcooled conditions using the quenching method. In the nucleate boiling regime, the boiling heat flux was found to decrease as the degree of subcooling was increased, especially at low heat flux levels.

4.1.3. Variations of the Local Critical Heat Flux

Figure 46 shows the variation of the critical heat flux with subcooling at different locations on the vessel outer surface. The CHF was found to increase when the subcooling level or the distance from the bottom center increased. To the first approximation, the critical heat flux varied almost linearly with the level of subcooling, which was consistent with other studies dealing with the conventional pool boiling case (Ref. 1). The saturated boiling CHF at the bottom center was about one third of the value 1.2 MW/m^2, usually used for the conventional pool boiling case. With a subcooling of 10°C, the CHF value at the bottom center increased to 0.59 MW/m^2, which was about one half of the value for conventional pool boiling. It was only close to the equator of the vessel and at high levels of subcooling that a high value on the order of 1.2 MW/m^2 for the critical heat flux was obtained in the present case.

Figure 47 shows the variation of the CHF with the spatial location on the vessel outer surface at different water temperatures. The critical heat flux increased by more than 100% when the location changed from the bottom center to the upper edge of the hemisphere. This was found to be the case for both saturated and subcooled boiling. The CHF value close to the bottom center was not that much different from the critical heat flux level exactly at $\ell/L = 0$. This was different from the abrupt increase in the CHF, reported by Guo and El-Genk (1991), for the case of a downward facing flat surface. They observed an increase in the critical heat flux of about 50% when the surface orientation changed from 0° (horizontally downward facing) to 5°. Therefore, CHF estimates obtained using flat surfaces should not be used to predict the critical heat flux along the outer surface of a hemispherical vessel.

It should be noted that unlike the regime of subcooled nucleate boiling, the critical heat flux varies with the subcooling level in an entirely different way. While the nucleate boiling heat transfer decreases with increasing subcooling, the critical heat flux always increases with subcooling. This is because the critical heat flux represents the condition corresponding to the occurrence of a local dryout region on the heating surface. As the subcooling level is increased, the bubble size decreases. Thus, with the effect of subcooling, much higher local heat fluxes are required to generate large vapor bubbles on the heating surface at a sufficiently high frequency such that a local dryout region would start to form. Hence, a higher critical heat flux is expected at a higher subcooling level.

4.2 Steady State Experiments

4.2.1 Characteristics of the Steady-State Two-Phase Boundary Layer

Figure 48 shows the two phase boundary layer observed during saturated and subcooled boiling. The bubble size and shape along the curved heating surface were found to vary significantly. For saturated boiling, the vapor bubbles in the bottom center region were an order of magnitude larger than those observed in the upper portion of the vessel with the entire surface heated at the same power level. The bubbles around the bottom center were elongated and resembled a pancake, whereas those in the upper portion were almost spherical. After departure, the large vapor bubbles from the bottom center region gradually transformed into the shape of a spherical cap while washing away the growing bubbles in the downstream location. As a result, the nucleate

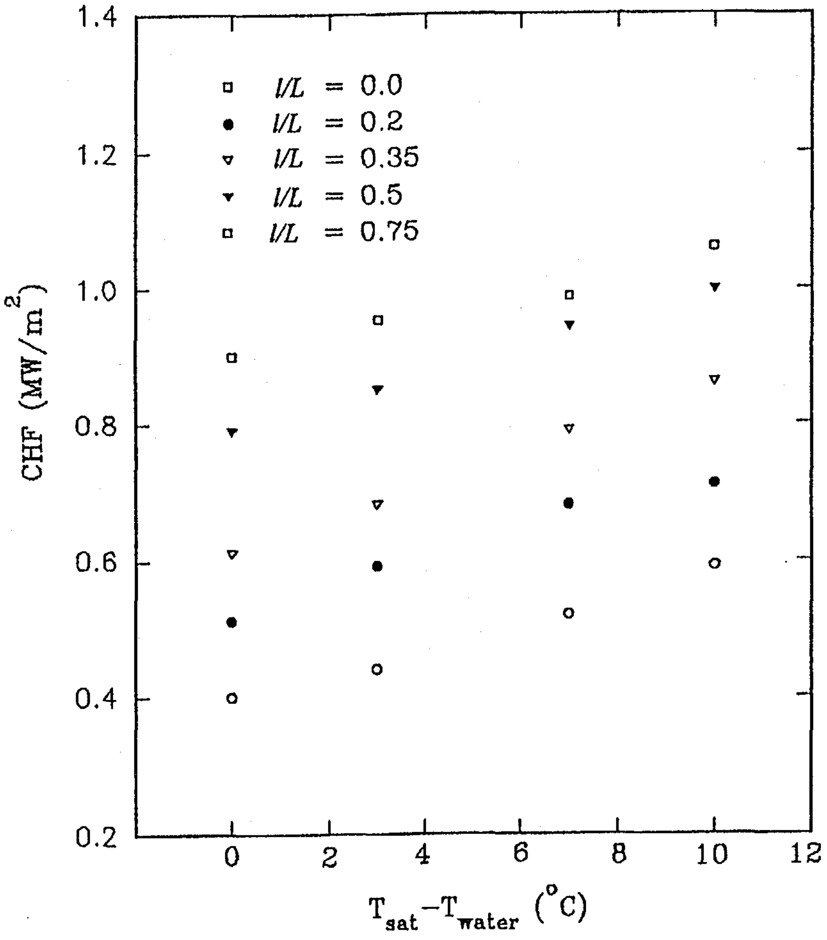

Figure 46. Variation of the Critical Heat Flux with Subcooling at Different Locations on the Vessel Outer Surface.

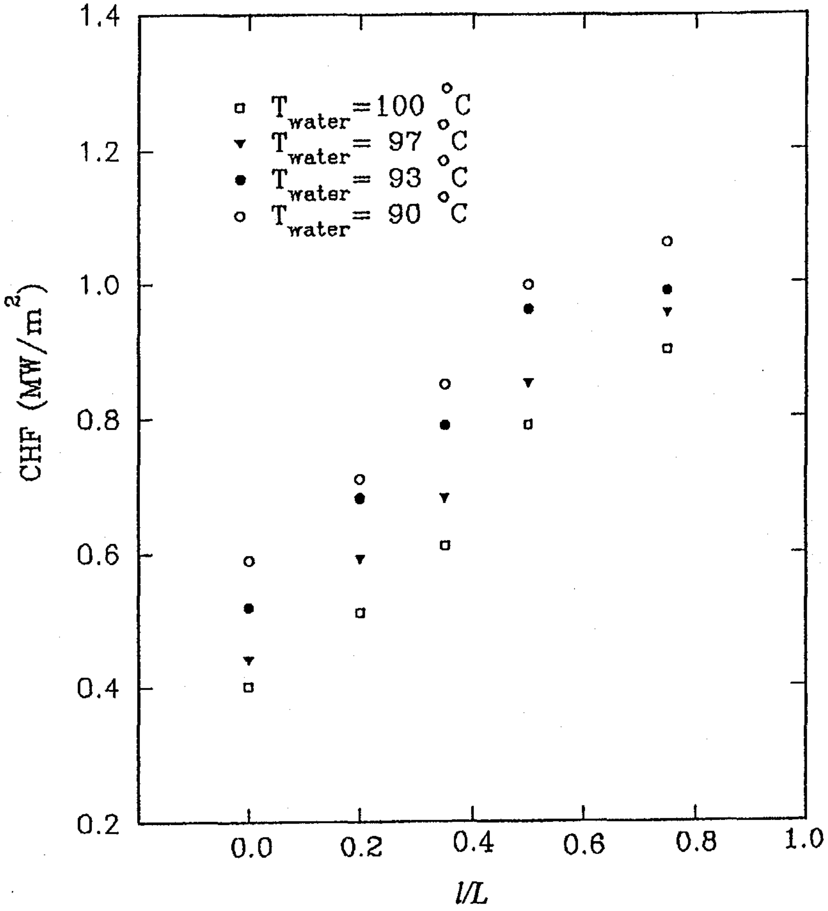

Figure 47. Spatial Variation of the Critical Heat Flux for Saturated and Subcooled Boiling.

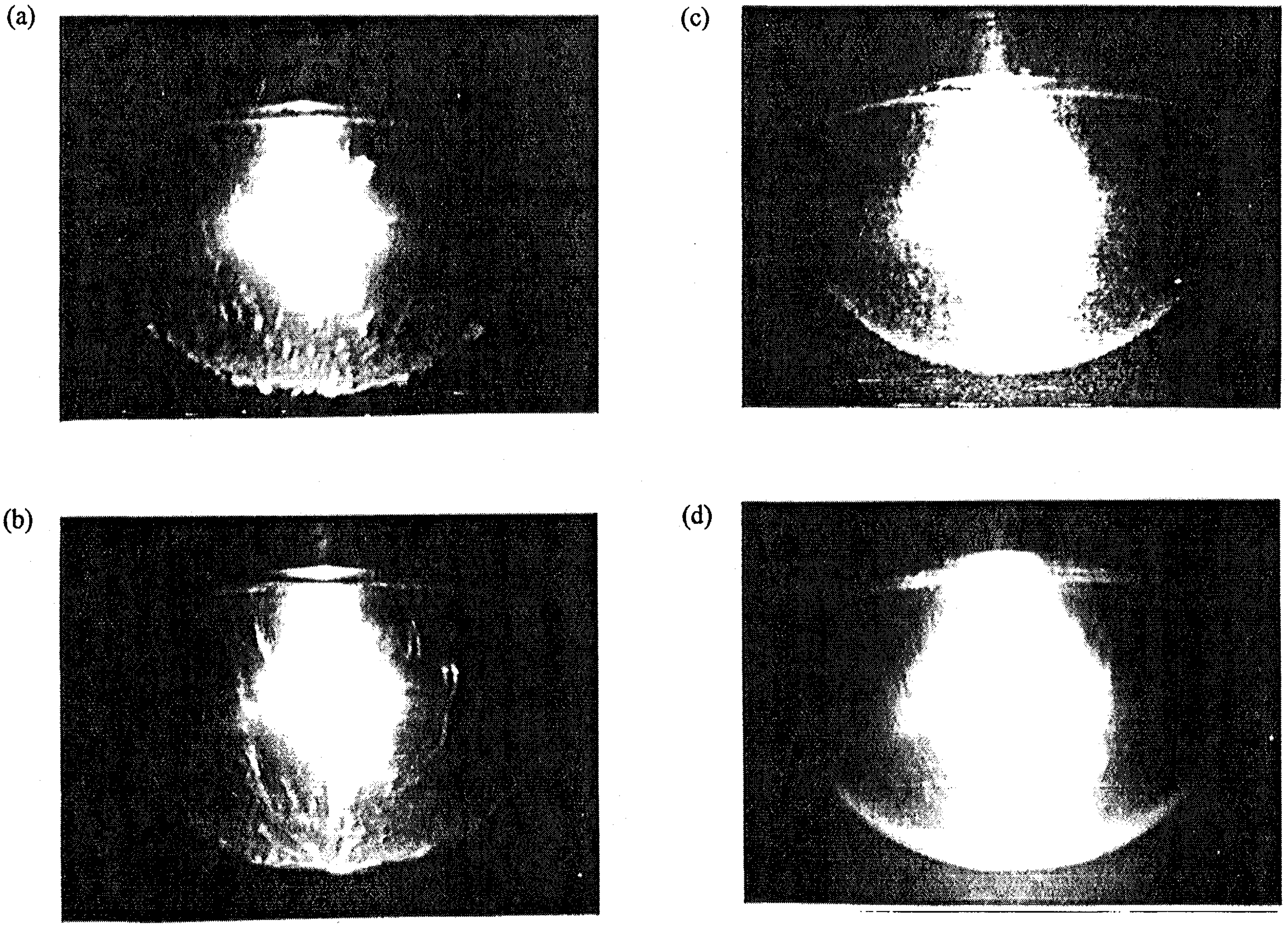

Figure 48. Configurations of the Two-Phase Boundary Layer During Steady-State Boiling.

boiling process in the downstream locations of the vessel surface depended strongly on the upstream conditions and cannot be treated as a localized event.

When the water was subcooled, the bubble growth and departure frequencies increased whereas the bubble sizes decreased substantially. The vapor bubbles, especially from around the bottom center, shrunk quickly after departure due to condensation. The size of the vapor bubbles from the bottom center region decreased by almost an order of magnitude, due to subcooling, compared to their size in the corresponding saturated boiling case. This situation can be seen by comparing the pictures shown in Figures 48(a) and 48(b) for saturated boiling with those shown in Figures 48(c) and 48(d) for subcooled boiling. Large variations in the bubble sizes are shown in Figures 48(a) and 48(c) where the pictures were taken by freezing the two-phase motions. On the other hand, significant differences in the vapor flow configuration are shown in Figures 48(b) and 48(d) where the pictures were taken using multiple exposures.

It should be stressed that for both saturated and subcooled boiling, the two-phase boundary layer flow was three-dimensional although it was axisymmetrical. The downward facing boiling process on the curved heating surface depended strongly upon the upstream flow conditions, particularly the activities of those large elongated bubbles in the bottom center region. Conceivably, it is not possible to simulate the boiling phenomena by performing two-dimensional experiments.

4.2.2 Effect of Subcooling on the Behavior of the Two-Phase Boundary Layer

Steady state pool boiling experiments were conducted at two subcooling levels and three heat flux levels. In these experiments, the two phase boundary layer in the bottom center region of the hemispherical vessel was videotaped and photographed. Figures 49 through 52 are photographic records of the boiling phenomenon on the outside of the vessel for heat flux levels of 0.01, 0.09, and 0.30 MW/m^2 corresponding to a low, intermediate, and high power level, respectively. These pictures were taken for saturated boiling and for boiling with a 10°C subcooling.

When the heat flux was low and the water was subcooled at 90°C, the outer surface of the vessel was covered with a large number of very small isolated water bubbles as shown in Fig. 49(a). When the water was saturated at the same heat flux level, the bubble size increased drastically while the bubble frequency decreased as shown in Fig. 49(b). In both of these cases, the bubbles were isolated from each other and there was no coalescence. Also, at this heat flux level, the four stages of the bubble formation process were clearly identified through direct observation of the bubbles on the vessel outer surface. The process started by the heating of the liquid in contact with the surface of the vessel. When the required local level of superheat was attained, the nucleation site became active and a very tiny bubble could be observed on the heating surface. Then, the vapor mass grew larger and larger as more liquid was evaporating at the surface. Finally, the bubble detached from the surface when it reached a certain critical size and the whole process was repeated again.

Figure 50 shows the boiling bottom center region at the intermediate power level. At this heat flux, it was also possible to distinguish the four stages of the bubble formation process through direct observation of the two-phase boundary layer. The bubble frequency for the saturated and the subcooled boiling was higher in this case than in the case of the low heat flux level. The bubble size is also larger as depicted clearly in Fig. 50(b). In the subcooled boiling case, the surface was still covered by a large number of isolated bubbles that did not interfere with each other. On the other hand, some local bubble coalescence started to occur in the saturated boiling case. In these regions of coalescence, two or more tiny bubbles started growing on the heating surface. As the size of these vapor masses grew, their external boundaries got closer to each other. At some

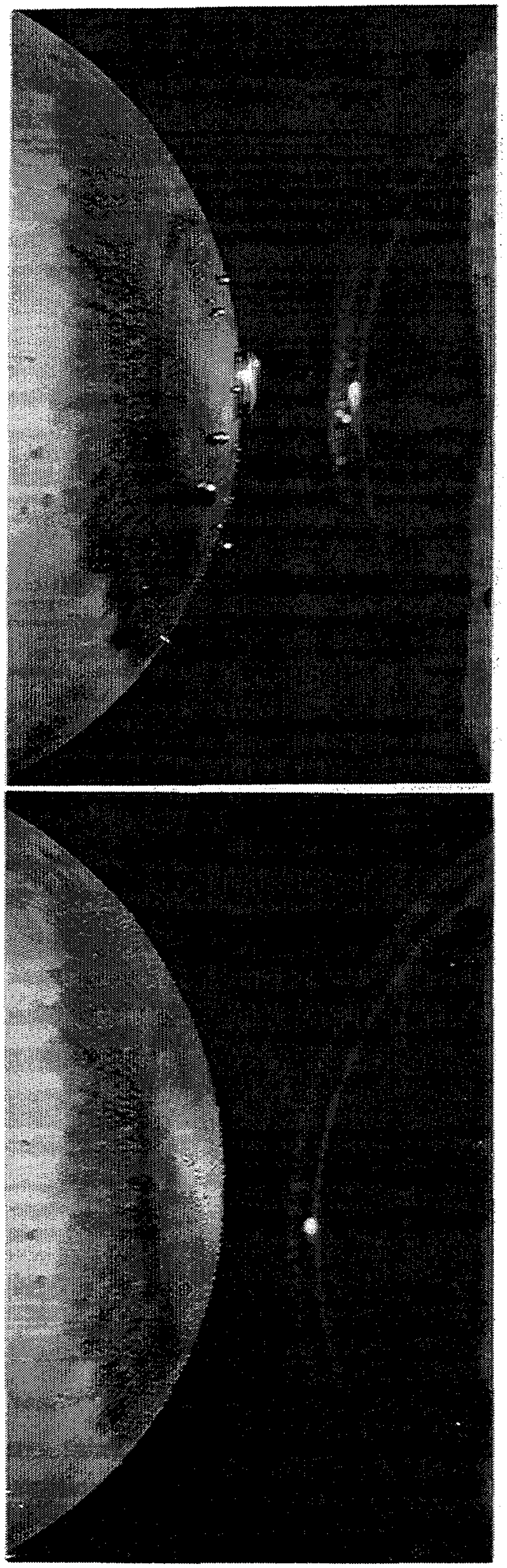

(a) Water Temperature = 90°C

(b) Water Temperature = 100°C

Figure 49. Nucleate Boiling in the Bottom Center Region of the Vessel at a Low Heat Flux Level.

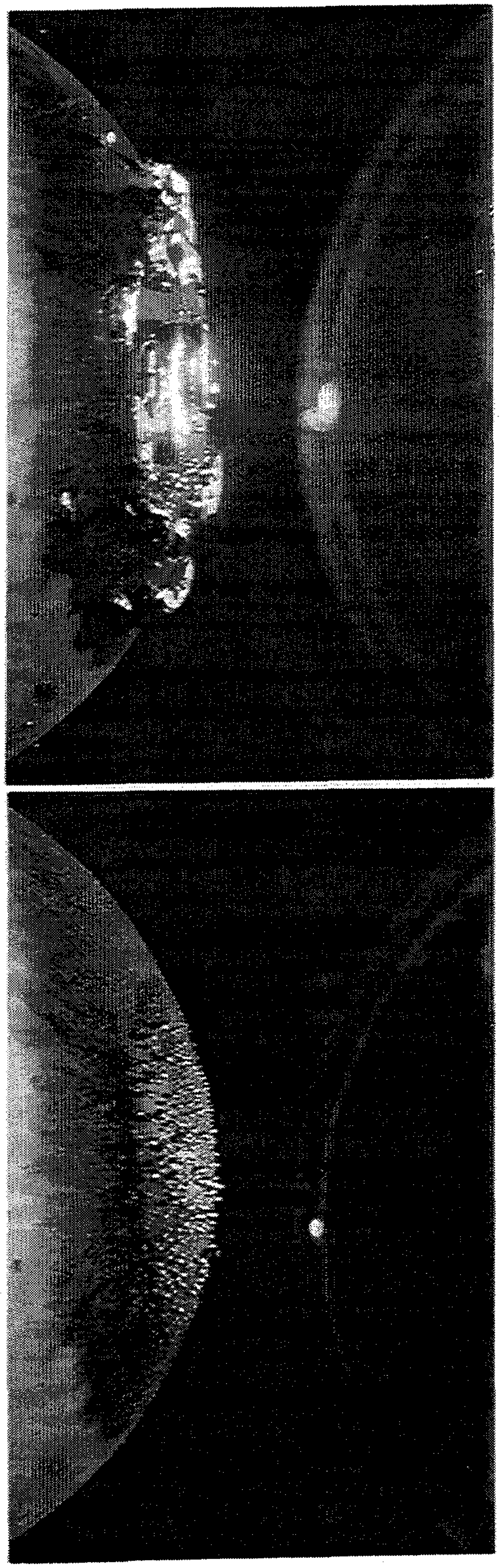

(a) Water Temperature = 90°C

(b) Water Temperature = 100°C

Figure 50. Nucleate Boiling in the Bottom Center Region of the Vessel at an Intermediate Heat Flux Level.

(a) Water Temperature = 90°C

(b) Water Temperature = 100°C

Figure 51. Nucleate Boiling in the Bottom Center Region of the Vessel at a High Heat Flux Level.

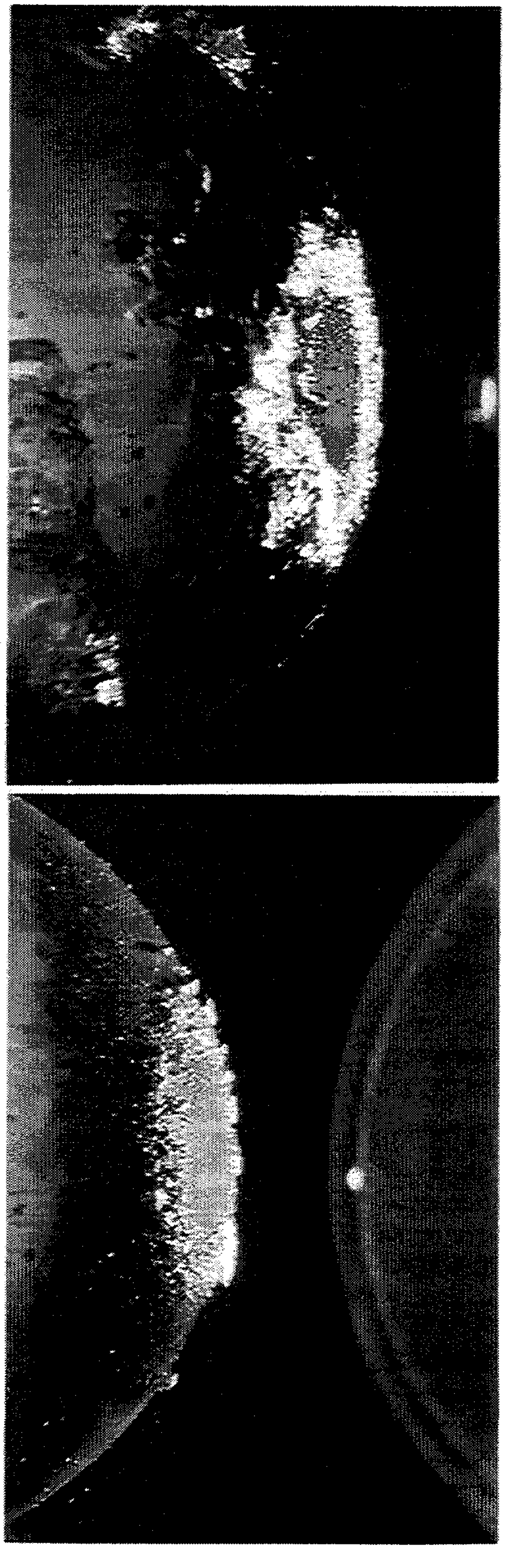

(a) Water Temperature = 90°C

(b) Water Temperature = 100°C

Figure 52. Nucleate Boiling in the Bottom Center Region of the Vessel With Heating of the Outer Segment Only.

point, these boundaries touched and the bubbles coalesced into one large vapor mass, which detached from the heating surface after reaching a certain critical size.

The high heat flux case shown in Fig. 51 was characterized by a very different vapor dynamic than in the cases of low and intermediate heat flux levels. In the case of saturated boiling, it was not possible to distinguish the various stages of the bubble formation process through direct observation of the boiling phenomenon. This was due to the very fast bubble activity at this heat flux level. It appeared as if the bottom center region of the hemisphere was covered by one large vapor mass. In this case, it was not possible to discover, by direct visual observation, the bubble coalescence that lead to the formation of the large vapor mass. It was only possible to observe the bubble coalescence process when the boiling phenomenon was observed in slow motion using the video system.

These observations revealed that the boiling process in the bottom center region was cyclic in nature with four distinct phases. First there was the phase of direct contact between the liquid and the solid during which water from the liquid pool was heated next to the heating surface. When the liquid superheat reached a critical value, bubble nucleation and growth started at various locations on the heating surface. At a certain point, the bubbles started to coalesce and formed a large vapor mass that covered the entire heating surface. This large bubble was ejected from underneath the hemisphere when it reached a certain critical size. Away from the bottom center, the ejected large vapor mass formed a ring as shown very clearly in Fig. 51(b). As it traveled toward the upper edge of the vessel, the ring was broken into vapor slugs due to the diverging area of the vessel.

These four phases of the boiling process and the cyclic nature of the evaporation around the bottom center of the vessel were also reported by Ref. 5 for a small heating surface with a large radius of curvature. Reference 6 also reported the same boiling characteristics for a large torispherical downward facing surface that was used for a full scale simulation of a reactor lower head. In the present study, the video system was used to observe the characteristics of the interface between the spherical heating surface and the large vapor mass in the bottom center. It was revealed that individual nucleation sites were feeding the envelope of the large vapor mass. This is also consistent with the observations of Refs. 6, 7 and 8. Therefore, it seems that the size of the heating surface does not influence the nature of the vapor dynamics for pool boiling on a downward facing curved surface.

In the subcooled boiling case at a high heat flux, the bubble activity was also much higher than in the low and the intermediate power levels, as shown in Fig. 51(a). In this case, we also observed a large vapor mass covering a large portion of the heating surface near the bottom center of the vessel. However, the large bubble was smaller than what was observed in the saturated boiling case. This was due to the nature of the vapor coalescence, which only took place in the region close to the bottom center of the hemisphere. As a result, individual bubbles could still be observed growing on the outer surface of the heated portion of the hemisphere, as shown in Fig. 51(a). This figure also shows very clearly that the bubbles condensed within the subcooled liquid pool very soon after they detached from the heating surface. This behavior was different from the saturated boiling case where the released bubbles did not condense while traveling along the vessel outer surface.

The photographic records of Fig. 52 were taken with the heaters of the inner segment of the hemisphere turned off and the heaters of the outer segment were still delivering a heat flux of 0.3 MW/m^2. The subcooled boiling case, Fig. 52(a), was characterized by isolated bubbles with the absence of any coalescence. This confirmed the fact that bubble coalescence in the subcooled boiling case of Fig. 51(a) was a local phenomenon limited to the region very close to the bottom center of the vessel. On the other hand, the bubbles formed on the outer segment in the saturated boiling case exhibited a high level of coalescence, as shown in Fig. 52(b). Therefore, the bubble coalescence of Fig. 51(b), when the two segments were heated, was not limited to a certain region of the hemisphere but rather a characteristic of boiling everywhere on the heating surface.

4.2.3 Variation of the Vapor Size Along the Vessel Outer Surface

A growing vapor mass stays attached to the surface as long as the surface tension force remains larger than the forces that tend to pull the vapor mass away from the heating surface. These latter forces include buoyancy, drag, lift, and/or inertia forces associated with the motion of the bulk fluid. In the case of pool boiling on the outer surface of a downward facing hemispherical vessel, only the component of the buoyancy force tangential to the vessel outer surface will aid in the release of the vapor mass. This component is the highest near the upper edge of the vessel and the lowest near the bottom center of the hemisphere. At exactly the bottom center of the vessel, buoyancy does not have any component along the tangent to the vessel surface and it will act solely to keep the vapor mass attached to the hemisphere. In addition, the two-phase boundary layer flow rate is very small near the bottom center and it increases toward the upper edge of the vessel. As a result, the drag and the inertia forces associated with the two-phase flow increase toward the upper edge of the hemisphere. Thus, both the buoyancy force and the forces associated with the two-phase flow increase toward the upper edge of the hemisphere. This explains the fact that the vapor masses in the bottom center region were large, flattened, and elongated whereas those near the upper edge were relatively small and spherical.

Experimental observations reveal that the departure diameter of the vapor masses decreases as the distance from the bottom center of the vessel increases. In the low and intermediate heat flux levels, this is especially apparent in the saturated boiling experiments. Figure 49(b) for saturated boiling at low heat flux level depicts a much larger vapor bubble near the bottom center than away from it. This is also observed in the case of saturated boiling at an intermediate heat flux level, as shown in Fig. 50(b). The large vapor masses away from the bottom center in Fig. 50(b) are traveling bubbles that originated near the bottom center of the vessel. The most obvious illustration of the decreasing vapor size away from the bottom center can be seen by comparing the bubble behavior in Fig. 51(a) to that in Fig. 52(a). When the heaters of the inner and outer segments were both on, the region around the bottom center was covered by a large vapor mass as shown in Fig. 51(a). This was due to the coalescence of large vapor bubbles in the vicinity of the bottom center of the vessel. When the heaters of the inner segment were turned off, Fig. 52(a), it was revealed that the bubbles forming away from the bottom center did not participate in the coalescence observed in Fig. 51(a). Therefore, the vapor masses that form on the outer segment are smaller in size than those that form closer to the bottom center of the vessel.

The decrease in the vapor size, away from the bottom center of a downward facing curved surface, provides an explanation for the increase in the critical heat flux from the bottom center toward the upper edge of a curved downward facing surface. When the size of the bubbles is large, coalescence will occur at a lower heat flux. Therefore, vapor blanketing of the heating surface will occur at lower heat flux levels. It is very well known that the occurrence of the CHF is linked to vapor blanketing of the heating surface. As a result, the decrease in the vapor size from the bottom center toward the upper edge of the vessel is responsible for the associated increase in CHF reported in the literature. It should be noted that the vapor masses are considerably smaller at higher levels of subcooling, leading to appreciably higher CHF limits.

4.2.4 High-Heat-Flux Nucleate Boiling Regime

Steady-state boiling experiments were conducted specifically for observing the local vapor dynamics and the two-phase boundary layer flow on the curved heating surface. The water was maintained at nearly 100°C in these experiments whereas the local wall heat flux was varied from 0.1 MW/m^2 to the vicinity of the local CHF limit. At these high-heat-flux levels, a cyclic vapor ejection process was clearly observed. Large and elongated vapor masses or slugs, being squeezed up against the wall by the local buoyancy force, were found to grow periodically on the heating surface. They were then ejected violently upward in all directions. The ejected vapor masses carried away the local vapor bubbles but tended to bypass those large vapor slugs growing on the heating surface in the downstream locations.

As the heat flux level was increased toward the local CHF limit, the cyclic ejection of the vapor masses appeared to be explosive and highly chaotic, especially in the bottom center region. The characteristic frequency of the vapor ejection cycle tended to increase with the heat flux level. However, the frequency increased very slowly as the CHF limit was approached. A close-up view of the vapor slugs revealed the existence of a thin liquid film, i.e., a micro-layer, underneath each elongated vapor slug. The small vapor masses that were generated at numerous discrete locations on the heating surface were fed in a continuous manner to the large vapor slug through the liquid film in the micro-layer. These small vapor masses had the shape of micro-vapor jets. Apparently, it was the thin liquid film underneath the large vapor slug that prevented local dryout of the heating surface from occurring.

Near the local CHF limit, the characteristic frequency of the vapor ejection cycle was found to be approximately 4 Hz. Thus the cycle duration was about 0.25 s. Over 90% of this duration, the heating surface was covered by the vapor slugs. The waiting period was less than 10% of the cycle duration. At the bottom center of the vessel, only a single large vapor mass was present in the local boundary layer region. However, in the downstream locations, two or three large vapor slugs could be present in the local boundary layer region at the same time. Upon departure, a vapor slug tended to flow around those that were growing on the heating surface in the downstream locations. The local boundary layer thickness increased considerably from the bottom center to the upper edge of the heated vessel.

The vapor dynamics and cyclic ejection frequencies recorded at various heat flux levels were analyzed in slow motions and compared. Results are summarized in Fig. 53. No apparent changes in the vapor dynamics and cyclic ejection process were observed as the CHF point was attained. The vapor/liquid morphology and the local flow behavior were essentially the same throughout the high-heat-flux regime up to the CHF point, although the characteristic frequency of the vapor ejection cycle tended to increase with the heat flux level. Clearly, the CHF point is a continuation of the nucleate boiling region and simply represents the upper limit of the high-heat-flux regime. Throughout the entire high-heat-flux region including the CHF point, nucleate boiling is subject to Helmholtz instability. The conventional assumptions that the critical heat flux is a peculiar point different radically from the nucleate boiling regime and that Helmholtz instability acts only on the CHF point causing a sudden collapse of the vapor removal path are not valid for downward facing surfaces.

4.2.5 Steady-State Heat Transfer Measurements

Steady-state boiling experiments were performed in the SBLB test facility under both saturated and subcooled conditions, with the water temperature varying from 90°C to 100°C. Measurements of the local boiling heat flux and the local wall superheat were made with the local input power to the heating elements in each segment of the test vessel as the key parameter. Input powers covering the entire range of nucleate boiling including the low-,

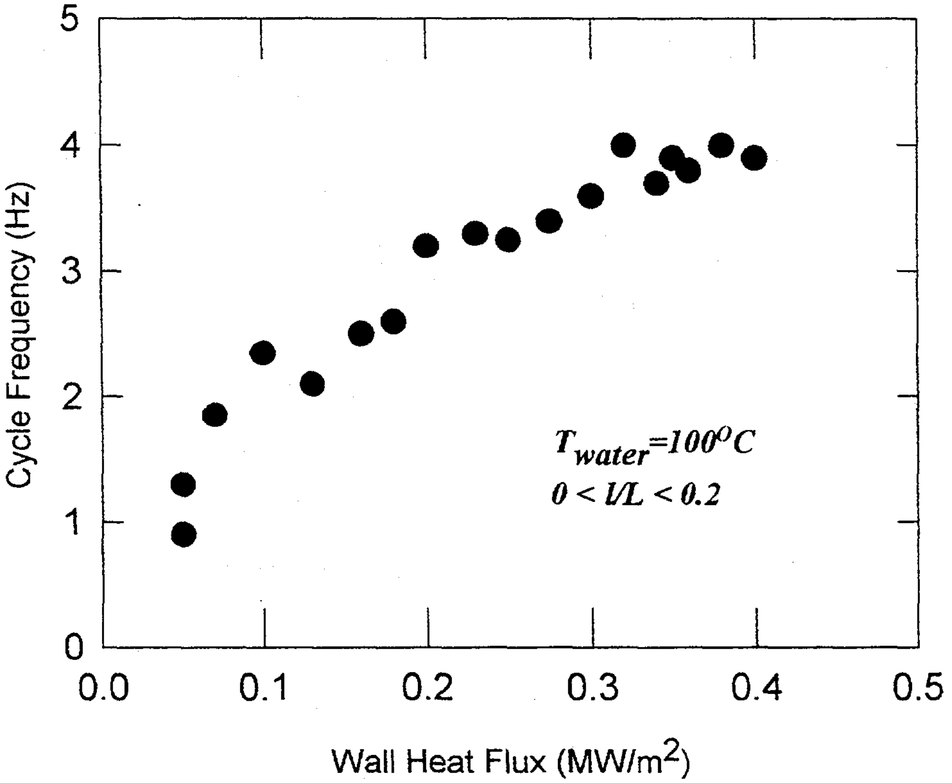

Figure 53. Variation of the Cyclic Ejection Frequency with the Heat Flux Level.

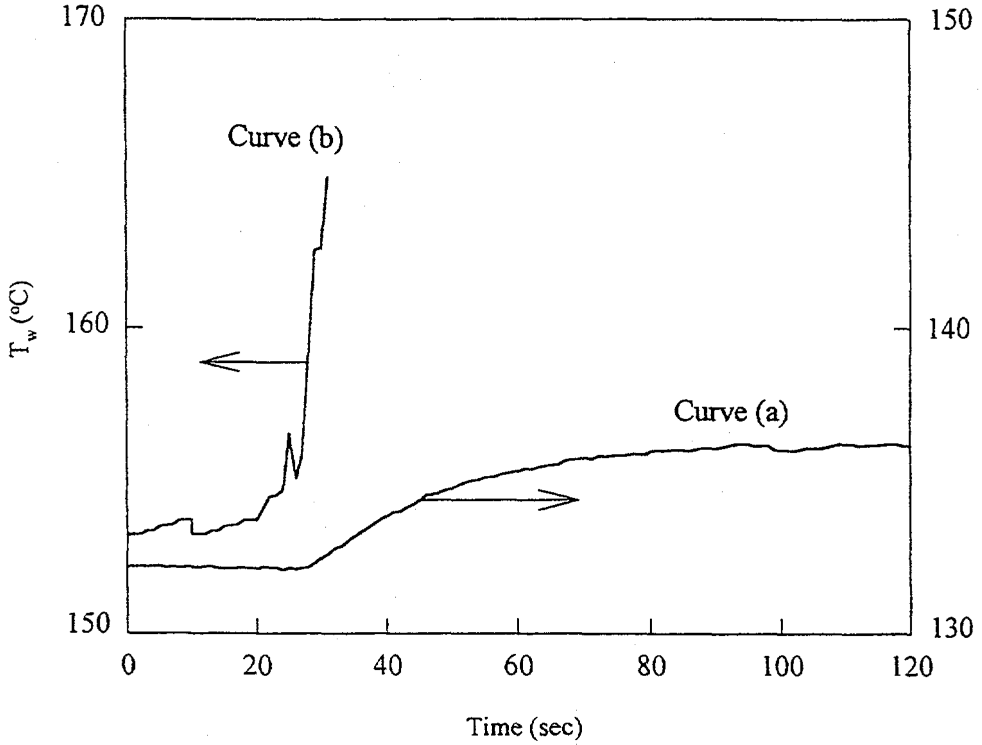

Figure 54. Typical Time Response of the Local Wall Temperature Following a Step Increase in the Wall Heat Flux.

intermediate-, and high-heat-flux regimes, were used in the experiments. The local wall superheat corresponding to a given power input was measured by thermocouples on the outer surface of the vessel. The local boiling heat flux, on the other hand, was determined by performing an inverse heat conduction analysis of the temperatures recorded by thermocouples embedded inside the wall. The boiling heat flux was found to agree satisfactorily with the local power input. The uncertainty in the embedded thermocouple locations was about ± 0.001 m, the maximum error in the temperature reading was ± 0.1°C, and the uncertainty in the calculated heat flux was ±7%.

Typical time responses of the local wall temperature following a step increase in the local wall heat flux observed in the SBLB experiments are shown in Figure 54. Curve (a) corresponds to the case for which the final steady-state wall heat flux was below the local CHF limit, whereas curve (b) corresponds to the case for which the final wall heat flux was at the local CHF limit. Initially, the wall temperature was at a steady state. Following a step increase in the wall heat flux, the local wall temperature rose rather moderately toward a new steady-state value in case (a). On the other hand, an abrupt increase in the local wall temperature beyond the set point was detected by the temperature control system in case (b) which triggered the solid state relay to cut off the power to all the heating elements. It should be noted that in the actual experiments, a very small step increase (0.005 MW/m^2) was employed as the local CHF limit was approached. The relatively large step increase (0.1 MW/m^2) in curve (a) was used for illustration purposes.

The steady-state nucleate boiling data at the bottom center ($\theta = 0°$) and off-center ($\theta > 0°$) locations of the test vessel are shown in Figures 55 to 59. Four sets of data including both the cases of saturated and subcooled boiling are presented in each of these figures. In contrast to the conventional case of pool boiling for which subcooling has very little effect on nucleate boiling heat transfer, in the present case, a strong subcooling effect was observed at low-to-moderate heat flux levels. This is evidently due to the influence of the two-phase boundary layer flow. As observed in the SBLB experiments, the size of the vapor mass decreased drastically with an increase in the degree of subcooling. The decrease in the vapor size not only reduces the local bubble agitation but also decreases the two-phase boundary layer flow. As a result, the convective heat transfer associated with the local bubble agitation and the two-phase boundary layer motion is considerably reduced. This reduction in the convective heat transfer cannot be compensated by the increase in the wall-to-liquid temperature difference. The net result is that the local boiling heat flux actually decreases as the degree of subcooling is increased. At high-heat-flux levels, however, latent heat transport dominates the convective heat transfer. Thus the subcooling effect becomes less important in the high-heat-flux regime.

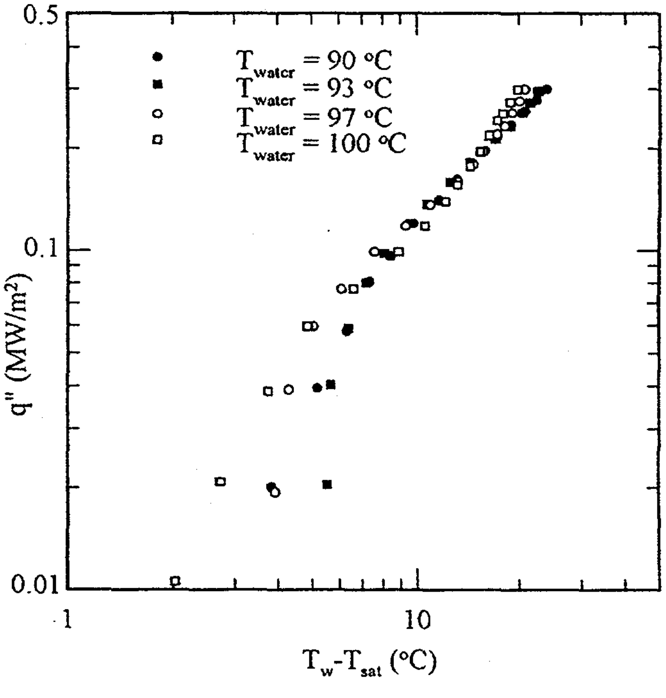

Figure 55. Steady-State Nucleate Boiling Measured at the Bottom Center of the Vessel ($\theta = 0°$).

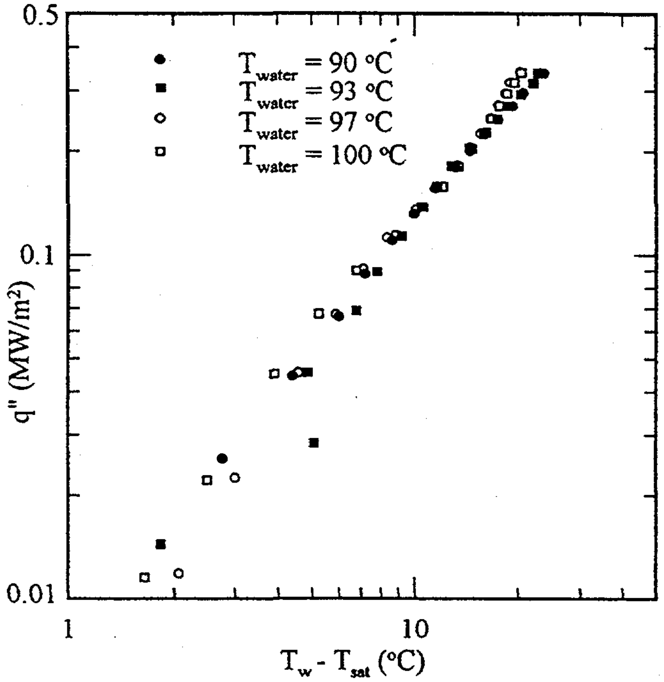

Figure 56. Steady-State Nucleate Boiling Data Measured at an Off-Center Location ($\theta = 18°$).

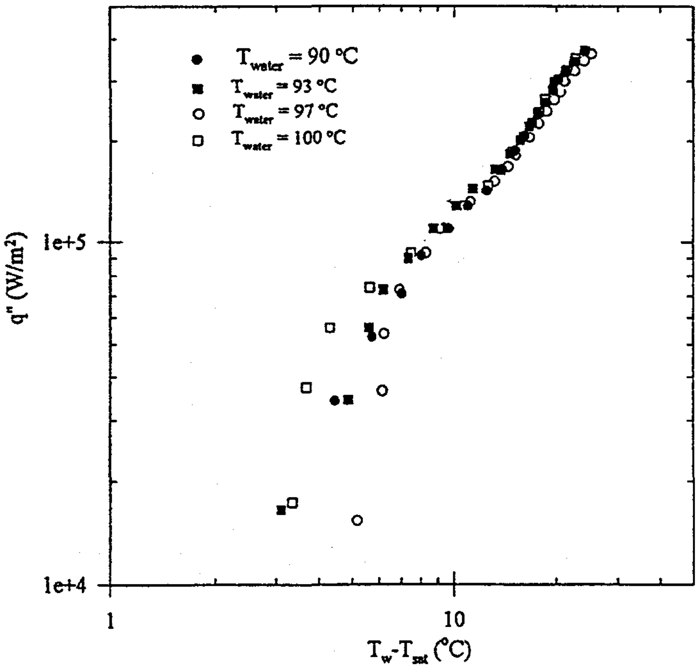

Figure 57. Steady-State Nucleate Boiling Data Measured at an Off-Center Location ($\theta = 36°$).

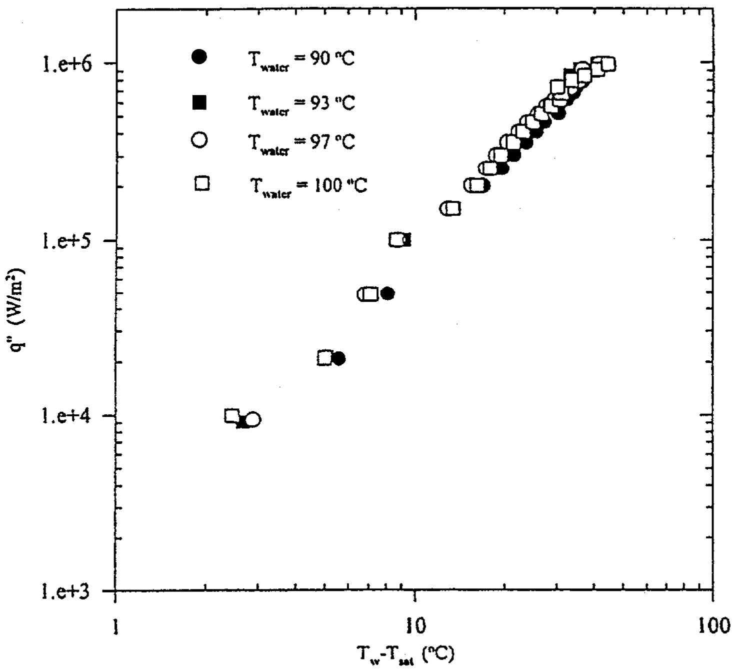

Figure 58. Steady-State Nucleate Boiling Data Measured at an Off-Center Location (θ = 60°).

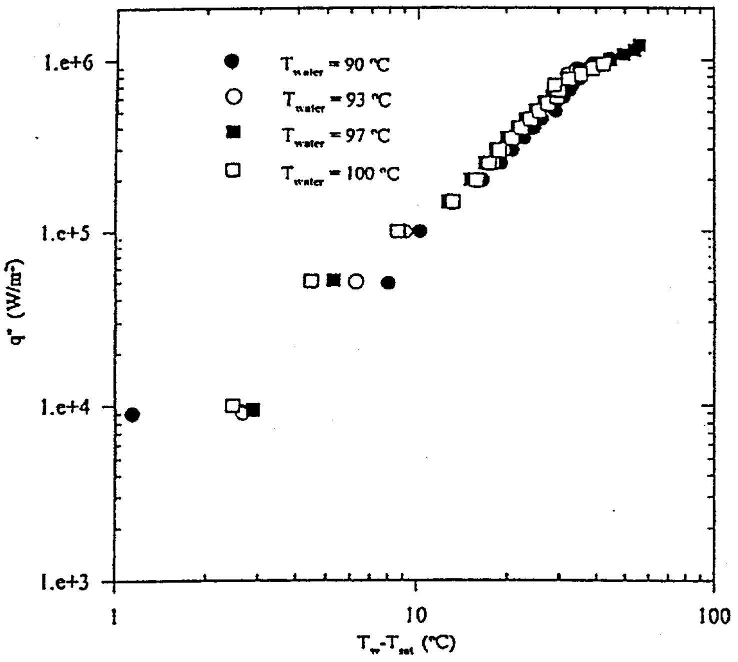

Figure 59. Steady-State Nucleate Boiling Data Measured at an Off-Center Location (θ = 75°).

4.2.6 Comparison of the Steady-State and Transient Quenching Results

A comparison of the steady-state results with the quenching data is shown in Figures 60 to 63 for four different water temperatures. It can be seen that for both saturated and subcooled boiling, the steady-state boiling data are consistently higher than those determined from transient quenching experiments, particularly at low heat flux levels. This is probably due to the fact that there were some errors associated with the data deduced from the transient experiments in the final stage of quenching. An order-of-magnitude analysis of the quenching process indicates that the time scales for the initial and intermediate stages of quenching were sufficiently large for the flow to establish a quasi-steady behavior. However, the time scale for the final stage of quenching was much too small for adequate flow development. As a result, the quenching data under-estimated the nucleate boiling rate. However, the difference between the steady-state and transient data becomes smaller as the heat flux level is increased. The local CHF limit obtained in the steady state experiments appears to be very close to those deduced from the quenching data.

4.3 Summary of the CHF Data Obtained in the SBLB Facility

In order to estimate the effect of vessel size on the critical heat flux, the CHF data obtained in the SBLB facility were compared with available full-scale data obtained under comparable saturated and subcooled boiling conditions. An empirical correlation of the SBLB critical heat flux data was also performed and is presented in this section.

4.3.1 Comparison with the Full-Scale Data

The full-scale CHF data for boundary layer boiling on downward facing surfaces obtained in the ULPU and CYBL experiments (see Refs. 3 to 6) were reviewed in detail. A comparison of the full-scale data was made with the CHF values measured in the SBLB experiments. The results are presented in Figure 64. In this figure, the local critical heat flux is plotted against the dimensionless location, ℓ/L, with the degree of subcooling as a parameter. The two solid curves represent the ULPU data reported in Refs. 3 and 4. The lower curve corresponds to the case of saturated boiling without natural circulation whereas the upper curve corresponds to the case of subcooled boiling with natural circulation. The data point with an error bar in it represents the CHF data obtained at Sandia. As can be seen from the figure, the small-scale and the full scale CHF data compare quite favorably with each other except near the bottom center of the vessel. At the bottom center where $\theta = 0$, the local CHF value measured in the SBLB tests was 0.4 MW/m^2 whereas it was only 0.28 MW/m^2 according to the ULPU data. This difference is probably due to the shape of the test vessels used in the SBLB and ULPU facilities (i.e., 3-D versus 2-D) rather than the size of the vessels. The divergence effect, which could not be simulated in a 2-D configuration, is most important at the bottom center. Elsewhere, the divergence effect is less important. As shown in Table 3, the CHF values measured in both the small-scale and full-scale facilities at locations away from the bottom center were quite close. The position of the heating surface (i.e., ℓ/L) and the degree of subcooling have dominant effects on the local critical heat flux. They totally dwarf the effect of the physical dimensions of the test vessels. Apparently, the local critical heat flux is a weak function of the size of the vessel provided that the vessel diameter is much larger than the dominant vapor bubble size.

4.3.2 Correlation of the SBLB Critical Heat Flux Data

An attempt was made to correlate all the SBLB critical heat flux data obtained to date for downward facing boiling on the exterior surface of a heated hemispherical vessel. The effect of subcooling was taken into account by using a linear function. In doing so, the subcooled boiling data were found to merge nicely with the saturated boiling data. The results are shown in Figure 65, where the local CHF data are plotted

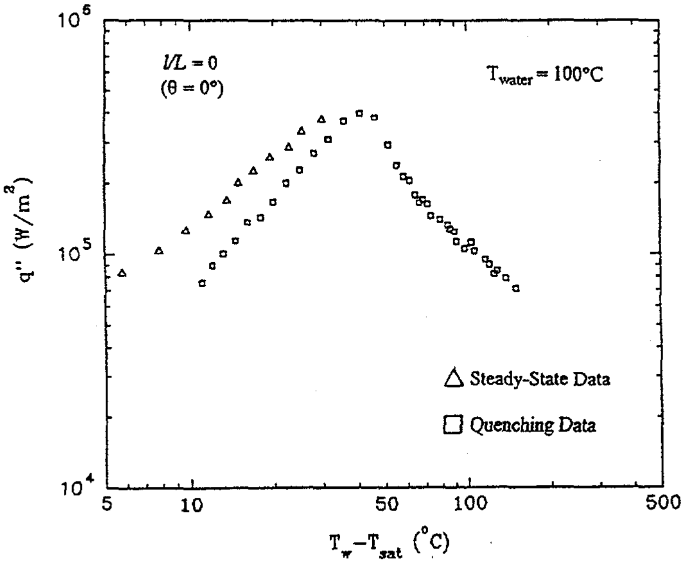

Figure 60. Comparison of the Steady-State and Transient Quenching Data (T_{water} = 100°).

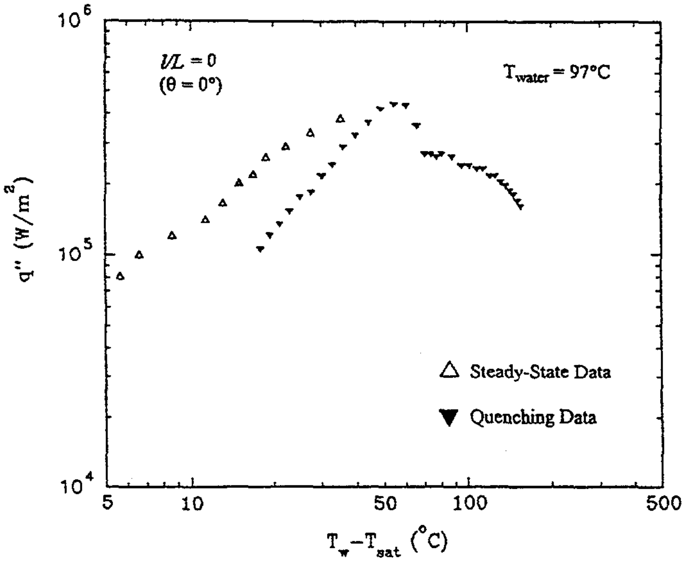

Figure 61. Comparison of the Steady-State and Transient Quenching Data (T_{water} = 97°).

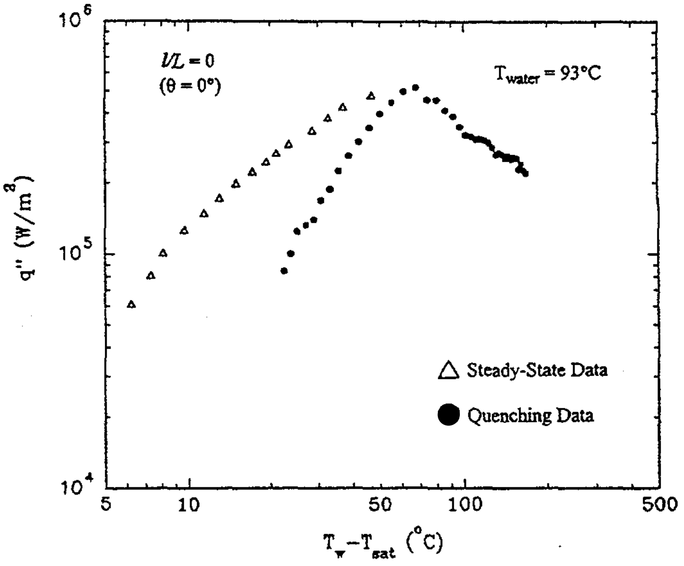

Figure 62. Comparison of the Steady-State and Transient Quenching Data (T_{water} = 93°).

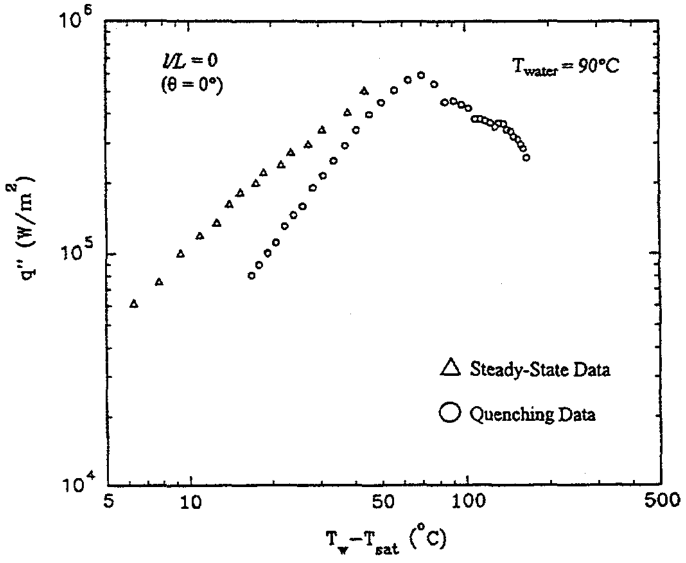

Figure 63. Comparison of the Steady-State and Transient Quenching Data (T_{water} = 90°).

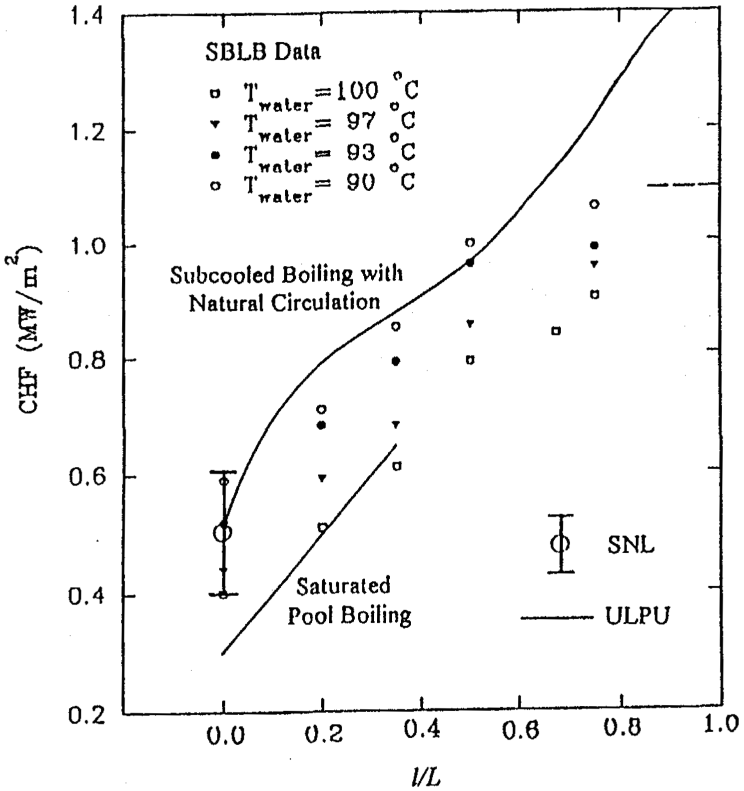

Figure 64. Comparison of the Small-Scale and the Full-Scale CHF Data.

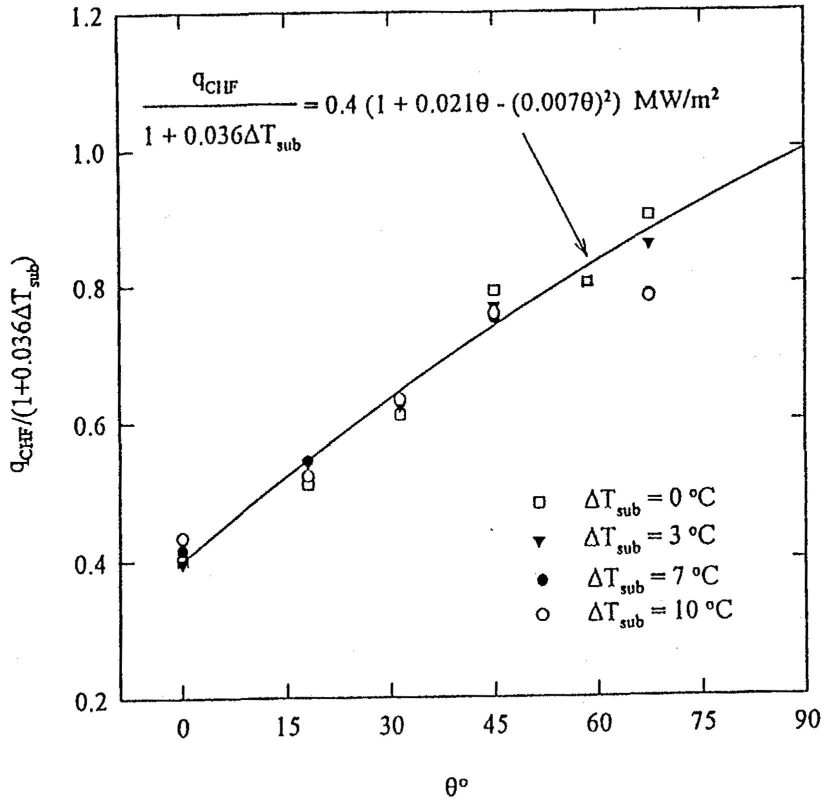

Figure 65. Empirical Correlation of the SBLB Critical Heat Flux Data.

Table 3 Comparison of the Local Critical Heat Fluxes Measured at Various Test Facilities Under Saturated and Subcooled Boiling Conditions

Local Angle of Inclination* θ	Local Critical Heat Flux, MW/m^2				
	SBLB at PSU		CYBL at SNL	ULPU at UCSB	
	Saturated Boiling	Subcooled Boiling**	Saturated Boiling+	Saturated Boiling	Subcooled Boiling++
0°	0.40	0.59	0.50	0.28	0.50
30°	0.61	0.86	--	0.65	0.89
60°	0.85	1.05	--	--	1.18
90°	(1.00)	(1.35)	--	--	1.50

* $\theta = 0^\circ$ corresponding to the bottom center and $\theta = 90^\circ$ corresponding to the upper edge of the test vessel

** Pool boiling with a subcooling of 10 °C

\+ Based largely on small-scale quenching data

++ Natural convection boiling with a subcooling of 14 °C at the bottom center as a function of the vessel outer surface location with the degree of subcooled as a parameter. The spatial variation of the critical heat flux data was represented by a parabolic function using the least-square technique. A correlating equation for the local critical heat flux, q_{CHF}, was derived accordingly as given below:

$$q_{\text{CHF}} = 0.4(1 + 0.036\Delta T_{\text{sub}}) \\ \left[1 + 0.021\theta - (0.007\theta)^2\right]\text{MW}/\text{m}^2 \qquad (4.1)$$

where ΔT_{sub} is the degree of subcooling and θ is the location angle of inclination relative to the horizontal direction on the vessel outer surface.

There are three important terms in the correlating equation. The first term is a coefficient representing the local CHF value at the bottom center of the vessel for saturated boiling, the second term is a linear function representing the effect of subcooling, and the third term is a parabolic function representing the spatial variation of the critical heat flux with the local angle of inclination. The equation shown in the figure correlates 90% of the CHF data within ±3% accuracy and the remaining 10% data within ±10% accuracy.

It should be noted that the effects of thermal insulation around the reactor pressure vessel on the downward facing boiling phenomenon and the resulting critical heat flux have not been taken into account in developing the correlating equation. Depending on the particular design of the reactor vessel insulation system, the spatial variation of the critical heat flux on the vessel outer surface could be significantly modified. Thus it is important to assess the influence of the thermal insulation. A preliminary scaling analysis of the effects of thermal insulation is presented in Appendix D.

4.4 References

1. Carey, V.P., Liquid-Vapor Phase-Change Phenomenon, Hemisphere Publishing Corporation, 1992.
2. Thibault, J. and Hoffman, T.W., “Local Boiling Heat Flux Density around a Horizontal Cylinder under Saturated and Subcooled Conditions”, Proc. Sixth Int. Heat Transfer Conf., toronto, Vol. 1, pp. 199-204, 1978.
3. Theofaneous, T.G., Syri, S., Salmassi, T., Kymalainen, O. and Tuomisto, H., “Critical Heat Flux through Curved Downward Facing Thick Walls”, Nuclear Engineering and Design, Vol. 151, pp. 247-258, 1994.
4. Theofaneous, T.G. and Syri, S., “The Coolability Limit of a Lower Reactor Pressure Vessel Head”, Proc. NURETH-7, 1995.
5. Chu, T. Y., Brainbridge, B. L., Bentz, J. H. and Simpson, R. B., "Observations of quenching downward facing surfaces", Sandia Report, SAND93-0688, 1994.
6. Chu, T.Y., Bentz, J.H. and Simpson, R.B., “Observation of the Boiling Process from a Large Downward-Facing Torispherical Surface”, 30th National Heat Transfer Conference, 1995.
7. Gaertner, R.F., “Photographic study of nucleate pool boiling on a horizontal surface”, Trans. Am. Soc. Mech. Engrs., Series C, J. Heat Transfer, Vol. 87, pp. 17-29, 1965.
8. Katto, Y., “Critical Heat Flux,” Advances in Heat Transfer, Vol. 17, pp. 1-65, 1985.

5 THEORETICAL MODELING

5.1 Introduction

Critical heat flux (CHF) is a critical phenomenon in nucleate boiling involving the dryout of liquid on a heating surface. It represents the upper bound of the excellent state of boiling where the heating surface is wetted with liquid and the heat transferred to the liquid is absorbed by the latent heat of vaporization in the immediate vicinity of the heating surface. The occurrence of the CHF state may be a result of (i) deficiency in vapor removal from the heating surface, (ii) inadequate supply of fresh liquid to the heating surface, (iii) premature liquid depletion on the heating surface, or (iv) the combination of all three factors.

The mechanism responsible for the occurrence of CHF in pool boiling has been the subject of extensive investigation and debate in the past several decades. For upward facing surfaces, widely accepted hydrodynamic CHF models have been developed by Refs. 1 to 8. However, there were no credible CHF models developed specifically for downward facing surfaces. Moreover, no attempt has ever been made to predict the spatial variation of the critical heat flux along a downward facing curved surface. Correlations for the maximum pool boiling heat flux for heated spheres and cylinders of varying sizes have been restricted to the geometrically averaged CHF value as summarized by Ref. 9. The reported data on the spatial variation of the local critical heat flux are limited to those by Refs. 10 to 13.

This section presents a comprehensive hydrodynamic CHF model for downward facing boiling on the external surface of a heated hemispherical vessel. For the purpose of comparison, the critical heat flux for the conventional case of upward facing surfaces will first be discussed before presenting the hydrodynamic CHF model.

5.2 Upward Facing Surfaces

For nucleate boiling on upward facing surfaces, vapor bubbles grow and depart from the active sites of the surface. The bubbles are acted upon by two major opposing forces. These are the surface tension force and the buoyancy force. The surface tension force tends to retain the bubbles on the surface whereas the buoyancy force tends to drive the bubbles away from the surface. The characteristic bubble size L_b is determined by the balance of these two opposing forces, i.e.,

$$L_b \sim \left[\frac{\sigma}{g(\rho_f-\rho_g)}\right]^{1/2} \qquad (5.1)$$

where σ is the surface tension, g the gravity constant, ρ_f the liquid density, and ρ_g the vapor density. At high heat fluxes, vapor columns begin to form. The diameter and the spacing of the vapor columns are on the order of the most dangerous wavelength λ_D due to Helmholtz instability, where

$$\lambda_D \sim 2\pi\sqrt{3}\, L_b \qquad (5.2)$$

Thus, equation (5.1) represents the only relevant length scale of the boiling process. A characteristic velocity scale, $\overline{V}$ can be determined from dimensional considerations. In terms of the fluid properties and the local gravity constant, the following expression can be obtained for the velocity scale:

$$\overline{V} \sim \left[\frac{\sigma g(\rho_f-\rho_g)}{\rho_g^{\,2}}\right]^{1/4} \qquad (5.3)$$

Note that both the characteristic length and velocity scales are intrinsic to the fluid, independent of the physical size of the surface. This is true as long as the heating surface is much larger than λ_D.

In terms of the characteristic length and velocity scales, the following dimensionless heat flux parameter H and characteristic Weber number We can be defined:

$$H = \frac{q_b''}{\rho_g h_{fg} \overline{V}} \quad \text{and} \quad We = \frac{\rho_g \overline{V}^2 L_b}{\sigma} \qquad (5.4)$$

where q_b'' is the nucleate boiling heat flux and h_{fg} is the latent heat of vaporization. Physically, H represents the ratio of the vapor velocity induced by boiling to the escape velocity of the vapor columns and We is a measure of the inertial force to surface tension force. Based upon the assumption that the occurrence of the CHF state is a result of the hydrodynamic instability of the columns, the conditions for the CHF state must be given by

$$H_c = f(We_c) \quad \text{or} \quad H_c = A\, We_c{}^n \qquad (5.5)$$

where the subscript c refers to the critical condition, A is a proportional factor, n an index, and a power-law relationship is assumed for the function $f(We_c)$. This leads to

$$\frac{q''_{\text{CHF}}}{\rho_g h_{fg} \overline{V}_c} = A \left[\frac{\rho_g \overline{V}_c^{\,2} L_b}{\sigma} \right]^n \qquad (5.6)$$

where q''_{CHF} is the critical heat flux and $\overline{V}_c$ is the critical vapor escape velocity. The latter quantity is essentially the same as the one given by equation (5.3). Substituting equations (5.1) and (5.3) into (5.6) gives

$$\begin{aligned} q_{\text{CHF}} &= A\, \rho_g h_{fg} \overline{V}_c \left[\frac{\rho_g \overline{V}_c^{\,2} L_b}{\sigma} \right]^n \\ &= A\, \rho_g h_{fg} \left[\frac{\sigma g (\rho_f - \rho_g)}{\rho_g{}^2} \right]^{1/4} \end{aligned} \qquad (5.7)$$

Equation (5.7) is the well-known CHF correlation for the case of conventional pool boiling on upward facing surfaces. The constant on the right hand side of the equation is A = 0.131 according to Ref. 1 and A = 0.149 according to Ref. 2 to 7. Note from equations (5.3) and (5.4) that the characteristic Weber number is a constant having a value on the order of unity. Physically this implies that the CHF state is given by the balance between the vapor generation rate and the critical vapor escape rate.

5.3 Downward Facing Hemispherical Surfaces

For downward facing boiling on the external surface of a heated hemispherical vessel, the relevant length and velocity scales are dictated by the buoyancy-induced two-phase boundary layer, described in Section 4. The buoyancy force and the surface tension force that act upon the vapor bubbles are not opposing to one another. As a result, the characteristic bubble size is no longer given by equation (5.1). For water at one atmosphere, the value of L_b predicted by equation (5.1) is about 2.5mm, which is the characteristic bubble size observed in conventional pool boiling of water on upward facing surfaces. In the present work, vapor bubbles with characteristic dimensions of 30 to 40mm were observed. For saturated boiling, large elongated bubbles were found to depart from the bottom center region of the vessel and flow upward along the curved heating surface within the boundary layer. The typical size of the elongated bubbles, which was much larger than those observed in the case of conventional pool boiling on upward facing surface, was on the same order of the boundary layer thickness. Evidently, the CHF expression for upward facing surfaces given by equation (5.7) is not applicable to downward facing surfaces.

It should be noted that most existing hydrodynamic CHF models were developed primarily for upward facing surfaces. The critical heat flux was treated as a peculiar point that was different radically from the nucleate boiling regime. Helmholtz instability was assumed to act on the CHF point only, causing a sudden collapse of the vapor removal path. The validity of these conventional models for downward facing surfaces is highly skeptical. The nucleate boiling phenomenon on the outer surface of a heated hemispherical vessel observed in the experimental part of this project clearly indicated that throughout the entire high heat flux regime, nucleate boiling was subject to

Helmholtz instability with cyclic ejection of large elongated vapor masses or slugs from the downward facing curved heating surface. Underneath each vapor slug was a micro-layer consisting of a continuous liquid film with numerous micro-vapor jets penetrating through it. The size of the micro-jets was dictated by Helmholtz instability. The CHF limit was reached as a result of insufficient supply of liquid from the two-phase boundary layer to the micro-layer, leading to depletion of the liquid film, i.e., local dryout of the heating surface. In view of this, the CHF point is a continuation of the nucleate boiling region in the high-heat-flux regime. This important new feature is employed in this section to develop an advanced hydrodynamic CHF model for pool boiling on a downward facing hemispherical heating surface.

5.3.1 Behavior of the Micro-Layer

Figure 66 shows schematically the configuration of a micro-layer underneath an elongated vapor slug growing on a downward facing curved heating surface. The micro-layer consists of a continuous liquid film with numerous micro-vapor jets or stems penetrating through it. The thickness of the liquid film, δ_m, is the same as the length of the vapor stems. Under steady-state saturated boiling conditions, the mass flow rate of the vapor jets must be equal to the local rate of nucleate boiling, i.e.,

$$\rho_g v_g A_v = q''_{\rm NB} A_w / h_{fg}$$

or (5.8)

$$v_g = \frac{q''_{\rm NB}}{\rho_g h_{fg}} \frac{A_w}{A_v}$$

where ρ_g is the vapor density, v_g the vapor jet velocity, A_v the surface area occupied by all the vapor jets, A_w the total heating area underneath the elongated vapor slug, $q''_{\rm NB}$ the local nucleate boiling heat flux, and h_{fg} the latent heat of vaporization. To satisfy continuity, the rate of liquid depletion of the micro-layer must be given by

$$\rho_\ell v_\ell (A_w - A_v) = q''_{\rm NB} A_w / h_{fg}$$

or (5.9)

$$v_\ell = \frac{q''_{\rm NB}}{\rho_\ell h_{fg}} \frac{A_w}{A_w - A_v}$$

where ρ_ℓ is the liquid density and v_ℓ the velocity of the liquid in the micro-layer flowing vertically toward the heating surface.

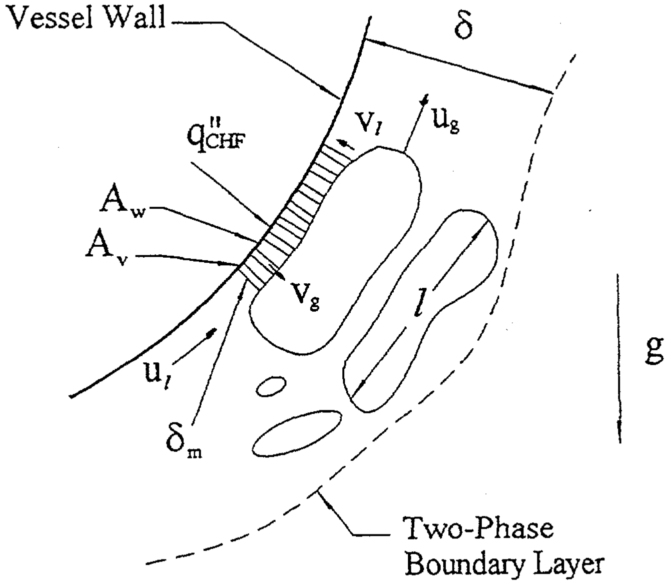

Figure 66. Schematic of the Micro-Layer Underneath an Elongated Vapor Slug.

According to the Helmholtz instability (Ref. 9), the relative velocity between the vapor jets and the liquid film in the micro-layer is given by

$$|v_g - v_\ell| = \left[\frac{2\pi\sigma(\rho_\ell + \rho_g)}{\lambda_H \rho_\ell \rho_g}\right]^{1/2} \qquad (5.10)$$

where σ is the surface tension and λ_H the Helmholtz wavelength. Rearranging the above equation, the Helmholtz wavelength can be expressed in terms of the relative velocity by

$$\lambda_H = \frac{2\pi\sigma}{\rho_g}\left(1+\frac{\rho_g}{\rho_\ell}\right)\left|v_g - v_\ell\right|^{-2} \qquad (5.11)$$

For the vapor jets to be hydrodynamically stable within the liquid film, the length of the jets should remain smaller than the Helmholtz wavelength. This implies that

$$\delta_m < \lambda_H \quad \text{or} \quad \delta_m = C_1\lambda_H \qquad (5.12)$$

where C_1 is a proportionality constant having a value less than unity.

Assuming a value of 0.25 for C_1, Ref. 8 have shown that the micro-layer area ratio is a function of the density ratio of the fluid satisfying the following form:

$$\frac{A_v}{A_w} = 0.0584\left(\frac{\rho_g}{\rho_\ell}\right)^{0.2} \qquad (5.13)$$

The above expression was found to match the conventional pool boiling data for water and R-113 very nicely, independent of the configuration of the heating surface. However, the liquid film thickness so predicted $(\delta_m \sim 0.056\ \text{mm})$ was almost a factor of two smaller than the measured value $(\delta_m \sim 0.12\ \text{mm})$. This discrepancy was evidently due to the assumption of $C_1 = 0.25$ which was somewhat arbitrary. To be general, the exact value of C_1 will not be assumed in this study and the following expression will be employed in place of equation (5.13)

$$\frac{A_v}{A_w} = C_2\left(\frac{\rho_g}{\rho_\ell}\right)^{0.2} \qquad (5.14)$$

where C_2 is treated as an unknown constant having a value much less than unity.

For most fluids at moderate pressures, the density ratio is usually much less than unity, i.e., $(\rho_g/\rho_\ell) << 1$. It follows from equations (5.8), (5.9) and (5.14) that

$$\frac{v_\ell}{v_g} = \frac{C_2(\rho_g/\rho_\ell)^{1.2}}{1 - C_2(\rho_g/\rho_\ell)^{0.2}} << 1 \qquad (5.15)$$

The above inequality is valid since both C_2 and ρ_g/ρ_l are much less than unity. Hence the relative velocity between the vapor jets and the liquid film is essentially the same as the vapor jet velocity itself. Combination of equations (5.9), (5.11), (5.12) and (5.14) gives

$$\delta_m = C_3\sigma\rho_g\left(1+\frac{\rho_g}{\rho_\ell}\right)\left(\frac{\rho_g}{\rho_\ell}\right)^{0.4}\left(\frac{h_{fg}}{q''_{\text{NB}}}\right)^2 \qquad (5.16)$$

where C_3 is a new constant equal to $2\pi C_1 C_2{}^2$.

5.3.2 Occurrence of the Local CHF

Referring to Figure 66, the local rate of liquid supply, $\dot{m}_s$, from the two-phase boundary layer to the micro-layer is given by

$$\dot{m}_s = \rho_\ell u_\ell A_m \qquad (5.17)$$

where u_ℓ is the local liquid velocity in the two phase boundary layer and A_m the net local flow area across the micro-layer. On the other hand, the local rate of depletion, $\dot{m}_d$, of the liquid film is given by

$$\dot{m}_d = q''_{\text{NB}} A_w / h_{fg} \qquad (5.18)$$

where A_w is the heating surface area underneath the elongated vapor slug. Local dryout of the liquid film is considered to occur when the local rate of liquid supply becomes smaller than the local rate of liquid depletion. In other words, the local critical heat flux limit is reached when the liquid supply from the two-phase boundary layer to the micro-layer is not sufficient to prevent local boil-dry of the liquid film. From equations (5.17) and (5.18), an expression for the local critical heat flux, q''_{CHF}, can be obtained by setting $\dot{m}_s$ equal to $\dot{m}_d$ and q''_{NB} equal to q''_{CHF}, i.e.,

$$q''_{\mathrm{CHF}} = \rho_\ell h_{fg} u_\ell \left(\frac{A_m}{A_w} \right) \tag{5.19}$$

where A_{m} is now the net flow area across the micro-layer at the local CHF point.

Assuming the characteristic length of the vapor slug to be ℓ, the net flow area A_{m} and the heating surface area A_{w} can be expressed by

$$A_m \sim (\delta_m)_{\mathrm{CHF}} \ell \quad \text{and} \quad A_w \sim \ell^2 \tag{5.20}$$

where $(\delta_m)_{\mathrm{CHF}}$ is the thickness of the micro-layer at the local CHF point, i.e., at q''_{CHF}. From the two-phase boundary layer flow observations made in the SBLB experiments, the characteristic length ℓ, is found to be proportional to the local two-phase boundary layer thickness, δ_0, in the bottom center region, i.e.,

$$\ell = C_4 \delta_0 \tag{5.21}$$

where C_4 is a constant having a value very close to four along the curved heating surface. Substituting equations (5.20) and (5,21) into (5.19), the following expression is obtained for the local critical heat flux:

$$q''_{\mathrm{CHF}} = \rho_\ell h_{fg} u_\ell (\delta_m)_{\mathrm{CHF}} / C_4 \delta_0 \tag{5.22}$$

where additional proportionality constants from equation (5.20) have been absorbed in C_4.

As discussed earlier, the CHF point is a continuation of the nucleate boiling region in the high-heat-flux regime. Helmholtz instability is acting upon the micro-layer throughout the entire high-heat-flux nucleate boiling regime including the CHF point. Hence, equation (5.16) should be applicable to the CHF limit.

By setting q''_{NB} equal to q''_{CHF}, equation (5.16) becomes

$$(\delta_m)_{\mathrm{CHF}} = C_3 \sigma \rho_g \left(1 + \frac{\rho_g}{\rho_\ell}\right) \left(\frac{\rho_g}{\rho_\ell}\right)^{0.4} \left(\frac{h_{fg}}{q''_{\mathrm{CHF}}}\right)^2 \tag{5.23}$$

Substitution of Equation (5.23) into (5.22) gives

$$q''_{\mathrm{CHF}} = B \rho_g h_{fg} \left[\frac{\sigma u_\ell}{\rho_\ell \delta_0} \left(1 + \frac{\rho_g}{\rho_\ell}\right) \left(\frac{\rho_g}{\rho_\ell}\right)^{-1.6} \right]^{1/3} \tag{5.24}$$

where $B = (C_3 / C_4)^{1/3}$ is a new constant. Evidently, the local critical heat flux varies according to the 1/3 power of the local liquid velocity. This local flow quantity, which is expected to increase significantly along the heating surface in the flow direction, will be determined by treating the two-phase boundary layer motion as an external buoyancy-driven flow.

It should be noted that the dependence of the CHF limit on the local liquid velocity in the two-phase boundary layer given by equation (5.24) is similar to the one observed for forced convection boiling of the external flow type where the critical heat flux is proportional to the 1/3 power of the mass velocity of the ambient liquid flow (Ref. 9). This similarity clearly shows the rather unconventional features associated with the present boundary-layer-type pool boiling process. Although it is a pool boiling phenomenon, the process exhibits flow boiling characteristics. Physically, this is because of the formation of the two-phase boundary layer along the downward facing curved heating surface in the present pool boiling case. Owing to the effect of the two-phase boundary layer, the CHF phenomenon at a given downstream location exhibits the same characteristic behavior as the one observed for external flow boiling.

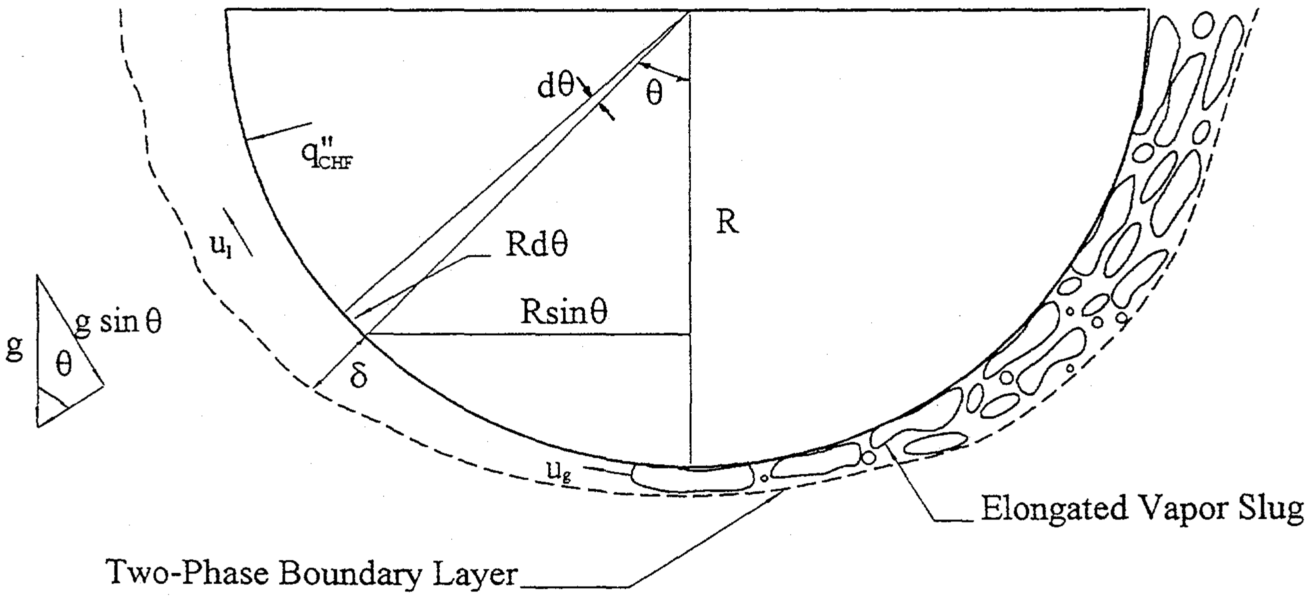

Figure 67. Configuration of the Two-Phase Boundary Layer on the Outer Surface of a Heated Hemispherical Vessel.

5.4 Two-Phase Boundary Layer Analysis

Figure 67 depicts the external buoyancy-driven two-phase boundary layer flow on the outer surface of a hemispherical vessel. The vessel has a radius R and is heated from inside. The ambient liquid is saturated and quiescent, and the boundary layer motion is induced entirely by pool boiling of the saturated liquid on the vessel outer surface. To describe the boundary layer variables, an axisymmetric spherical coordinate system is employed. The radial and angular positions in the boundary layer are given by r and θ, respectively. The important length scales are the local heating length $R\theta$ and the local boundary layer thickness δ, whereas the important velocity scales are the local liquid and vapor velocities, u_ℓ and u_g, respectively. The latter two quantities are defined for the local velocities in the direction parallel to the curved heating surface. Under the influence of gravity, the buoyancy force driving the two-phase motion is proportional to $\alpha(\rho_\ell - \rho_g)g\sin\theta$, where α is the local void fraction of the two-phase mixture and $g \sin \theta$ is the local acceleration of gravity in the direction parallel to the heating surface.

According to Ref. 14, the momentum relation for the vapor-liquid mixture in the two-phase boundary layer is governed by the following differential equation applicable to any location θ along the hemispherical heating surface:

$$\begin{aligned}&\frac{d}{d\theta}\left\{\left[\rho_g \alpha u_g^{\,2} + \rho_\ell (1-\alpha) u_\ell^{\,2}\right]\delta \sin\theta\right\} \\ &= \alpha\delta R g(\rho_\ell - \rho_g)\sin^2\theta \qquad (5.25) \\ &-(\tau_w + \tau_i)R\sin\theta\end{aligned}$$

where τ_w and τ_I are the wall and the interfacial shear stresses. These quantities are given by (Ref. 14):

$$\tau_w + \tau_i = 0.5C_f\left[\alpha u_g + (1-\alpha)u_\ell\right] \left[\rho_g \alpha u_g + \rho_\ell (1-\alpha)u_\ell\right] \qquad (5.26)$$

where C_f is a friction coefficient having the value of 0.005.

A mass balance on the liquid phase across the thickness of the two-phase boundary layer at any location θ gives

$$\frac{d}{d\theta}\left[(1-\alpha)u_\ell \delta \sin\theta\right] = j_\ell R \sin\theta \qquad (5.27)$$

where j_ℓ is the net liquid velocity entrained from the ambient fluid into the two-phase boundary layer at θ. Physically, the quantity j_ℓ represents the "entrained" component of the liquid mass swept into the boundary layer by the two-phase motion, excluding the "suction" component of the liquid mass due to liquid depletion by boiling on the heating surface. A detailed description of the quantity j_ℓ will be given later. Similarly, a mass balance on the vapor phase across the thickness of the two-phase boundary layer under saturated boiling conditions at any location θ gives

$$\frac{d}{d\theta}\left[\alpha u_g \delta \sin\theta\right] = \frac{q''_{\mathrm{CHF}} R \sin\theta}{\rho_g h_{fg}} \qquad (5.28)$$

where in deriving the above expression, the local wall heat flux on the heating surface has been assumed equal to the local critical heat flux. This corresponds to the critical heating condition for which the local CHF limit is reached in all upstream locations on the outer surface of the hemispherical vessel. This situation gives rise to the maximum local vapor velocity and boundary layer thickness that can possibly be attained at a given downstream location θ. Physically, the use of q''_{CHF} in equation (5.28) is consistent with the notion that CHF represents the upper bound of the excellent state of nucleate boiling. Beyond this upper limit, dryout will occur on the heating surface.

To close the governing system, an independent expression is needed for the relative velocity between the liquid and vapor phases. This is obtained by assuming that once the vapor mass departs from the heating surface, it would attain its terminal rise velocity relative to the liquid phase in the two-phase boundary layer. It follows that (Ref. 15)

$$u_g = u_\ell + 1.53\left[\frac{\sigma g \sin\theta\left(\rho_\ell - \rho_g\right)}{\rho_\ell^{\,2}}\right]^{1/4} \qquad (5.29)$$

where $g \sin\theta$ represents the local gravitational force tangential to the heating surface. As will be seen in the numerical solution, the relative velocity is important only in the upstream locations near the bottom center. In most downstream locations, the relative velocity is considerably smaller than the vapor and liquid velocities themselves. This is owing to the fact that the vapor generation rate is extremely high at the CHF limit, resulting in very large vapor and liquid velocities in the two phase boundary layer. Thus any errors associated with the relative velocity used in equation (5.29) will not materially affect the predicted boundary layer flow behavior.

Inspection of equations (5.24) to (5.29) indicates that the following local boundary layer variables, namely, the dimensionless critical heat flux, Q_{CHF}, dimensionless boundary layer thickness, Δ, dimensionless vapor velocity, U_g, and dimensionless liquid velocity, U_ℓ, can be introduced to simplify the governing system:

$$q''_{\mathrm{CHF}} = \rho_g h_{fg}\left[\frac{\sigma g\left(\rho_\ell - \rho_g\right)}{\rho_g^{\,2}}\right]^{1/4} \left(1+\frac{\rho_g}{\rho_\ell}\right)^{1/3} Q_{\mathrm{CHF}} \qquad (5.30)$$

$$\delta = \left[\frac{\sigma R^2}{g\left(\rho_\ell - \rho_g\right)}\right]^{1/4} \left(\frac{\rho_g}{\rho_\ell}\right)^{-0.1} \Delta \qquad (5.31)$$

$$u_g = \left[\frac{Rg(\rho_\ell - \rho_g)}{\rho_g}\right]^{1/2} \left(\frac{\rho_g}{\rho_\ell}\right)^{0.1} U_g \qquad (5.32)$$

$$u_\ell = \left[\frac{Rg(\rho_\ell - \rho_g)}{\rho_\ell}\right]^{1/2} U_\ell \qquad (5.33)$$

In terms of the dimensionless local variables, equations (5.24) to (5.29) can be written as

$$Q_{\text{CHF}} = B(U_\ell / \Delta_0)^{1/3} \qquad (5.34)$$

$$\frac{d}{d\theta}\left\{\left[\alpha U_g^{\,2} + \left(\frac{\rho_g}{\rho_\ell}\right)^{-0.2} (1-\alpha) U_\ell^{\,2}\right] \Delta \sin\theta\right\}$$

$$= \alpha \Delta \sin^2\theta \left(\frac{\rho_g}{\rho_\ell}\right)^{-0.2}$$

$$-0.5 C_f L_b^{-1/2} \left(\frac{\rho_g}{\rho_\ell}\right)^{0.1} \sin\theta \qquad (5.35)$$

$$\left[\alpha U_g + \left(\frac{\rho_g}{\rho_\ell}\right)^{-0.6} (1-\alpha) U_\ell\right]$$

$$\left[\alpha U_g + \left(\frac{\rho_g}{\rho_\ell}\right)^{0.4} (1-\alpha) U_\ell\right]$$

$$\frac{d}{d\theta}\left[(1-\alpha) U_\ell \Delta \sin\theta\right] \qquad (5.36)$$

$$= J_\ell \left(\frac{\rho_g}{\rho_\ell}\right)^{0.1} L_b^{-1/2} \sin\theta$$

$$\frac{d}{d\theta}\left[\alpha U_g \Delta \sin\theta\right] = Q_{\text{CHF}} \sin\theta \qquad (5.37)$$

$$U_\ell = \left(\frac{\rho_g}{\rho_\ell}\right)^{-0.4} U_g - 1.53 (L_b^{\,2} \sin\theta)^{1/4} \qquad (5.38)$$

where

$$\Delta_0 = \left[\frac{\sigma R^2}{g(\rho_\ell - \rho_g)}\right]^{-1/4} \left(\frac{\rho_g}{\rho_\ell}\right)^{0.1} \delta_0 \qquad (5.39)$$

$$J_\ell = \left[\frac{Rg(\rho_\ell - \rho_g)}{\rho_\ell}\right]^{-1/2} j_\ell \qquad (5.40)$$

$$L_b = \frac{1}{R}\left[\frac{\sigma}{g(\rho_\ell - \rho_g)}\right]^{1/2} \qquad (5.41)$$

Physically, the dimensionless parameter L_b represents the length ratio between the intrinsic bubble size and the vessel radius.

5.5 Initial Conditions and the Universal Constant

It remains necessary to determine the initial value, Δ_0, for the dimensionless boundary layer thickness. This requires considerations of the vapor mass that forms in the bottom center region of the heated vessel. Based upon the vapor dynamics observed in the SBLB experiments, the aspect ratio of the vapor mass is very close to four, i.e., $C_4 = 4$ in equation (5.21). The vapor velocity, u_{g_0}, at an initial location θ_0 near the bottom center can be determined from a mass balance, i.e.,

$$\rho_g u_{g_0} \alpha (2\pi R \delta_0 \sin\theta_0)$$

$$= \frac{1}{h_{fg}} \int_0^{\theta_0} q''_{\text{CHF}} \, 2\pi R^2 \sin\theta \, d\theta \qquad (5.42)$$

Since $\theta_0 << 1$, the local critical heat flux can be treated as a constant equal to $(q''_{\text{CHF}})_0$. An expression for u_{g_0}, may thus be obtained by carrying out the integration in equation (5.42).

The result is

$$u_{g_0} = \frac{(q''_{\text{CHF}})_0}{\alpha \rho_g h_{fg}} \left[\frac{1 - \cos\theta_0}{\sin\theta_0}\right] \left(\frac{R}{\delta_0}\right) \qquad (5.43)$$

For $\theta_0 << 1$, it can be shown that

$$\sin\theta_0 = \theta_0 \quad \text{and} \quad \cos\theta_0 = 1 - \frac{1}{2}\theta_0^{\,2} \qquad (5.44)$$

Substituting equations (5.44) into (5.43), the following expression is obtained for u_{g_0},

$$u_{g_0} = \frac{(q''_{\mathrm{CHF}})_0}{\alpha\rho_g h_{fg}}\left(\frac{R}{\delta_0}\right)\frac{\theta_0}{2} \qquad (5.45)$$

In terms of the dimensionless quantities, equation (5.45) can be written as

$$U_{g_0} = \frac{(Q_{\mathrm{CHF}})_0}{\alpha\Delta_0}\frac{\theta_0}{2} \qquad (5.46)$$

where U_{g_0} and $(Q_{\mathrm{CHF}})_0$ are the initial values of U_g and Q_{CHF} at $\theta = \theta_0$. From equations (5.38) and (5.44), the dimensionless liquid velocity at θ_0 is given by

$$U_{\ell_0} = \left(\frac{\rho_g}{\rho_\ell}\right)^{-0.4}\frac{(Q_{\mathrm{CHF}})_0}{\alpha\Delta_0}\frac{\theta_0}{2} - 1.53L_b^{1/2}\theta_0^{\,1/4} \qquad (5.47)$$

Applying equation (5.34) at $\theta = \theta_0$ and using equation (5.47), an implicit relationship can be derived for Δ_0. This is

$$\left(\frac{\rho_g}{\rho_\ell}\right)^{-0.4}\frac{(Q_{\mathrm{CHF}})_0}{\alpha\Delta_0}\frac{\theta_0}{2} - 1.53L_b^{1/2}\theta_0^{\,1/4} = \left[\frac{(Q_{\mathrm{CHF}})_0}{B}\right]^3\Delta_0 \qquad (5.48)$$

Assuming the boundary-layer flow quantities to be nearly constant over the bottom-center region where $0 \le \theta \le \theta_0$ and that $d\Delta/d\theta = 0$ at $\theta = \theta_0$, equation (5.35) can be integrated to give

$$\begin{aligned}
&\alpha U_{g_0}^{\;2} + \left(\frac{\rho_g}{\rho_\ell}\right)^{-0.2}(1-\alpha)U_{\ell_0}^{\;2} \\
&= \frac{\alpha\theta_0^{\,2}}{3}\left(\frac{\rho_g}{\rho_\ell}\right)^{-0.2} \\
&-0.25C_f L_b^{-1/2}\left(\frac{\rho_g}{\rho_\ell}\right)^{0.1}\theta_0 \qquad (5.49) \\
&\left[\alpha U_{g_0} + \left(\frac{\rho_g}{\rho_\ell}\right)^{-0.6}(1-\alpha)U_{\ell_0}\right] \\
&\left[\alpha U_{g_0} + \left(\frac{\rho_g}{\rho_\ell}\right)^{0.4}(1-\alpha)U_{\ell_0}\right]
\end{aligned}$$

where equation (5.44) has been employed in deriving the above equation. The value of Δ_0 can be determined iteratively from equations (5.46) to (5.49). Once Δ_0 is known, equations (5.34) to (5.38) can be solved simultaneously to determine the spatial variation of Q_{CHF}.

The above formulation results in one universal constant that needs to be determined from experimental data. To do this, the vapor dynamic and the local CHF limit at $\theta = \theta_0$ observed in the SBLB experiments, are employed. The criterion for the occurrence of the local CHF limit in the bottom center region is based on the depletion of the liquid film in the micro-layer before the departure of the vapor mass from the heating surface. The mass of the liquid film is $\rho_\ell\delta_m(A_w - A_v)$ whereas the total rate of nucleate boiling heat transfer is $q''_{\mathrm{NB}}A_w$. If the duration of the vapor ejection cycle is Δt_v, then local dryout would occur if $q''_{\mathrm{NB}}A_w\Delta t_v / h_{fg}$ becomes equal to or larger than the mass of the liquid film. Thus the local CHF limit is given by (see Ref. 16)

$$(q''_{\text{CHF}})_0 = \frac{1}{A_w \Delta t_v} \left[\rho_\ell (\delta_m)_{\text{CHF}} (A_w - A_v) h_{fg}\right] = \frac{\rho_\ell h_{fg} (\delta_m)_{\text{CHF}}}{\Delta t_v} \tag{5.50}$$

where the term involving the area ratio has been ignored as $A_v / A_w << 1$. Substituting equation (5.23) into (5.50) and rearranging, an expression for the universal constant can be derived. This is

$$C_3 = \frac{\Delta t_v}{\sigma \rho_\ell \rho_g} \left(1 + \frac{\rho_g}{\rho_\ell}\right)^{-1} \left(\frac{\rho_g}{\rho_\ell}\right)^{-0.4} \left[\frac{(q''_{\text{CHF}})_0}{h_{fg}}\right]^3 \tag{5.51}$$

In the SBLB experiments, the duration Δt_v, was found to be 0.25 s whereas the local CHF limit was 0.4 MW/m^2. Using the properties for water at one atmospheric pressure, i.e., $\sigma = 0.0588$ N/m, $\rho_\ell = 958$ kg/m^3, $\rho = 0.598$kg/m^3, and $h_{fg} = 2.257$ MJ/kg, the value of C_3 is calculated to be 0.00079. It follows that the universal constant in equations (5.34) and (5.38) is given by

$$B = (C_3 / C_4)^{1/3} = 0.0582 \tag{5.52}$$

where the value of $C_4 = 4$ has been used.

5.6 Spatial Variation of the Critical Heat Flux on a Downward Facing Hemispherical Surface

Equations (5.34) to (5.38) form a complete set of coupled equations governing the local variations of the critical heat flux, Q_{CHF}, the vapor and liquid velocities U_g and U_ℓ respectively, the boundary layer thickness, Δ, and the void fraction, α. To solve this set of equations, however, input information is needed for the liquid entrainment rate, J_ℓ, in equation (5.36). Unfortunately, no experimental evidence on the liquid entrainment is available to date. To circumvent this difficulty, it is postulated that the local void fraction in the two-phase boundary layer assumes a constant value as the CHF limit is approached on the heating surface. This postulation, which is consistent with the experimental observation of phenomenon observed in the SBLB experiments, will be justified from a theoretical point of view in the next section. By setting α equal to 0.915 according to the SBLB data, equation (5.36) which contains the liquid entrainment term, can be eliminated from the governing system. The remaining unknown quantities (i.e., Q_{CHF}, U_g, U_ℓ and Δ) can readily be determined from equations (5.34) to (5.38).

Based upon the constant-void-fraction postulation, calculations of the local boundary layer flow quantities and the local CHF limits have been made over the range of $0 \le \theta \le \pi / 2$ for water. In these calculations, the value of L_b has been set equal to 0.164, 0.0164, 0.00164, and 0.000164, corresponding respectively to a diameter of 1.2" (0.0305 m), 12" (0.305 m), 120" (3.05 m), and 1,200" (30.5 m) for the heated hemispherical vessel under consideration. Results are shown in Figures 68 to 71. For all values of L_b, the boundary layer thickness increases considerably from the bottom center to the upper edge of the vessel (see Figure 68). However, the dimensionless boundary layer thickness is a weak function of the physical size of the vessel. The size effect is important only when the vessel diameter is very small. The actual boundary layer thickness, on the other hand, is a strong function of L_b. For $L_b < 0.05$, however, δ is almost inversely proportional to the square root of L_b. Thus for vessels larger than 0.1 m in diameter, δ would vary according to the square root of the vessel diameter whereas Δ is essentially independent of the vessel size.

The spatial variations of the vapor and liquid velocities are presented in Figures 69 and 70. For all values of L_b, the vapor and liquid velocities increase by more than an order of

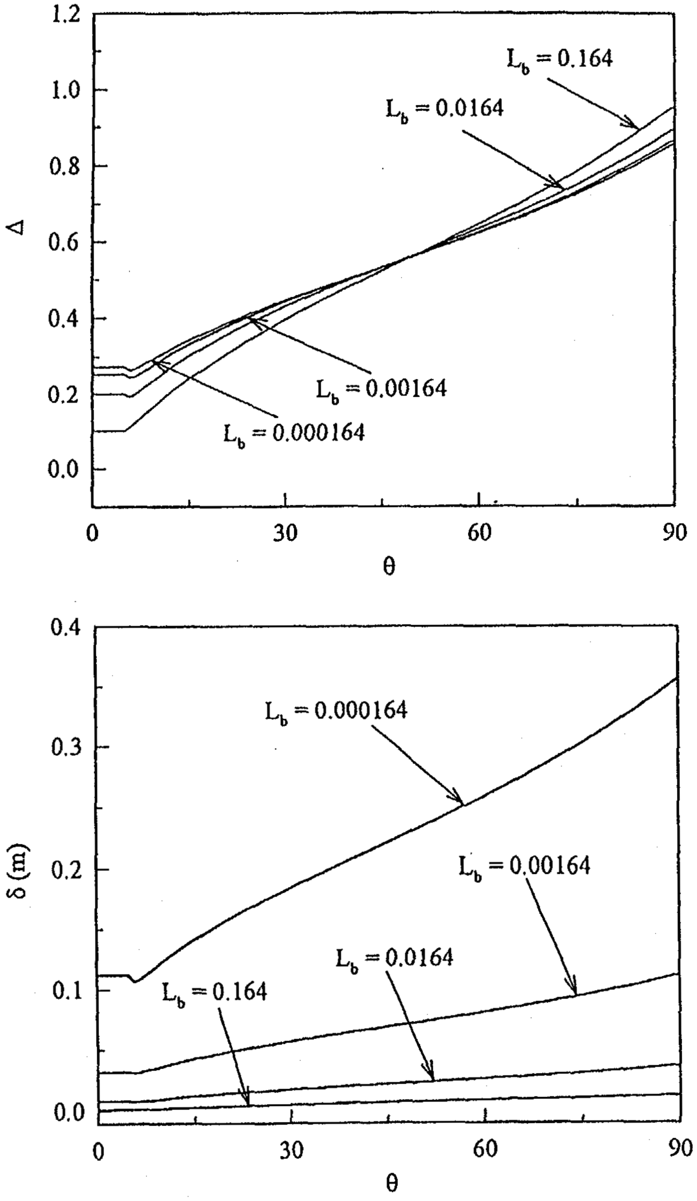

Figure 68. Spatial Variation of the Local Thickness of the Two-Phase Boundary Layer.

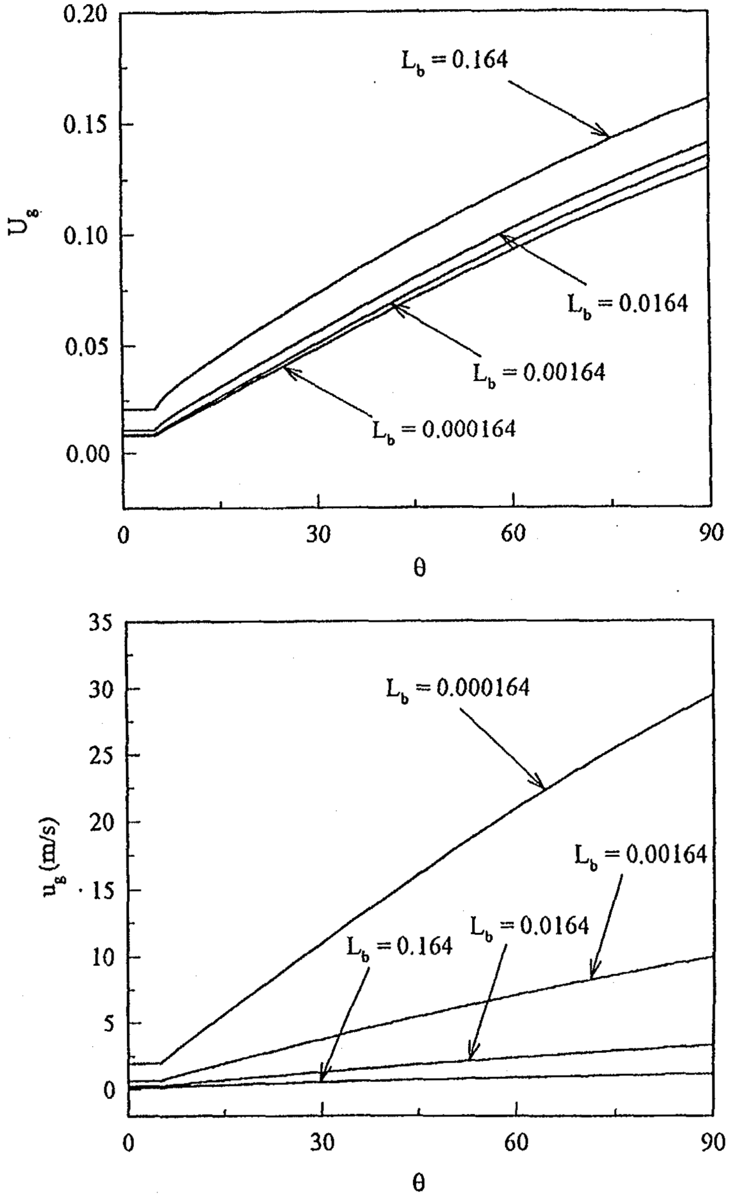

Figure 69. Spatial Variation of the Local Vapor Velocity in the Two-Phase Boundary Layer.

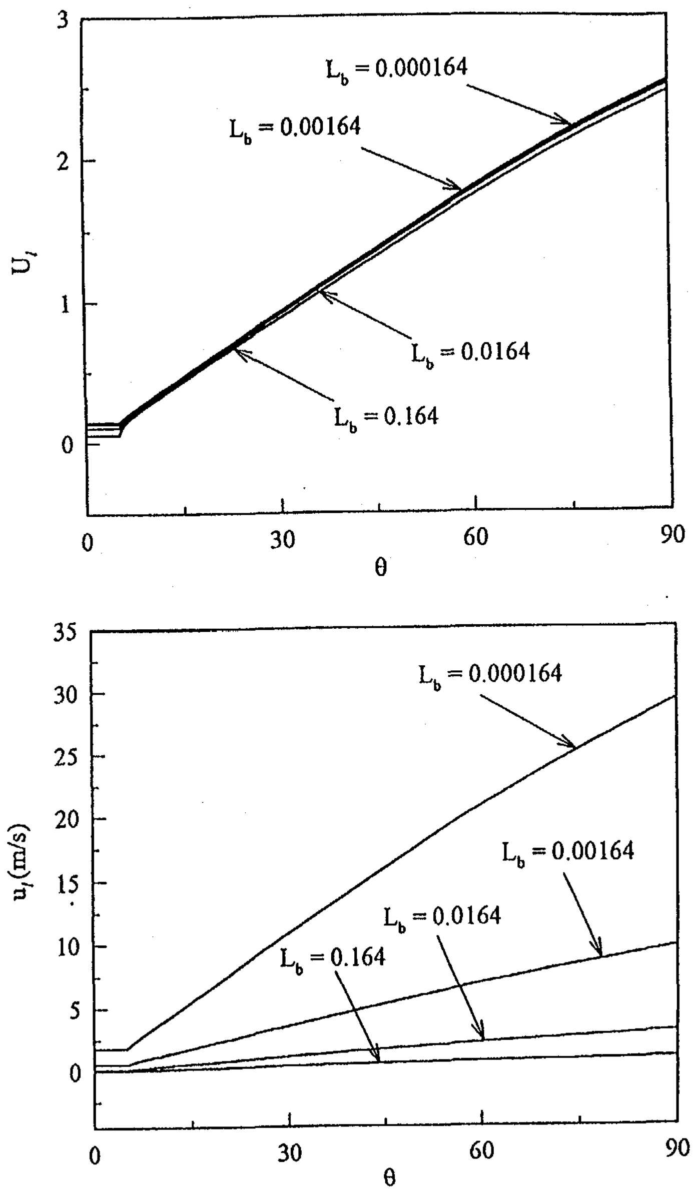

Figure 70. Spatial Variation of the Local Liquid Velocity in the Two-Phase Boundary Layer.

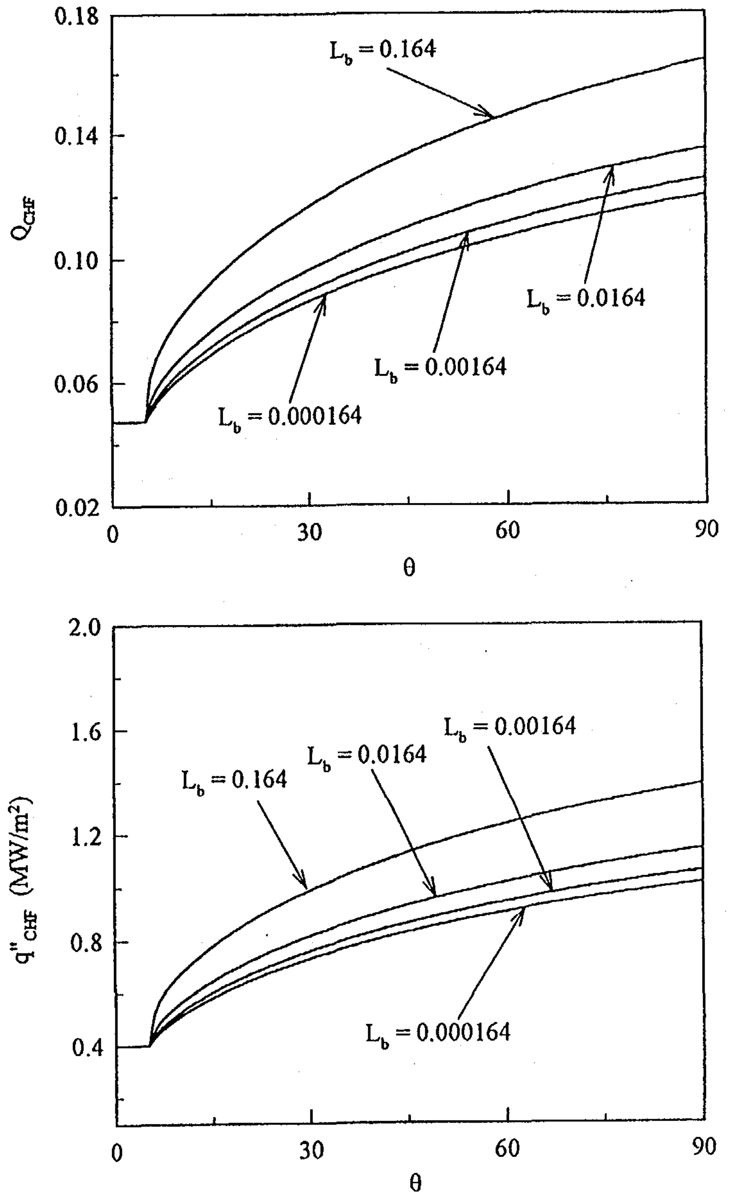

Figure 71. Spatial Variation of the Local Critical Heat Flux on the Heating Surface.

magnitude from the bottom center to the upper edge of the vessel. The relative velocity between the liquid and vapor phases is on the same order of the vapor and liquid velocities when θ is small. For large values of θ, the relative velocity is an order of magnitude smaller than the liquid and vapor velocities. The effect of L_b is quite strong on u_ℓ and u_g but very weak on the dimensionless quantities U_ℓ and U_g. For $L_b < 0.05$, both u_ℓ and u_g are almost inversely proportional to the square root of L_b. Thus for vessels larger than 0.1 m in diameter, u_ℓ and u_g would vary according to the square root of the vessel diameter whereas U_ℓ and U_g are essentially independent of the vessel size.

Figure 71 shows the spatial variations of the dimensionless critical heat flux and the actual critical heat flux. Both Q_{CHF} and q''_{CHF} are weak functions of the size parameter L_b for the cases of L_b equal to or less than 0.0164. This clearly demonstrates the fact that for heated vessels with diameters considerably larger than the characteristic bubble size, the critical heat flux is weakly dependent on the vessel size. As shown in equation (5.24), the local critical heat flux is given by the 1/3 power of the ratio between the local liquid velocity and the local boundary layer thickness. For $L_b < 0.05$, both u_ℓ and δ vary according to the square root of the vessel diameter. Thus the size effect on u_ℓ and δ_0 cancels out and q''_{CHF} becomes almost independent of L_b. Note that the local critical heat flux increases by more than 100% from the bottom center to the upper edge of the vessel. This result is similar to the spatial variations of CHF observed in the SBLB and ULPU experiments. However, it is opposite to the CHF variation observed by in Ref. 17. Physically, this is because of the two-phase boundary layer flow effect, which was present in the SBLB and ULPU experiments but not present in the transient experiments in Ref. 17. In the latter case the heating surface was too small (~50 mm) for a two-phase boundary layer to develop. For the downward facing heating surface under consideration, the local liquid velocity increases by more than an order of magnitude over the range of $0 \le \theta \le \pi/2$. As a result, there is a large increase in the local liquid supply rate, resulting in a significant spatial variation of the critical heat flux.

5.7 Liquid Entrainment and the Constant-Void-Fraction Postulation

The results presented in the previous section were based on the postulation that the local void fraction assumes a constant value as the CHF limit is approached on the heating surface. Although the constant-void-fraction postulation is consistent with the SBLB experimental observation, it is necessary to justify the postulation from a theoretical point of view. To do this, an expression is needed for the liquid entrainment j_ℓ in equation (5.27). Experimental measurements of entrainment with turbulent gas jets having a density different than the ambient fluid have been performed in Ref. 18. They found that the entrainment velocity, j_ℓ, is proportional to the mean velocity u_j of the jet as well as the square root of the ratio of the density ρ_j of the jet to the density ρ_∞ of the ambient fluid, e.g.,

$$j_\ell = E_0\, u_j \left(\frac{\rho_j}{\rho_\infty} \right)^{1/2} \tag{5.53}$$

where the proportionality constant E_0 is the so-called entrainment coefficient. By extending the finding of Ref. 18 to the two-phase boundary layer under consideration, the following expressions can be written:

$$u_j = \alpha u_g + (1-\alpha) u_\ell$$

and (5.54)

$$\frac{\rho_j}{\rho_\infty} = \frac{\alpha \rho_g + (1-\alpha)\rho_\ell}{\rho_\ell \sin\theta}$$

where the term sin θ is included in the denominator of the density ratio to account for the downward facing orientation of the heating surface. Whereas the turbulent jets studied by

Ref. 18 are vertically oriented, the two-phase boundary layer under consideration is inclined along the heating surface. The component of the gravity force parallel to the flow is given by $g \sin\theta$. Physically the second expression in equation (5.54) represents the ratio of the body force acting on the two phase mixture to that acting on the ambient fluid. From equations (5.53) and (5.54), an expression for the liquid entrainment from the ambient fluid to the two-phase boundary layer can be obtained. This is

$$j_\ell = E_0\left[\alpha u_g + (1-\alpha)u_\ell\right] \left[\frac{\alpha\rho_g + (1-\alpha)\rho_\ell}{\rho_\ell \sin\theta}\right]^{1/2} \tag{5.55}$$

The above expression can be viewed as the two-phase version of the expression proposed by Ref. 19 for turbulent jets driven by buoyancy. A similar expression has also been employed by Ref. 14 to study the behavior of a two-phase boundary layer on inclined flat surfaces. Substituting equations (5.40) and (5.55) into (5.36), the following dimensionless liquid continuity equation can be obtained:

$$\frac{d}{d\theta}\left[(1-\alpha)U_\ell\Delta\sin\theta\right] = E_0 \sin^{1/2}\theta\left(\frac{\rho_g}{\rho_\ell}\right)^{0.1} L_b^{-1/2} \left[\left(\frac{\rho_g}{\rho_\ell}\right)^{-0.4}\alpha U_g + (1-\alpha)U_\ell\right] \left[\frac{\alpha\rho_g + (1-\alpha)\rho_\ell}{\rho_\ell}\right]^{1/2} \tag{5.56}$$

Calculations of the local boundary layer flow quantities and the local CHF limits have been made by solving equations (5.34), (5.35), (5.37), (5.38) and (5.56) for water, treating the local void fraction α as an unknown quantity. In these calculations, the value of L_b has been fixed at 0.0164, corresponding to a vessel diameter of 12" (0.305 m), which is the same as the vessel size employed in the SBLB experiments. Meanwhile, various values have been assumed for the entrainment coefficient by setting E_0 equal to 0.116 C_5, where C_5 is a constant factor having a value varying from 0.5 to 1.0. The value of $C_5 = 1.0$ (i.e., $E_0 = 0.116$) has been used by Ref. 19 for turbulent jets and by Ref. 14 for two-phase boundary layer flows. In the present case, however, E_0 is expected to be smaller than 0.116 because of the configuration of the downward facing curved heating surface and the wall effect on liquid entrainment. For all values of $0.5 \le C_5 \le 1.0$ employed in the calculations, the local void fraction was found to be nearly constant over the length of the hemispherical heating surface. Results for two special cases are presented in Figure 72. For the case of $E_0 = 0.116$ (i.e., $C_5 = 1.0$), the local void fraction is bounded within ± 2.5% of 0.892, whereas for the case of $E_0 = 0.0878$ (i.e., $C_5 = 0.75$), α is bounded within ± 0.5% of 0.915. These results clearly indicate that the constant-void-fraction postulation is a valid approach as it complies with the conservation of liquid mass, i.e., the liquid continuity equation. Based on the value of $\alpha = 0.915$ observed in the SBLB experiments, the entrainment coefficient for the present two-phase boundary layer flow is determined to be $E_0 = 0.0878$.

5.8 Comparison with the SBLB Data

The initial values of the boundary layer quantities employed in the present work are treated constant throughout the bottom center region of the hemispherical vessel where $0 \le \theta \le \theta_0$. This treatment is consistent with the experimental observation where a single large elongated vapor mass was always found present in the bottom center region. For a given value of L_b, the initial location θ_0 is determined by numerical iteration from equations (5.46) to (5.49). It is found that for L_b much less than unity θ_0 is a weak function of L_b having a value approximately equal to 4.5°. This value is very close to the one obtained experimentally based on the observed vapor size at the bottom center. For the purpose of comparison, results obtained for θ_0 equal to 4° and 5° are shown in Figure 73

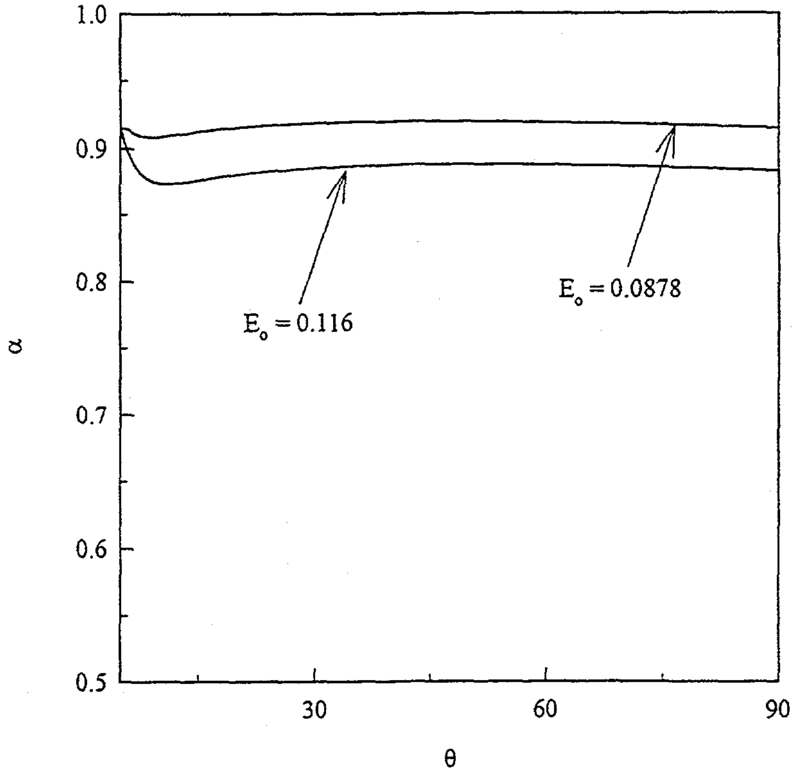

Figure 72. The Predicted Local Void Fraction Profiles in the Two-Phase Boundary Layer.

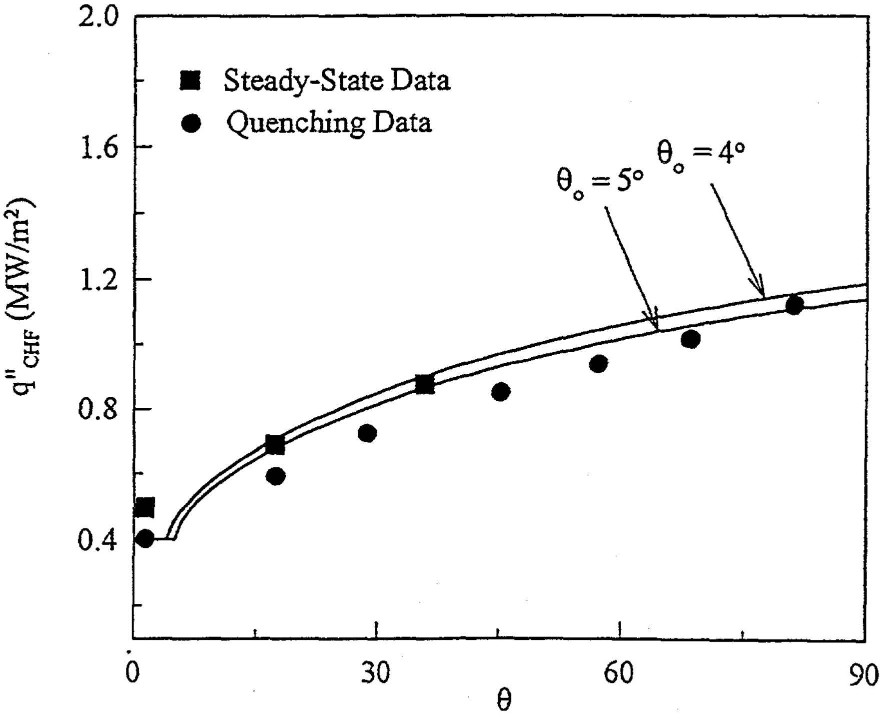

Figure 73. Comparison of the Predicted Critical Heat Fluxes with Experimental Data.

along with the SBLB data from quenching experiments and steady-state measurements. Relative to the case of $\theta_0 = 5°$, the CHF value predicted for the case of $\theta_0 = 4°$ is slightly higher. However, the differences are well within the scatter of the experimental data. More importantly, the same trend (i.e., the same spatial variation) is predicted for the critical heat flux, independent of the initial location θ_0. Apparently, the CHF variation is not sensitive to the value of θ_0. In both cases, the predicted spatial variations of the critical heat flux are found to compare reasonably well with the experimental data.

Extension of the hydrodynamic CHF model to the case of pool boiling on a downward facing torridal surface has been made. A detailed description of the extended model is given in Appendix E.

5.9 References

1. Zuber, N., “Hydrodynamics aspects of boiling heat transfer”, AEC Rep., AECU-4439, June 1959.
2. Lienhard, J.H. and Eichorn, R., “On predicting boiling burnout for heaters cooled by liquid jets”, Int. J. Heat Mass Transfer, Vol. 22, pp. 774-776, 1979.
3. Lienhard, J.H. and Eichorn, R., “Peak boiling heat flux on cylinders in cross flow”, Int. J. Heat and Mass Transfer, Vol. 19, pp. 1135-1142, 1976.
4. Lienhard, J.H., Dhir, V.K. and Riherd, D.M., “Peak pool boiling heat-flux measurements on finite horizontal flat plates”, Trans. Am. Soc. Mech. Engrs., Series C, J. Heat Transfer, Vol 95, pp. 477-482, 1973.
5. Lienhard, J. H. and Dhir, V. K., "Hydrodynamic predictions of peak pool-boiling heat fluxes from finite bodies", Trans. Am. Soc. Mech Engrs., Series C, J. Heat Transfer, Vol. 95, pp. 152-158, 1973.
6. Lienhard, J. H. and Dhir, V. K., "Extended hydrodynamic theory of the peak and minimum pool boiling heat fluxes", NASA CR-2270, July, 1973.
7. Lienhard, J. H. and Hassan, Mojibul, "On predicting boiling burnout with the mechanical energy stability criterion", Trans. Am. Soc. Mech. Engrs., Series C., J. Heat Transfer, Vol. 101, pp.276-279, 1979.
8. Haramura, Y. and Katto, Y., "A new hydrodynamic model of critical heat flux, applicable widely to both pool and forced convection boiling on submerged bodies in saturated liquids", Int. J. Heat Mass Transfer, Vol. 26, No. 3, pp. 389-399, 1983
9. Carey, V. P., Liquid-Vapor Phase-Change Phenomenon, Hemisphere Publishing Corporation, 1992.
10. Cheung, F.B. and Haddad, K.H., “Observation of the Dynamic Behavior of the Two-Phase Boundary Layers in the SBLB Experiments,” Proceedings of the 22nd Water Reactor Safety Meeting, Washington, D.C., Vol. 2, 87-112, 1994
11. Cheung, F.B. and Haddad, K.H., “Steady-State Observations of Critical Heat Flux Phenomenon on a Downward Facing Hemispherical Surface,” Proceedings of the 23rd Water Reactor Safety Meeting, Washington, D.C., Vol. 2, 277-302, 1995.
12. Theofaneous, T. G., Syri, S, Salmassi, T., Kymäläinen, O. and Tuomisto,H., "Critical heat flux through curved, downward facing, thick walls", Nuclear Engineering and Design, Vol. 151, pp.247-258, 1994.
13. Theofaneous, T. G. and Syri, S., "The coolability limit of a lower reactor pressure vessel head", Proc. NURETH-7, 1995.
14. Cheung, F.B. and Epstein, M., “Two-phase gas bubble-liquid boundary layer flow along vertical and inclined surfaces”, Nuclear

Engineering and Design, Vol. 99, pp. 93-100, 1987.

15. Wallis, G.B., One-Dimensional Two-Phase Flow, McGraw-Hill, New York, 1969.

16. F.B. Cheung and K.H. Haddad, "A Hydrodynamic Critical Heat Flux Model for Saturated Pool Boiling on a Downward Facing Curved Heating Surface," Int. J. Heat Mass Transfer, Vol. 40, No. 6, 1291-1302, 1997.

17. El-Genk, M.S. and Glebov, A.G., "Transient Pool Boiling from Downward Facing Curved Surfaces," Int. J. Heat and Mass Transfer, Vol. 38, 2209-2224, 1995.

18. Ricou, F.P. and Spalding, D.B., "Measurements of entrainment of axisymmetric jets", J. Fluid Mechanics, Vol. 11, pp. 21-32, 1961.

19. Morton, B.R., "Modeling Fire Plumes," Tenth Symp. On Combustion, The Combustion Institute, Pittsburgh, PA, 1965.

6. DEVELOPMENT OF THE SCALING LAW

6.1 Saturated Boiling Conditions

A scaling law for estimating the local critical heat flux on the outer surface of a heated hemispherical vessel that is fully submerged in water is developed in this section based upon the CHF model described in Section 5. The special case of saturated boiling is first investigated, followed by the case of subcooled boiling.

From equations (5.21) to (5.25), it can be seen that for saturated boiling the dimensionless local critical heat flux Q_{CHF}, is a function of the vapor size-to-vessel radius ratio, L_b, and the angular position, θ, of the hemispherical vessel. For all vessel sizes, the spatial variations of Q_{CHF} with θ are quite similar, as shown in Figure 74. Morever the local value of Q_{CHF} tends to approach asymptotically to a constant value as L_b approaches zero. This functional behavior of Q_{CHF} indicates that

$$Q_{\mathrm{CHF}} = F_{L_b}(L_b,\theta)\,F_\theta(\theta) \qquad (6.1)$$

and

$$\operatorname*{Limit}_{L_b \to 0}\; F_{L_b}(L_b,\theta) = 1 \qquad (6.2)$$

where $F_{L_b}(L_b,\theta)$ is a size correction factor and $F_\theta(\theta)$ is a spatial variation function. In view of the fact that the local buoyancy force that is parallel to the curved heating surface is proportional to $g\sin\theta$, the effect of vessel size is expected to vary with the local angular position, θ. Thus the size correction factor, F_{L_b}, is dependent upon both L_b and $\sin\theta$. Using a power-law expression, the following functional form of F_{L_b} that satisfies equation (6.2) is proposed:

$$F_{L_b}(L_b,\theta) = \exp\left[A\,L_b^{\,m}(\sin\theta)^n\right] \qquad (6.3)$$

where the coefficient A and the indices m and n are positive constants. It follows from equations (6.1) and (6.3) that

$$Q_{\mathrm{CHF}}\left\{\exp\left[A\,L_b^{\,m}(\sin\theta)^n\right]\right\}^{-1} = F_\theta(\theta) \qquad (6.4)$$

If A, m and n are truly universal constants, then a plot of $Q_{\mathrm{CHF}} / F_{L_b}$ versus θ is a single curve for all values of L_b. From the four sets of numerical data of Q_{CHF} shown in Figure 74, the values of A, m and n that best merge all four curves into one are found to be $A = 0.8$, $m = 1/2$, and $n = 1/3$. Equation (6.3) thus becomes

$$F_{L_b}(L_b,\theta) = \exp\left[0.8\,L_b^{\,1/2}(\sin\theta)^{1/3}\right] \qquad (6.5)$$

Results are shown in Figure 75. Even though L_b varies by four orders of magnitude, the spatial variation function varies less than ± 5%. A least-square fit gives

$$F_\theta(\theta) = 0.0473\,(1 + 1.78\,\theta - 0.51\,\theta^2) \qquad (6.6)$$

where θ is in radians.

From equations (5.30) and (6.1) the local critical heat flux, $(q''_{\mathrm{CHF}})_{\mathrm{SAT}}$, for saturated boiling can be written as the product of three functional groups. This is

$$(q''_{\mathrm{CHF}})_{\mathrm{SAT}} = F_p(P)\;F_{Lb}(L_b,\theta)\;F_\theta(\theta) \qquad (6.7)$$

where $F_p(P)$ is the property or pressure function given by

$$F_p(P) = \rho_g\,h_{fg}\left[\frac{\sigma g(\rho_\ell - \rho_g)}{\rho_g^{\,2}}\right]^{1/4} \left(1 + \frac{\rho_g}{\rho_\ell}\right)^{1/3} \qquad (6.8)$$

The value of F_p depends on the fluid properties.

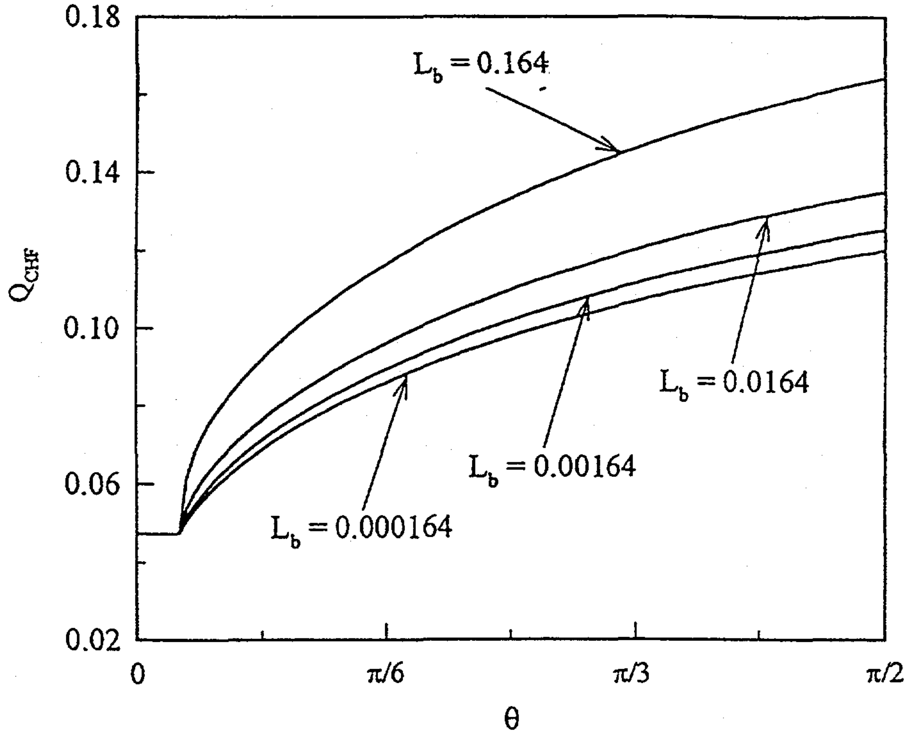

Figure 74. Spatial Variation of the Critical Heat Flux on the Outer Surface of a Hemispherical Vessel.

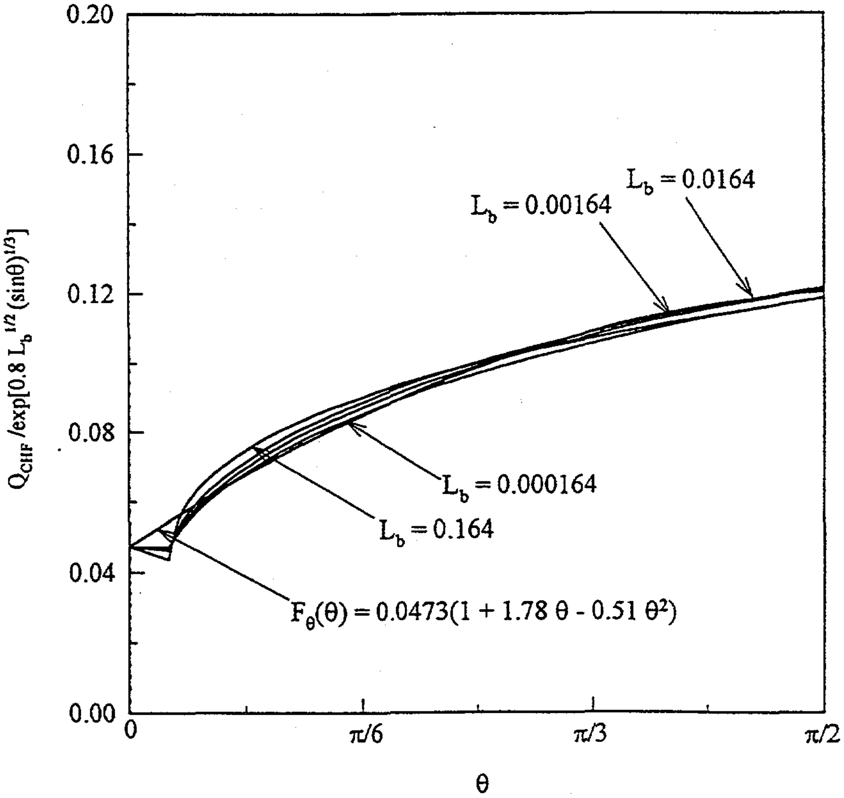

Figure 75. Scaling of the Vessel Size Effect on the CHF Limit.

For a given fluid, F_p would vary with the system pressure. From equations (6.5) to (6.8), it can be seen that the local critical heat flux is a strong function of the vessel size for L_b on the order of 0.1 or higher. For vessels much larger than the characteristic vapor mass (i.e., for L_b on the order of 0.01 or smaller), the local critical heat flux is a weak function of the vessel size. To demonstrate this point, the scaling law given by equation (6.7) is compared with the SBLB data and the ULPU data by Refs. 1 and 2 in Figure 76. The heating surface employed in the work of Refs. 1 and 2 was an order of magnitude larger than the heating surface employed in the SBLB experiments. However, all CHF data shown in the figure compare reasonably well with the scaling law. The relatively large differences between the ULPU natural convection boiling data and the spatial variation function is believed to be due to the effect of subcooling associated with the liquid head that was present in the experiments performed by Refs. 1 and 2. This point will be further discussed in the next section.

6.2 Subcooled Boiling Conditions

It is widely recognized that subcooling enhances the critical heat flux limit (Ref. 3). For pool boiling, the effect of subcooling can be represented as a linear function of the Jakob number, Ja, as

$$q''_{\text{CHF}} = (1 + b\ Ja)\,(q''_{\text{CHF}})_{\text{SAT}} \qquad (6.9)$$

where q''_{CHF} is the local critical heat flux under subcooled boiling conditions and b is a proportionality constant. The Jakob number is simply the sensible-to-latent heat ratio defined by

$$\text{Ja} = C_p \Delta T_{\text{sub}} / h_{fg} \qquad (6.10)$$

where C_p is the specific heat of the liquid and ΔT_{sub} the degree of subcooling. From the SBLB data, the constant b is found to be 19.25. Results are shown in Figure 77, where except one data point at $\text{Ja} = 1.87 \times 10^{-2}$, all the saturated and subcooled data obtained at different spatial locations can be correlated nicely by equation (6.9) with $b = 19.25$. For given fluid and vessel size, the CHF data when accounted for the subcooling effect, is practically a function of θ only, as demonstrated in the figure.

From equations (6.5) to (6.9), a generalized scaling law can be obtained. The local critical heat flux on the outer surface of a hemispherical vessel can be expressed by the product of four functional groups. This is

$$q''_{\text{CHF}} = F_p(P)\, F_{L_b}(L_b, \theta)\, F_{\text{Ja}}(\text{Ja})\, F_\theta(\theta) \qquad (6.11)$$

where F_p, F_{L_b} and F_θ are given respectively by equations (6.8), (6.5), and (6.6), and F_{Ja} is the correction factor given by

$$F_{\text{Ja}}(\text{Ja}) = 1 + 19.25\ \text{Ja} \qquad (6.12)$$

The generalized scaling law, which accounts for the effects of the size of the vessel, the level of vessel subcooling, the intrinsic properties of the fluid, and the spatial variation of the local critical heat flux, is applicable to both saturated and subcooled boiling conditions.

Equation (6.11) is compared with the SBLB data and the ULPU data in Figure 78. In preparing this figure, the ULPU natural convection data have been corrected for the effect of liquid head by use of the property variation function, F_p, and the correction factor for subcooling, F_{Ja}. By accounting for the liquid head that was present in the experiments performed by Refs. 1 and 2, the relatively large difference between the ULPU natural convection boiling data and the spatial variation function shown in Figure 76 disappear. The generalized scaling law given by equation (6.11) tends to merge, within the experimental uncertainties, all the available local CHF data obtained for various vessel sizes under both saturated and subcooled boiling conditions into a single curve.

6.3 Applications to Commercial-Size Vessels

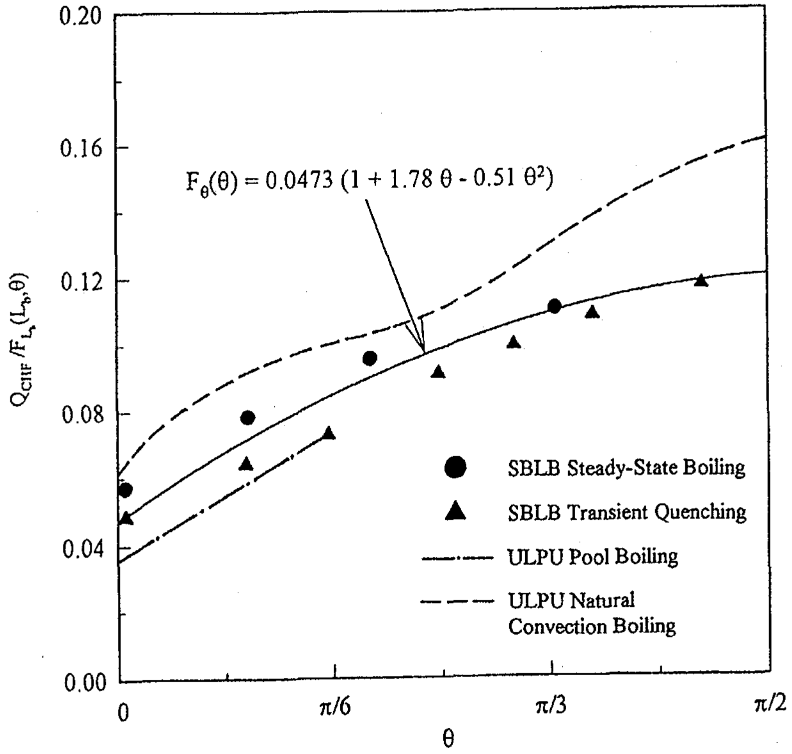

Figure 76. Comparison of the Scaling Law for Saturated Boiling with CHF Data.

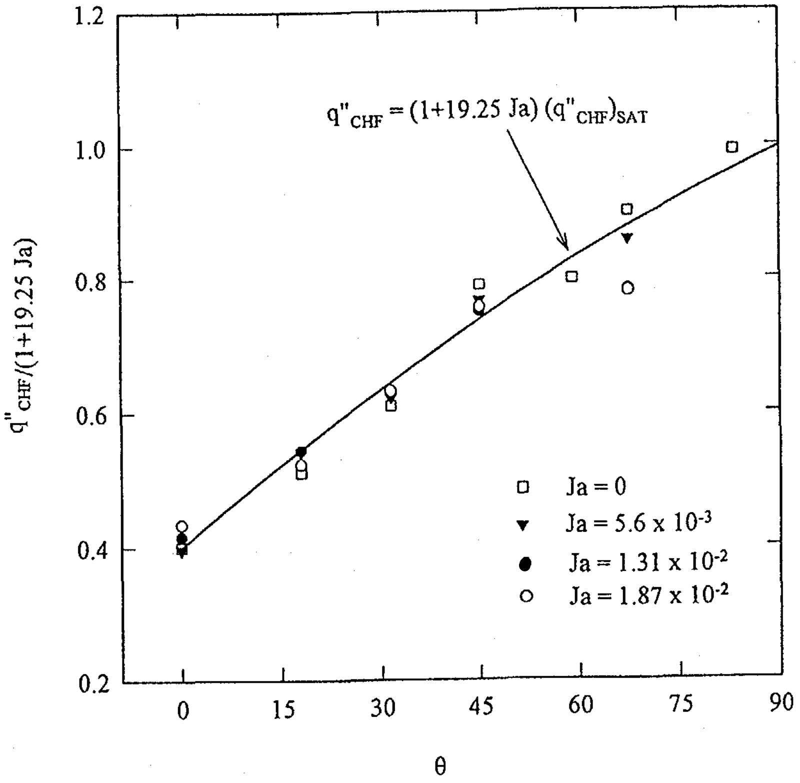

Figure 77. Experimental Data Showing the Effect of Subcooling on the Local Critical Heat Flux.

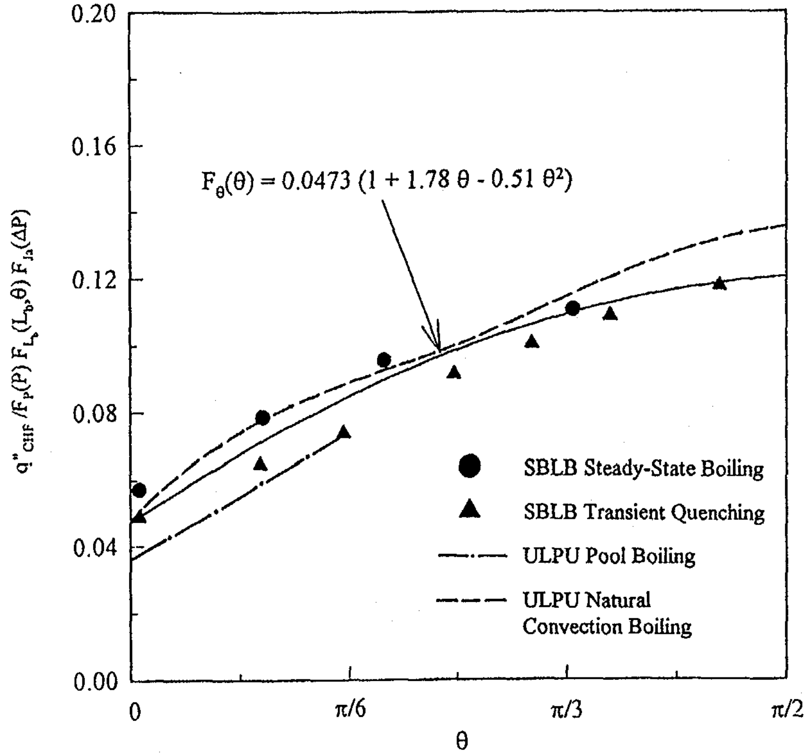

Figure 78. Comparison of the Scaling Law for Subcooled Boiling with CHF Data.

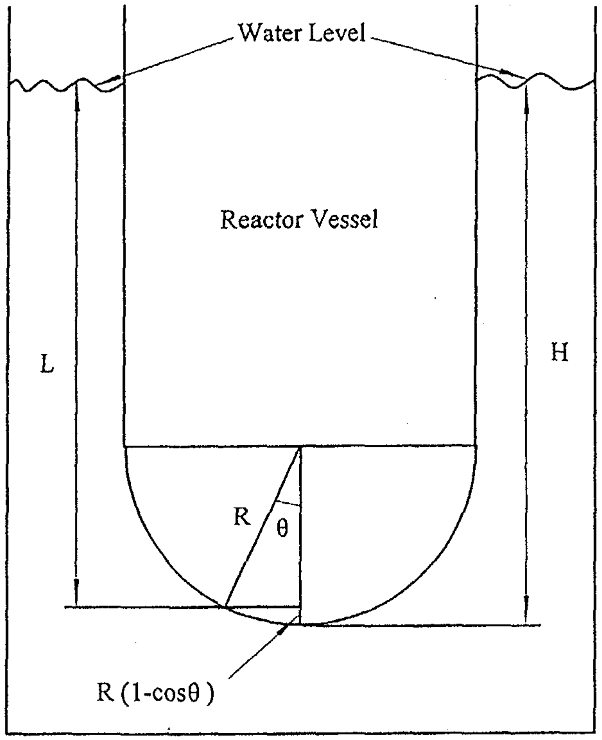

Figure 79. Schematic of a Hemispherical Reactor Vessel in a Flooded Cavity.

Figure 79 shows schematically a large commercial-size hemispherical vessel submerged in a flooded cavity. The water level, H, is measured from the external bottom center of the vessel. The local liquid head, L, at a given angular position on the hemispherical heating surface is given by

$$L = H - R(1-\cos\theta)$$
$$\text{or}\quad L = H\left[1-\frac{R}{H}(1-\cos\theta)\right] \tag{6.13}$$

where R is the radius of the vessel. It follows that the difference between the local water pressure at θ and the system pressure above the water surface is

$$\Delta P = \rho_\ell gH\left[1-\frac{R}{H}(1-\cos\theta)\right] \tag{6.14}$$
$$\text{for}\quad 0 \le \theta \le \pi/2$$

Because of this pressure difference, the water on the hemispherical heating surface is always subcooled. This is true even though the water temperature is at the saturation temperature corresponding to the system pressure at the free surface. In addition to the subcooling, the pressure difference also affect the local fluid properties. Thus the values of F_p and F_{Ja} are dependent on the local liquid level, L, which in turn is a function of the liquid head, H, the length ratio, H/R, and the angular position, θ, as given by equation (6.13).

To provide an example for application of the present scaling law, the water temperature is assumed to be at the saturation temperature corresponding to the system pressure above the water surface. Two saturation temperatures are considered. These are 373K and 393K, corresponding approximately to a system pressure of one and two atmospheres, respectively. At the saturation temperature of T_{sat} = 373K, the degree of subcooling due to the local liquid head can be determined from equation (6.14) along with the property of saturated water. This is

$$\Delta T_{sub} = 2.54H\left[1-\frac{R}{H}(1-\cos\theta)\right]\left\{1-0.0192H\left[1-\frac{R}{H}(1-\cos\theta)\right]\right\} \tag{6.15}$$

where H is in meter. From equations (6.10) and (6.12), the correction factor for subcooling is given by

$$F_{Ja} = 1+0.0914H\left[1-\frac{R}{H}(1-\cos\theta)\right]\left\{1-0.0192H\left[1-\frac{R}{H}(1-\cos\theta)\right]\right\} \tag{6.16}$$

Similarly, at the saturation temperature of T_{sat} = 393K, the correction factor for subcooling is given by

$$F_{Ja} = 1+0.056H\left[1-\frac{R}{H}(1-\cos\theta)\right]\left\{1-0.0139H\left[1-\frac{R}{H}(1-\cos\theta)\right]\right\} \tag{6.17}$$

Calculations of the local critical heat fluxes have been made for vessels having diameters of 3m, 4m, and 6m with water levels varying from $H = R$ to $H = 3R$. Results are shown in Figures 80 to 83. The baseline case under consideration is shown in Figure 80 where R = 2m and T_{sat} = 373K. The dashed line corresponds to the value of q''_{CHF} given by equation (6.7), which is located below all the solid lines. Evidently, the presence of subcooling due to the liquid head always results in a higher local critical heat flux. The largest increase in q''_{CHF} occurs at the upper edge of the vessel. For a given θ, the local CHF limit increases appreciably as the liquid head is increased.

The calculated critical heat flux variations for the cases of R = 1.5m and R = 3m are shown in Figures 81 and 82 respectively, with T_{sat} being fixed at 373. Again, the dashed lines represent the saturated values given by equation (6.7), which are always located below the solid lines

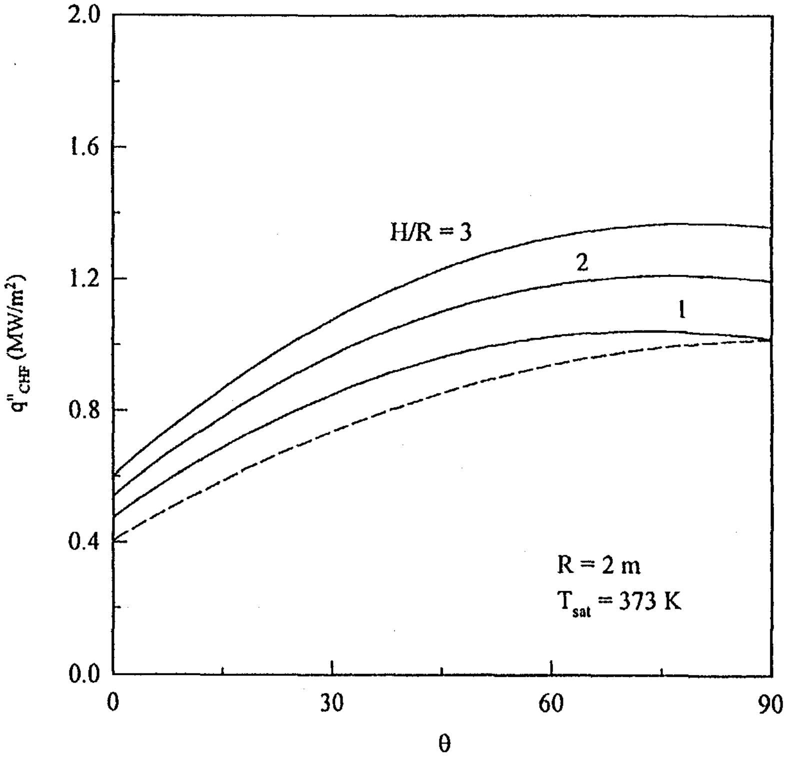

Figure 80. Application of the CHF Scaling Law: Baseline Case (R = 2m, P ~ 1atm).

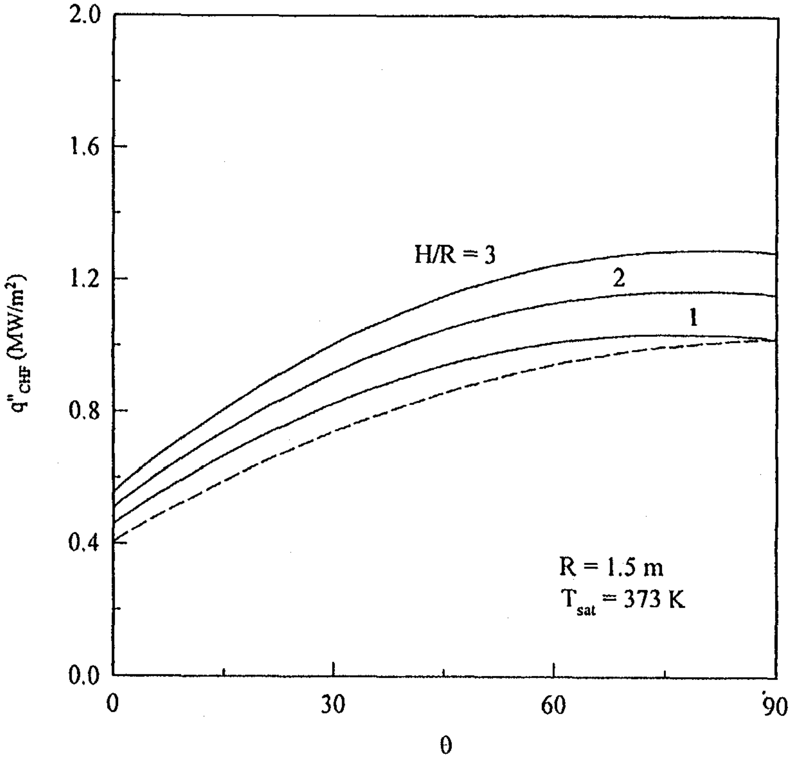

Figure 81. Application of the CHF Scaling Law: Smaller vessel (R = 1.5m, P ~ 1atm).

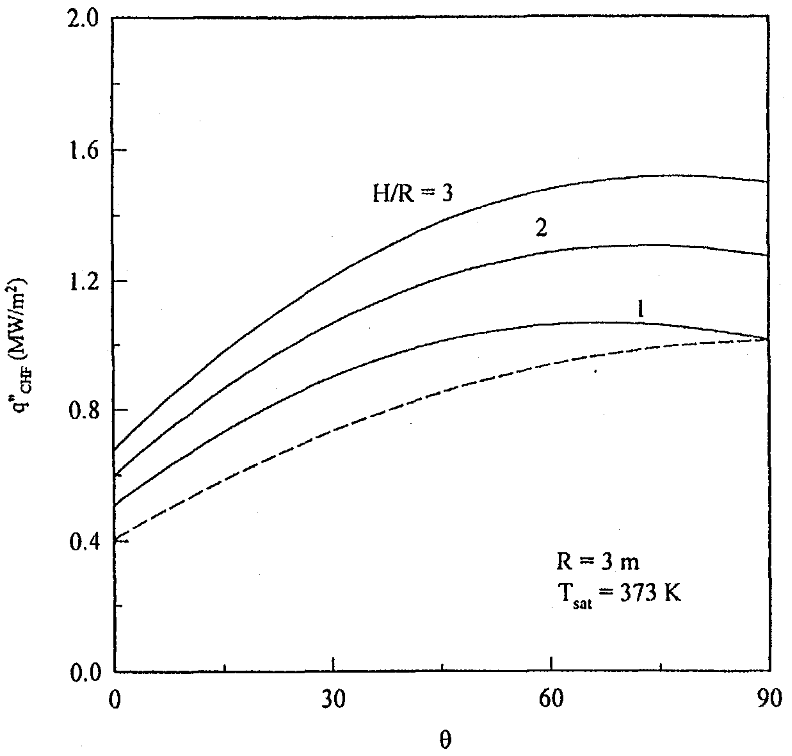

Figure 82. Application of the CHF Scaling Law: Larger Vessel (R = 3m, P ~1 atm).

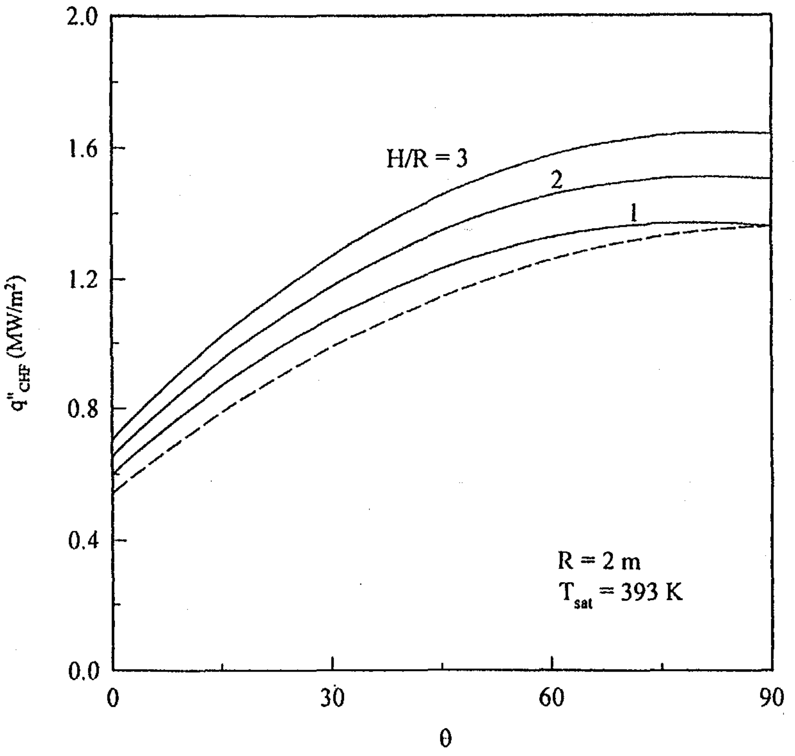

Figure 83. Application of the CHF Scaling Law: Higher Pressure (R = 2m, P ~ 2atm).

for subcooled boiling. Comparing to the baseline case (Figure 80), the positions of the three solid lines shown in Figure 81 are relatively lower whereas those in Figure 82 are relatively higher. These differences in the position are due to the subcooling effect associated with the liquid head. Whereas the total liquid head varies from 1.5 to 4.5m in Figure 81, it varies from 3 to 9m in Figure 82. As a result, much higher values of q''_{CHF} are obtained for the case shown in Figure 82.

The effect of system pressure can be seen by comparing the critical heat flux variations shown in Figure 83 with those shown in Figure 80 for the baseline case. In both figures, the vessel size and the water levels are the same. The only difference is the system pressure or, equivalently, the saturation temperature at the free surface of the flooded cavity. For all values of θ and H/R, a high local critical heat flux is obtained as the system pressure is increased, i.e., as the saturation temperature is increased from 373K to 393K. Evidently, the local critical heat flux can vary considerably with the liquid head and the system pressure. Thus both the system pressure and the local liquid head need to be taken into account in estimating the spatial variation of the CHF limit.

6.4 References

1. Theofaneous, T. G., Syri, S, Salmassi, T., Kymäläinen, O. and Tuomisto,H., "Critical heat flux through curved, downward facing, thick walls", Nuclear Engineering and Design, Vol. 151, pp.247-258, 1994.

2. Theofaneous, T. G. and Syri, S., "The coolability limit of a lower reactor pressure vessel head", Proc. NURETH-7, 1995.

3. Carey, V. P., Liquid-Vapor Phase-Change Phenomenon, Hemisphere Publishing Corporation, 1992.

7 CONCLUSIONS

7.1 Major Conclusions

Based on the results of the present work, the following conclusions can be drawn:

1) When a heated vessel is quenched in water, transition from film to nucleate boiling does not take place simultaneously throughout the entire external surface of the vessel. Rather, it occurs at the upper positions of the vessel first and then propagates downward toward the bottom center. The resulting two-phase boundary layer configuration exhibits significant spatial variations during quenching. The rate of heat removal is highly non-uniform on the vessel outer surface and depends strongly on subcooling.

2) For steady-state boiling, large elongated vapor bubbles or slugs tend to form at the bottom center whereas those in the upper positions of the vessel are considerably smaller. In the high heat flux regime, boiling around the bottom center region of the vessel is cyclic in nature, with violent ejection of large vapor masses or slugs from underneath the heating surface. This phenomenon is similar to that observed by Ref. 1 for a full scale simulation of a reactor lower head. The vessel size does not seem to affect the bubble dynamics on a downward facing curved heating surface. Subcooling tends to increase the bubble frequency while decreasing the bubble size.

3) For both saturated and subcooled boiling, the two-phase boundary layer flow is three-dimensional although it is axisymmetrical. Strong upstream influences are observed as a result of the activities of large elongated bubbles in the bottom center region of the vessel. These 3-D flow configurations as well as the divergence effect of the flow in the external bottom region of the vessel cannot be simulated by two-dimensional experiments or by downward facing inclined flat plates.

4) The nucleate boiling heat fluxes measured under steady-state conditions are consistently higher than those determined from transient quenching data. However, the local CHF values deduced from the transient quenching data appear to be very close to those obtained in the steady-state boiling experiments. This is found to be the case under both saturated and subcooled boiling conditions throughout the curved heating surface.

5) The local boiling curves and the critical heat flux vary significantly along the vessel outer surface. In particular, the local critical heat flux increases by more than 100% from the bottom center to the upper edge of the vessel under both saturated and subcooled boiling conditions. It has the lowest value of 0.4 MW/m^2 at the bottom center of the vessel under saturated boiling conditions and a high value of about 1.4 MW/m^2 near the top with a subcooling of 10°C.

6) Significant quantitative as well as qualitative differences in the boiling curves, the CHF values, and the corresponding wall superheats exist between the present results and those for downward facing inclined flat plates (Refs. 2 and 3). On the other hand, the spatial variation of CHF observed the the SBLB experiments are quite similar to those observed in the ULPU experiments (Refs. 4 and 5), except near the bottom center where a considerable lower value of CHF (~0.28 MW/m^2) was reported in the ULPU experiments. This difference is probably due to the 3-D divergence effect which was absent in the 2-D ULPU experiments.

7) The surface configuration (hemispherical versus toroidal and 3-D versus 2-D test vessels) appears to have a significant effect on the local critical heat flux near the bottom center of the vessel. On the other hand, the difference between the small-scale

and full-scale CHF data are relatively small when compared at the same dimensionless downstream locations of the vessel. The angular position of the curved heating surface and the degree of subcooling of water have dominant effects on the local critical heat flux. They totally dwarf the effect of the physical dimensions of the test vessel.

8) For nucleate boiling on a downward facing surface, there is a micro-layer underneath each vapor slug growing on the surface. This is in agreement with the studies of Refs. 6 and 7. The micro-layer consists of a thin liquid film with numerous micro-vapor jets penetrating through it. In the entire high-heat-flux region including the CHF point, the micro-jets are subject to Helmholtz instability. Local dryout of the surface occurs when the local rate of liquid supply to the micro-layer becomes smaller than the rate of depletion of the liquid film by boiling. This critical condition determines the maximum wall heat flux corresponding to the local CHF limit.

9) Owing to the formation of an external buoyancy-driven two-phase liquid/vapor boundary layer flow on the heating surface, the local rate of liquid supply increases significantly from the bottom center to the upper edge of the vessel, thus greatly enhancing the local CHF limit. This provides a physical explanation for the large spatial variation of the critical heat flux observed in the SBLB experiments as well as in the ULPU experiments. Evidently, for downward facing surfaces, the critical heat flux cannot be assumed uniform over the entire heating surface.

10) For hemispherical vessels with diameters considerably larger than the characteristic bubble size (i.e., for small values of L_b), both the local liquid supply rate and the local boundary layer thickness are approximately proportional to the square root of the vessel diameter. Since the critical heat flux depends only on the ratio of the liquid supply rate to the boundary layer thickness, the size effect tends to cancel out altogether. As a result, the critical heat flux for large vessels is almost independent of the physical size of the vessel (see Ref. 8).

11) Based upon the scaling law developed in this work, it is possible to merge, within the experimental uncertainties, all the available local CHF data obtained for various vessel sizes under both saturated and subcooled boiling conditions into a single curve. It follows that for large vessels, the only effect of the vessel size is due to the local subcooling effect. When the effect of subcooling associated with the local liquid head is accounted for separately, the local CHF limit depends primarily on the intrinsic properties of the fluid and the angular position of the vessel under consideration.

12) The present scaling law, which accounts for the effects of vessel size, the level of liquid subcooling, the intrinsic properties of the fluid, and the spatial variation of the local critical heat flux, can be used to predict the local CHF limits on large commercial-size vessels.

7.2 References

1. Chu, T.Y., Bentz, J.H. and Simpson, R.B., "Observation of the Boiling Process from a Large Downward-Facing Torispherical Surface", 30th National Heat Transfer Conference, 1995.

2. El-Genk, M.S. and Glebov, A.G., "Transient Pool Boiling from Downward Facing Curved Surfaces," Int. J. Heat and Mass Transfer, Vol. 38, 2209-2224, 1995.

3. Guo, Z. and El-Genk, M. S., "An experimental study of the effect of surface orientation on boiling heat transfer during quenching", ASME Winter Annual Meeting, Paper No. 91-WA-HT-1, Atlanta, GA, 1991.

4. Theofaneous, T. G., Syri, S, Salmassi, T., Kymäläinen, O. and Tuomisto,H., "Critical heat flux through curved, downward facing, thick walls", Nuclear Engineering and Design, Vol. 151, pp.247-258, 1994.

5. Theofaneous, T. G. and Syri, S., "The coolability limit of a lower reactor pressure vessel head", Proc. NURETH-7, 1995.

6. Gaertner, R.F., "Photographic study of nucleate pool boiling on a horizontal surface", Trans. Am. Soc. Mech. Engrs., Series C, J. Heat Transfer, Vol. 87, pp. 17-29, 1965.

7. Katto, Y., "Critical Heat Flux," Advances in Heat Transfer, Vol. 17, pp. 1-65, 1985.

8. F.B. Cheung and K.H. Haddad, "A Hydrodynamic Critical Heat Flux Model for Saturated Pool Boiling on a Downward Facing Curved Heating Surface," Int. J. Heat Mass Transfer, Vol. 40, No. 6, 1291-1302, 1997.

Appendix A
Development of an Inverse Heat Conduction Code for the Segmented Hemispherical Test Vessel

The grid structures and thermocouple locations of each segment are shown in Figures A.1 to A.3. The grid structures are determined by equally dividing the segments in the angular direction and radial direction. Specifically the first and second segments are divided equally into five shells in the radial direction, four regular slices in the angular direction, and four small slices in the bottom of the segment. The third segment is divided into four slices with same angle except for the first slice which is larger than the others. All the shells in the radial direction have the same thickness. The fourth segment is divided into twelve shells having the same thickness except for the forth one, six slices having the same angle in the angular direction, and two different size slices.

The problem formulation starts from the differential equations for symmetrical heat conduction problem in a hemispherical vessel. This is followed by a finite difference analysis of each segment to get a set of finite difference equations for the interior, boundary, and corner nodes. There are five thermocouple locations for each segment except for the bottom segment where eight thermocouple locations are present. One of these thermocouples is used to check the symmetrical conditions around the hemisphere. In order to reduce the truncation error and account for the uncertainty involved in the corner nodes, the exterior surface is divided by 4.5 intervals, with several finer grids (i.e., smaller $\Delta\theta$) being implemented in the lower part of segment as shown in Figure A.1. The boiling heat flux is then determined by integrating the local values which are at the same locations as the five exterior nodes after the set of finite difference equations are solved numerically. The major challenge in deducing the finite difference equations is to formulate the mathematical expressions for the nodes located along the adiabatic boundary. Because of the irregularity of the shape of each segment, the adiabatic boundary condition applied for constant θ has to be modified. The modified shape-fitted boundary condition is achieved by adjusting the coordinates of cylindrical system into another coordinate system in which unit vector is pointing outward and perpendicular to its boundary.

The governing equation for steady-state two-dimensional heat conduction in a hemispherical system is :

$$\frac{\partial}{\partial r}\left(r^2 k\frac{\partial T}{\partial r}\right)+\frac{1}{\sin\theta}\frac{\partial}{\partial\theta}\left(k\sin\theta\frac{\partial T}{\partial\theta}\right)=0 \qquad \text{(A-1)}$$

If k is treated as a constant, then the above equation can be reduced to:

$$\frac{\partial}{\partial r}\left(r^2\frac{\partial T}{\partial r}\right)+\frac{1}{\sin}\frac{\partial}{\partial\theta}\left(\sin\theta\frac{\partial T}{\partial\theta}\right)=0 \qquad \text{(A-2)}$$

Expanding the above equation, the following equation can be obtained:

$$2r\frac{\partial T}{\partial r}+r^2\frac{\partial^2 T}{\partial r^2}+\frac{\partial^2 T}{\partial\theta^2}+\frac{1}{\tan}\frac{\partial T}{\partial\theta}=0 \qquad \text{(A-3)}$$

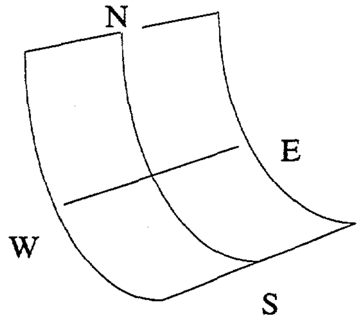

Using Taylor's series expansion, the temperatures at various nodal locations can be expressed by:

$$T_N = T_O + \Delta\theta\frac{\partial T}{\partial\theta}|_O + \frac{\Delta\theta^2}{2!}\frac{\partial^2 T}{\partial\theta^2}|_O + \frac{\Delta\theta^3}{3!}\frac{\partial^3 T}{\partial\theta^3} + \bullet\bullet\bullet \qquad \text{(A-4)}$$

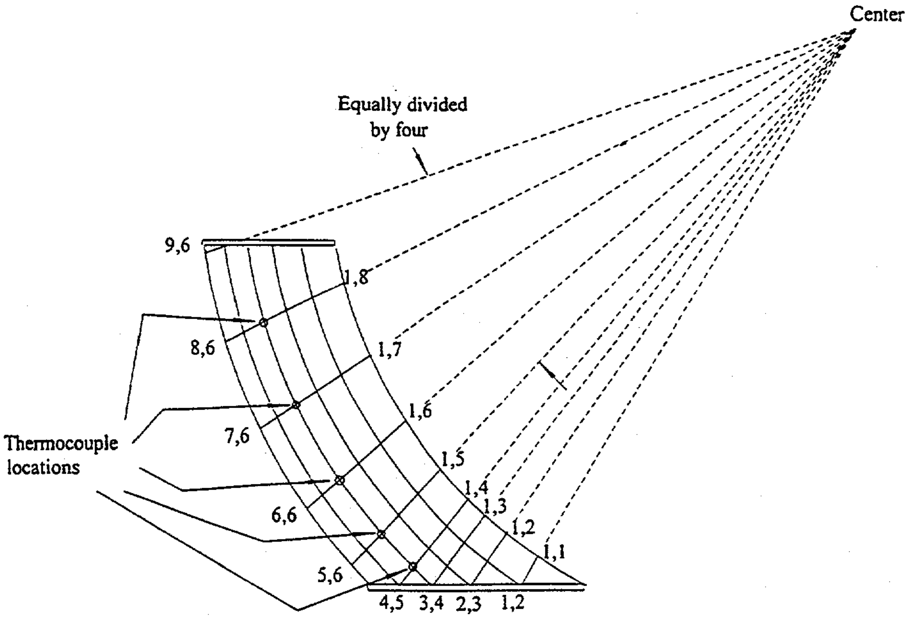

Figure A.1. Grid Structure for the First and Second Segments.

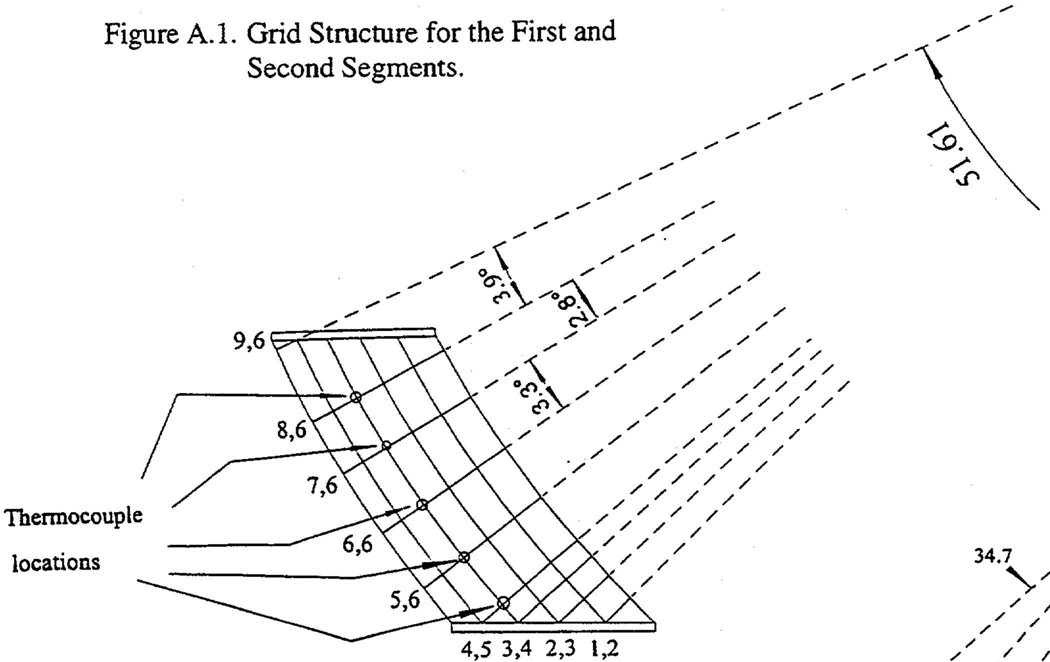

Figure A.2. Grid Structure for the Third Segment.

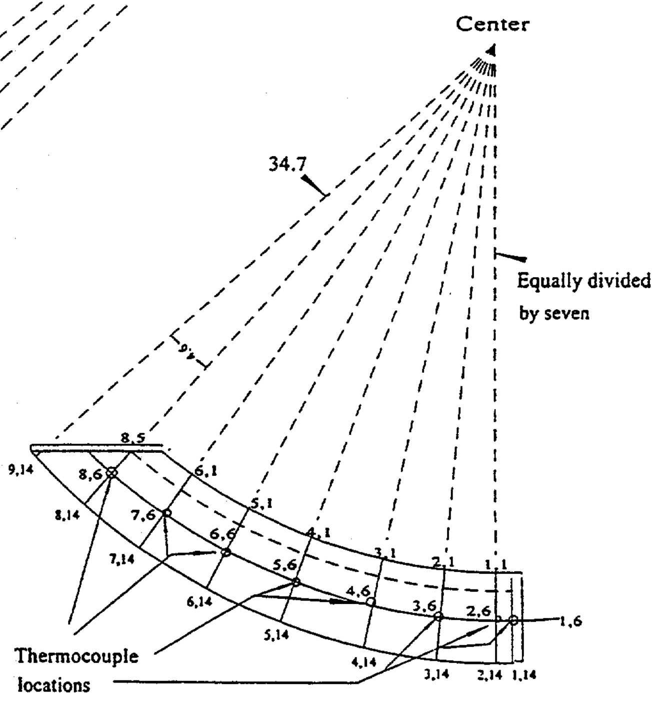

Figure A.3. Grid Structure for the Fourth Segment.

$$T_S = T_O - \Delta\theta \frac{\partial T}{\partial \theta}|_O + \frac{\Delta\theta^2}{2!}\frac{\partial^2 T}{\partial \theta^2}|_O - \frac{\Delta\theta^3}{3!}\frac{\partial^3 T}{\partial \theta^3}|_O + \bullet\bullet\bullet \qquad \text{(A-5)}$$

$$T_W = T_0 + \Delta r \frac{\partial T}{\partial r}|_O + \frac{\Delta r^2}{2!}\frac{\partial^2 T}{\partial r^2}|_O + \frac{\Delta r^3}{3!}\frac{\partial^3 T}{\partial r^3} + \bullet\bullet\bullet \qquad \text{(A-6)}$$

$$T_E = T_O - \Delta r \frac{\partial T}{\partial r}|_O + \frac{\Delta r^2}{2!}\frac{\partial^2 T}{\partial r^2} - \frac{\Delta r^3}{3!}\frac{\partial^3 T}{\partial r^3}|_O + \bullet\bullet\bullet \qquad \text{(A-7)}$$

Subtracting equation (A-5) from equation (A-4), the following equation can be obtained:

$$\frac{\partial T}{\partial \theta}|_O = \frac{T_N - T_S}{2\Delta\theta} + O(\Delta\theta^2) \qquad \text{(A-8)}$$

Adding equation (A-5) to equation (A-4), the following equation can be derived:

$$\frac{\partial^2 T}{\partial \theta^2}|_O = \frac{T_N + T_S - 2T_O}{\Delta\theta} + O(\Delta\theta) \qquad \text{(A-9)}$$

Similarly, subtracting equation (A-7) from equation (A-6), the following equation can be derived:

$$\frac{\partial T}{\partial r}|_O = \frac{T_W - T_E}{2\Delta r} + O(\Delta r^2) \qquad \text{(A-10)}$$

Again, adding equation (A-7) to equation (A-6), the following equation can be obtained:

$$\frac{\partial^2 T}{\partial r^2}|_2 = \frac{T_W + T_E - 2T_O}{\Delta r^2} + O(\Delta r) \qquad \text{(A-11)}$$

Substituting the above equations into equation (A-3), the following finite difference equation is obtained for the interior nodes :

$$2r_O(\frac{T_W - T_E}{2\Delta r}) + r^2 \frac{(T_W + T_E - 2T_O)}{\Delta r^2} + \frac{T_N + T_S - 2T_O}{\Delta\theta^2} + \cot\theta_O \frac{(T_N - T_S)}{2\Delta\theta} = 0 \qquad \text{(A-12)}$$

The above equation can be rearranged as:

$$-2(\frac{r_O{}^2}{\Delta r^2} + \frac{1}{\Delta\theta^2})T_O + (\frac{r_O}{\Delta r} + \frac{r_O{}^2}{\Delta r^2})T_W + (\frac{1}{\Delta\theta^2} + \frac{\cot\theta_O}{2\Delta\theta})T_N + (\frac{1}{\Delta\theta^2} - \frac{\cot\theta}{2\Delta\theta})T = 0 \qquad \text{(A-13)}$$

The truncation errors are:

$$2r_O O(\Delta r^2) + r_O O(\Delta r^2) + O(\Delta\theta^2) + \cot\theta_0 O(\Delta\theta^2) \qquad \text{(A-14)}$$

Boundary Conditions:

(i) Nodes for the Bottom Segment

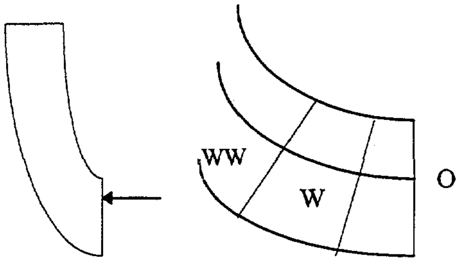

$$T_W = T_O + \Delta\theta \frac{\partial T}{\partial \theta}|_0 + \frac{\Delta\theta^2}{2!}\frac{\partial^2 T}{\partial \theta^2} + \frac{\Delta\theta^3}{3!}\frac{\partial^3 T}{\partial \theta^3} + \bullet\bullet\bullet \qquad \text{(A-15)}$$

$$T_{WW} = T_O + 2\Delta\theta \frac{\partial T}{\partial \theta}|_0 + \frac{(2\Delta\theta)^2}{2!}\frac{\partial^2 T}{\partial \theta^2} + \frac{(2\Delta\theta)^3}{3!}\frac{\partial^3 T}{\partial \theta^3} + \bullet\bullet\bullet \qquad \text{(A-16)}$$

Multiplying equation (A-15) by four and subtracting equation (A-16) from the resulting equation, the following equation is obtained:

$$\frac{\partial T}{\partial \theta} = \frac{4T_W - T_{WW} - 3T_O}{2\Delta\theta} = 0 \qquad \text{(A-17)}$$

or

$$4T_W - T_{WW} - 3T_O = 0 \qquad \text{(A-18)}$$

(ii) Boundary at the Inner Surface

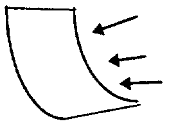

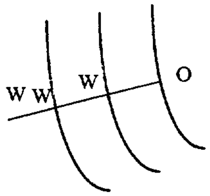

$$-k\frac{\partial T}{\partial r}|_O = Q_{in} \qquad \text{(A-19)}$$

$$T_W = T_0 + \Delta r \frac{\partial T}{\partial r}|_O + \frac{\Delta r^2}{2!}\frac{\partial^2 T}{\partial r^2} + \frac{\Delta r^3}{3!}\frac{\partial^3 T}{\partial r^3} + \bullet\bullet\bullet \qquad \text{(A-20)}$$

$$T_{WW} = T_O + 2\Delta r \frac{\partial T}{\partial r}|_O + \frac{(2\Delta r)^2}{2!}\frac{\partial^2 T}{\partial r^2} + \frac{(2\Delta r)^3}{3!}\frac{\partial^3 T}{\partial r^3} + \bullet\bullet\bullet \qquad \text{(A-21)}$$

Multiplying equation (A-20) by four and subtracting equation (A-16) from the resulting equation, the following equation is obtained:

$$\frac{\partial T}{\partial r} = \frac{4T_W - T_{WW} - 3T_O}{2\Delta r} + O(\Delta r^2) \qquad \text{(A-22)}$$

Substituting the above equation into equation (A-19), the following equation is obtained:

$$\frac{4T_W - T_{WW} - 3T_O}{2\Delta r} = -\frac{Q_{in}}{k} \qquad \text{(A-23)}$$

or

$$4T_W - T_{WW} - 3T_O = -\frac{2\Delta r Q_{in}}{k} \qquad \text{(A-24)}$$

(iii) Boundary At Outer Surface

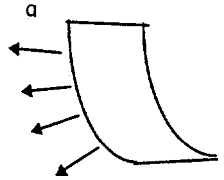

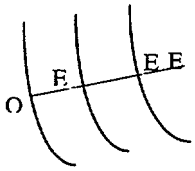

$$-k\frac{\partial T}{\partial r}|_O = h(T_{SURFCACE} - T_{SAT}) \qquad \text{(A-25)}$$

Applying the Taylor's series expansion, the temperatures at nodes E and EE can be expressed by:

$$T_E = T_O - \Delta r \frac{\partial T}{\partial r}|_O + \frac{\Delta r^2}{2!}\frac{\partial^2 T}{\partial r^2}|_O - \frac{\Delta r^3}{3!}\frac{\partial^3 T}{\partial r^3} + \bullet\bullet\bullet \qquad \text{(A-26)}$$

$$T_{EE} = T_0 - 2\Delta r \frac{\partial T}{\partial r} + 2\Delta r^2 \frac{\partial^2 T}{\partial r^2} - \frac{8\Delta r^3}{6}\frac{\partial^3 T}{\partial r^3} +.\bullet\bullet\bullet \qquad \text{(A-27)}$$

Multiplying equation (A-26) by four and subtracting equation (A-27) from the resulting equation, the following equation is obtained:

$$\frac{\partial T}{\partial r}|_O = \frac{T_{EE} - 4T_E + 3T_O}{2\Delta r} + O(\Delta r^2) \qquad \text{(A-28)}$$

Substituting the above equation into equation (A-25), the following finite difference equation is obtained:

$$\frac{T_{EE}-4T_E+3T_O}{2\Delta r}=\frac{h}{k}(T_{SAT}-T_O) \qquad \text{(A-29)}$$

or

$$\begin{aligned}&(\frac{3}{\Delta r}+\frac{h}{k})T_O+\frac{T_{EE}}{2\Delta r}\\&-\frac{2T_E}{\Delta r}-\frac{h}{k}T_{SAT}=0\end{aligned} \qquad \text{(A-30)}$$

(iv) Boundary nodes at the Adiabatic Shape-Fitted Surface:

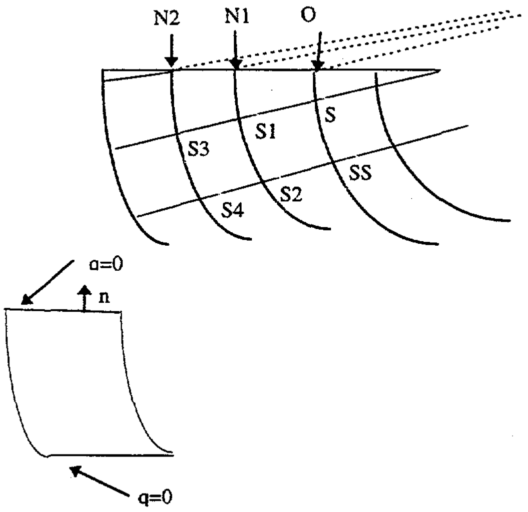

$$\frac{\partial T}{\partial n}=0 \qquad \text{(A-31)}$$

Modifying the boundary conditions for hemispherical coordinates, the following boundary condition can be established:

$$-\cos\theta\frac{\partial T}{\partial r}+\frac{\sin\theta}{r}\frac{\partial T}{\partial\theta}=0 \qquad \text{(A-32)}$$

Applying Taylor's series expansion, the following equation can be obtained:

$$\begin{aligned}&T_S=T_O-\alpha\Delta\theta\frac{\partial T}{\partial\theta}|_O\\&+\frac{(\alpha\Delta\theta)^2}{2!}\frac{\partial^2 T}{\partial\theta^2}|_O-\frac{(\alpha\Delta\theta)^3}{3!}\frac{\partial^3 T}{\partial\theta^3}|_O+\bullet\bullet\bullet\end{aligned} \qquad \text{(A-33)}$$

$$\begin{aligned}&T_{SS}=T_O-(\alpha+1)\Delta\theta\frac{\partial T}{\partial\theta}|_O\\&+\frac{(\alpha+1)^2\Delta\theta^2}{2!}\frac{\partial^2 T}{\partial\theta^2}\\&-\frac{(\alpha+1)^3\Delta\theta^3}{3!}\frac{\partial^3 T}{\partial\theta^3}+\bullet\bullet\bullet\end{aligned} \qquad \text{(A-34)}$$

Multiplying equation (A-33) by α^2 and equation (A-34) by $(\alpha+1)^2$ then taking the difference between the two resulting equations, the following expression for the temperature gradient is obtained:

$$\begin{aligned}&\frac{\partial T}{\partial\theta}|_O=\\&\frac{\alpha^2 T_{SS}-(\alpha+1)^2T_S+(2\alpha+1)T_O}{\alpha(\alpha+1)\Delta\theta}\\&+O(\Delta\theta)\end{aligned} \qquad \text{(A-35)}$$

Applying the Taylor's series expansion, the temperatures at nodes W and WW can be expressed by:

$$\begin{aligned}&T_W=T_0+\Delta r\frac{\partial T}{\partial r}|_O\\&+\frac{\Delta r^2}{2!}\frac{\partial^2 T}{\partial r^2}+\frac{\Delta r^3}{3!}\frac{\partial^3 T}{\partial r^3}+\bullet\bullet\bullet\end{aligned} \qquad \text{(A-36)}$$

$$\begin{aligned}&T_{WW}=T_O+2\Delta r\frac{\partial T}{\partial r}|_O\\&+\frac{(2\Delta r)^2}{2!}\frac{\partial^2 T}{\partial r^2}+\frac{(2\Delta r)^3}{3!}\frac{\partial^3 T}{\partial r^3}+\bullet\bullet\bullet\end{aligned} \qquad \text{(A-37)}$$

Multiplying equation (A-36) by four and subtracting equation (A-37) from the resulting equation, the following equation is obtained:

$$\frac{\partial T}{\partial r}=\frac{4T_W-T_{WW}-3T_O}{2\Delta r}+O(\Delta r^2) \qquad \text{(A-38)}$$

Substituting the above equation into equation (A-32), the following equation is obtained:

$$-\cos\theta_O \frac{(4T_W - T_{WW} - 3T_O)}{2\Delta r} + \frac{\sin\theta_O}{r_O} \frac{\left[\alpha^2 T_{SS} - (\alpha+1)T_S + (2\alpha+1)T_O\right]}{\alpha(\alpha+1)\Delta\theta} = 0 \qquad \text{(A-39)}$$

The above equation can be rearranged as

$$[\frac{(2\alpha+1)\sin\theta_O}{(\alpha+1)\alpha r_O\Delta\theta} + \frac{3\cos\theta_O}{2\Delta r}]T_O - \frac{2\cos\theta_O}{\Delta r}T_W + \frac{\cos\theta_O}{2\Delta r}T_{WW}$$

$$\frac{\alpha\sin\theta_O}{(\alpha+1)r\Delta\theta}T_{SS} - \frac{(\alpha+1)\sin\theta_O}{\alpha r_O\Delta\theta}T_S = 0 \qquad \text{(A-40)}$$

The following is to relate the nodes w, and ww to the other regular nodes by applying Taylor's series expansion:

$$T_W = T_{S1} + \Delta\theta_1 \frac{\partial T}{\partial\theta}|_{S1} + O(\Delta\theta^2) \qquad \text{(A-41)}$$

$$T_N = T_{S1} + \Delta\theta_1 \frac{\partial T}{\partial\theta}|_{S1} + \frac{\Delta\theta_1{}^2}{2!}\frac{\partial^2 T}{\partial\theta^2} + \bullet\bullet\bullet \qquad \text{(A-42)}$$

$$T_{S2} = T_{S1} - \Delta\theta \frac{\partial T}{\partial\theta}|_{S1} + \frac{\Delta\theta^2}{2!}\frac{\partial^2 T}{\partial\theta^2}|_{S1} + \bullet\bullet\bullet \qquad \text{(A-43)}$$

Set $\Delta\theta_1$ equal to $\alpha_1\Delta\theta$ and subtract equation (A-42) from equation (A-43) multiplied by $\alpha_1{}^2$. The result is:

$$\frac{\partial T}{\partial\theta}|_{S1} = \frac{\left[T_N - \alpha_1{}^2 T_{S2} - (1-\alpha_1{}^2)T_{S1}\right]}{(\alpha_1+1)\alpha_1\Delta\theta} + O(\Delta\theta^2) \qquad \text{(A-44)}$$

Substituting the above equation into equation (A-41), the following equation can be obtained:

$$T_W = T_{S1} + \Delta\theta_1 \frac{\left[T_N - \alpha_1 T_{S2} - (1-\alpha_1{}^2)T_{S1}\right]}{(\alpha_1+1)\alpha_1\Delta\theta} + O(\Delta\theta^2) \qquad \text{(A-45)}$$

The same procedure can be applied to the lower adiabatic shape-fitted boundary to yield:

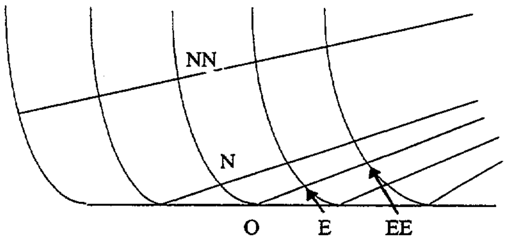

$$T_{NN} = T_O + (\alpha+1)\Delta\theta\frac{\partial T}{\partial\theta}|_O + \frac{(\alpha+1)^2\Delta\theta^2}{2!}\frac{\partial^2 T}{\partial\theta^2} + O(\Delta\theta^3) \qquad \text{(A-46)}$$

$$T_N = T_O + \alpha\Delta\theta\frac{\partial T}{\partial\theta}|_O + \frac{(\alpha\Delta\theta)^2}{2!}\frac{\partial^2 T}{\partial\theta^2}|_O + O(\Delta\theta^2) \qquad \text{(A-47)}$$

Multiplying equation (A-47) by $(\alpha+1)^2$ and equation (A-46) by α^2 then taking the difference between the two resulting equations, the following expression for the temperature gradient is obtained:

$$\frac{\partial T}{\partial \theta} = \frac{\left[(\alpha+1)^2 T_N - \alpha^2 T_{NN} - (2\alpha+1)T_O\right]}{(\alpha+1)\alpha\Delta\theta} \tag{A-48}$$

Applying Taylor's series expansion, the following equations can be obtained:

$$\begin{aligned} T_E &= T_O - \Delta r \frac{\partial T}{\partial r}|_O \\ &\quad + \frac{\Delta r^2}{2!}\frac{\partial^2 T}{\partial r^2}|_0 + O(\Delta r^3) \end{aligned} \tag{A-49}$$

$$\begin{aligned} T_{EE} &= T_O - 2\Delta r \frac{\partial T}{\partial r} \\ &\quad + \frac{4\Delta r^2}{2!}\frac{\partial^2 T}{\partial r^2} + O(\Delta r^2) \end{aligned} \tag{A-50}$$

Multiplying equation (A-50) by four and subtracting from equation (A-49) gives:

$$\frac{\partial T}{\partial r}|_O = \frac{T_{EE} - 4T_E + 3T_O}{2\Delta r} + O(\Delta r^2) \tag{A-51}$$

Substituting the above equation into equation (A-32), the following equation is obtained:

$$\begin{aligned} &-\frac{\cos\theta_O (T_{EE} - 4T_E + 3T_O)}{2\Delta r} + \frac{\sin\theta_O}{r_O} \\ &\frac{\left[(\alpha+1)^2 T_N - \alpha^2 T_{NN} - (2\alpha+1)T_O\right]}{(\alpha+1)\alpha\Delta\theta} = 0 \end{aligned} \tag{A-52}$$

$$\begin{aligned} &-\left(\frac{3\cos\theta_O}{2\Delta r} + \frac{(2\alpha+1)\sin\theta_O}{r_O(\alpha+1)\alpha\Delta\theta}\right)T_O \\ &+ \frac{2\cos\theta_O}{\Delta r}T_O - \frac{\cos\theta_O}{2\Delta r}T_{EE} \\ &+ \frac{(\alpha+1)\sin\theta_O}{\alpha r_O\Delta\theta}T_N - \frac{\alpha\sin\theta_O}{(\alpha+1)r_O\Delta\theta} \\ &T_{NN} = 0 \end{aligned} \tag{A-53}$$

At the adiabatic boundary surface, the nodes can be expressed by applying Taylor's series expansion:

$$\begin{aligned} T_S &= T_O - \Delta\theta \frac{\partial T}{\partial \theta}|_O \\ &\quad + \frac{\Delta\theta^2}{2!}\frac{\partial^2 T}{\partial \theta^2}|_O + O(\Delta\theta^3) \end{aligned} \tag{A-54}$$

or

$$\begin{aligned} T_{SS} &= T_O - 2\Delta\theta \frac{\partial T}{\partial \theta}|_O \\ &\quad + \frac{(2\Delta\theta)^2}{2!}\frac{\partial^2 T}{\partial \theta^2} + O(\Delta\theta^3) \end{aligned} \tag{A-55}$$

Multiplying equation (A-54) by four and subtracting equation (A-55) from the resulting equation, the following equation can be obtained:

$$\frac{\partial T}{\partial \theta}|_O = \frac{T_{SS} - 4T_S + 3T_O}{2\Delta\theta} + O(\Delta\theta^3) \tag{A-56}$$

Applying Taylor's series expansion to the nodes, the following equation can be obtained:

$$\begin{aligned} T_E &= T_O + \alpha\Delta r \frac{\partial T}{\partial r}|_O \\ &\quad + \frac{(\alpha\Delta r)^2}{2!}\frac{\partial^2 T}{\partial r^2}|_O + O(\Delta r^3) \end{aligned} \tag{A-57}$$

$$\begin{aligned} T_{EE} &= T_O + (\alpha+1)\Delta r \frac{\partial T}{\partial r}|_O \\ &\quad + \frac{(\alpha+1)^2 \Delta r^2}{2!}\frac{\partial^2 T}{\partial r^2} + O(\Delta r^3) \end{aligned} \tag{A-58}$$

Multiplying Equation (A-57) by $(\alpha+1)^2$ and equation (A-58) by α^2 then taking the difference between the two resulting equations, the following expression for the temperature gradient can be derived:

$$\begin{aligned} &\frac{\partial T}{\partial r}|_O = \\ &\frac{(\alpha+1)^2 T_E - \alpha^2 T_{EE} - (2\alpha+1)T_O}{(\alpha+1)\alpha\Delta r} \\ &+ O(\Delta r^2) \end{aligned} \tag{A-59}$$

Substituting the above equation into equation (A-32), the following equation is obtained:

$$-\cos\theta_O \frac{\left[(\alpha+1)^2 T_E - \alpha^2 T_{EE} - (2\alpha+1)T_O\right]}{(\alpha+1)\alpha\Delta r} + \frac{\sin\theta_O}{r_O}\frac{(T_{SS} - 4T_S + 3T_O)}{2\Delta\theta} = 0 \qquad \text{(A-60)}$$

The above equation can be rearranged to gives:

$$\left(\frac{(2\alpha+1)\cos\theta_O}{(\alpha+1)\alpha\Delta r} + \frac{3\sin\theta_o}{2r_O\Delta\theta}\right)T_O - \frac{(\alpha+1)\cos\theta_O}{\alpha\Delta r}T_E + \frac{\alpha\cos\theta_O}{(\alpha+1)\Delta r}T_{EE} + \frac{\sin\theta_O}{2r_O\Delta\theta}T_{SS} \qquad \text{(A-61)}$$

$$-\frac{2\sin\theta_O}{r_O\Delta\theta}T_S = 0 \qquad \text{(A-62)}$$

(vii) Upper corner nodes

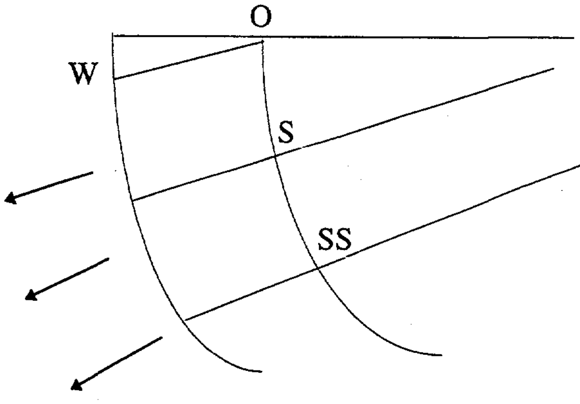

$$\frac{\partial T}{\partial r}\Big|_O = \frac{T_W - T_O}{\Delta r} + O(\Delta r) \qquad \text{(A-63)}$$

$$\frac{\partial T}{\partial \theta}\Big|_O = \frac{T_{SS} - 4T_S + 3T_O}{2\Delta\theta} + O(\Delta\theta) \qquad \text{(A-64)}$$

The finite difference is obtained by substituting the above equations into (v):

$$-\cos\theta_O \frac{(T_W - T_O)}{\Delta r} + \frac{\sin\theta_O}{r_O}\frac{(T_{SS} - 4T_S + 3T_O)}{2\Delta\theta} = 0 \qquad \text{(A-65)}$$

Rearranging the above equation , the following equation is obtained:

$$\left(\frac{3\sin\theta_O}{2r_O\Delta\theta} + \frac{\cos\theta_O}{\Delta r}\right)T_O - \frac{\cos\theta_O}{\Delta r}T_W + \frac{\sin\theta_O}{2r_O\Delta\theta}T_{SS} - \frac{2\sin\theta_O}{r_O\Delta\theta}T_S = 0 \qquad \text{(A-66)}$$

(2) Lower corner node :

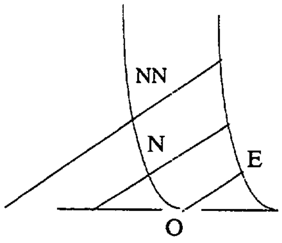

Applying Taylor's series expansion to the nodes, the following equations are obtained:

$$\frac{\partial T}{\partial r}\Big|_0 = \frac{T_O - T_E}{\Delta r} + O(\Delta r) \qquad \text{(A-67)}$$

$$\frac{\partial T}{\partial \theta}\Big|_O = \frac{4T_N - T_{NN} - 3T_O}{2\Delta r} + O(\Delta\theta) \qquad \text{(A-68)}$$

Substituting the above equation into (A-32), gives:

$$-\cos\theta_O \frac{(T_O - T_E)}{\Delta r} + \frac{\sin\theta_O}{r_O}\frac{(4T_N - T_{NN} - 3T_O)}{2\Delta\theta} = 0 \tag{A-69}$$

or

$$-\left(\frac{\cos\theta_O}{\Delta r} + \frac{3\sin\theta_O}{2r_O\Delta\theta}\right)T_O + \frac{\cos\theta_O}{\Delta r}T_E + \frac{2\sin\theta_O}{r_O\Delta\theta}T_N - \frac{\sin\theta_O}{2r_O\Delta\theta}T_{NN} = 0 \tag{A-70}$$

The boundary conditions for the simple regular shape can be easily specified. In terms of the finite difference equation, the upper boundary condition can be written as:

$$T_{i,j} = \frac{4}{3}T_{i-1,j} - \frac{1}{3}T_{i-2,j} \tag{A-71}$$

The lower boundary condition is similar to the one described above. i.e.:

$$T_{i,j} = \frac{4}{3}T_{i+1,j} - \frac{1}{3}T_{i+2,j} \tag{A-72}$$

An inverse heat conduction code has been developed for each segment of the heated hemispherical vessel using an implicit finite-difference formulation along with a linear estimation scheme. Appropriate shape-fitted boundary conditions were implemented to match the adiabatic conditions between the various segments so as to assure the accuracy of the outer surface heat transfer determined in the data reduction analysis. The inverse code was found to produce converging numerical results satisfying the conservation of energy and was unconditionally stable over the entire range of the downward facing boiling conditions. A detailed description of the code is given by Liu (M.S. Thesis, The Pennsylvania State University, 1995).

Appendix B
Measurement Errors

B-1 Temperature Measurement Error

There are four sources of error associated with temperature measurements using a thermocouple along with a data acquisition system. First, there is a difference in the emf vs. temperature relationship between manufactured thermocouple wire and the standards published by the National Bureau of Standards. This is a consequence of the change in the homogeneity and the purity of the material used. Second, there are errors associated with measuring the low voltage difference, i.e., less than 100 mV, generated by the thermocouple. Since the Analog to Digital Converter input range is typically ± 5 V or ± 10 V, the low level thermocouple signals must be amplified in order to maximize the measurement's resolution. Third, a reference junction is required because thermocouples are differential devices which adds another source of error. Finally there is an error associated with converting the measured analog voltage into temperature.

These error sources can lead to two types of deviations of the measurements from the true temperature value. The first is called Random Error, *e*, and the second is Fixed Error which is also called Bias. To assess these errors, the thermocouples and the data acquisition system were used to collect *N* temperature measurements of boiling water under normal atmospheric conditions. Under these circumstances, the temperatures measured should all be exactly 100 °C. In reality, the temperature readings are going to fluctuate about a mean value *T* given by

$$\overline{T} = \frac{\sum_1^N T_i}{N} \qquad \text{(B.1)}$$

which is not necessarily equal to 100 °C because of the existence of a Fixed Error. The differences between the measured values, T_i, and the mean temperature of the sample represent a set of *N* Random Errors e_i such that

$$e_i = T_i - \overline{T} \qquad \text{(B.2)}$$

where *i* varies from 1 to *N*. Each of the Random Errors defined by equation B.2 can be characterized by the number of times, n_i, it occurs within the sample of size *N*. For a sufficiently large sample size, the distribution of n_i will be normal or Gausian about the mean error given by

$$\overline{e} = \frac{\sum_1^N e_i}{N} \qquad \text{(B.3)}$$

When the average temperature given by equation B.1 is equal to the true value, it is an indication that the Bias or fixed error in the collected data is zero. If the Bias is not zero, it can be used to correct the data set by reducing each of the measurements by the computed fixed error given by

$$Bias = \overline{T} - 100\,^\circ C \qquad \text{(B.4)}$$

As a result, the corrected data set will have a Bias equal to zero and a mean temperature of 100 °C. The temperatures of the modified sample are denoted by $T_{c,i}$, where *i* varies from 1 to *N*. These new temperature values can be used to define a new set of errors $e_{c,i}$ given by

$$e_{c,i} = T_{c,i} - 100 \qquad \text{(B.5)}$$

The Standard Deviation *S* of the corrected data set is given by

$$S = \left[\frac{\sum_1^N e_{c,i}^2}{N-1}\right]^{1/2} \qquad \text{(B.6)}$$

and it is used to define the error range for a certain confidence level. The following error interval

$$100 - 3.92S \le T_{c,i} \le 100 + 3.92S \qquad \text{(B.7)}$$

is associated with a 95 % confidence level. The error in equation B.7 accounts for Random Error and the error associated with using a finite sample size.

The sensors employed in the quenching experiments were gauge 30 K-type thermocouples with a beaded tip. Those used for the steady state experiments were also K-type with a 0.04" stainless steel sheathing, which was also used to measure the water temperature inside the tank. Both of these thermocouples were products of Omega Engineering. One of each of these thermocouple types was used to measure the temperature of boiling water. This was accomplished by connecting the thermocouple to the terminal panel of the data acquisition system while the sensing tip of the sensor was submerged in boiling water.

The left and the right columns of Table B.1 are portions of the collected raw temperature data collected using the thermocouples employed in the quenching experiments and in the steady state experiments, respectively. A total of 600 readings were collected with each of the thermocouples. The data of the first column of Table B.1 was collected using the Basic program DATACOL. On the other hand, the data in the second column of Table B.1 was collected using the computer program Quicklog from Strawberry Tree Inc. Based on the equations presented previously, the errors and the biases for a 95 % confidence interval were found to be ± 0.17 and 0.97 °C for the thermocouples of the quenching experiments and ± 0.38 and 0.24 °C for the thermocouples of the steady state heating experiments. The Fixed Errors were used to correct all the temperature data generated during this study.

Table B.1: Raw data for the boiling water temperature measurements using two kinds of thermocouples

Beaded Tip Thermocouple	Stainless Steel Sheathing Thermocouple
101.050	100.225
101.100	100.250
101.075	100.188
101.075	100.300
101.100	100.300
101.100	100.425
101.075	100.475
101.075	100.475
101.100	100.200
101.100	100.425
101.050	100.188
101.075	100.275
101.050	100.113
101.075	100.113
101.075	100.375
101.025	100.162
101.025	100.250
101.025	100.275
101.050	100.113
101.050	100.325
101.050	100.350
101.050	100.350
101.000	100.300
101.025	100.300
101.025	100.375
101.025	100.275
101.050	100.200
101.100	100.375
101.075	100.400
101.100	100.325
101.050	100.300
101.050	100.375
101.050	100.350
101.075	100.350
101.050	100.375
101.075	100.300
101.050	100.250
101.025	100.275
101.75	100.325

B-2 Heat Flux Measurement Error For Steady State Experiments

The error analysis presented here is associated with the heat transfer measurements made using the hemisphere described in Section 3.

There are three sources of error in the estimate of the heat flux during steady state heating experiments. First, there is the error associated with the measurement of the voltage across the variacs supplying the cartridge heaters. Second, measurements of the current traveling through each heating element add another source of error. The third source of uncertainty is due to estimating the heat loss from the segment to the environment by natural convection and to the adjacent segment by conduction.

An energy balance on the segment gives

$$q_b'' A_b = \dot{Q}_{in} - \dot{Q}_{lost} \qquad \text{(B.8)}$$

which indicates that the heat removed by boiling is equal to the total heat supplied to the segment reduced by the total heat loss to the adjacent segment by conduction and to the surrounding by natural convection. During the steady state experiments, the back of the test section was covered by a large quantity of fiber glass insulation. As a result, it is very reasonable to assume that the heat loss by natural convection is negligible in equation B.8. In addition, the total heat supplied to the segment is equal to the product of the current, *I*, and the voltage, *VT*, of every cartridge heater multiplied by the total number, *N*, of heaters. Therefore, we can write

$$q_b'' A_b = N I VT - \dot{Q}_c \qquad \text{(B.9)}$$

where A_b is the boiling heat transfer area and Q_c is the heat loss by conduction to the adjacent segment which is given by

$$\dot{Q}_c = \lambda Ac \frac{\Delta T}{\Delta s} \qquad \text{(B.10)}$$

where *Ac* is the conduction heat transfer area between the two segments, ΔT is the temperature difference between the two segments, Δs is the distance between the two nodes representing the two segments, and λ is the thermal conductivity of the vessel wall. The heat transfer area, *Ac*, between the inner and the outer segments and the distance between the nodes, Δs, are estimated to be 3.00×10^{-4} m^2 and 0.04 m, respectively. The node representing the inner segment is chosen to be the bottom center and the node representing the outer segment is 15.25° from the bottom center. The temperature difference, ΔT, between the inner and the outer segments is of the order of 1 °C. Using these estimates and a thermal conductivity for aluminum equal to 170 W/m-K, we can use equation B.10 to show that Q_c is of the order of 1.275 W.

The error in estimating the conduction term in equation B.10 can be obtained from the following equation:

$$\frac{\delta \dot{Q}_c}{\dot{Q}_c} = \left[\left(\frac{\delta \Delta T}{\Delta T}\right)^2 + \left(\frac{\delta \Delta s}{\Delta s}\right)^2 + \left(\frac{\delta Ac}{Ac}\right)^2 \right]^{1/2} \qquad \text{(B.11)}$$

where the error associated with the thermal conductivity has been neglected. It will be shown later that this is a good assumption, because the error in the temperature measurements accounts for almost all the uncertainty in Q_c. The error in the temperature measurements can be estimated, and the uncertainty in *Ac* and Δs are estimated based on a machining tolerance of 2.54×10^{-5} m. Therefore, we have

$$\begin{aligned} \delta \Delta T &= 2\delta T = 0.8\,^\circ\mathrm{C} \\ \delta \Delta s &= 2\delta s = 5.08 \times 10^{-5}\ \mathrm{m} \qquad \text{(B.12)} \\ \delta A_c &= 2\delta R_o = 5.08 \times 10^{-5}\ \mathrm{m} \end{aligned}$$

where R_o is the outside radius of the vessel. Using these error estimates and equation B.11, the uncertainty in estimating Q_c is evaluated to be 80%. This value is high due to the fact that the uncertainty in the temperature measurements is of the same order as the temperature difference between the inner and the outer segments.

Next, we need to find the error associated with Q_{in} in order to find the total experimental uncertainty in measuring the total boiling heat flux q''_b, which is the product of the boiling heat flux and the boiling heat transfer area. The error in the voltage and the current measurements are obtained from manufacturer's information about the multimeter used. This multimeter is characterized by high errors for low voltage and current values. For heat flux levels greater than 0.01 MW/m^2, the maximum uncertainties in the voltage and current measurements are equal to 10 and 4% respectively. On the other hand, when the heat flux is higher than 0.1 MW/m^2, these maximum errors drop to 6% for the voltage and 1.75% for the current. Using these error estimates for I and VT, the uncertainty in the total heat input can be estimated based on the following equation:

$$\frac{\delta \dot{Q}_{in}}{\dot{Q}_{in}} = \left[\left(\frac{\delta I}{I} \right)^2 + \left(\frac{\delta VT}{VT} \right)^2 \right]^{1/2} \tag{B.13}$$

which gives

$$\frac{\delta \dot{Q}_{in}}{\dot{Q}_{in}} = 11\% \tag{B.14}$$

for the low heat flux range of 0.01 MW/m^2 < q_b'' < 0.08 MW/m^2

$$\frac{\delta \dot{Q}_{in}}{\dot{Q}_{in}} = 6\% \tag{B.15}$$

for the high heat flux range of q_b'' > 0.08 MW/m^2.

These relative uncertainties in the heat input along with the error in estimating the conduction heat transfer are used to estimate the relative error associated with the boiling heat flux given by equation B.9, which leads to

$$\frac{\delta q_b''}{q_b''} = 17\% \tag{B.16}$$

for the low heat flux range of 0.01 MW/m^2 < q_b'' < 0.08 MW/m^2

$$\frac{\delta q_b''}{q_b''} = 7\% \tag{B.17}$$

for the high heat flux range of q_b'' > 0.08 MW/m^2.

Appendix C
Steady-State Nucleate Boiling Data for a Downward Facing Hemispherical Surface

The five sets of steady-state nucleate boiling data measured at five distinct spatial locations of the heated vessel under both saturated and subcooled conditions have been used to determine the heat transfer coefficients. Results are shown in Figures C-1 to C-5. In the high-heat-flux nucleate boiling regime, the heat transfer coefficient tends to approach an asymptotic value. The numerical data are listed in Table C-1 through C-5.

Figure C.1: Nucleate Boiling Heat Transfer Coefficients at the Bottom Center of the Heated Vessel (Theta = 0°)

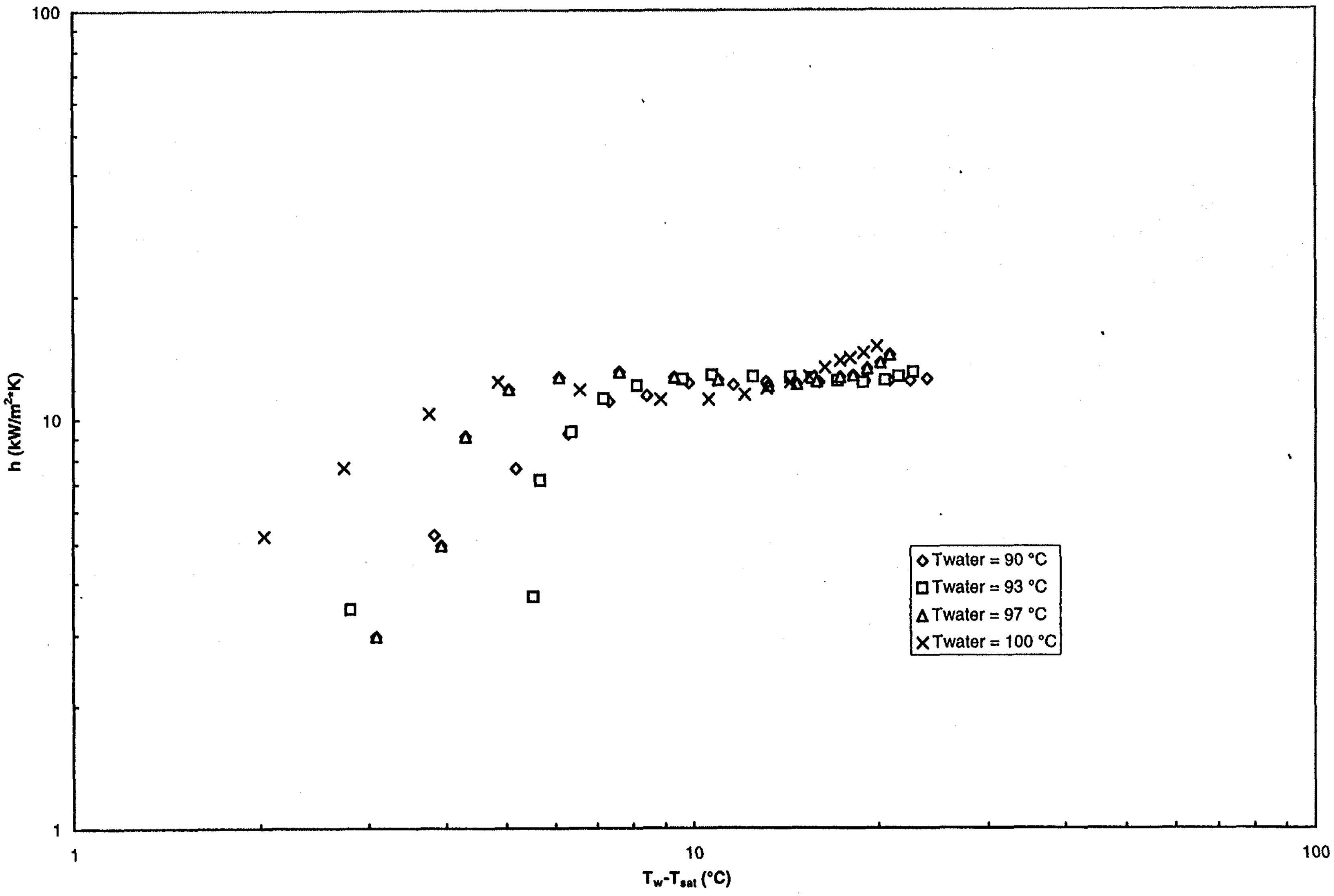

Figure C.2: Nucleate Boiling Heat Transfer Coefficients at an Off-Center Location (Theta = 18°)

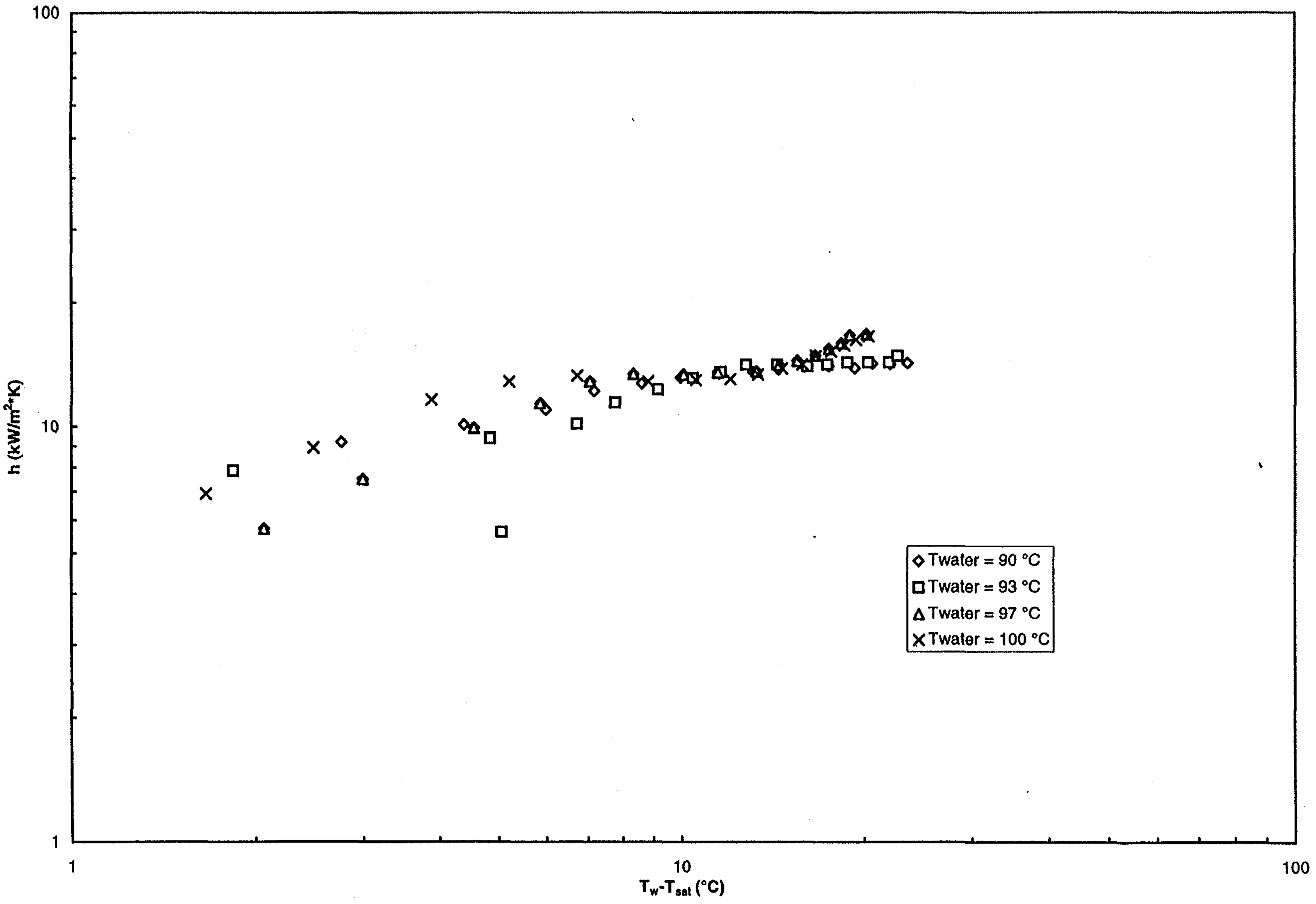

Figure C.3: Nucleate Boiling Heat Transfer Coefficients at an Off-Center Location (Theta = 36°)

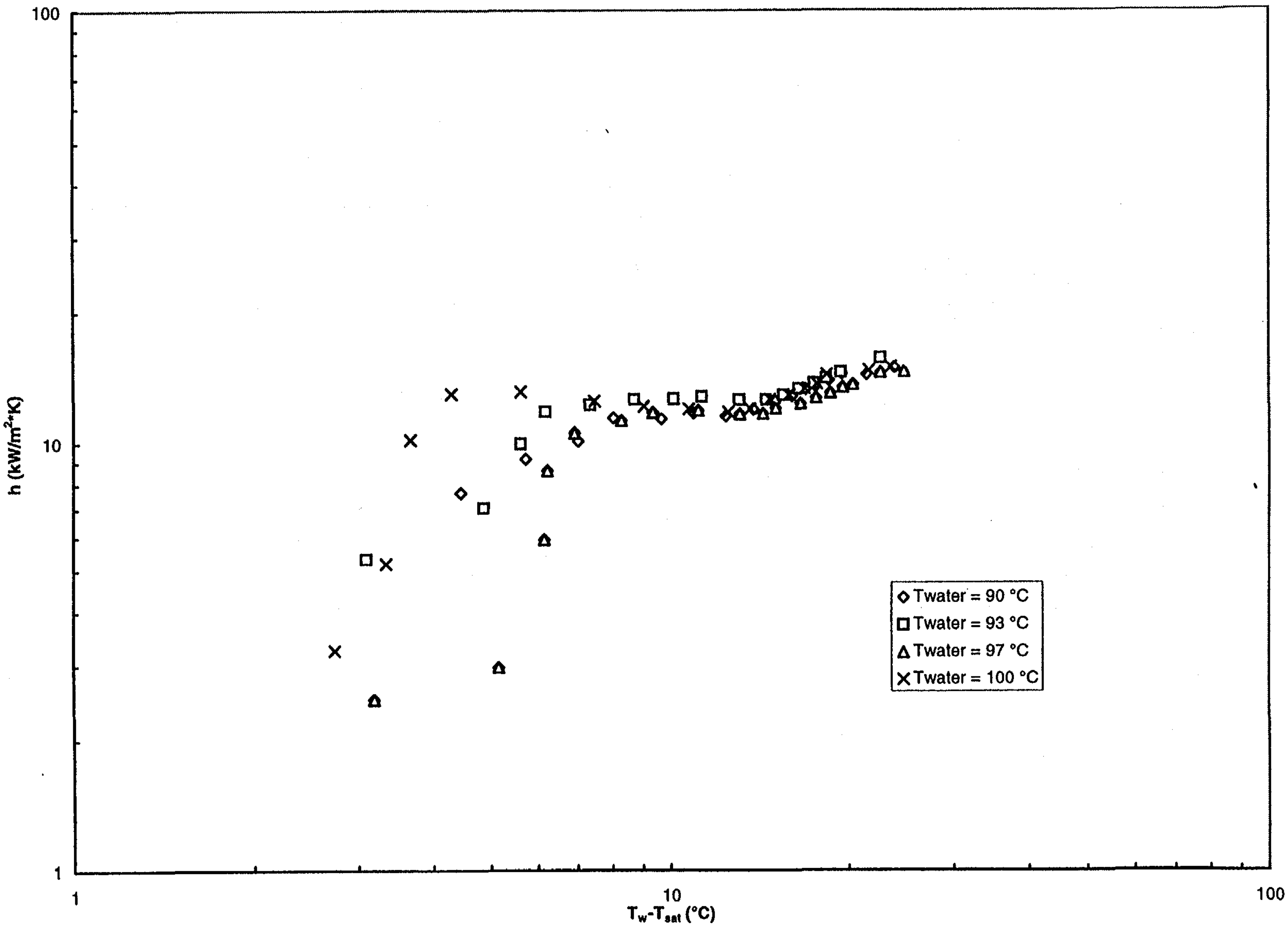

Figure C.4: Nucleate Boiling Heat Transfer Coefficients at an Off-Center Location (Theta = 60°)

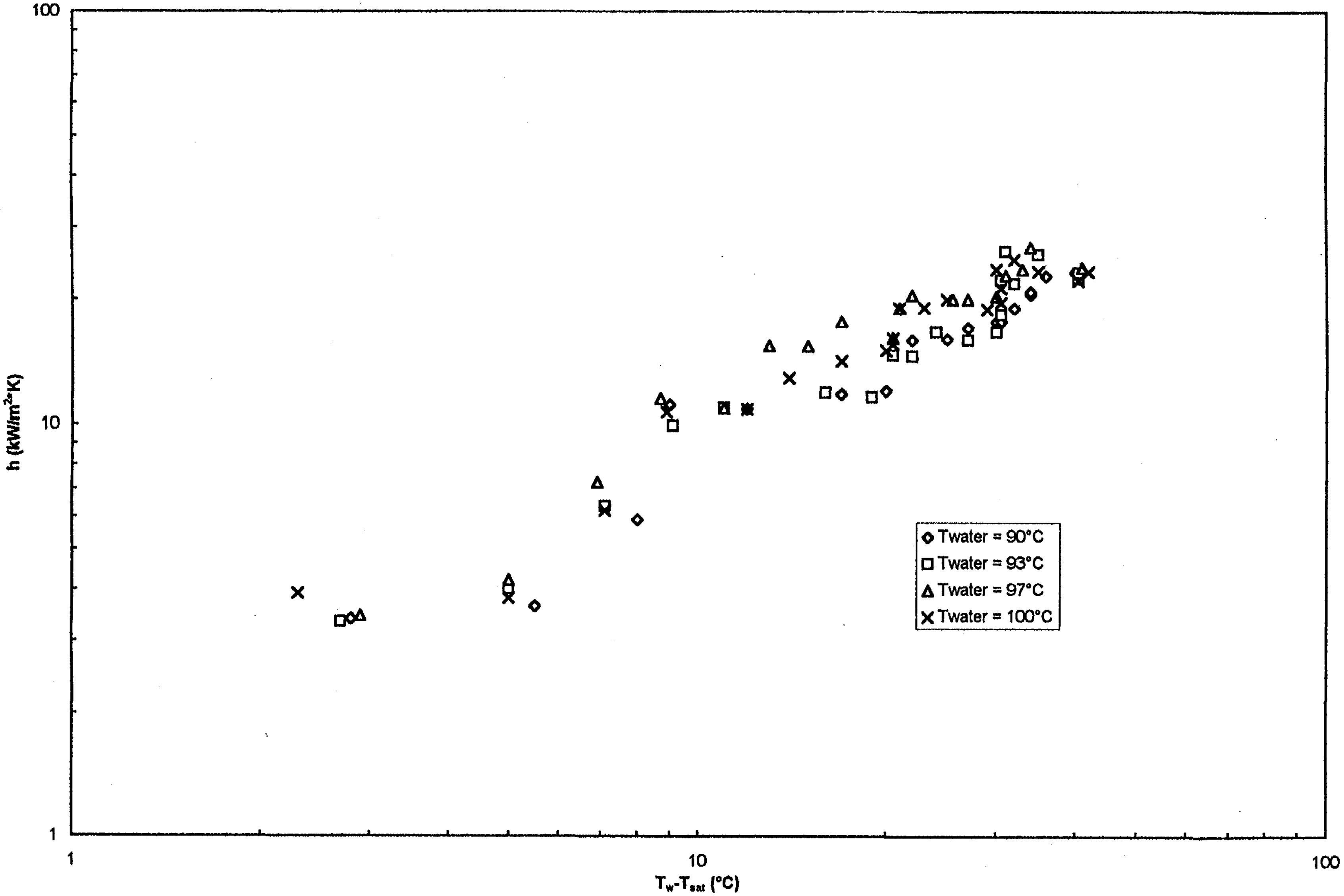

Figure C.5: Nucleate Boiling Heat Transfer Coefficients at an Off-Center Location (Theta = 75°)

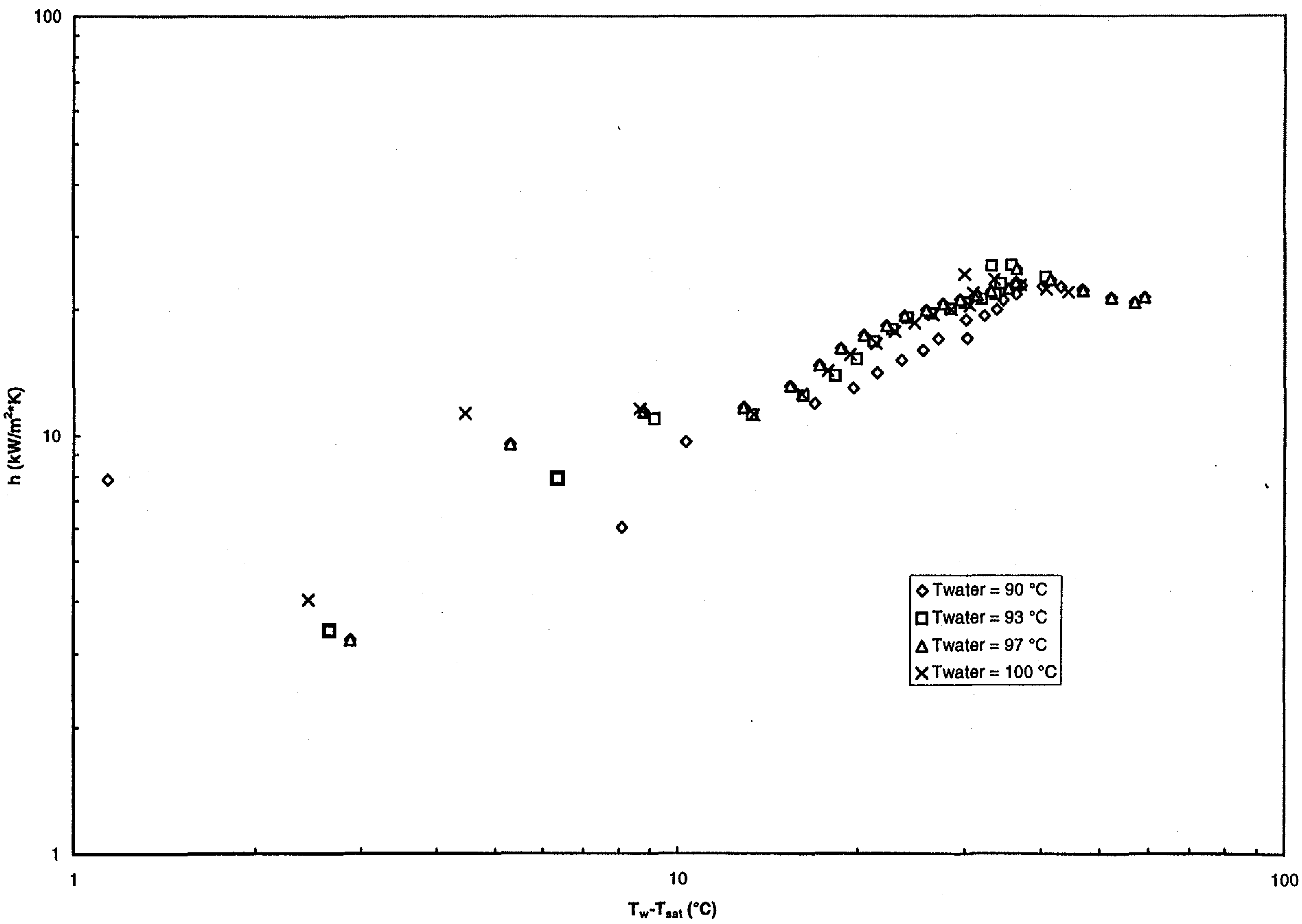

Table C-1: Steady State Nucleate Boiling Data at the Bottom Center of the Hemispherical Test Vessel ($\theta = 0°$)

T_{sub} (°C)	$T_w - T_{sat}$ (°C)	q''_{nb} (MW/m^2)	h_{nb} (kW/m^2*K)
90	3.8296	0.020092	5.246501
90	5.1893	0.039434	7.599098
90	6.2989	0.057933	9.19732
90	7.3285	0.080715	11.01385
90	8.4383	0.095965	11.37255
90	9.8378	0.12019	12.21716
90	11.6274	0.14057	12.08955
90	13.1571	0.1618	12.29754
90	14.6167	0.17938	12.27226
90	16.0264	0.19652	12.26227
90	17.2961	0.21634	12.50802
90	19.0257	0.23441	12.3207
90	20.8553	0.25766	12.35465
90	22.4949	0.27803	12.35969
90	23.9445	0.29868	12.47385
93	2.7998	0.009666	3.452479
93	5.5296	0.020459	3.699906
93	5.6693	0.040332	7.114106
93	6.3589	0.059065	9.288556
93	7.1785	0.080193	11.17128
93	8.1182	0.097696	12.03419
93	9.6078	0.11994	12.48361
93	10.7275	0.13687	12.7588
93	12.5071	0.15861	12.6816
93	14.4067	0.18189	12.62538
93	15.5964	0.19566	12.5452
93	17.1761	0.2122	12.35438
93	18.8658	0.23155	12.27353
93	20.5154	0.25412	12.38679
93	21.555	0.27287	12.65924
93	22.7346	0.29507	12.9789
97	3.0798	0.009129	2.9643
97	3.9296	0.019428	4.944015
97	4.2993	0.039053	9.083572
97	5.0489	0.059653	11.81505
97	6.0786	0.076812	12.63646
97	7.5982	0.098771	12.99926
97	9.3279	0.11793	12.64272
97	10.9675	0.13631	12.42854

Table C-1 (continued):

97	13.2571	0.15902	11.99508
97	14.7567	0.17929	12.14974
97	15.8764	0.19551	12.3145
97	17.356	0.21908	12.62272
97	18.1958	0.2321	12.75569
97	19.1854	0.25378	13.22777
97	20.145	0.2755	13.67585
97	20.8645	0.29847	14.30516
100	2.0298	0.010561	5.202976
100	2.7296	0.020869	7.645443
100	3.7493	0.038624	10.30166
100	4.8489	0.059788	12.33022
100	6.5686	0.077155	11.74603
100	8.8682	0.098776	11.13822
100	10.5978	0.1183	11.16269
100	12.1375	0.13913	11.46282
100	13.1772	0.15587	11.82876
100	14.3868	0.17679	12.28835
100	15.4464	0.1955	12.65667
100	16.366	0.21799	13.31969
100	17.3556	0.24024	13.84222
100	17.9854	0.25273	14.05195
100	18.905	0.27367	14.47606
100	19.8746	0.29764	14.9759

Table C-2: Steady State Nucleate Boiling Data at an Off-Center Location (θ = 18°)

T_{sub} (°C)	$T_w - T_{sat}$ (°C)	q''_{nb} (MW/m^2)	h_{nb} (kW/m^2*K)
90	2.7686	0.025521	9.218016
90	4.3976	0.044494	10.11779
90	5.9965	0.065909	10.99124
90	7.1753	0.087596	12.20799
90	8.6042	0.10967	12.7461
90	9.983	0.13145	13.16738
90	11.5417	0.15562	13.48328
90	13.1605	0.17892	13.59523
90	14.4994	0.19996	13.79092
90	15.9881	0.22398	14.00917
90	17.5269	0.24606	14.03899
90	19.3457	0.26905	13.90748
90	20.6643	0.29466	14.25937
90	22.1133	0.31416	14.20683
90	23.5921	0.33683	14.27724
93	1.8392	0.01444	7.85124
93	5.0685	0.028389	5.601065
93	4.8476	0.045562	9.398878
93	6.7464	0.068628	10.17254
93	7.7853	0.088989	11.43039
93	9.164	0.11294	12.32431
93	10.4627	0.13736	13.12854
93	11.6316	0.15792	13.57681
93	12.8104	0.18086	14.11822
93	14.4391	0.20426	14.14631
93	16.1679	0.22669	14.02099
93	17.4568	0.24722	14.16182
93	18.8056	0.26954	14.33296
93	20.3345	0.2915	14.33524
93	22.0132	0.31504	14.31141
93	22.752	0.33775	14.84485
97	2.0694	0.01183	5.716633
97	2.9988	0.022519	7.509337
97	4.5676	0.045436	9.947456
97	5.8664	0.066973	11.41637
97	7.0752	0.091055	12.8696
97	8.334	0.1121	13.45092
97	10.0928	0.13527	13.40262

Table C-2 (continued):

97	11.5117	0.15605	13.55577
97	13.3403	0.18166	13.61738
97	14.5191	0.20503	14.1214
97	15.568	0.22522	14.46686
97	16.6768	0.24862	14.90814
97	17.5555	0.27128	15.45271
97	18.4143	0.29382	15.95608
97	19.0131	0.31693	16.66903
97	20.2319	0.33938	16.7745
100	1.6594	0.011497	6.928408
100	2.4888	0.022216	8.92639
100	3.8876	0.045202	11.62723
100	5.2164	0.06723	12.8882
100	6.7452	0.089757	13.3068
100	8.824	0.11359	12.87285
100	10.5927	0.13754	12.98441
100	12.0716	0.15772	13.06538
100	13.4204	0.17976	13.39453
100	14.6792	0.20368	13.87542
100	15.868	0.22463	14.15616
100	16.7168	0.24818	14.84614
100	17.6756	0.26966	15.25606
100	18.6044	0.29331	15.76563
100	19.4532	0.31626	16.25748
100	20.382	0.33823	16.59454

Table C-3: Steady State Nucleate Boiling Data at an Off-Center Location ($\theta = 36^\circ$)

T_{sub} (°C)	$T_w - T_{sat}$ (°C)	q''_{nb} (MW/m^2)	h_{nb} (kW/m^2*K)
90	0.4097	0.016215	39.57774
90	4.4594	0.034088	7.644078
90	5.729	0.05247	9.158666
90	7.0287	0.070862	10.08181
90	8.0483	0.09135	11.35022
90	9.678	0.1093	11.29366
90	10.9777	0.12797	11.65727
90	12.4474	0.14255	11.45219
90	13.847	0.1644	11.87261
90	15.1066	0.18717	12.38995
90	16.1162	0.20566	12.76107
90	16.9959	0.22493	13.23437
90	17.6757	0.23739	13.4303
90	18.6253	0.25857	13.88273
90	19.5749	0.28115	14.36278
93	3.0997	0.016488	5.319224
93	4.8694	0.034315	7.047069
93	5.609	0.055637	9.919237
93	6.1787	0.072698	11.76591
93	7.3584	0.089711	12.19164
93	8.728	0.10938	12.53208
93	10.1777	0.12799	12.57553
93	11.3474	0.14427	12.71393
93	13.147	0.16417	12.48726
93	14.5767	0.18249	12.51929
93	15.5964	0.19985	12.81385
93	16.556	0.21951	13.25864
93	17.5656	0.23993	13.65908
93	18.4453	0.25851	14.01495
93	19.4749	0.28167	14.46323
97	3.1899	0.007976	2.500445
97	5.1597	0.015347	2.974398
97	6.1493	0.036437	5.92539
97	6.229	0.053557	8.598009
97	6.9287	0.07268	10.4897
97	8.2983	0.092942	11.20013
97	9.368	0.10959	11.69833
97	11.1676	0.13206	11.82528

Table C-3 (continued):

97	13.1372	0.15205	11.574
97	14.3769	0.16725	11.63324
97	15.1167	0.18063	11.94904
97	16.6563	0.20405	12.25062
97	17.7059	0.2238	12.63985
97	18.7256	0.24304	12.97902
97	19.6552	0.26266	13.36338
97	20.4649	0.27769	13.56909
100	2.7398	0.008925	3.257446
100	3.3397	0.017316	5.184897
100	3.6693	0.037238	10.14853
100	4.309	0.055729	12.93316
100	5.6287	0.07369	13.09183
100	7.4883	0.093024	12.42258
100	9.058	0.10936	12.07331
100	10.7877	0.12866	11.92655
100	12.5673	0.14726	11.71771
100	13.687	0.16301	11.90984
100	14.8066	0.18558	12.5336
100	15.9463	0.20475	12.83997
100	16.9559	0.22493	13.26559
100	17.7656	0.24179	13.61001
100	18.4552	0.26432	14.32225
100	19.4145	0.25296	14.18303
100	21.4135	0.30128	15.5183
100	23.0126	0.35385	16.52462

Table C-4: Steady-State Nucleate Boiling Data at an Off-Center Location ($\theta = 60°$)

T_{sub} (°C)	$T_w - T_{sat}$ (°C)	q''_{nb}(MW/m2)	h_{nb}(kW/m^2*K)
90	2.8	0.0095	3.392857
90	5.5	0.02	3.636364
90	8	0.047	5.875
90	9	0.1	11.11111
90	12	0.13	10.83333
90	17	0.2	11.76471
90	20	0.24	12
90	20.5	0.31	15.12195
90	22	0.35	15.90909
90	25	0.4	16
90	27	0.46	17.03704
90	30	0.53	17.66667
90	30.5	0.54	17.70492
90	32	0.61	19.0625
90	34	0.7	20.58824
90	34	0.71	20.88235
90	36	0.82	22.77778
90	40	0.93	23.25
93	2.7	0.009	3.333333
93	5	0.02	4
93	7.1	0.045	6.338028
93	9.1	0.09	9.89011
93	11	0.12	10.90909
93	16	0.19	11.875
93	19	0.22	11.57895
93	20.5	0.3	14.63415
93	22	0.32	14.54545
93	24	0.4	16.66667
93	27	0.43	15.92593
93	30	0.5	16.66667
93	30.5	0.56	18.36066
93	30.5	0.68	22.29508
93	32	0.7	21.875
93	31	0.81	26.12903
93	35	0.9	25.71429
93	40.5	0.91	22.46914

Table C-4:(continued):

93	40.5	0.94	23.20988
97	2.9	0.01	3.448276
97	5	0.021	4.2
97	6.9	0.05	7.246377
97	8.7	0.1	11.49425
97	11	0.12	10.90909
97	13	0.2	15.38462
97	15	0.23	15.33333
97	17	0.3	17.64706
97	20.5	0.33	16.09756
97	21	0.4	19.04762
97	22	0.45	20.45455
97	25.5	0.51	20
97	27	0.54	20
97	30	0.61	20.33333
97	31	0.71	22.90323
97	33	0.78	23.63636
97	34	0.91	26.76471
97	41	0.98	23.90244
100	2.3	0.009	3.913043
100	5	0.019	3.8
100	7.1	0.044	6.197183
100	8.9	0.095	10.67416
100	12	0.13	10.83333
100	14	0.18	12.85714
100	17	0.24	14.11765
100	20	0.3	15
100	20.5	0.33	16.09756
100	21	0.4	19.04762
100	23	0.44	19.13043
100	25	0.5	20
100	29	0.55	18.96552
100	30.5	0.6	19.67213
100	30.5	0.65	21.31148
100	30	0.71	23.66667
100	32	0.8	25
100	35	0.82	23.42857
100	40.5	0.9	22.22222
100	42	0.98	23.33333

Table C-5: Steady State Nucleate Boiling Data at an Off-Center Location ($\theta = 75°$)

T_{sub} (°C)	$T_w - T_{sat}$ (°C)	q''_{nb} (MW/m^2)	h_{nb} (kW/m^2*K)
90	1.1398	0.008966	7.866433
90	8.1091	0.048932	6.034208
90	10.3182	0.099407	9.634142
90	12.9173	0.14992	11.60614
90	16.9463	0.20117	11.87103
90	19.6554	0.25362	12.90332
90	21.5045	0.30229	14.05706
90	23.6035	0.35491	15.03633
90	25.6026	0.40672	15.88589
90	27.1216	0.45984	16.95475
90	30.2606	0.51458	17.00495
90	30.1197	0.56668	18.81426
90	32.2787	0.61997	19.20678
90	33.8677	0.67459	19.91839
90	34.6767	0.72695	20.96364
90	36.4356	0.78818	21.63214
90	37.1046	0.84449	22.75971
90	40.2534	0.90961	22.5971
90	43.1523	0.97156	22.51467
90	46.821	1.0397	22.20585
93	2.6598	0.009072	3.410817
93	6.3391	0.050128	7.907747
93	9.1482	0.099823	10.91176
93	13.3173	0.14887	11.17869
93	16.2163	0.20088	12.38754
93	18.3154	0.25335	13.83262
93	19.9145	0.30174	15.15177
93	21.2435	0.35466	16.69499
93	22.7726	0.40636	17.84425
93	24.1616	0.45957	19.02068
93	26.3906	0.51372	19.46602
93	28.4396	0.56728	19.94683
93	29.9887	0.62043	20.68879
93	31.9677	0.67526	21.1232
93	33.6467	0.72915	21.67077
93	34.2956	0.78908	23.0082
93	33.1846	0.84151	25.35845
93	35.7534	0.90941	25.43562
93	40.7823	0.97086	23.80592

Table C-5 (continued):

97	2.8798	0.009352	3.247465
97	5.2891	0.050491	9.546237
97	8.7682	0.099815	11.38375
97	12.8573	0.14902	11.5903
97	15.4263	0.20158	13.06729
97	17.2854	0.25334	14.6563
97	18.7345	0.3014	16.08797
97	20.4835	0.35405	17.28464
97	22.3126	0.40605	18.19824
97	23.8916	0.45907	19.2147
97	25.8906	0.51402	19.85354
97	27.5896	0.56763	20.57406
97	29.4687	0.62065	21.06133
97	31.3977	0.67542	21.51177
97	33.1067	0.72885	22.01518
97	35.3756	0.78986	22.32782
97	36.4146	0.8435	23.16379
97	36.4434	0.9082	24.92084
97	41.4622	0.97218	23.44738
97	46.9011	1.0349	22.06558
97	52.1598	1.1063	21.20982
97	56.8685	1.1766	20.68984
97	59.0871	1.2557	21.25168
100	2.4498	0.009867	4.0275
100	4.4491	0.050113	11.26363
100	8.6482	0.09977	11.5365
100	13.3773	0.14931	11.16145
100	16.1163	0.20141	12.49729
100	17.8354	0.25296	14.18303
100	19.4145	0.30128	15.5183
100	21.4135	0.35385	16.52462
100	23.0126	0.40597	17.64121
100	24.8316	0.45924	18.49418
100	26.5706	0.51407	19.34732
100	28.5096	0.56794	19.92101
100	30.5287	0.62077	20.33398
100	30.8877	0.67427	21.82973
100	29.9268	0.72504	24.22711
100	33.4856	0.78935	23.57282
100	37.0046	0.84278	22.77501
100	40.8234	0.90857	22.25611
100	44.3623	0.97015	21.86879

Appendix D
Preliminary Scaling Analysis of the Effects of Thermal Insulation on the Cooling of the Lower Head in a Flooded Cavity

D.1 Reactor Vessel Thermal Insulation System

A thermal insulation system, consisting of insulation panel segments, has been incorporated into the AP 600 design. The panels are about 0.1m thick, made of stainless steel reflective insulation with air gaps between relatively thin sheets of metal. Figure D.1 shows a schematic of the thermal insulation system. The reactor vessel at elevations below the hot leg nozzles is completely encapsulated by the insulation structure. This includes a complete coverage of the reactor lower head. The insulation panels are supported by engineered sections that make a transition from the octagonal cavity shape to circular configuration. The insulation panels are hung from the walls with a 0.05m outside clearance that allows for normal ventilation to cool the concrete during plant operation. The inside clearance adjacent to the lower head is 0.23m. A special water-inlet module located below the bottom center of the lower head, is designed to provide an open flow path for water to enter the annular gap. The weight of each panel is such that it would not be lifted out of position during flooding. However, the insulation structure is not rigid. The panels may pop-up or blow out as a result of strong flow oscillations and flow surges. Dislocated panels would facilitate water ingression and steam venting. They might also adversely affect the local downward facing boiling process on the vessel outer surface if one or more dislocated panels are in contact with the reactor vessel. Among others, the size of the minimum gap between the insulation structure and the reactor vessel represents an important parameter of the system to be considered. In this Appendix a preliminary scaling analysis is performed to assess the effects of thermal insulation on the cooling of the lower head in a flooded cavity under severe accident conditions.

D.2 Major Issues and Key Transfer Processes

The performance of the insulation system in the in-vessel cooling stage of a severe accident is uncertain and needs to be carefully assessed. At present, it is not clear whether there is any limitation to the regime of boundary layer boiling on the outer surface of the reactor vessel due to thermal insulation. If a severe limitation exists, it could significantly lower the critical heat flux on the vessel outer surface and adversely affect the efficacy of external cooling of core melt by cavity flooding.

Among others, there are two major issues that need to be addressed. One is related to the supply of fresh liquid to the heating surface by ingression of water through the insulation panels (i.e., the liquid supply issue). The other is related to the removal of water vapor or steam through the minimum gap between the reactor vessel and the insulation structure (i.e., the steam venting issue). If the water ingression rate is below the rate of water consumption by boiling, then boil-dry of water may occur on the vessel outer surface. On the other hand, if steam cannot be vented efficiently, then water vapor may accumulate on the heating surface, leading to premature dryout of the vessel outer surface. Unless the insulation design allows adequate supply of liquid and efficient venting of steam, a severe limitation to the regime of boundary layer boiling may arise. To address these two important issues, it is necessary to consider the key transfer processes that take place in the system.

There are five transfer processes that take place simultaneously in the thermal

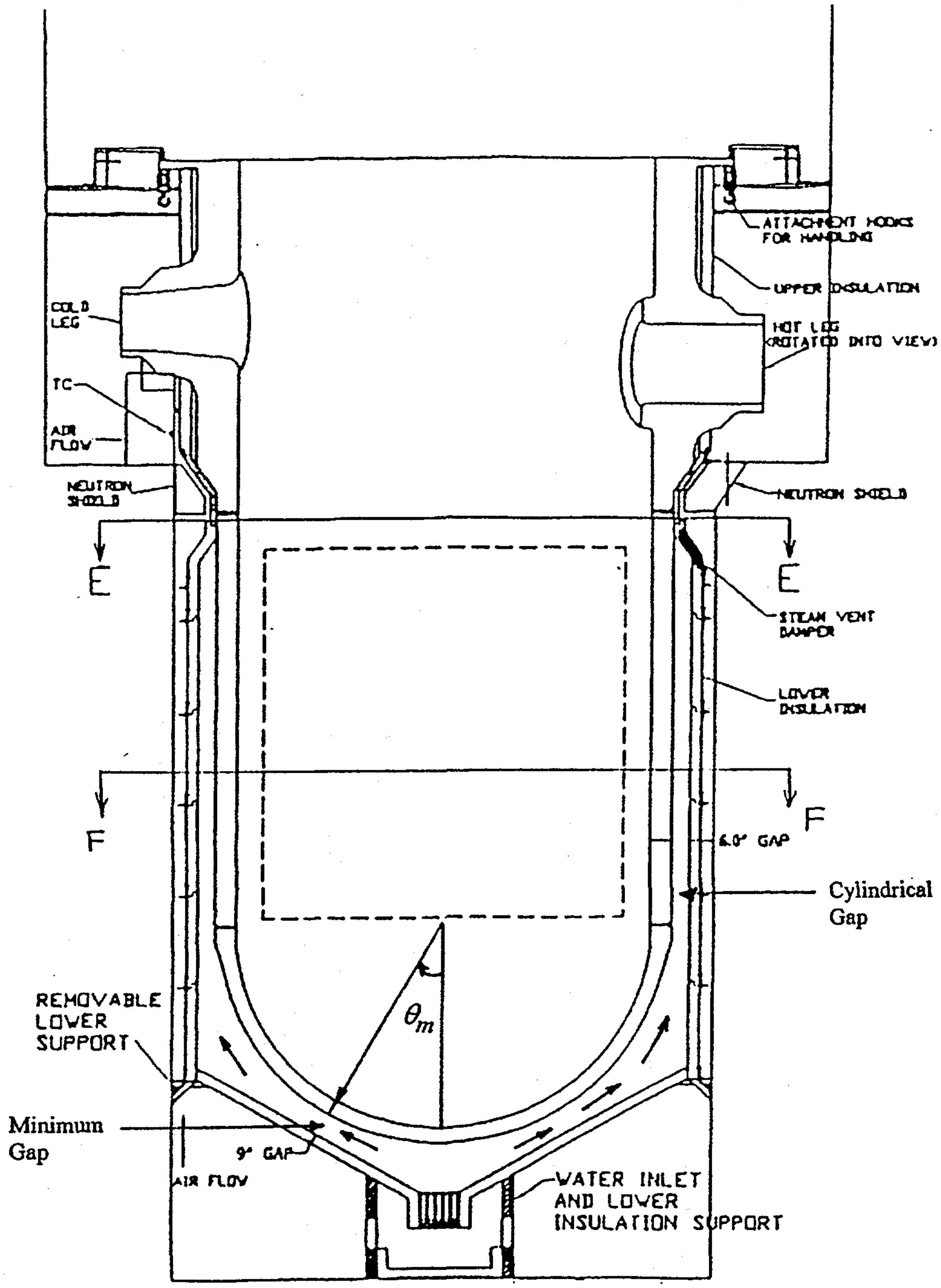

Figure D.1. Schematic of the AP600 Reactor Vessel Thermal Insulation System.

insulation/reactor vessel system. These are (i) heat conduction in the vessel wall, (ii) steam generation by boundary layer boiling on the vessel outer surface, (iii) water ingression through the insulation panels, (iv) two-phase boundary layer flow through the minimum gap between the reactor vessel and the insulation structure, and (v) heat transfer in the insulation structure. In view of the liquid supply and steam venting issues, item (v) is of secondary importance. By performing an order of magnitude analysis, it can be shown that the time scale involved in item (i) is considerably larger than those involved in items (ii) to (iv). Thus, heat conduction in the vessel wall is a slow process whereas steam generation, water ingression and steam venting are fast processes. With respect to the other three processes, the heat conduction process is of secondary importance. Hence, the steam generation, water ingression, and steam venting processes represent the key transfer processes that need to be considered in assessing the performance of the thermal insulation in the in-vessel cooling stage of a severe accident.

D.3 Preliminary Scaling Analysis

A schematic diagram of the insulation/reactor vessel system is shown in Figure D.2. Since the reactor lower head is hemispherical and the reactor cavity is octagonal in shape, there is a transition in the configuration of the thermal insulation panel structure to accommodate the change in the system geometry. As a result, a minimum gap exists between the reactor vessel and the insulation structure. The size of the minimum gap is δ and its location is θ_m, with an elevation of H relative to the bottom part of the insulation structure. The heating length from the bottom center of the lower head to the location of the minimum gap is $\theta_m D/2$, where D is the outer diameter of the vessel. This quantity can be viewed as the length, L_g, of the vapor flow path in the annular channel formed between the reactor vessel and the insulation structure. By choosing the region bounded by the vessel outer surface and the insulation panels up to the minimum gap as the control volume, the important time scales involved in each of the three key transfer processes can be estimated. This is presented below.

D.3.1 Steam Generation Process and the Residence Time

Let q_w'' be the local wall heat flux transferred from the melt pool to the vessel outer surface. From experimental evidence, it is expected that q_w'' is a function of θ under quasi-steady condition, i.e., $q_w'' = q_w''(\theta)$. For given values of $q_w''(\theta)$, the steam generation rate in the control volume is

$$\dot{m}_b = \frac{1}{h_{fg}} \int_0^{\theta_m} q_w''(\theta) \left[(\pi D \sin\theta)\left(\frac{D}{2}\right) d\theta \right] \qquad \text{(D-1)}$$

where h_{fg} is the latent heat of vaporization of water. Defining an average wall heat flux by

$$q_b'' = \int_0^{\theta_m} q_w''(\theta) \sin\theta \, d\theta \qquad \text{(D-2)}$$

equation (D-1) can be written as

$$\dot{m}_b = \frac{\pi D^2 q_b''}{2 h_{fg}} \qquad \text{(D-3)}$$

Under quasi-steady conditions, all the water vapor generated on the vessel outer surface must be vented through the minimum gap. This requires

$$v_g = \frac{\dot{m}_b}{\rho_g A_\delta} \qquad \text{(D-4)}$$

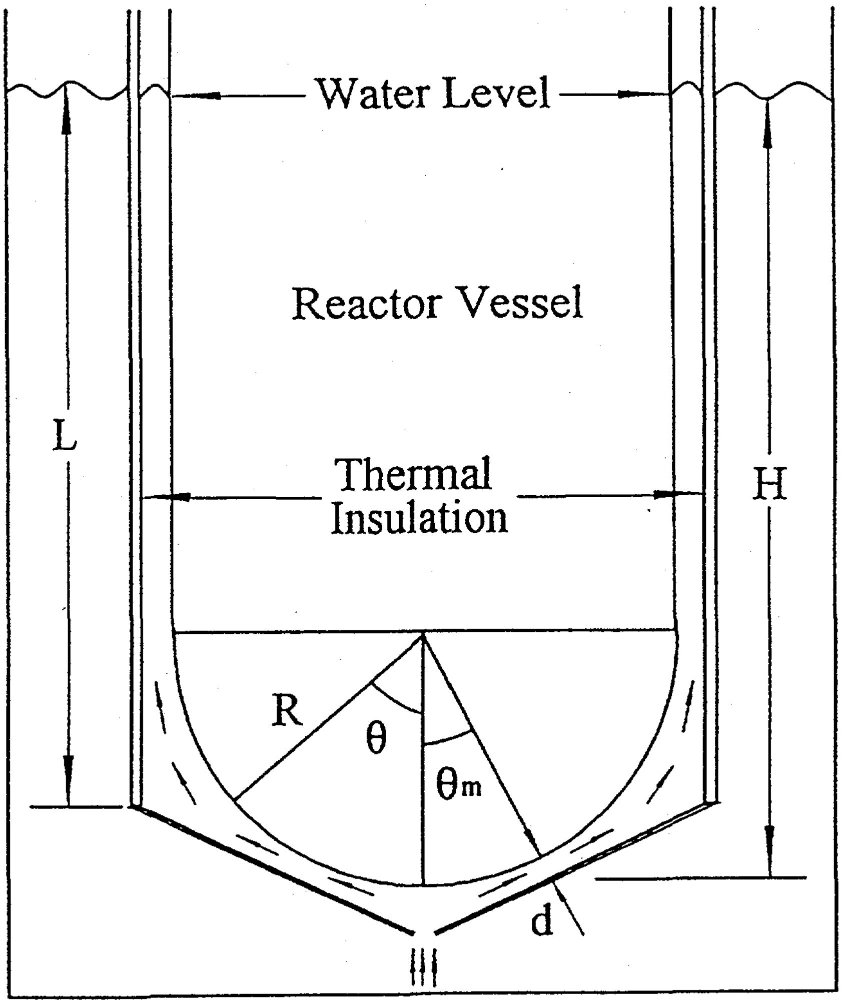

Figure D.2. Schematic of the Control Volume (C.V.) Selected for the Insulation System.

where v_g is the superficial vapor velocity, ρ_g is the vapor density, and A_δ the flow area of the minimum gap. The latter is given by

$$A_\delta = \pi D \delta \sin\theta_m \qquad \text{(D-5)}$$

Substitution of equations (D-3) and (D-5) into equation (D-4) gives

$$v_g = \frac{D q_b''}{2\rho_g h_{fg} \delta \sin\theta_m} \qquad \text{(D-6)}$$

In terms of v_g and the vapor length L_g where

$$L_g = \theta_m D/2 \qquad \text{(D-7)}$$

the following residence time can be obtained:

$$\tau_R = \frac{L_g}{v_g} = \frac{\rho_g h_{fg} \delta \theta_m \sin\theta_m}{q_b''} \qquad \text{(D-8)}$$

This temporal scale will be used as a reference to evaluate the time scales involved in the water ingression and steam venting processes.

D.3.2 Water Ingression Process and the Ingression Time Scale

Let $\dot{m}_i$ represent the rate of water ingression in kg/s through the inlet module into the control volume under consideration. The average liquid velocity, v_f, flowing toward the vessel outer surface is

$$v_f = \frac{\dot{m}_i}{\rho_f A_w} \qquad \text{(D-9)}$$

where ρ_f is the liquid density and A_w the vessel outer surface area. The latter is given by

$$\begin{aligned} A_w &= \int_0^{\theta_m} (\pi D \sin\theta)\left(\frac{D}{2} d\theta\right) \\ &= \frac{\pi D^2}{2}(1-\cos\theta_m) \end{aligned} \qquad \text{(D-10)}$$

The liquid flow length, L_f, may vary locally. However, it should be on the order of the gap size, i.e., $L_f \sim \delta$. In terms of v_f and L_f, the ingression time scale can be estimated as

$$\tau_i = \frac{L_f}{v_f} = \frac{\pi D^2 (1-\cos\theta_m)\rho_f \delta}{2\dot{m}_i} \qquad \text{(D-11)}$$

where equations (D-9) and (D-10) have been employed in deriving the above expression. From equations (D-8) and (D-11), the following specific time ratio can be determined for the water ingression process:

$$\begin{aligned} \pi_i &= \frac{\tau_R}{\tau_i} \\ &= \frac{2\theta_m \sin\theta_m \rho_g h_{fg} \dot{m}_i}{(1-\cos\theta_m)\rho_f \pi D^2 q_b''} \end{aligned} \qquad \text{(D-12)}$$

This time ratio should be preserved in simulating the water ingression process to insure the prototypicality of test data.

D.3.3 Steam Venting Process and the Venting Time Scales

To address the steam venting issue, it is necessary to consider the two-phase boundary layer flow through the minimum gap between the reactor vessel and the insulation structure. The flow is driven mainly by buoyancy force but is affected by viscous and surface tension forces. These three separate forces may give rise to different venting time scales. The transfer quantity in question is the momentum of the steam in the control volume, i.e.,

$$\psi = \rho_g v_g = \frac{D q_b''}{2 h_{fg} \delta \sin\theta_m} \qquad \text{(D-13)}$$

where equation (D-6) has been employed in deriving the above expression. The quantity ψ may be increased or decreased at different rates as the two-phase boundary layer is acted upon by the three separate forces.

D.3.3.1 Time Scale Associated with the Buoyance Force

The appropriate length scale, L_B, for the buoyance force is the local elevation H. The flux for the momentum ψ is given by

$$j_B = g(\rho_f - \rho_g)H = g\Delta\rho H \qquad \text{(D-14)}$$

where g is the gravity constant. In terms of ψ, L_B, and j_B, the time scale associated with the buoyancy force can be estimated as

$$\tau_B = \frac{\psi L_B}{j_B} = \frac{D q_b''}{2g\Delta\rho h_{fg}\delta \sin\theta_m} \qquad \text{(D-15)}$$

From equations (D-8) and (D-15), the following specific time ratio can be determined for the buoyancy-controlled steam venting process:

$$\pi_B = \frac{\tau_R}{\tau_B} = \frac{2\rho_g g\Delta\rho h_{fg}{}^2\delta^2\theta_m \sin^2\theta_m}{D q_b''^2} \qquad \text{(D-16)}$$

This time ratio should be preserved in simulating the steam venting process in a subscale experimental model.

D.3.3.2 Time Scale Associated with the Viscous Force

As the two-phase boundary layer flow passes through the minimum gap, there could be a significant frictional loss due to the viscous effect. The appropriate length scale, L_μ, for the viscous force is the hydraulic diameter of the flow channel which is the minimum gap size δ. The flux for the momentum ψ is given by

$$j_\mu = \frac{\mu v_g}{\delta} = \frac{\mu D q_b''}{2\rho_g h_{fg}\delta^2 \sin\theta_m} \qquad \text{(D-17)}$$

where equations (D-6) has been employed in deriving the above expression. In terms of ψ, L_μ, and j_μ, the time scale associated with the viscous force can be estimated as

$$\tau_\mu = \frac{\psi L_\mu}{j_\mu} = \frac{\rho_g \delta^2}{\mu} \qquad \text{(D-18)}$$

From equations (D-8) and (D-18), the following specific time ratio can be determined for the viscous-controlled steam venting process:

$$\pi_\mu = \frac{\tau_R}{\tau_\mu} = \frac{\mu h_{fg}\theta_m \sin\theta_m}{\delta q_b''} \qquad \text{(D-19)}$$

This time ratio should be preserved in simulating the steam venting process in a subscale experimental model.

D.3.3.3 Time Scale Associated with the Surface Tension Force

The appropriate length scale, L_σ, for the surface tension force depends on the interfacial area between the vapor and liquid phases. The interfacial area, in turn, depends on the prevailing two-phase boundary layer flow regime. Relative to the surface tension force, the flux for the momentum ψ is given by

$$j_\sigma = \frac{\sigma}{L_\sigma} \qquad \text{(D-20)}$$

where σ is the surface tension of water. In terms of ψ, L_σ, and j_σ, the time scale associated with the surface tension force can be estimated as

$$\tau_\sigma = \frac{\psi L_\sigma}{j_\sigma} = \frac{D q_b'' L_\sigma{}^2}{2h_{fg}\sigma\delta \sin\theta_m} \qquad \text{(D-21)}$$

From equations (D-8) and (D-21), the following specific time ratio can be determined for the surface-tension-controlled steam venting process:

$$\pi_\sigma = \frac{\tau_R}{\tau_\sigma} = \frac{2\rho_g h_{fg}{}^2 \sigma \delta^2 \theta_m \sin^2\theta_m}{D q_b''^2 L_\sigma{}^2} \qquad \text{(D-22)}$$

This time ratio should be preserved in simulating the steam venting process in a subscale experimental model.

D.4 Experimental Simulation - Subscale Models

In the preceding section, an important time ratio, π_i, has been obtained for the water ingression process whereas three separate time ratios, π_B, π_μ, and π_σ, have been obtained for the steam venting process. By preserving these time ratios, subscale models can be developed to simulate experimentally the effects of the thermal insulation on the boundary layer boiling process. These subscale models are presented below.

D.4.1 Water Ingression Process

The time ratio given by equation (D-12) must be preserved if the water ingression process in the simulation experiment is to have the same effect as that in the actual reactor system. This requires

$$(\pi_i)_{\text{EXP}} = (\pi_i)_{\text{RPV}} \qquad \text{(D-23)}$$

where the subscript "EXP" represents the experimental conditions and the subscript "RPV" represents the reactor pressure vessel conditions. The available experimental evidence indicates that the spatial variation of the local critical heat flux obtained in the subscale SBLB experiments is essentially the same as the full-scale results. By setting $q_w''(\theta)$ equal to $q_{\text{CHF}}''(\theta)$ in equation (D-2), it is expected that

$$[q_b'']_{\text{EXP}} = [q_b'']_{\text{RPV}} \quad \text{if} \quad (\theta_m)_{\text{EXP}} = (\theta_m)_{\text{RPV}} \qquad \text{(D-24)}$$

Thus, it is desirable to use the same location θ_m, of the minimum gap in the simulation experiment. From equations (D-12), (D-23), and (D-24), the following subscale model can be developed:

$$\left(\frac{\dot m_i}{D^2}\right)_{\text{EXP}} = \left(\frac{\dot m_i}{D^2}\right)_{\text{RPV}} \quad \text{or} \quad (\dot m_i)_{\text{EXP}} = \left(\frac{D_{\text{EXP}}}{D_{\text{RPV}}}\right)^2 (\dot m_i)_{\text{RPV}} \qquad \text{(D-25)}$$

Once the value of $\dot m_i$ for the reactor pressure vessel is known, the value of $\dot m_i$ used in the experiment can be determined.

D.4.2 Steam Venting Process

The time ratios given by equations (D-16), (D-19), and (D-22) should be preserved if the steam venting process in the simulation experiment is to have the same effect as that in the actual reactor system. This requires:

$$(\pi_B)_{\text{EXP}} = (\pi_B)_{\text{RPV}} \qquad \text{(D-26a)}$$

$$(\pi_\mu)_{\text{EXP}} = (\pi_\mu)_{\text{RPV}} \qquad \text{(D-26b)}$$

$$(\pi_\sigma)_{\text{EXP}} = (\pi_\sigma)_{\text{RPV}} \qquad \text{(D-26c)}$$

From equations (D-16), (D-24), and (D-26a), the following subscale model can be developed for a buoyancy-controlled steam venting process:

$$\left(\frac{\delta^2}{D}\right)_{\mathrm{EXP}} = \left(\frac{\delta^2}{D}\right)_{\mathrm{RPV}}$$

or (D-27)

$$\delta_{\mathrm{EXP}} = \left(\frac{D_{\mathrm{EXP}}}{D_{\mathrm{RPV}}}\right)^{1/2} \delta_{\mathrm{RPV}}$$

Similarly, from equations (D-19), (D-24), and (D-26b), the following subscale model can be developed for a viscous-controlled steam venting process:

$$\delta_{\mathrm{EXP}} = \delta_{\mathrm{RPV}} \qquad \text{(D-28)}$$

Finally, from equations (D-22), (D-24), and (D-26c), the following subscale model can be developed for a surface-tension-controlled steam venting process:

$$\left(\frac{\delta^2}{DL_\sigma{}^2}\right)_{\mathrm{EXP}} = \left(\frac{\delta^2}{DL_\sigma{}^2}\right)_{\mathrm{RPV}}$$

or (D-29)

$$\delta_{\mathrm{EXP}} = \frac{(L_\sigma)_{\mathrm{EXP}}}{(L_\sigma)_{\mathrm{RPV}}}\left(\frac{D_{\mathrm{EXP}}}{D_{\mathrm{RPV}}}\right)^{1/2} \delta_{\mathrm{RPV}}$$

D.4.3 Scale Distortions and Quantification of Uncertainties

The criteria for developing a subscale model to correctly simulate the water ingression process are given by equations (D-24) and (D-25), whereas those for the steam venting process are given by equations (D-24), (D-27), (D-28), and (D-29). The water ingression process can be fully simulated by choosing appropriate values for θ_m and $\dot{m}_i$ in a subscale experiment according to equations (D-24) and (D-25). On the other hand, the steam venting process cannot be fully simulated. This is because an appropriate value for δ cannot be selected to satisfy equations (D-27) to (D-29) simultaneously. To circumvent this difficulty, it is necessary to optimize the subscale model for the steam venting process and to quantify the uncertainties associated with scale distortions by conducting separate effect tests.

Since the two-phase boundary layer flow resulting from downward facing boiling on the external bottom surface of a reactor pressure vessel is driven mainly by buoyancy, the criterion given by equation (D-27) represents the most important one. This criterion needs to be satisfied in order to preserve the time ratio π_B for the buoyancy-controlled steam venting process. However, by selecting the value of δ according to equation (D-27), some errors will be introduced in the subscale experimental model due to the effects of scale distortions on the time ratios π_μ and π_σ. To quantify the uncertainties, separate effect tests should be performed by using varying gap sizes in the simulation experiment. The effects of scale distortions may then be evaluated from

$$\varepsilon_\mu = \frac{(\pi_\mu)_{\mathrm{RPV}} - (\pi_\mu)_{\mathrm{EXP}}}{(\pi_\mu)_{\mathrm{RPV}}}$$

and (D-30)

$$\varepsilon_\sigma = \frac{(\pi_\sigma)_{\mathrm{RPV}} - (\pi_\sigma)_{\mathrm{EXP}}}{(\pi_\sigma)_{\mathrm{RPV}}}$$

D.5 Concluding Remarks

The key transfer processes that need to be considered in assessing the effect of thermal insulation are the steam generation process, the water ingression process, and the steam venting process. By considering these key transfer processes, four similarity groups that should be preserved to insure the prototypicality of test data have been identified. They are the time ratios π_i for the water ingression process, π_B for the buoyancy-controlled steam venting process, π_μ for the viscous-controlled steam venting process, and π_σ for the surface-tension-controlled steam venting process. The top-ranking parameters that need to be simulated experimentally include the wall heat flux $q_b''(\theta_m)$, the minimum gap size δ, the minimum gap location θ_m, and the water ingression rate $\dot{m}_i$. The foregoing scaling analysis, though preliminary, clearly indicates that a subscale experimental model can be developed to obtain physically meaningful data on the effects of thermal insulation.

It should be noted that an intact insulation structure has been assumed in the present analysis. The situation in which the insulation structure is no longer intact as a result of panel dislocation should be studies as a separate case. Dislocated panels might accumulate in positions where they would contact the reactor vessel. The major issue in such a situation is the adverse effects of thermal insulation on local boiling and dryout at the contact positions. Conceivably, the local CHF value could be lowered significantly if there is a severe limitation to steam venting from the contact positions.

Appendix E
Hydrodynamic CHF Model for Downward Facing Torispherical Surfaces

E-1 Torispherical Surface

A typical torispherical heating surface along with the coordinate systems employed in the present analysis are shown in Figure E.1. Using the (ξ,η) coordinate system, the ellipse describing the heating surface is given by

$$\frac{\xi^2}{a^2} + \frac{\eta^2}{b^2} = 1 \qquad \text{(E.1)}$$

where a and b are the major and the minor axes, respectively, of the ellipse. The angle between the local tangent to the heating surface and the horizontal is $\theta_t(\xi)$ given by

$$\theta_t(\xi) = \tan^{-1}\left[\frac{b\xi}{a^2\left(1-\frac{\xi^2}{a^2}\right)^{1/2}}\right] \qquad \text{(E.2)}$$

A variable cartesian (x,y) coordinate system will be used to formulate the conservation equations for the vapor mass and the linear momentum. The local x direction is tangential to the heating surface, whereas the local y direction is perpendicular to the vessel outer surface. At a given location along the torispherical surface, the arc length x is equal to

$$x = \int_0^{\xi} \frac{[a^4+(b^2-1)\xi^2]^{1/2}}{a(a^2-\xi^2)^{1/2}}\, d\xi \qquad \text{(E.3)}$$

Similar to the case of a hemispherical heating surface, there are four flow variables that need to be solved for. These are the vapor velocity, u_g, the liquid velocity, u_l, the critical heat flux, q''_{CHF}, and the boundary layer thickness, δ. Each of these flow variables is a function of the location x along the heating surface. The first equation given by

$$q_{CHF}'' = B\rho_g h_{fg}\left[\frac{\sigma u_l}{\rho_l \delta_o}\left(1+\frac{\rho_g}{\rho_l}\right)\left(\frac{\rho_g}{\rho_l}\right)^{-1.6}\right]^{1/3} \qquad \text{(E.4)}$$

is obtained by applying Helmholtz instability theory to the micro-layer underneath the vapor slugs forming on the heating surface. The other three equations are obtained from the conservation of the vapor mass, the conservation of the linear momentum, and an independent equation for the relative velocity between the liquid phase and the vapor phase.

E-2 Analysis of the Two-Phase Boundary Layer

Using the variable (x,y) coordinate system of Figure E-1, the vapor continuity equation takes on the following form:

$$\frac{d}{dx}\left[\alpha u_g \delta(\xi(x,y=0)+0.5\delta\sin\theta_t)\right] = \frac{q_{CHF}''\xi(x,y=0)}{\rho_g h_{fg}} \qquad \text{(E.5)}$$

where $\xi(x,y=0)$ is related to x through equation (E.3). The conservation of the linear momentum gives

$$\begin{aligned}
&\frac{d}{dx}\left[\begin{matrix}(\rho_l(1-\alpha)u_l^2+\rho_g\alpha u_g^2)\\ (\xi(x,y=0)+0.5\delta\sin\theta_t)\delta\end{matrix}\right]\\
&= (\rho_l-\rho_g)\alpha g\sin\theta_t\delta\\
&[\xi(x,y=0)+0.5\delta\sin\theta_t] \qquad \text{(E.6)}\\
&-0.5\,C_f[\rho_g\alpha u_g+\rho_l(1-\alpha)u_l]\\
&[\alpha u_g+(1-\alpha)u_l]\\
&[\xi(x,y=0)+0.5\delta\sin\theta_t]
\end{aligned}$$

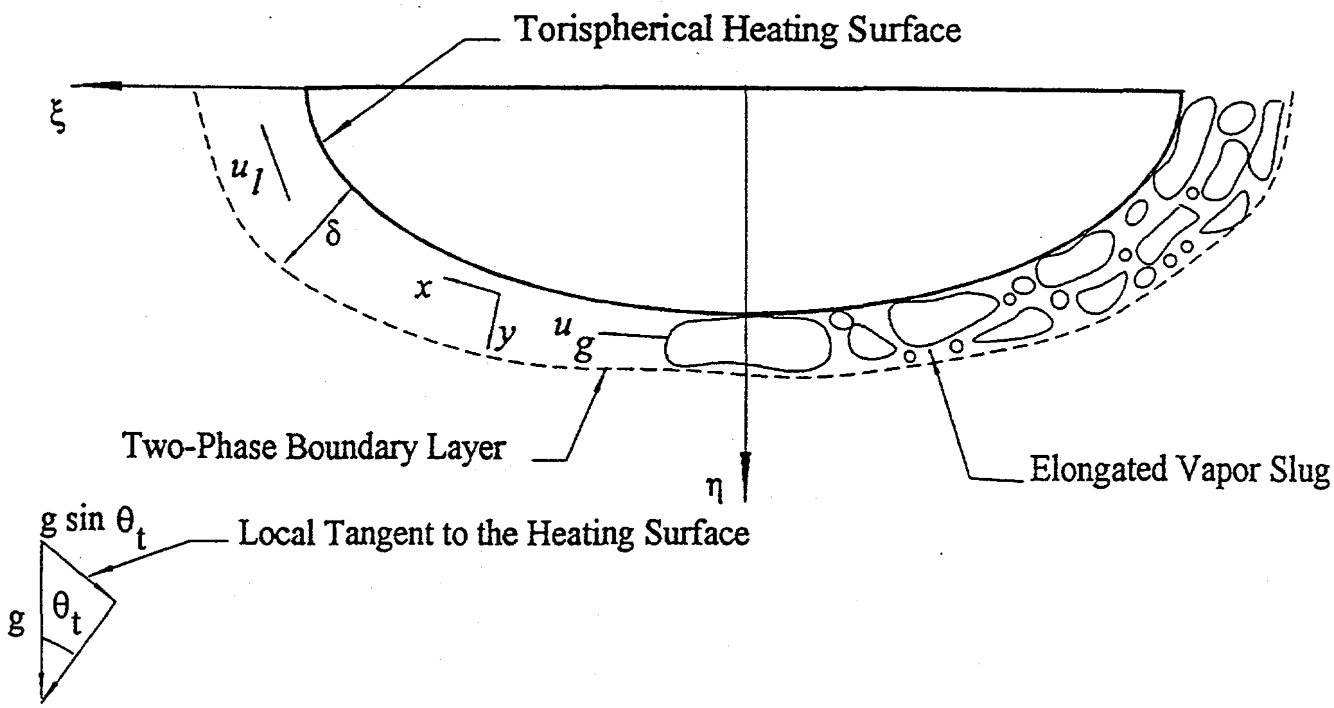

Figure E.1. Schematic of the Two-Phase Boundary Layer on the Outside of a Torispherical Heating Surface.

The fourth equation is an independent expression for the relative velocity between the liquid and the vapor phases, which is given by

$$u_g = u_l + 1.53\left[\frac{\sigma g \sin\theta_t(\rho_l - \rho_g)}{\rho_l^2}\right]^{1/4} \qquad \text{(E.7)}$$

In order to simplify the governing equations, the following dimensionless flow variables Q_{CHF}, Δ, u_g, u_l, X, and Ψ are introduced such that

$$q_{CHF}'' = \rho_g h_{fg}\left[\frac{\sigma g(\rho_l - \rho_g)}{\rho_g^2}\right]^{1/4}\left(1 + \frac{\rho_g}{\rho_l}\right)^{1/3} Q_{CHF} \qquad \text{(E.8a)}$$

$$\delta = \left[\frac{\sigma a^2}{g(\rho_l - \rho_g)}\right]^{1/4}\left(\frac{\rho_g}{\rho_l}\right)^{-0.1}\Delta \qquad \text{(E.8b)}$$

$$X = \frac{x}{a} \qquad \text{(E.8c)}$$

$$u_l = \left[\frac{ag(\rho_l - \rho_g)}{\rho_l}\right]^{1/2} U_l \qquad \text{(E.8d)}$$

$$X = \frac{x}{a} \qquad \text{(E.8e)}$$

$$\xi = \left[\frac{\sigma a^2}{g(\rho_l - \rho_g)}\right]^{1/4}\left(\frac{\rho_g}{\rho_l}\right)^{-0.1}\psi \qquad \text{(E.8f)}$$

Using these dimensionless variables, the governing equations take on the following forms:

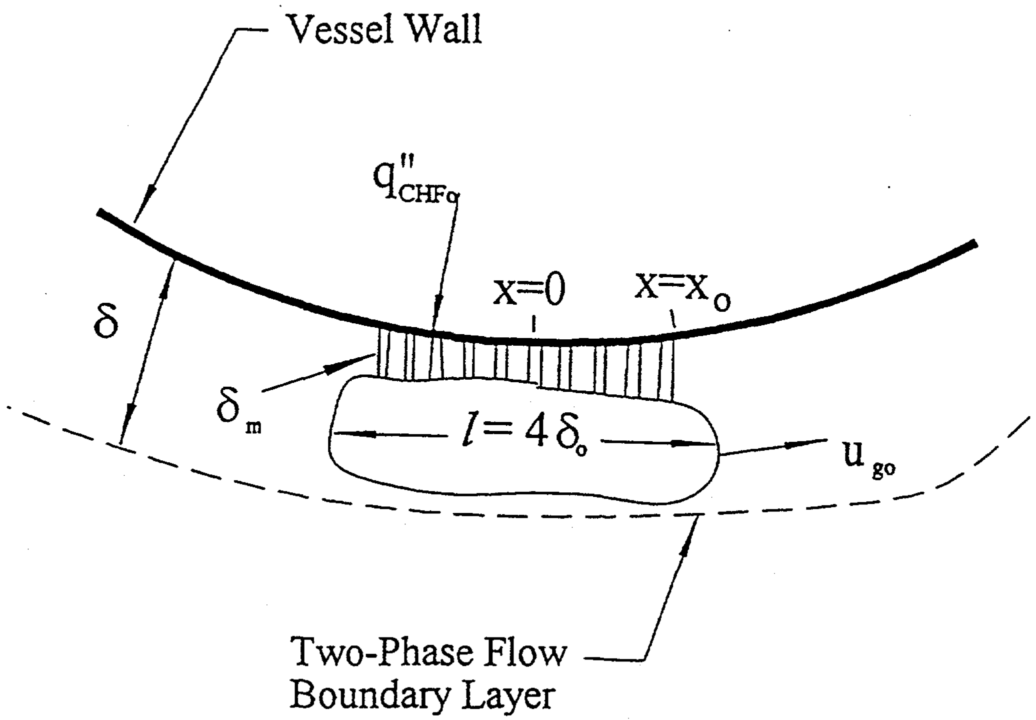

Figure E.2. The Micro-Layer and the Vapor Slug at the Bottom Center of the Vessel.

$$Q_{CHF} = B\left(\frac{U_l}{\Delta_o}\right)^{1/3} \tag{E.9}$$

$$\begin{aligned}&\frac{d}{dX}\left[\alpha U_g \Delta(\psi + 0.5\Delta\sin\theta_t)\right]\\ &= Q_{CHF}\psi\end{aligned} \tag{E.10}$$

$$\begin{aligned}&\frac{d}{dX}\left\{\begin{matrix}\left[(1-\alpha)\left(\frac{\rho_g}{\rho_l}\right)^{-0.2} U_l^2 + \alpha U_g^2\right]\\ \Delta(\psi + 0.5\Delta\sin\theta_t)\end{matrix}\right\}\\ &= \alpha\Delta(\psi + 0.5\Delta\sin\theta_t)\sin\theta_t\left(\frac{\rho_g}{\rho_l}\right)^{-0.2}\\ &-0.5\,C_f\,L_b^{-1/2}\left(\frac{\rho_g}{\rho_l}\right)^{0.1}\end{aligned}$$

$$\begin{aligned}&\left[\alpha U_g + \left(\frac{\rho_g}{\rho_l}\right)^{-0.6}(1-\alpha)U_l\right]\\ &\left[\alpha U_g + \left(\frac{\rho_g}{\rho_l}\right)^{0.4}(1-\alpha)U_l\right]\\ &\left[\psi + 0.5\Delta\sin\theta_t\right]\end{aligned} \tag{E.11}$$

$$\begin{aligned}U_l &= \left(\frac{\rho_g}{\rho_l}\right)^{-0.4} U_g\\ &-1.53\,(L_b{}^2\sin\theta_t)^{1/4}\end{aligned} \tag{E.12}$$

where L_b is given by

$$L_b = \frac{1}{a}\left[\frac{\sigma}{g(\rho_l - \rho_g)}\right]^{1/2} \tag{E.13}$$

E-3 Initial Conditions

In order to solve equations (E.9) to (E.12), a set of initial conditions is needed for the various flow variables. This requires consideration of the vapor mass that forms in the bottom center region. It is assumed that the critical heat flux throughout this region, shown in Figure E.2, is constant equal to q''_{CHFo}. Based on the fact that all the vapor that is generated in this part of the heating surface has to cross the boundary layer at $x = x_o$, we can write

$$\begin{aligned} &\rho_g \xi(x = x_o, y = 0) \\ &\delta_o \alpha u_{go} h_{fg} \;=\; q_{CHFo}{}'' \int_0^{x_o} \xi dx \end{aligned} \qquad \text{(E.14)}$$

Equations (E.4) and (E.7) can be used to eliminate the vapor velocity from equation (E.13), which results in the following quadratic equation:

$$\begin{aligned} &\frac{q_{CHFo}{}''^{3}}{B^3 \rho_g^{1.4} h_{fg}^3 \rho_l^{0.6} \sigma} \delta_o^2 \\ &+1.53 \left[\frac{\sigma g \sin\theta_t (\rho_l - \rho_g)}{\rho_l^2} \right]^{1/4} \delta_o - \\ &\frac{q_{CHFo}{}''}{\rho_g \xi(x = x_o, y = 0) \alpha h_{fg}} \\ &\int_0^{x_o} \xi dx \;=\; 0 \end{aligned} \qquad \text{(E.15)}$$

The integral in equation (E.14) can be evaluated using equation (E.3) and the Simpson's Method. Then equation (E.14) can be solved for the boundary layer thickness in the bottom center region for a given location x_o and a given value for the critical heat flux, q''_{CHFo}. Once the boundary layer thickness is known, equation (E.4) can then be used to estimate the velocity of the liquid phase. This value for u_l can be used in equation (E.7) to find the vapor phase velocity. Finally, these initial conditions for the dimensional flow quantities can be used in equation (E.8) to deduce initial conditions for the dimensionless flow variables, which are used in the numerical routine to solve for Q_{CHF}, U_l, U_g, and Δ along the outer surface of the vessel.

E-4 Numerical Solution Method

Equations (E.9) and (E.12) are used to rearrange equations (E.10) and (E.11) so that they can be solved using the Runga-Kutta method. As a result, the following two first order equations are obtained:

$$\begin{aligned} &\frac{d\Delta^*}{dX} \;=\; Q_{CHF} \psi \alpha^{-1} U_g^{-1} \\ &-0.0522 \Delta^* U_g^{-1} \frac{dU_l}{dX} - \\ &0.0799 L_b^{1/2} \Delta^* U_g^{-1} \frac{d}{dX} \left[(\sin\theta_t)^{1/4} \right] \end{aligned} \qquad \text{(E.16)}$$

$$\begin{aligned} &\frac{dU_l}{dX} \;=\; \{4.374 \alpha \Delta (\psi + 0.5 \Delta \sin\theta_t) \\ &-0.00195 [\alpha U_g + 83.71 (1 - \alpha) U_l] \\ &[\alpha U_g + 0.0522 (1 - \alpha) U_l] \\ &[\psi + 0.5 \Delta \sin\theta_t] \\ &-4.37 (1 - \alpha) U_l^2 Q_{CHF} \psi \alpha^{-1} U_g^{-1} + \\ &[0.349 (1 - \alpha) L_b^{1/2} U_l^2 \Delta^* U_g^{-1} \\ &-0.0799 \alpha U_g \Delta^*] \frac{d}{dX} \\ &\left[(\sin\theta_t)^{1/4} \right] - U_g Q_{CHF} \psi \} \\ &\{8.75 U_l \Delta^* (1 - \alpha) - 0.228 (1 - \alpha) U_l^2 \Delta^* U_g^{-1} \\ &+0.0522 \alpha U_g \Delta^* \}^{-1} \end{aligned} \qquad \text{(E.17)}$$

where,

$$\Delta^* \;=\; \Delta (\psi + 0.5 \Delta \sin\theta_t) \qquad \text{(E.18)}$$

Equations (E.15) and (E.16) were obtained using the following water properties: $\sigma = 0.0588$ N/m, $\rho_l = 958$ kg/m^3, and $\rho_g = 0.598$ kg/m^3. In addition, it can be shown that the derivative with respect to X of the sine of the angle of inclination, θ_t, raised to the power 0.25 is given by

$$\begin{aligned} &\frac{d}{dX} \left[(\sin\theta_t)^{1/4} \right] \\ &\;=\; 0.25 \cos\theta_t (\sin\theta_t)^{-3/4} \frac{d\theta_t}{dX} \end{aligned} \qquad \text{(E.19)}$$

where,

$$\frac{d\theta_t}{dX} = a\left[1+\frac{b^2\xi^2}{a^4(1-\xi^2/a^2)}\right]^{-1/2} \left[1+\left(\frac{b\xi}{a^2(1-\xi^2/a^2)^{1/2}}\right)^2\right] \left[\frac{a^2 b(1-r^2/a^2)^{1/2} + b\,r^2(1-r^2/a^2)^{-1/2}}{a^4(1-r^2/a^2)}\right] \qquad \text{(E.20)}$$

Equations (E.15) and (E.16) along with all the other relevant equations can be solved using the Runga-Kutta method. The computer program *CHFELLIP*, was developed to carry out the numerical solution.

E-5 Comparison with Experiments

Measurements of the critical heat flux on the external bottom surface of a torispherical vessel having a nominal diameter of 12" (0.305 m) have been made in the SBLB test facility using saturated water as the working fluid. The CHF data indicated that the critical heat flux was almost constant throughout the entire flat bottom region of the vessel, with a value very close to 0.5 MW/m^2. Results of the model prediction, on the other hand, indicate that the local critical heat flux has a value of 0.4 MW/m^2 in the bottom center region of the vessel and increases to 0.65 MW/m^2 near the edge. The agreement between the prediction and the data is within the numerical and experimental uncertainties.